Triplet Exciton Management via Solid-State Interactions in Organic Semiconductors

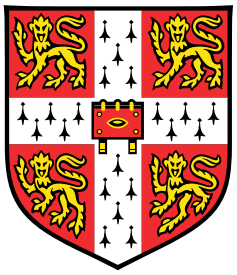

Jiale Feng

Department of Physics
University of Cambridge

This dissertation is submitted for the degree of
Doctor of Philosophy

Selwyn College May 2020

I would like to dedicate this thesis to my loving parents, my family, and all the people who make my life colourful.

Declaration

I hereby declare that except where specific reference is made to the work of others, the contents of this dissertation are original and have not been submitted in whole or in part for consideration for any other degree or qualification in this, or any other university. This dissertation is my own work and contains nothing which is the outcome of work done in collaboration with others, except as specified in the text and Acknowledgements. This dissertation contains fewer than 65,000 words including appendices, bibliography, footnotes, tables and equations and has fewer than 150 figures.

Jiale Feng
May 2020

Acknowledgements

I would like to acknowledge many wonderful people who made this academic journey and this thesis possible and also made the last three years memorable.

Firstly, I am deeply grateful to my supervisors, Prof. Neil Greenham and Dr. Dan Credgington, for giving me the opportunity to embark on such an exciting research journey and for their unfailing support, guidance, and encouragement, not to mention funding my trips to conferences and experiments.

I am so lucky to collaborate with many brilliant people throughout my Ph.D. Deep gratitude goes to Dr. Alex Romanov for synthesising and generously supplying countless new materials. Further thanks go to Prof. Mikko Linnolahti, Dr. Elliot Taffet, Prof. David Beljonne, and Dr. Tom Penfold for your computational work and discussions to help with the data interpretation. Thank you to Dr. Tim Hele for the inspiring discussions we had about the molecular symmetry analysis. I must thank Prof. Anna Köhler and Prof. Heinz Bässler for your kind support and patience since we first met at the conference in Dubrovnik. I am grateful to my peer collaborator and friend Lupeng Yang for helping me with the coding and simulations, and for exciting discussions we had in the Kapitza and Mott buildings.

To the members of the Optoelectronics group, I would like to profoundly thank you all for being helpful and generously lending me your time, effort and expertise from the beginning to the end of my Ph.D. Especially, thank you to Dr. Patrick Conaghan, Dr. Emrys Evans, Dr. Alex Gillett, Dr. Tudor Thomas, Dr. David Palecek, Heather Goodwin, Saul Jones, and Chana Phansa for patiently training and helping me on those complicated spectroscopy experiments. I am so proud of being part of this group and working with you all. I also need to say a big thank you to all of the technical and administrative staff: Richard Gymer, Alex Crook, Roger Beadle, Jennie Nelson, William Mortimer, and Egle Bunkute for running the lab and the group smoothly.

Thank you to my friends who have supported me firmly through the highs and lows of research. I am really thankful to be around so many interesting and amazing people. Thank you to Bluebell for not only being such a wonderful deskmate with me, but also for your constant support, encouragement and friendship. Thank you to Xinyu, Qinying, Baodan, Kexin, Chen, Xinyi, Peicheng, Kangyu, Jiaming, Linjie for all your company, afternoon tea

we had and gossips we shared. I will cherish all these precious memories forever. Thank you also goes to my old friends who have encouraged me all the time by calls and messages even if we are in different time zones. I would like to thank all the former Credgington group members: Bluebell, Xinyu, Qinying, Saul, Xinyi, Campbell, Antti, Dan S, Hwan Hee, Paloma, and Joe for all the joyful formals, bars, fish and chips we had.

I am further thankful to Selwyn College for being very supportive, and providing me with such a well-equipped and comfortable living environment, especially the piano in the music room which helps me to calm my nerves, also for funding my trips to conferences. Thanks to my friends living in college together, Chenyang, Wenyan, and Yuejia, for all those cooking nights and drinking nights we spent together. I will miss the courts, the sakura, the dining hall, the chapel, the bar, the garden, the MCR, everything.

Finally, I would like to express my deepest appreciation to my parents and my family for your unwavering love and support, giving me strength and courage to be what I want to be. Thank you for always being there for me. This thesis would never have been completed without you.

Abstract

Tightly-bound excitons play an important role in the function of molecular materials for light emission and light harvesting. This thesis investigates the effects of solid-state interactions on triplet excitons in a new family of organometallic light emitters, carbene-metal-amides (CMAs). Triplet excitons are normally silent in luminescence due to the spin-forbidden decay process, whereas effectively harvesting triplet excitons helps to boost the performance of light-emitting devices. As the triplet excitons are sensitive to both molecular properties and external environment, in this thesis we deploy optical spectroscopy techniques to understand the effect of solid-state interactions on triplet excitons.

After introducing the relevant theoretical and experimental background of triplet formation in a single molecule and interactions between molecules, we firstly describe the intermolecular electrostatic interactions and the role of triplet diffusion and find that the combined effects of both blueshift the charge-transfer energy while other photophysical properties remain relatively constant in gold-bridged CMA1.

We then describe the crystallisation of CMA1 thin films, which allows us to experimentally investigate the link between molecular conformations and photophysical properties. A combination of restricted torsional distortion and molecular electronic polarisation greatly blueshifts the charge-transfer emission by around 400 meV in the crystalline versus the amorphous phase. We also discover that the intersystem crossing rate and emission kinetics are unaffected by the extent of torsional distortion.

Finally, we apply electrostatic interactions to the other two coinage metal-bridged CMAs to explore the effect of heavy metal atoms on the intersystem crossing and luminescence mechanism. We show that the photophysical properties do not reflect expected trends based upon the heavy atom effect as both direct coupling between charge-transfers states and spin-vibronic coupling via an intermediate state are present.

Table of contents

List of figures **xv**

List of tables **xxi**

List of publications **xxiii**

1 Introduction **1**

2 Theoretical Considerations **5**

2.1 Introduction 5

2.2 Electronic structure 5

2.2.1 Atomic orbitals 6

2.2.2 Hybridisation 7

2.2.3 Molecular orbitals 8

2.2.4 From orbitals to states 9

2.3 Neutral excitations and excitons 10

2.3.1 Singlets, triplets and exchange energy 11

2.3.2 Photoexcitation and electrical-excitation 13

2.3.3 Radiative transitions between molecular states: absorption and emission 14

2.3.4 Non-radiative transitions between molecular states: internal conversion and intersystem crossing 19

2.3.5 Exciton interactions 22

2.4 Environmental effects on excited states and charge transfer 23

2.4.1 From single molecule to the condensed phase 23

2.4.2 Energy transfer process 27

2.4.3 Charge transfer process 28

3 Experimental Methods **37**

3.1 Introduction 37

3.2 Sample preparation . . . 37
3.3 Spectroscopy . . . 38
3.3.1 Steady state absorption . . . 38
3.3.2 Steady state photoluminescence . . . 39
3.3.3 Transient absorption spectroscopy . . . 39
3.3.4 Time-resolved photoluminescence spectroscopy . . . 40
3.3.5 Raman spectroscopy . . . 42
3.3.6 Photoluminescence quantum efficiency measurement . . . 45
3.4 Structural characterisation . . . 47
3.4.1 X-ray diffraction . . . 47
3.5 Computation . . . 47
3.5.1 Density functional theory calculations . . . 47

4 Non-Chemical Control of Triplet Emission in Donor-Bridge-Acceptor Organometallics 51
4.1 Abstract . . . 51
4.2 Introduction . . . 52
4.3 Results and Discussion . . . 53
4.3.1 The CMA1 molecule . . . 53
4.3.2 Dopant concentration and role of diffusion for CMA1 in PVK host . 54
4.3.3 Organic polar molecule hosts and role of electrostatic interactions . 67
4.3.4 Coupling mechanism for triplet harvesting . . . 74
4.3.5 Extension to other CMAs . . . 84
4.4 Conclusions . . . 84

5 Influence of Nuclear Reorganisation and Polarisation on Crystalline Carbene-Metal-Amide Photoemitters 87
5.1 Abstract . . . 87
5.2 Introduction . . . 88
5.3 Results and Discussion . . . 90
5.3.1 Thin-film crystallisation . . . 90
5.3.2 Steady-state spectroscopy investigations . . . 93
5.3.3 Time-resolved spectroscopy investigations . . . 93
5.3.4 Computational simulations . . . 103
5.4 Conclusions . . . 107

6 Influence of the Heavy Atom Effect on the Photophysics of Carbene-Metal-Amide Light Emitters 109
6.1 Abstract . . . 109
6.2 Introduction . . . 110
6.3 Results and discussion . . . 111
6.3.1 Coinage metal CMA molecules . . . 111
6.3.2 Intersystem crossing rate of coinage metal CMAs in a non-polar solid-state matrix . . . 114
6.3.3 Photophysical characterisations of coinage metal CMAs in a non-polar solid-state matrix . . . 117
6.3.4 Photophysical characterisations of coinage metal CMAs with the presence of strong solid-state electrostatic interactions . . . 125
6.3.5 Discussion of the luminescence mechanism of the coinage metal CMAs . . . 135
6.4 Conclusions . . . 136

7 Conclusions and Outlook 139
7.1 Influence of triplet diffusion and electrostatic interactions . . . 139
7.2 Influence of nuclear reorganisation and polarisation . . . 140
7.3 Influence of the heavy atom effect . . . 141
7.4 Outlook and concluding remarks . . . 142

References 145

List of figures

1.1 (A) Conventional and (B) inverted OLED device structures. 3

2.1 (a) sp hybridisation of atomic orbitals for the valence electrons of the C atom. (b) sp^2 hybridisation. (c) The four hybrid functions for the sp^3 hybridisation. 8

2.2 Simple energy level diagram illustrating the formation of σ and π bonds from atomic orbitals for ethene. 9

2.3 Illustration of configuration interaction. 10

2.4 The singlet states S_0, S_1, and S_2 represented (a) in an orbital diagram and (b) in a state diagram 11

2.5 Vector diagram of orientations of two electron spins for the singlet and triplet state. 13

2.6 (A) Potential energy diagram showing the relaxation energies $E_{rel,abs}$ and $E_{rel,em}$ associated with the process of absorption and emission. (B) Geometric relaxation process shown in a molecular illustration. 17

2.7 The potential energy curves of S_1 and T_1 states for the case of (A) weak coupling and (B) strong coupling between two states. 22

2.8 Schematic illustrating the effect of van der Waals interactions between a chromophore and adjacent molecules. 24

2.9 Schematic illustrating the effect of polarization on the excited state energy levels ε of chromophores. 25

2.10 Illustration of the energy shifts associated with solvation. 26

2.11 (A) Diagram illustrating Förster resonance energy transfer (FRET) from a singlet donor to a singlet acceptor. (B) Diagram illustrating Dexter energy transfer (DET) from a singlet donor to a singlet acceptor. (C) Diagram illustrating Dexter Energy Transfer (DET) from a triplet donor to a triplet acceptor. 29

2.12 Illustration of a charge carrier, generated at an arbitrary energy, that hops within a Gaussian DOS. 30

2.13 (A) Frontier orbital representation of the triplet transfer mechanism as charge transfer. (B) The inner reorganisation energy consists of the geometric relaxation energies of molecule A and B. (C) The potential energy of the entire system (molecule A, B and surrounding molecules) versus a generalised configuration coordinate describing the entire system. 32
2.14 Schematic representation of (A) adiabatic and (B) non-adiabatic transports in the configurational coordinates for a two-site system. The arrow indicates the path of the excited state. 35
2.15 Illustration of the adiabatic potential energy surfaces for the electronic charge-transfer (CT) and ground (G) states. 36

3.1 Configuration and working principle of an image intensifier tube in an intensified CCD camera (ICCD). 41
3.2 Jablonski diagram of Rayleigh scattering, Stokes Raman scattering and Anti-stokes Raman scattering. 44
3.3 Illustration of three configurations of PLQE measurements: (A) the empty measurement; (B) laser beam indirectly strikes the sample; (C) laser beam directly strikes the sample. 46
3.4 (A) Bragg's law for constructive interference of two parallel X-rays after diffracting from two adjacent crystal planes. (B) Geometry of the Bragg condition in experimental situations. 48

4.1 (A) Chemical structure of CMA1. (B) HOMO and LUMO wavefunctions of CMA1 from DFT calculations. 54
4.2 Optical steady state absorption spectrum of CMA1 neat thin film. 55
4.3 Steady state absorption and photoluminescence of CMA1 in PVK host at different concentrations. 55
4.4 Steady state absorption spectra of CMA1 in various solvents at 300 K. . . . 56
4.5 Steady state photoluminescence spectra of CMA1 in various solvents at 300 K. 56
4.6 Room temperature emission integral of CMA1 and PVK composites. 57
4.7 Room temperature time resolved PL peak energy of CMA1 in PVK at different concentrations to track the spectral diffusion. 59
4.8 Cryogenic time resolved PL peak position of 10% CMA1 in PVK at 10 K, 150 K, and 300 K. 60
4.9 Cryogenic time resolved PL peak position of 80% CMA1 in PVK at 10 K, 150 K, and 300 K. 60
4.10 Cryogenic emission integral of 10% CMA1 in PVK. 61

4.11 Cryogenic emission integral of 80% CMA1 in PVK. 61
4.12 Integrated PL intensity plotted against temperature of 10% CMA1 in PVK. 62
4.13 Steady state PL peak energy of CMA1 in a range of hosts varying weight concentrations from 100% to 5%. 64
4.14 Steady state photoluminescence of various hosts in solid thin films. 65
4.15 Chemical structures and electric dipole moments of various small-molecule hosts. 66
4.16 Steady state absorption and photoluminescence of CMA1 in TSPO1 host at different concentrations. 67
4.17 Room temperature emission integral of CMA1 and TSPO1 composites. . . 68
4.18 Cryogenic emission integral of 10% CMA1 in TSPO1. 69
4.19 Cryogenic emission integral of 80% CMA1 in TSPO1. 69
4.20 Integrated PL intensity plotted against temperature of 10% CMA1 in TSPO1. 70
4.21 Room-temperature time-resolved PL peak energy of CMA1 in TSPO1 at different concentrations to track the spectral diffusion. 71
4.22 Cryogenic time resolved PL peak position of 10% CMA1 in TSPO1 at 10 K, 150 K, and 300 K. 71
4.23 Cryogenic time resolved PL peak position of 80% CMA1 in TSPO1 at 10 K, 150 K, and 300 K. 72
4.24 PXRD patterns of: (a) neat CMA1; (b) 10 wt.% CMA1 in PVK; (c) 10 wt.% CMA1 in TSPO1; (d) 80 wt.% CMA1 in TSPO1 thin films. 73
4.25 Energy diagram for CMA1 with various orientation between the planes of CAAC carbene and carbazole: planar (0°), twisted (45°) and rotated (90°). . 75
4.26 Steady state photoluminescence of CMA1 in 2-MeTHF glass at 77 K. . . . 76
4.27 Steady state PL peak energy of 10% and 80% concentration of CMA1 in TSPO1 and PVK host at different temperatures. 77
4.28 PL decay rate of 10% and 80% concentration of CMA1 in TSPO1 and PVK at different temperatures as a function of 1/Temperature. 78
4.29 Transient absorption (TA) colour map of 5 wt.% CMA1 in TSPO1 films under various pump power. 79
4.30 Molecular orbitals of CMA1 from DFT calculations, red/green corresponds to positive/negative sign of wavefunctions. 81
4.31 Charge transfer upon excitation, from blue region to red region. 82
4.32 (A) Dependence of PL peak energy of various CMAs on the doping concentration in TSPO1 host. (B) Chemical structures of CMA1, CMA4, CMA5 and CMA6. 84

5.1 Pictures show the crystallisation of 80 w.t% CMA1 in polymer matrix PEO(100,000) (right), for comparison with neat CMA1 thin film (left). . . . 91
5.2 X-ray diffraction of crystalline and amorphous CMA1. 92
5.3 Raman spectra of crystalline and amorphous CMA1. 92
5.4 Steady-state absorption and normalised photoluminescence spectra of CMA1 in toluene solution (1 mg/mL), amorphous and crystalline CMA1 thin films. 94
5.5 Room temperature time-resolved photoluminescence peak energy of amorphous and crystalline CMA1 to track the spectral diffusion. 95
5.6 Normalised delayed emission kinetics with monoexponential fits to crystalline and amorphous CMA1 within the 5 – 4000 ns time range. 95
5.7 Cryogenic emission integral of crystalline CMA1 film at a temperature series. 96
5.8 Cryogenic total emission integral of neat amorphous CMA1 film at a temperature series. 97
5.9 PL decay rate and integrated PL intensity of crystalline and amorphous CMA1 at different temperatures as a function of 1/Temperature. 98
5.10 Cryogenic time-resolved PL peak position of crystalline CMA1 at 10 K, 150 K, and 300 K. 98
5.11 Temperature dependent steady-state photoluminescence of crystalline CMA1 film. 99
5.12 Temperature dependent steady-state photoluminescence of neat amorphous CMA1 film. 100
5.13 Room temperature transient absorption spectra of (a) CMA1 in toluene at 1 mg/mL, (b) neat amorphous CMA1 film, and (c) crystalline CMA1 film on picosecond-nanosecond time scales. 101
5.14 Kinetics of singlet and triplet species deconvoluted from transient absorption spectra in Fig. 5.13 of (a) CMA1 in toluene (1 mg/mL), (b) neat amorphous CMA1 drop-cast film, and (c) crystalline CMA1 drop-cast film. 102
5.15 Illustration of a molecular cluster used to simulate the crystal environment. 103
5.16 Summary of CMA1 phase-dependent photophysics. 107

6.1 Chemical structure of coinage metal bridged carbene-metal-amide (CMA) photoemitters. 111
6.2 Highest occupied molecular orbital (HOMO) and lowest unoccupied molecular orbital (LUMO) wavefunctions of coinage-metal-bridged CMAs from DFT calculations. 112
6.3 Steady-state molar absorptivity spectra of CMA(Au), CMA(Ag), and CMA(Cu) in toluene at 300 K. 113

6.4 Steady-state photoluminescence spectra of CMA(Au), CMA(Ag), and CMA(Cu) in toluene at 300 K. 113
6.5 Room temperature transient absorption spectra of (a) 5 wt.% CMA(Au) in PS thin film, (b) 5 wt.% CMA(Ag) in PS thin film, and (c) 5 wt.% CMA(Cu) in PS thin film on picosecond-nanosecond time scales. 115
6.6 Kinetics of singlet and triplet species decomposed from transient absorption spectra in Fig. 6.5 of (a) 5 wt.% CMA(Au) in PS thin film, (b) 5 wt.% CMA(Ag) in PS thin film, and (c) 5 wt.% CMA(Cu) in PS thin film on picosecond-nanosecond time scales. 116
6.7 Steady-state absorption and photoluminescence of CMA(Cu) in PS host at different concentrations. 118
6.8 Steady-state absorption and photoluminescence of CMA(Ag) in PS host at different concentrations. 118
6.9 Steady-state absorption and photoluminescence of CMA(Au) in PS host at different concentrations. 119
6.10 Room temperature emission integral of CMA(Cu) in PS composites. 119
6.11 Room temperature emission integral of CMA(Ag) in PS composites. 120
6.12 Room temperature emission integral of CMA(Ag) in PS composites. 121
6.13 Temperature dependent steady-state photoluminescence of 10% CMA(Cu) in PS thin film. 121
6.14 Temperature dependent steady-state photoluminescence of 10% CMA(Au) in PS thin film. 122
6.15 Cryogenic emission integral of 10% CMA(Cu) in PS. 122
6.16 Cryogenic emission integral of 10% CMA(Ag) in PS. 123
6.17 Temperature dependent steady-state photoluminescence of 10% CMA(Ag) in PS thin film. 123
6.18 Steady-state photoluminescence of CMA(Au), CMA(Ag), and CMA(Cu) in 2-MeTHF at 77 K. 124
6.19 Steady-state absorption and photoluminescence of CMA(Cu) in TSPO1 host at different concentrations. 127
6.20 Steady-state absorption and photoluminescence of CMA(Ag) in TSPO1 host at different concentrations. 127
6.21 Room temperature emission integral of CMA(Cu) in TSPO1 composites. . 128
6.22 Room temperature emission integral of CMA(Ag) in TSPO1 composites. . 128
6.23 Room temperature time-resolved PL peak energy of CMA(Cu) in TSPO1 at different concentrations to track the spectral diffusion. 129

6.24 Room temperature time-resolved PL peak energy of CMA(Ag) in TSPO1 at different concentrations to track the spectral diffusion. 129
6.25 Cryogenic emission integral of 10% CMA(Cu) in TSPO1. 130
6.26 Temperature dependent steady-state photoluminescence of 10% CMA(Cu) in TSPO1. 130
6.27 PL decay rate of 10% and 80% concentration of CMA(Cu) in TSPO1 and 10% in PS at different temperatures as a function of 1/Temperature. 131
6.28 Temperature dependent steady-state photoluminescence of 10% CMA(Au) in TSPO1. 131
6.29 PL decay rate and integrated PL intensity plotted against temperature of 10% and 80% CMA(Cu) in TSPO1 host and 10% CMA(Cu) in PS host. 132
6.30 Cryogenic emission integral of 10% CMA(Ag) in TSPO1. 133
6.31 Temperature dependent steady-state photoluminescence of 10% CMA(Ag) in TSPO1. 133
6.32 Time-resolved photoluminescence spectra of 10% CMA(Ag) in TSPO1 at 10 K. 134
6.33 PL decay rate of 10% and 80% concentration of CMA(Ag) in TSPO1 and 10% in PS at different temperatures as a function of 1/Temperature. 134

List of tables

4.1 Luminescence lifetime and photoluminescence quantum efficiency (PLQE) of CMA1 in PVK host varying concentrations from 5 wt.% to neat CMA1 films. 58
4.2 Mean energy and standard deviation of density of states (DOS) input in Monte Carlo simulations of CMA1 in PVK concentration series at 300 K. . 63
4.3 Mean energy and standard deviation of density of states (DOS) input in Monte Carlo simulations of 10% and 80% CMA1 in PVK at 10 K and 150 K. 63
4.4 Luminescence lifetime and photoluminescence quantum efficiency (PLQE) of CMA1 in TSPO1 host varying concentrations from 5 wt.% to neat CMA1 films. 68
4.5 Mean energy and deviation of density of states (DOS) input in Monte Carlo simulations of CMA1 in TSPO1 concentration series at 300 K. 70
4.6 Mean energy and deviation of density of states (DOS) input in Monte Carlo simulations of 10% and 80% CMA1 in TSPO1 at 10 K and 150 K. 72
4.7 Luminescence lifetime and photoluminescence quantum efficiency (PLQE) of CMA1 in different solvents. 76
4.8 Estimated intersystem crossing (ISC) time extracted from Fig. 4.29. 77
4.9 Orbital contributions to vertical excitations ($S_0 \rightarrow S_1$ - S_6). 83
4.10 Character table for point group C_{2v}. 83
4.11 Character table for point group C_s. 83
4.12 Character table for point group C_1. 83

5.1 Annealing conditions for crystallisation in different CMA1:polymer composites. 91
5.2 Mean energy and deviation of density of states (DOS) input in Monte Carlo simulations of amorphous CMA1 at 300 K, and crystalline CMA1 at 300 K, 150 K and 10 K. 99

5.3 Emission Energy and colour in the simulated crystal phase compared to vacuum at the TDA(LC-ω-PBE/def2-SVP) level of theory. 105

6.1 Luminescence lifetime of CMA(Au), CMA(Ag), and CMA(Cu) in PS host varying concentrations from 5 wt.% to neat CMA films. 120
6.2 Luminescence lifetime of CMA(Au), CMA(Ag), and CMA(Cu) in TSPO1 host varying concentrations from 5 wt.% to neat CMA films. 126

List of publications

- **Jiale Feng**, Lupeng Yang, Alexander S. Romanov, Jirawit Ratanapreechachai, Antti-Pekka M. Reponen, Saul T. E. Jones, Mikko Linnolahti, Timothy J. H. Hele, Anna Köhler, Heinz Bässler, Manfred Bochmann, Dan Credgington. Environmental Control of Triplet Emission in Donor-Bridge-Acceptor Organometallics. *Advanced Functional Materials*, 2020, 30(9), 1908715.

- **Jiale Feng**, Elliot J. Taffet, Antti-Pekka M. Reponen, Alexander S. Romanov, Yoann Olivier, Vincent Lemaur, Lupeng Yang, Mikko Linnolahti, Manfred Bochmann, David Beljonne, Dan Credgington. Carbene-Metal-Amide Polycrystalline Materials Feature Blueshifted Energy yet Unchanged Kinetics of Emission. *Chemistry of Materials*, 2020, 32, 4743-4753.

- **Jiale Feng**, Antti-Pekka M. Reponen, Alexander S. Romanov, Mikko Linnolahti, Manfred Bochmann, Dan Credgington, Thomas Penfold, Neil Greenham. Influence of the Heavy Atom Effect on the Photophysics of Carbane-Metal-Amide Emitters. *Manuscript submitted*.

- Alexander S. Romanov, Saul T. E. Jones, Qinying Gu, Patrick J. Conaghan, Bluebell H. Drummond, **Jiale Feng**, Florian Chotard, Leonardo Buizza, Morgan Foley, Mikko Linnolahti, Dan Credgington, Manfred Bochmann. *Chemical Science*, 2020, 11, 435-446.

Chapter 1

Introduction

Organic semiconductors are a class of organic compounds exhibiting semiconducting properties, which means the absorption and emission of light, and electrical conductivity when doped or excited. Benefiting from the tuneability of the chemical structures, organic semiconductors now have a broad range of applications, from energy-conversion optoelectronic devices, such as organic light-emitting diodes (OLEDs)[1] and organic photovoltaics (OPVs)[2], to electrical switching devices such as organic field-effect transistors (OFETs)[3]. There are several advantages of organic semiconductors compared with traditional inorganic semiconductors, such as silicon, germanium, and gallium nitride (GaN), with potential for broader applications: (1) the versatility of molecular design to achieve various material properties[4, 5]; (2) the potential for lightweight, flexible and mechanically-robust devices[6, 7]; (3) good scalability, compatible with different device fabrication techniques, such as solution processing and thermal evaporation[8–11]. This thesis primarily explores the properties of light-emitting organic molecules used for OLEDs.

Organic electroluminescence was first revealed in 1953 by Bernanose et al. using a cellulose film doped with acridine organic,[12] and was further developed during the 1960s using anthracene single crystals connected to high-field carrier injection electrodes.[13–15] In 1987, a ground-breaking advance was made by Tang and Van Slyke, who first demonstrated efficient thin-film organic electroluminescence in a "sandwich structure" light-emitting device.[16] Afterwards, in 1990, the first polymer light emitting diode (PLED) was proposed by Friend and coworkers.[17] Conjugated polymers are compatible with direct solution processing to form thin-films in PLEDs, which broadens the pathways for the processing, design and operation of organic light-emitting diodes (OLEDs).[1, 18] The device structures for OLEDs are relatively simple, as shown in Fig. 1.1[19], where electrons and holes are injected from the cathode and anode respectively and recombine in the emissive layer with photons released. The spin-statistics in quantum mechanics limits the formation of singlet

excitons from the injected charges to 25%, while the rest 75% form triplet excitons, which do not contribute to luminescence directly due to their emission being spin-forbidden. Therefore, the quantum efficiency of first-generation OLED devices employing fluorescent emitters is limited to 25%.[20, 21] In order to break this efficiency limitation, the second generation of OLEDs used organometallic complexes containing heavy metals such as iridium to facilitate efficient radiative decay of triplets, known as phosphorescence, via spin-orbit coupling.[22] As a result, the quantum efficiency of phosphorescent emitters can approach unity. However, there are some remaining problems for commercial applications: (1) the high cost of metal-ligand complexes; (2) toxicity of heavy metals; (3) low device stability in the deep-blue spectral region.[23, 24] In 2011, a new class of pure organic emitters was developed, featuring a small singlet-triplet energy gap so that the reverse intersystem crossing is efficient and the triplets decay radiatively through the singlet pathway, known as thermally-activated delayed fluorescence (TADF).[25] TADF is also termed as E-type delayed fluorescence as it was firstly discovered in a fully organic compound eosin in 1961[26], and was further investigated using aromatic thiones in 1986[27]. TADF-type emitters were reported to show close to 100% quantum efficiency.[28–31] Recently, a new type of organometallic emitters named carbene-metal-amides (CMAs) has shown high quantum efficiency, with the presence of both heavy metals and small singlet-triplet splitting, lying in the middle of the phosphorescent- and TADF-type emitters.[32] However, the mechanism of triplet-to-singlet upconversion in these emitters has not been fully understood, which is the main focus of this thesis.

This thesis investigates the influence of solid-state intermolecular interactions on the photophysics, especially triplet excitons of carbene-metal-amides (CMAs). The thesis is presented in seven chapters. Chapter 2 presents the theoretical considerations which are fundamental to interpreting the results in this thesis. The electronic structures in atoms and molecules are first introduced, followed by discussing the interaction between light and matter, excitons, radiative and non-radiative transitions in organic semiconductors. Finally, the chapter extends the discussion from a single molecule to an ensemble of molecules in condensed phases, and the energy transfer, and charge transfer process between molecules.

Chapter 3 describes the experimental methods employed in this thesis to obtain results including (1) preparing solution-processed thin films; (2) spectroscopy techniques: steady-state absorption and photoluminescence spectroscopy, transient absorption spectroscopy, room-temperature and cryogenic time-resolved photoluminescence spectroscopy, Raman spectroscopy, and photoluminescence quantum efficiency measurements; (3) structural characterisation using X-ray diffraction; (4) computational methods using density functional theory (DFT) calculations.

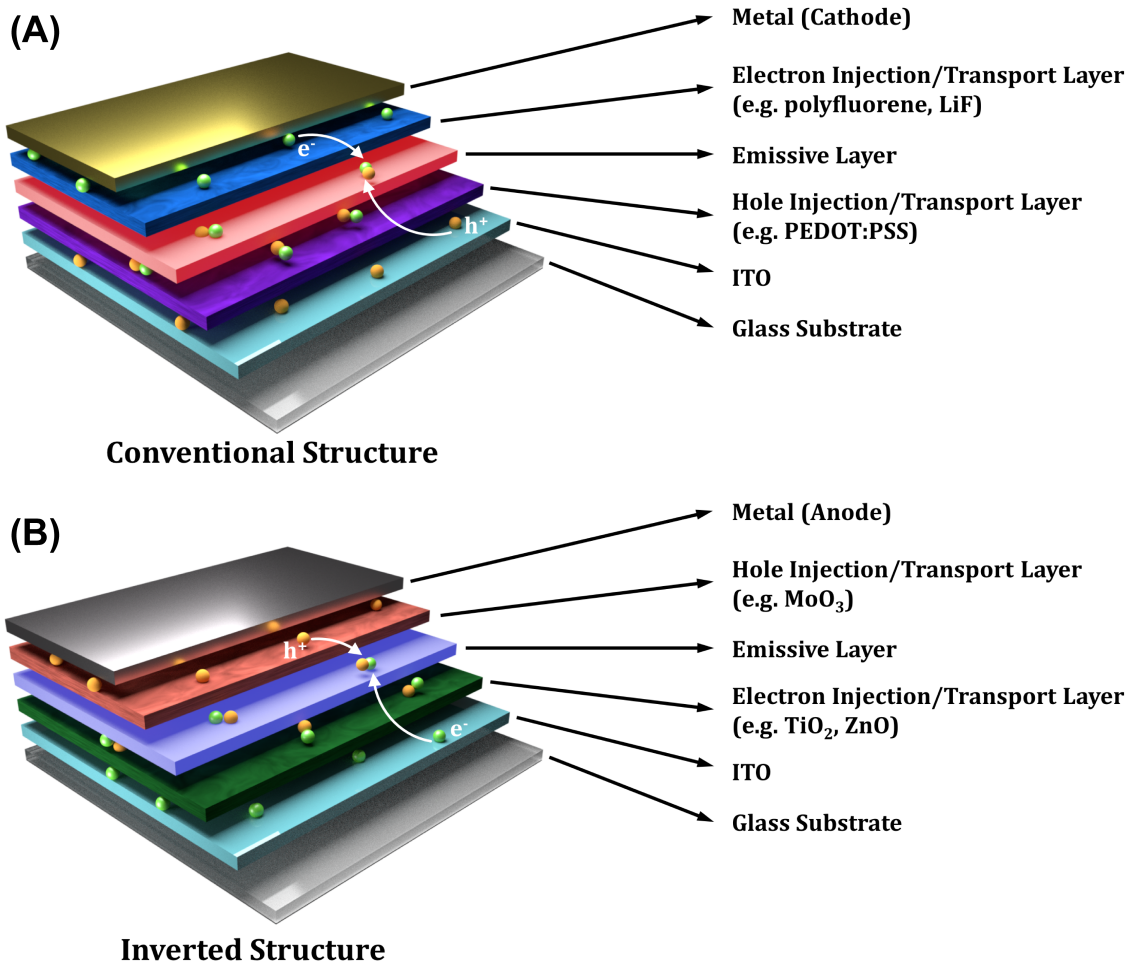

Fig. 1.1 (A) Conventional and (B) inverted OLED device structures.[19] Green and orange spheres represent electrons and holes respectively. They are injected into the device from electrodes and recombine at emissive layer.

Chapter 4 focuses on the control of triplet emission of gold-centred CMA1 by exploring intermolecular interactions with a variety of host materials to both restrict the thermally-activated triplet diffusion and shift the density of states. The luminescence peak of CMA1 can be significantly blueshifted by 210 meV without chemical modifications, which is attributed to the electrostatic interactions between the emitters and the host molecules. Despite the large increase in emission energy, the fast emission properties and low activation energy for delayed emission are unaffected. This approach can also be applied to probe the triplet harvesting mechanisms described by quantum-chemical models. Besides CMA1, this method has also been extended to other gold-bridged CMA complexes to tune the emission energy over a 150-200 meV range.

Chapter 5 investigates the link between molecular conformations and photophysical properties by crystallising the CMA1 thin films, which provides well-defined coplanar geometries. The charge-transfer emission of crystalline phase blueshifts by around 400 meV versus the amorphous phase, which is due to the combination of restricted torsional distortion and molecular electronic polarisation. This blueshift brings the lowest charge-transfer states very close to the localised carbazole triplet state, whose structured emission is uncovered at low temperature. Surprisingly, the rate of intersystem crossing and emission kinetics are not affected by the extent of torsional distortion. It has been discovered that partially twisted triplet equilibrium conformations primarily control the photophysics of CMAs.

Chapter 6 presents the heavy atom effect on the coinage-metal bridged CMAs to reveal its influence on the intersystem crossing and luminescence mechanism. The photophysical properties do not reflect expected trends based upon the heavy atom effect as both direct (^{1}CT$-^3$CT) coupling and spin-vibronic coupling via a local triplet state ^{3}LE(Cz) are present. CMA(Ag) possesses the weakest direct coupling and thus the slowest intersystem crossing rate, making the spin-vibronic coupling more important and the photophysical properties more sensitive to the CT$-$LE energy gap than the CMA(Au) and CMA(Cu). In order to achieve high radiative decay rates and high luminescence quantum efficiency, CMA complexes require the removal of parasitic local triplet states close to the CT energy and the minimisation of exchange energy.

All together, the experimental and theoretical findings described in this thesis shed light on the effects of various solid-state interactions on the photophysics of triplet excitons in organic light emitters. The results highlight the tunable emission energy via electrostatic interactions, the link between molecular conformations and the energy landscape, and the underlying singlet-triplet coupling mechanisms. These properties expand the range of possible uses of solid-state interactions in optoelectronic devices, assisting the design of efficient emitters and spin-dependent dynamics in organic semiconductors.

Chapter 2

Theoretical Considerations

2.1 Introduction

This chapter presents the theoretical considerations which are fundamental to interpreting the results in this thesis. It contains three main sections. The first section will introduce the electronic structure in atoms, and the hybridisation between atomic orbitals and extend this concept to molecular orbitals, followed by building up different energetic states in molecules. Secondly, the interaction between light and matter will be discussed, particularly in the context of neutral excitations and excitons in organic semiconductors, transitions between molecular states, and exciton interactions. Finally, the chapter will end by considering the environmental effects on excited states, from a single molecule to an ensemble of molecules in condensed phases, and the energy transfer and charge transfer process in organic semiconductors.

2.2 Electronic structure

For a particle of mass m moving in an external potential with potential energy $E_{pot}(\vec{r})$ at an arbitrary point, the Hamiltonian $\hat{H}$ comprises two parts: a kinetic energy term $\hat{E}_{kin}$, and a potential energy term $\hat{E}_{pot}$. The solution of three-dimensional time-independent Schrödinger equation leads to energy eigenvalues $E(n)$ and eigenstates $|n\rangle$,

$$\hat{H}|n\rangle = \left(\hat{E}_{kin} + \hat{E}_{pot}\right)|n\rangle = \left(-\frac{\hbar^2}{2m}\nabla^2 + E_{pot}(\vec{r})\right)|n\rangle = E(n)|n\rangle \tag{2.1}$$

where $\vec{r}$ is the position vector, $\hbar = h/2\pi$ (h is the Planck constant), and $n = 0, 1, 2, ..., |n\rangle$ are a complete set of orthogonal basis for the system. Any eigenfunction of the system $|\psi\rangle$ can be expressed as a linear combination of the basis set $|\psi\rangle = \sum_n a_n |n\rangle$ with $\sum_n |a_n|^2 = 1$.[33]

2.2.1 Atomic orbitals

The Hamiltonian of electrons in a static atomic system comprises the electron momentum, electron-nucleus potential energy, and the electron-electron potential energy. In the situation of single electron, i.e. a hydrogen atom, the complete wavefunctions will be separable into radial and angular components, and have the form[34]

$$\psi_{nlm_l}(r, \theta, \phi) = R_{nl}(r) Y_{lm_l}(\theta, \phi) \tag{2.2}$$

where n, l, m_l are quantum numbers (the spin quantum number m_s will not be discussed here): n is the principle quantum number which determines the energy of an electron through the Eq. 2.3 and controls the range of values of $l = 0, 1, ..., n-1$; l is the orbital angular momentum quantum number which determines the orbital angular momentum of an electron through the Eq. 2.4, and the number of orbitals as $2l$+1 at given n and l; m_l is the magnetic quantum number which determines the component of orbital angular momentum of an electron through $m_l\hbar$, and an individual single electron wavefunction at given n and l.

$$E_n = -\left(\frac{Z^2 \mu e^4}{32\pi^2 \varepsilon_0^2 \hbar^2}\right) \frac{1}{n^2} \qquad n = 1, 2, ... \tag{2.3}$$

where Z is the atomic number, μ is the reduced mass, e is the elementary charge, ε_0 is the vacuum permittivity.

$$\text{Magnitude of the angular momentum} = l(l+1)^{1/2}\hbar \tag{2.4}$$

Atomic orbitals with $l = 0$ are called s-orbitals, those with $l = 1$ are called p-orbitals, those with $l = 2$ are called d-orbitals, those with $l = 3$ are called f-orbitals. s-orbitals are spherically symmetrical. The three p-orbitals with given n correspond to three distinct m_l values, 0 and ±1. The orbital with $m_l = 0$ has zero angular momentum around z-axis and is called p_z-orbital. The other two orbitals p_+ and p_- have the same double-lobed shape aligned along x- and y- axes, and thus noted as p_x and p_y. d and f orbitals adopt more complicated geometries. Since the probability density function of an electron in a volume element is described by $|\psi_{nlm_l}(r, \theta, \phi)|^2 d\tau$, the solutions have probability function

geometries depending on n, l, m_l quantum numbers. This quantisation is fundamental to the atomic systems, and can be extended to multi-electron atoms.

2.2.2 Hybridisation

Due to the presence of multiple atoms in a molecule, the interactions between atomic orbitals determine the molecular electronic structure. If the $2s$ and $2p$ atomic orbitals of different atoms are energetically close and of the same symmetry, they can interact and combine to form new molecular orbitals, which is known as s-p mixing, in order to minimise the total energy. The spatial distribution of the molecular orbitals can be mathematically described by a hybrid function from a linear combination of the constituent atomic orbitals, which is known as hybridisation.[33]

A carbon atom is used as an example here as it is a fundamental element in organic semiconductors. The electron configuration in the electronic ground state of the C atom is $(1s)^2(2s)^2(2p_x)^1(2p_y)^1(2p_z)^0$. There are six electrons for an unexcited carbon atom. Two of these electrons occupy $1s$ orbital while the other four are outer shell electrons and involved in chemical bond formation. Two paired electrons fill in $2s$ orbital and one unpaired electron occupies in each of the $2p$ orbitals $2p_x$ and $2p_y$, with the third arbitrary $2p_z$ orbital remaining unoccupied.

There are three types of hybridisation by combining functions of one $2s$ orbital and three 2p orbitals illustrated in Fig. 2.1: (1) The sp hybridisation mixes one $2s$ orbital with only one $2p$ orbital and creates two sp hybrid functions at an angle of 180° with a linear conformation. (2) The sp^2 hybridisation hybridises one $2s$ and two $2p$ orbitals ($2p_x$ and $2p_y$) and creates three sp^2 hybrid functions in the xy-plane with an angle of 120° between them, with a hexagonal conformation. The remaining $2p_z$ orbital is perpendicular to the plane. This hybridisation results in conducting properties and is typical for graphite, graphene, conjugated polymers and molecules. (3) The sp^3 hybridisation hybridises one $2s$ and three $2p$ orbitals (one $2s$ electron is promoted to the third $2p$ orbital), and creates four equivalent sp^3 hybrid functions with an angle of 109.5° between them with a tetrahedral conformation. All the valence electrons are involved in covalent bonds and cannot participate in electronic transport, which is the reason why materials formed by sp^3 hybridised carbon atoms such as diamond are usually colourless insulators.

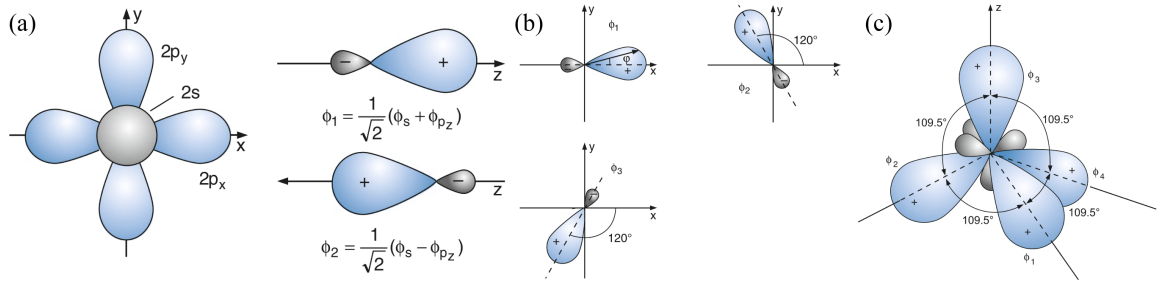

Fig. 2.1 (a) sp hybridisation of atomic orbitals for the valence electrons of the C atom. $2p_x$, $2p_y$ and $2s$ atomic orbitals of the C atom, and the hybrid functions. (b) sp^2 hybridisation with the three hybrid functions pointing into the directions 0°, 120° and 240° from the x-axis. (c) The four hybrid functions for the sp^3 hybridisation. Figure adapted from reference [33].

2.2.3 Molecular orbitals

When atoms constitute molecules, atomic orbitals are mixed in order to share electrons and the atomic electronic structure may be altered to a lower energy configuration. The mixing of these atomic orbitals forms molecular orbitals (MOs), which are eigenstates of the multiple-atom system, and can usually be described by a linear combination of the atomic orbitals as a good approximation. Overlap of two atomic orbitals ψ_a and ψ_b creates two types of molecular orbitals. If two orbitals add in phase, two electron wavefunctions interfere constructively, and thus the electron density between nuclei increases. This type of molecular orbital is termed as a "bonding orbital" with lower energy. In contrast, if two orbitals add out of phase, destructive interference happens between two electron wavefunctions and a node where electron density is zero appears between the nuclei. This type of molecular orbital is termed as an "anti-bonding orbital" with higher energy.

We take C atoms as an example. Constructive overlap of sp^2 hybridised carbon orbitals forms σ-type bonds which are localised between the atomic nuclei and constructs molecular backbones, but they do not contribute to electron transportations. Electronic properties of organics are mainly determined by the unhybridised $2p_z$ orbitals of the carbon atoms which constructively overlap with the other carbon $2p_z$ orbitals and form π-type bonds. Electrons in these π bonds are located above and below the molecular axis and thus can delocalise along the backbone. This property of some organic molecules is termed as π conjugation. π conjugation normally rigidifies the backbone and impedes molecular rotations around the σ bond. The large overlap between σ-orbitals results in a high energy difference between σ (bonding σ orbital) and σ^* (anti-bonding σ orbital). Due to the smaller overlap of π orbitals, the energy splitting between π (bonding π orbital) and π^* (anti-bonding π orbital) is much smaller. This is the reason why for many organic semiconductors the

lowest electronic excitation occurs between the bonding π orbital, also known as the highest occupied molecular orbital (HOMO) and the anti-bonding π orbital, also known as the lowest unoccupied molecular orbital (LUMO). HOMO and LUMO are also called the frontier orbitals. They play a critical role in the optical and electrical processes of the molecule. Fig. 2.2 shows an example of bond formation in the ethene molecule.[35]

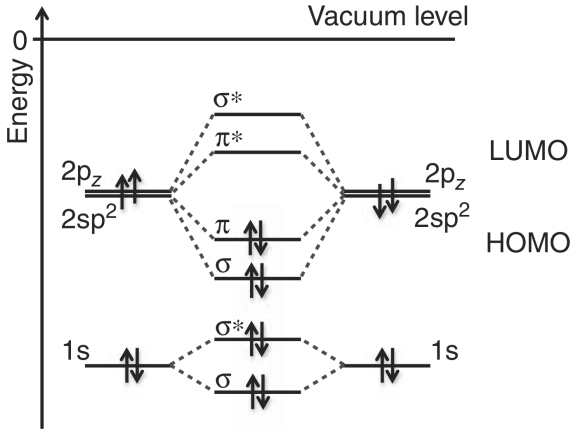

Fig. 2.2 Simple energy level diagram illustrating the formation of σ and π bonds from atomic orbitals for ethene. Only orbitals involved in the carbon-carbon interaction are shown. The two $2sp^2$ hybrid orbitals forming σ-bonds with hydrogen atoms are omitted. Figure adapted from reference [35].

2.2.4 From orbitals to states

In order to obtain the ground state and excited states of the molecule from the molecular orbitals, one possible way that considers electron-correlation effects is to compose the excited state as a linear combination of different configurations. This is known as configuration interaction (CI). Configuration indicates the electron distribution over the molecular orbitals. Under this definition, the configuration of the ground state is that all electrons are pairwise in the lowest possible orbitals and thus the molecule has the lowest possible energy, denoted as S_0. Other configurations may include that one electron is in the HOMO and another electron is in the LUMO, or in the orbital above the LUMO (termed LUMO+1). Considering the interactions between electrons, an excited state can be nicely approximated by a superposition of different configurations, which is illustrated in Fig. 2.3. The excited states usually comprise superpositions of several configurations with different weights. For many organic molecules, the first excited state is predominantly contributed to the configuration with one electron in the HOMO, and one in the LUMO. The two single electrons may have a parallel spin or an antiparallel spin, which corresponds to different excited states of the molecule with

different energies and different overall wavefunctions. As detailed in the next section, the spin-antiparallel case is called the spin-singlet excited state, and the spin-parallel case is called the spin-triplet excited state, with lower energy.

Electrons in orbitals are bound to the nuclei, so orbital energies are below the vacuum energy, which is defined as 0 eV. For example, the energy of the HOMO may be at -6 eV and the energy of the LUMO may be at -3 eV. Another way to present energies is a state picture: the ground state, i.e. the lowest possible state of a molecule is set to zero, and the energies of excited states have positive values above zero. In the state diagram, spin-singlet and spin-triplet can be clearly indicated. Fig. 2.4 compares an orbital picture and a state picture for singlet states.

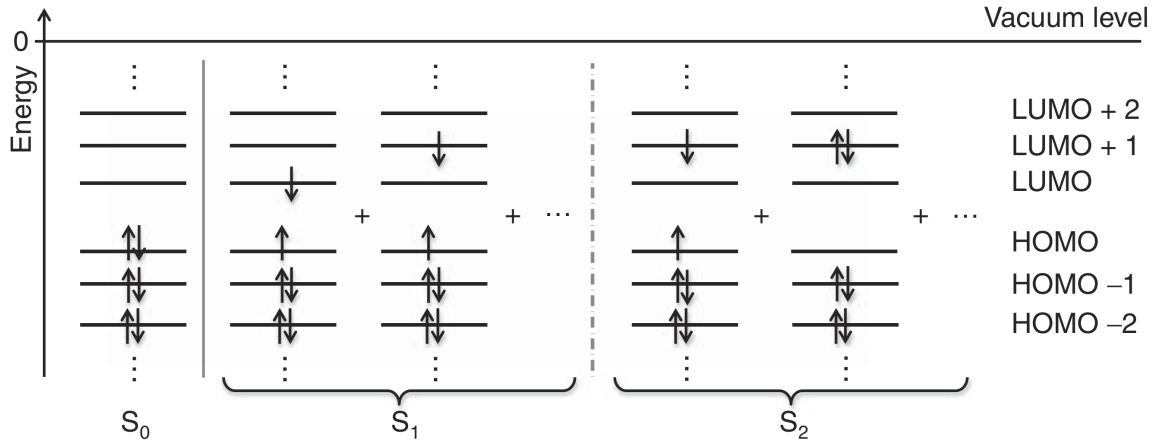

Fig. 2.3 Illustration of configuration interaction. The configuration associated with the ground state S_0 is shown, as well as configurations that may contribute to different degrees, to the first excited state S_1 and to the second excited state S_2. While several contributing configurations are shown here, it is common practice to only depict the dominating configuration for each state. Figure adapted from reference [35].

2.3 Neutral excitations and excitons

After absorbing some extra energy in the ground state, a molecule can reach excited states, which can be achieved either by photoexcitation or electrical excitation. When an electron is excited into the LUMO, a positively charged vacancy called a hole is created in the HOMO. As a result of the coulombic attraction, the electron and the hole are bound to create an electrically neutral quasi-particle – an exciton. The radius of the exciton, defined as the average distance between electron and hole. Three types of excitons are distinguished based

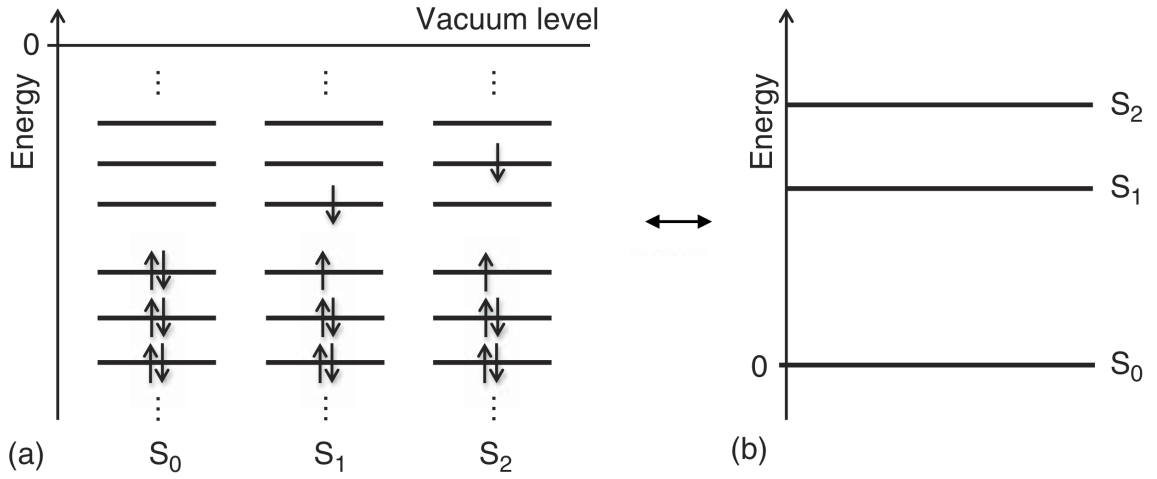

Fig. 2.4 The singlet states S_0, S_1, and S_2 represented (a) in an orbital diagram, showing the one-electron orbital energies for the dominant configuration and (b) in a state diagram, showing the relative energies of the molecular electronic state. Figure adapted from reference [35].

on the exciton radius: Frenkel excitons, Wannier-Mott excitons and charge transfer (CT) excitons. (1) Frenkel excitons are typical in organic semiconductors, which usually exhibit low dielectric constants ($\varepsilon \sim 3$)[36]. They have short radius (typically below 1 nm) and high Coulomb binding energy around 0.5 eV.[19, 36] (2) Wannier-Mott excitons are typically observed in inorganic semiconductors. Due to high dielectric constant of these materials, the radius is much larger, and the binding energy is lower (few tens of meV). (3) Charge transfer excitons are an intermediate case: electron and hole are located in two different molecules or two different moieties of one molecule while stay bound.[35]

2.3.1 Singlets, triplets and exchange energy

Fundamental rules of quantum mechanics determine that excitons exist as either singlets or triplets.[37–41] An exciton is composed of two half-spin particles, one electron and one hole. The Pauli exclusion principle states that for two identical fermions, such as electrons and holes, the total wavefunction: $\psi_{total} = \psi_{space}\psi_{spin}$ must be antisymmetric with respect to particle (electron) exchange. The spin wavefunctions of the four eigenstates with eigenvalues S and M_s to the two-particle system can be written as

$$\psi_{(symm\,spin,T_+)} = \alpha_1\alpha_2 \qquad \text{yielding} \quad S=1, M_s=1 \tag{2.5}$$

$$\psi_{(symm\,spin,T_0)} = 1/\sqrt{2}(\alpha_1\beta_2+\beta_1\alpha_2) \qquad \text{yielding} \quad S=1, M_s=0 \tag{2.6}$$

$$\psi_{(symm\,spin,T_-)} = \beta_1\beta_1 \qquad \text{yielding} \quad S=1, M_s=-1 \tag{2.7}$$

$$\psi_{(antisymm\,spin,S)} = 1/\sqrt{2}(\alpha_1\beta_2-\beta_1\alpha_2) \qquad \text{yielding} \quad S=0, M_s=0 \tag{2.8}$$

where α and β are spin wavefunctions of one-electron state and index 1 and 2 refer to electron 1 and 2. The first three spin wavefunctions with $S=1$ have three different eigenvalues $M_s = 1, 0, -1$ in z direction (the direction of a local magnetic field), and all have symmetric spin components. These three states are defined as triplet states. The fourth wavefunction with $S=0$ has only one eigenvalue $M_s = 0$, and exhibits antisymmetric spin. This state is defined as singlet state[35], illustrated in Fig. 2.5.

For two electrons 1 and 2 in two different orbitals ϕ_H (HOMO) and ϕ_L (LUMO) at distance r_{12} staying in the singlet state, the spatial wavefunction is symmetric: $\psi_{(symm\,space)} = \phi_H(1)\phi_L(2) + \phi_H(2)\phi_L(1)$. The energy from coulombic repulsion between the two electrons can therefore be written as

$$E_{singlet} = \iint \phi_H(1)\phi_H(1)\frac{e^2}{r_{12}}\phi_L(2)\phi_L(2)\,dr_1\,dr_2 + \iint \phi_H(1)\phi_L(1)\frac{e^2}{r_{12}}\phi_H(2)\phi_L(2)\,dr_1\,dr_2 \tag{2.9}$$

The first term describes the repulsion energy between electron densities of electron 1 in orbital ϕ_H and electron 2 in orbital ϕ_L. The second term describes the energy in the overlapped region of ϕ_H and ϕ_L, which is also known as electron exchange integral (J).

For triplet state, the spatial wavefunction is antisymmetric: $\psi_{(antisymm\,space)} = \phi_H(1)\phi_L(2) - \phi_H(2)\phi_L(1)$. The energy can then be expressed as

$$E_{triplet} = \iint \phi_H(1)\phi_H(1)\frac{e^2}{r_{12}}\phi_L(2)\phi_L(2)\,dr_1\,dr_2 - \iint \phi_H(1)\phi_L(1)\frac{e^2}{r_{12}}\phi_H(2)\phi_L(2)\,dr_1\,dr_2 \tag{2.10}$$

It is clear that the lowest singlet energy E_{S1} lies above the lowest triplet energy E_{T1} and the energy splitting is termed as the exchange energy ΔE_{ST}.

$$\Delta E_{ST} = E_{S1} - E_{T1} = 2J = 2\iint \phi_H(1)\phi_L(1)\frac{e^2}{r_{12}}\phi_H(2)\phi_L(2)\,dr_1\,dr_2 \tag{2.11}$$

The exchange energy ΔE_{ST} is dependent on the spatial separation and wavefunction overlap between HOMO (ϕ_H) and LUMO (ϕ_L). Generally, the exchange energy is approximately 0.7-1.0 eV for many organic semiconductors due to significant overlap between HOMO and LUMO[42–44]. Some molecular modifications can be applied to localise HOMO and LUMO on different parts of the molecule so that the ΔE_{ST} can decrease to 0.2-0.5 eV.[25, 28, 45, 46]

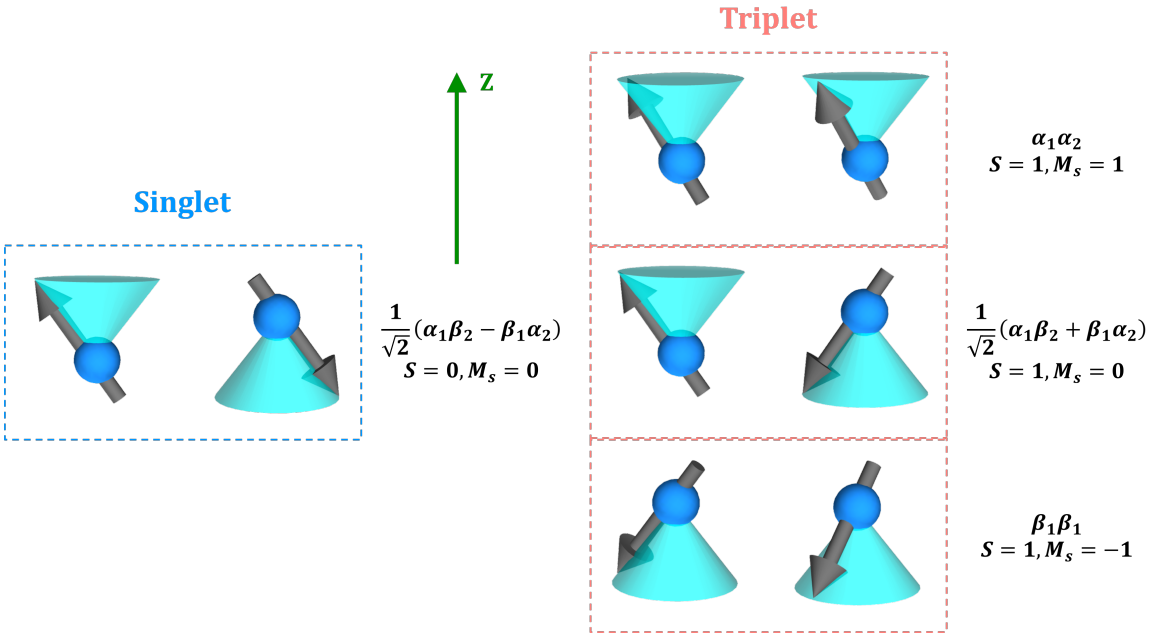

Fig. 2.5 Vector diagram of orientations of two electron spins for the singlet and triplet state. Z is the direction of a local magnetic field. The singlet has antisymmetric spin configuration and three spin configurations for triplet are symmetric.

2.3.2 Photoexcitation and electrical-excitation

The ground state can be promoted to excited states by both photoexcitation and electrical-excitation. However, the spin statistics underlying these two excitations is fundamentally different. In the process of photoexcitation, a photon with appropriate energy is absorbed to promote an electron from an occupied molecular orbital, for instance, the HOMO (ground state S_0) to a unoccupied molecular orbital, for instance, the LUMO, and an exciton is created. Since a photon has an integer angular momentum of $\hbar$, the transition is between singlet

states, $S_0 \rightarrow S_n$. After some time, the exciton recombines with a photon released, which is defined as the exciton lifetime. This process is defined as photoluminescence, including fluorescence if it is from the singlets and phosphorescence if it is from the triplets. However, in the process of electrical-excitation, where electrons and holes with half spin have random spin orientations in the material. An exciton is formed when two charges recombine and exists in either singlet or triplet state depending on the recombination process. According to spin statistics mentioned above, around 25% of electron-hole recombination will yield singlet excitons ($S = 0$) and the remaining 75% will end up with triplet excitons ($S = 1$ with $M_s = 1, 0, -1$). Due to intrinsically weak spin-orbit coupling in organic semiconductors and thus low radiative decay rates of triplets, triplet states are considered not to contribute to electroluminescence, and the electroluminescence quantum efficiency is drastically limited to 25%.

2.3.3 Radiative transitions between molecular states: absorption and emission

The interaction of light with semiconductors can be approximated as a perturbation induced by an oscillating electromagnetic field ($\vec{E}(t)$) on an ensemble of electric dipoles in molecules. The perturbation Hamiltonian $\hat{H}'$ can be written as:

$$\hat{H}' = -e\hat{r} \cdot \vec{E}(t) \tag{2.12}$$

where $e\hat{r}$ is the electronic dipole operator of the system. If the energy of an incident photon is in resonance with transitions in the system, then two processes may happen: (1) absorption of the incident photon energy leading to a neutral excitation. The absorption of photons increases the total energy of a molecule while the emission decreases it; (2) the stimulated emission of a photon with the same energy. If energetically non-resonant, the photon can be scattered by the electron density of the system.

First-order perturbation theory — Fermi's golden rule

If the coupling between the initial and final states of transition is small compared to their adiabatic energy difference, the transition rate k_{if} can be described by perturbation theory. First-order perturbation theory, well-known as Fermi's golden rule states that the rate of the transition k_{if} between an initial state ψ_i and a final state ψ_f is determined by the perturbing

Hamiltonian $\hat{H}'$ that causes the transition:

$$k_{if} = \frac{2\pi}{\hbar}|\langle\psi_f|\hat{H}'|\psi_i\rangle|^2\delta(E_f - E_i)\rho \tag{2.13}$$

where E_f and E_i are energy of final and initial state, and ρ is the density of states (DOS) of the final state. The δ-function conserves the molecular energy.

Franck-Condon principle

The Born-Oppenheimer approximation assumes that during the process of electronic transitions, nuclear motion is slow compared to electrons due to their large mass difference, so an electronic transition occurs within a stationary nuclear framework. The nuclear locations start to reorganise once the electronic transition has completed. Under this assumption, the total wavefunction of a molecular state ψ_{total} can be approximated by the product of the electronic wavefunction ψ_{el}, the spin wavefunction ψ_{spin} and the vibrational wavefunction ψ_{vib}.

$$\psi_{total} = \psi_{el}\psi_{spin}\psi_{vib} \tag{2.14}$$

Radiative transitions

For the situation of interactions between matter and light, a suitable operator is the electronic dipole operator $e\hat{r}$. By inserting the molecular wavefunction Eq. 2.14 into Eq. 2.13, since the spin wavefunction $\psi_{spin}(\alpha_i, \beta_i)$ (α_i and β_i represent electrons' individual spin wavefunctions) and the vibrational wavefunction $\psi_{vib}(R_i)$ (R_i represents the positions of the nuclei) are insensitive to the dipole operator, the dipole operator acts only on the electronic wavefunction $\psi_{el}(r_i, R_i)$ (r_i represents the positions of the electrons), which gives the expression:

$$k_{if} = \frac{2\pi}{\hbar}\rho|\langle\psi_{el,f}|e\hat{r}|\psi_{el,i}\rangle|^2|\langle\psi_{vib,f}|\psi_{vib,i}\rangle|^2|\langle\psi_{spin,f}|\psi_{spin,i}\rangle|^2 \tag{2.15}$$

The first integral is the electronic factor, which controls the overall intensity of the transition and scales with the overlap of the initial and final state wavefunctions, and the value of the transition dipole moment $e\hat{r}$. If this integral is non-zero, the transition is dipole-allowed, otherwise it is dipole-forbidden. The oscillator strength f is used to indicate the strength of the transition, ranging from 0 to 1.

The component of vibrational wavefunctions decides the spectral shape of the absorption and emission. Typical vibrational energy quanta range from 100-300 meV, which means that absorption starts from the 0th vibrational level of the ground state at room temperature. The

square of the integral $|\langle\psi_{vib,f}|\psi_{vib,i}\rangle|^2$ is the Franck-Condon-factor F. It gives the transition (here the absorption) probability from the 0th vibrational level of the ground state to the mth vibrational level of the excited state, and can be denoted as I_{0-m}.

$$I_{0-m} = |\langle\psi_{vib,f}|\psi_{vib,i}\rangle|^2 = \frac{S^m}{m!}e^{-S} \tag{2.16}$$

where S is the Huang-Rhys parameter, which gives the strength of coupling to the mth vibrational level. After being excited into the mth (m>0) vibrational level of the S_1 excited state, the molecule will lose the vibrational energy by internal conversion, i.e. by releasing phonons with energy $\hbar\omega$ and return to the 0th vibrational level of the S_1 excited state within around a picosecond.[47, 48] Since this process is much faster than exciton decay via luminescence, the emission takes place from the 0th vibrational level of the S_1 to any of the vibrational levels of the ground state. This is Kasha's rule, which will be discussed in the next section.[35] The potential energy curve for excited states is generally displaced by ΔQ along the configuration coordinate with respect to the ground-state potential energy curve. The molecule is excited from the ground-state equilibrium position Q_{GS} and possesses extra potential energy with respect to the excited state equilibrium position Q_{ES}. This extra energy is released via emission of vibrational quanta when the nuclei respond to the change in electronic charge distribution, which is termed as geometric reorganisation energy or relaxation energy, as illustrated in Fig 2.6.

The last term is the spin integral $\langle\psi_{spin,f}|\psi_{spin,i}\rangle$, which has only two values: 0 if the spins of initial state are different from the spins of final state, and 1 if they are the same. Therefore, transitions between singlet states or triplet states, such as $S_1 \rightarrow S_0$ or $T_1 \rightarrow T_n$ are spin allowed whereas transitions from singlet to triplet or vice versa, such as $T_1 \rightarrow S_0$ are spin-forbidden. However, it is possible to obtain a finite transition rate for this spin-forbidden process only if the singlet state wavefunction is mixed with triplet state wavefunction by some perturbation. Such a perturbation can be provided by the mechanism of spin-orbit coupling (SOC). That is, if the spin angular momentum s is coupled with orbital angular momentum l of an electron, since only the total angular momentum $j = l + s$ has to be conserved during the optical transition, a change in spin angular momentum can be compensated by an opposite change in orbital angular momentum, which makes spin flip of an electron feasible, and thus the transition from triplet state T_1 to singlet state such as ground state S_0. The spin-orbit coupling Hamiltonian, $\hat{H}_{SO}$ for a single electron can be written as

$$\hat{H}_{SO} = \frac{Zq^2}{2m^2c^2r^3}\hat{\mathbf{L}}\cdot\hat{\mathbf{S}} \tag{2.17}$$

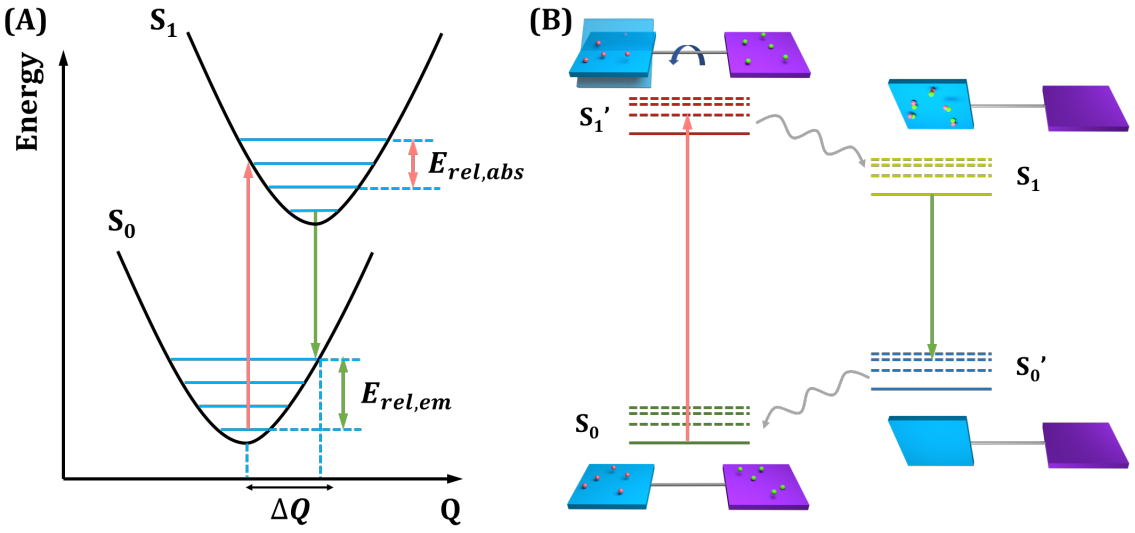

Fig. 2.6 (A) Potential energy diagram showing the relaxation energies $E_{rel,abs}$ and $E_{rel,em}$ associated with the process of absorption and emission. (B) Geometric relaxation process shown in a molecular illustration. S_0 and S_1 denote the relaxed ground-state and excited-state conformation at minimum potential curve and S_0' and S_1' denote unrelaxed conformations. Figure adapted from reference [35, 49].

where Z is the atomic charge, q and m are the charge and mass of an electron, c is the speed of light in vacuum, $\hat{\mathbf{L}}$ and $\hat{\mathbf{S}}$ are the orbital and spin angular momentum operators.[50]

In order to distinguish the $S_1 \rightarrow S_0$ and $T_1 \rightarrow S_0$ transitions, the former is defined as fluorescence, and the latter is defined as phosphorescence. The admixture of pure triplet state and singlet state can be expressed mathematically as

$$|^3\psi_1'\rangle = |^3\psi_1^0\rangle + \sum_k \frac{\langle ^1\psi_k^0|\hat{H}_{SO}|^3\psi_1^0\rangle}{E(T_1) - E(S_k)} |^1\psi_k^0\rangle \tag{2.18}$$

where $|^3\psi_1'\rangle$ is the perturbed triplet state, $|^3\psi_1^0\rangle$ is the pure triplet state, $|^1\psi_k^0\rangle$ is the pure kth singlet state, $\hat{H}_{SO}$ is the Hamiltonian of the perturbing spin-orbit coupling, $E(n)$ is the energy of the state. A similar expression can also be derived for the singlet ground state

$$|^1\psi_0'\rangle = |^1\psi_0^0\rangle + \sum_k \frac{\langle ^3\psi_k^0|\hat{H}_{SO}|^1\psi_0^0\rangle}{E(S_0) - E(T_k)} |^3\psi_k^0\rangle \tag{2.19}$$

By inserting the perturbed triplet excited state and singlet ground state into Fermi's golden rule Eq. 2.13, the transition rate can be obtained

$$k_{if} = \frac{2\pi}{\hbar}\rho|\langle {}^3\psi_1'|e\hat{r}|{}^1\psi_0'\rangle|^2 = \frac{2\pi}{\hbar}\rho(A+B+C+D)^2 \quad \text{with} \tag{2.20}$$

$$A = \langle {}^3\psi_1^0|e\hat{r}|{}^1\psi_0^0\rangle \tag{2.21}$$

$$B = \sum_k \frac{\langle {}^1\psi_k^0|\hat{H}_{SO}|{}^3\psi_1^0\rangle}{E(T_1)-E(S_k)}\langle {}^1\psi_k^0|e\hat{r}|{}^1\psi_0^0\rangle \tag{2.22}$$

$$C = \sum_k \frac{\langle {}^3\psi_k^0|\hat{H}_{SO}|{}^1\psi_0^0\rangle}{E(S_0)-E(T_k)}\langle {}^3\psi_1^0|e\hat{r}|{}^3\psi_k^0\rangle \tag{2.23}$$

$$D = \sum_k \frac{\langle {}^1\psi_k^0|\hat{H}_{SO}|{}^3\psi_1^0\rangle}{E(T_1)-E(S_k)}\sum_j \frac{\langle {}^3\psi_j^0|\hat{H}_{SO}|{}^1\psi_0^0\rangle}{E(S_0)-E(T_j)}\langle {}^1\psi_k^0|e\hat{r}|{}^3\psi_j^0\rangle \tag{2.24}$$

Terms A and D contain a product of orthogonal spins and thus equal zero. The value of term C is small since the energy difference between S_0 and T_k is large compared to that between T_1 and S_k in term B. Therefore, the major contribution is from term B. The admixture depends on the (1) energy separation between T_1 and S_k, and (2) the magnitude of the spin-orbit coupling $\hat{H}_{SO}$. For atoms, the perturbing Hamiltonian is proportional to the fourth power of the atomic charge, $\hat{H}_{SO} \propto Z^4/(n^3(l+1)(l+0.5)l)$, with n and l being the quantum numbers.[51] Therefore, strong phosphorescence is observed from transition metal complexes containing $4d$ and $5d$ metals, such as iridium and platinum, which are used in phosphorescent OLEDs.[22, 52–54] Phosphorescence can still happen at a much slower rate with the absence of heavy elements, in which case molecular vibrations provide the perturbation to mix orbitals with different angular momentum and thus make the spin-flip possible, where vibrational degrees of freedom has to be considered.[55]

Second-order perturbation theory — Spin-vibronic coupling

The spin-orbit coupling (SOC) discussed above is limited to a static nuclear configuration. If the SOC is dependent on the vibrational motions, it is necessary to consider spin-vibronic coupling mixed with spin-orbit coupling simultaneously. There are four mechanisms for mixing the singlet and triplet states: (1) Direct spin-orbit coupling, H_{SO} determined by the electronic character of the states and independent on the nuclear coordinates; (2) Vibrational spin-orbit,$(\partial\hat{H}_{SO}/\partial Q_\alpha)Q_\alpha$, depending on the motion along a specific nuclear degree of freedom Q_α. This is the expression of first order. Higher orders can also be included; (3) Spin-vibronic, $\hat{H}_{SO}\hat{T}_N$, spin-orbit coupling with vibronic coupling in the triplet manifold; (4) Spin-vibronic, $\hat{T}_N\hat{H}_{SO}$, spin-orbit coupling with vibronic coupling in the singlet manifold.

[56, 57] It should be noted that term (1) and (2) appear in first-order perturbation theory while terms (3) and (4) which mix spin-orbit and non-adiabatic coupling are present only at second-order perturbation theory. Combining all these terms, the full spin-orbit interaction up to second order can be expressed as[51]

$$\begin{aligned}\hat{H}_{SO} =& \langle \psi_{S_1} | \hat{H}_{SO} | \psi_{T_1} \rangle + \sum_{\alpha} \frac{\partial \langle \psi_{S_1} | \hat{H}_{SO} | \psi_{T_1} \rangle}{\partial Q_\alpha} Q_\alpha \\ &+ \frac{1}{2} \sum_{\alpha} \sum_{\beta} \frac{\partial^2 \langle \psi_{S_1} | \hat{H}_{SO} | \psi_{T_1} \rangle}{\partial Q_\alpha \partial Q_\beta} Q_\alpha Q_\beta \\ &+ \sum_{n} \frac{\langle \psi_{S_1} | \hat{H}_{SO} | \psi_{T_n} \rangle \langle \psi_{T_n} | \hat{T}_N | \psi_{T_1} \rangle}{E_{T_2} - E_{S_1}} \\ &+ \sum_{m} \frac{\langle \psi_{S_1} | \hat{T}_N | \psi_{S_m} \rangle \langle \psi_{S_m} | \hat{H}_{SO} | \psi_{T_1} \rangle}{E_{S_2} - E_{T_1}}\end{aligned} \tag{2.25}$$

where ψ is the molecular wavefunction for a particular state, ψ_{T_n} is an intermediate triplet state and ψ_{S_m} is an intermediate singlet state, $\hat{T}_N$ is the vibronic mixing operator and $\hat{H}_{SO}$ is the spin-orbit operator. Similar to the Fermi's golden rule, Eq. 2.13 where only first order of the perturbation theory is considered, if an intermediate state is involved in coupling, the transition rate k_{if} incorporating second-order expansion can be written as[51, 58, 59]

$$k_{if} = \frac{2\pi}{\hbar} \left| \frac{\langle \psi_f | \hat{H}_{SO} | \psi_n \rangle \langle \psi_n | \hat{T}_N | \psi_i \rangle}{E_i - E_n} \right|^2 \delta(E_f - E_i) \tag{2.26}$$

where the initial ψ_i and final ψ_f states are coupled via an intermediate ψ_n state.

2.3.4 Non-radiative transitions between molecular states: internal conversion and intersystem crossing

There are two types of non-radiative transition: internal conversion (IC) and intersystem crossing (ISC). Internal conversion occurs between lower and higher states at the same spin manifold, such as $S_2 \rightarrow S_1$, $T_2 \rightarrow T_1$, with a rate of k_{IC}. Intersystem crossing occurs between different spin manifolds, i.e. spin change is involved, such as $S_1 \rightarrow T_1$, with a rate of k_{ISC}. Reverse intersystem crossing (rISC), $T_1 \rightarrow S_1$ is also possible. If the energy splitting between two states is small, rISC can be activated by thermal energy. The luminescence via rISC $T_1 \rightarrow S_1 \rightarrow S_0$ is known as thermally activated delayed fluorescence (TADF), also referred to as E-type delayed fluorescence, which has been widely investigated to achieve efficient OLEDs.[25, 60–62]

The rate for a non-radiative transition k_{if} between an initial state ψ_i and a final state ψ_f can also be determined by Fermi's golden rule, Eq. 2.13. For non-radiative transitions, the perturbing Hamiltonian $\hat{H}'$ is the nuclear kinetic energy operator $\partial/\partial Q$, where Q is a normal mode displacement. The rate of intersystem crossing (ISC) is of great importance for efficient triplet harvesting and high-performance light-emitting devices. Within the Condon approximation, the electronic and vibrational wavefunction can be separated and the rate can be expressed as

$$k_{ISC} = \frac{2\pi}{\hbar}\rho \sum_f |\langle \psi_{el,f}|\hat{H}_{SO}|\psi_{el,i}\rangle|^2 \sum_{jk} |\langle \psi_{vib,fk}|\psi_{vib,ij}\rangle|^2 \delta(E_{ij} - E_{fk}) \tag{2.27}$$

$$k_{ISC} = \frac{2\pi}{\hbar}\rho J^2 F \tag{2.28}$$

where $\hat{H}_{SO}$ is the spin-orbit coupling operator, ρ is the density of states of the final state, $J = \sum_f |\langle \psi_{el,f}|\hat{H}_{SO}|\psi_{el,i}\rangle|$ represents the electronic coupling between two states containing electronic and spin wavefunctions, and the Frank-Condon factor $F = \sum_{jk} |\langle \psi_{vib,fk}|\psi_{vib,ij}\rangle|^2$ represents the overlap of vibrational wavefunctions of initial and final state.

Eq. 2.27 and Eq. 2.28 highlight the three components which can be engineered to increase k_{ISC}: (1) The J term; (2) The F term; (3) The ρ term, which will be discussed in the following subsections.

El-Sayed Rules — electronic coupling

The ISC rate dependence of electronic coupling J is described by the *El-Sayed rules*[63], which state that for effective SOC, any change in spin must be compensated by a corresponding change in orbital in order to conserve total angular momentum. Therefore, a transition involving the same orbitals, such as $^1(\pi\pi*) \rightarrow^3 (\pi\pi*)$ would be slower than the transition between different orbitals, such as $^1(\pi\pi*) \rightarrow^3 (n\pi*)$. It should be noted that the El-Sayed rules assume pure electronic states of a single character at a static nuclear configuration. In the cases where mixing between states of different characters and vibronic interactions occur, the El-Sayed rules break down. The spin-orbit coupling matrix elements (SOCMEs) can be improved by employing heavy elements such as transition metals.[64–66] However, for pure organic TADF molecules where the heavy elements are absent, the spin-orbit coupling (SOC) is highly limited with the largest SOCMEs reported between 3-4 cm^{-1}.[67]

Energy gap law — vibrational coupling

The Franck-Condon factor F describes the overlap of the overall vibrational wavefunction $|\langle\psi_{vib,f}|\psi_{vib,i}\rangle|^2$ as discussed in previous section. In the high-temperature limit, where energies of all modes relevant in transfer are below k_BT, the transition rate k_{ISC} can be written in a semi-classical (Marcus-like) form [51]

$$k_{ISC} \propto \frac{1}{\sqrt{4\pi\lambda k_BT}}\exp\left(-\frac{(\Delta E+\lambda)^2}{4\lambda k_BT}\right) \tag{2.29}$$

where λ is the reorganisation energy, and ΔE is the adiabatic energy minimum difference between the initial and final states.[51, 68–71] Within the weak coupling limit, see Fig. 2.7 (A), where the configurational displacement Q between the final and initial state minima is small, i.e. small structural change and small reorganisation energy, the transition rate depends exponentially on the adiabatic energy difference ΔE. This is known as the *energy gap law*. Due to the small energy gaps of S_2-S_1 or T_2-T_1, the rate of internal conversion ($\sim 10^{12}$ s^{-1}) is usually faster than the radiative decay of S_2-S_0 or T_2-T_0 ($\sim 10^9$ s^{-1}). Consequently, emission always happens from the lowest excited state of a spin manifold, which is known as Kasha's rule. Based on the energy gap law, one can derive the empirical formula for the temperature-dependent non-radiative transition rate:

$$k_{nr}(T) = k_{nr}^0 + k_{nr}'\exp(-\frac{E_a}{kT}) \tag{2.30}$$

where k_{nr}^0 and k_{nr}' are terms independent of temperature and E_a is an activation energy.[35] However, in the case of strong coupling, where large configurational displacement happens along a collective nuclear coordinate Q, and the potential energy surfaces intersect, the rate of ISC exhibits a Gaussian dependency on the value of $(\Delta E+\lambda)$. A similar semi-classical (Marcus-like) formula of transition rate can also be derived if spin-vibronic coupling is considered, see Eq. 2.26. In the weak coupling limit, $\lambda \approx 0$, the rate k depends exponentially on the energy gap between the initial and final states and quadratically on the energy gap between the initial and intermediate states.[51] Therefore, the rate of ISC is generally improved by decreasing the energy gap between the two states. This is a common strategy of designing TADF emitters.[72–74]

The influence of density of states

The ρ term, i.e. the density of states of the final state. This approach is to increase the number of final states (density of coupled states), i.e. increasing the overall transition rate by introducing more available pathways for (r)ISC.[75] This approach has been demonstrated

to be able to accelerate rISC rate and achieve short delayed fluorescence lifetime as low as around 100 ns.[76]

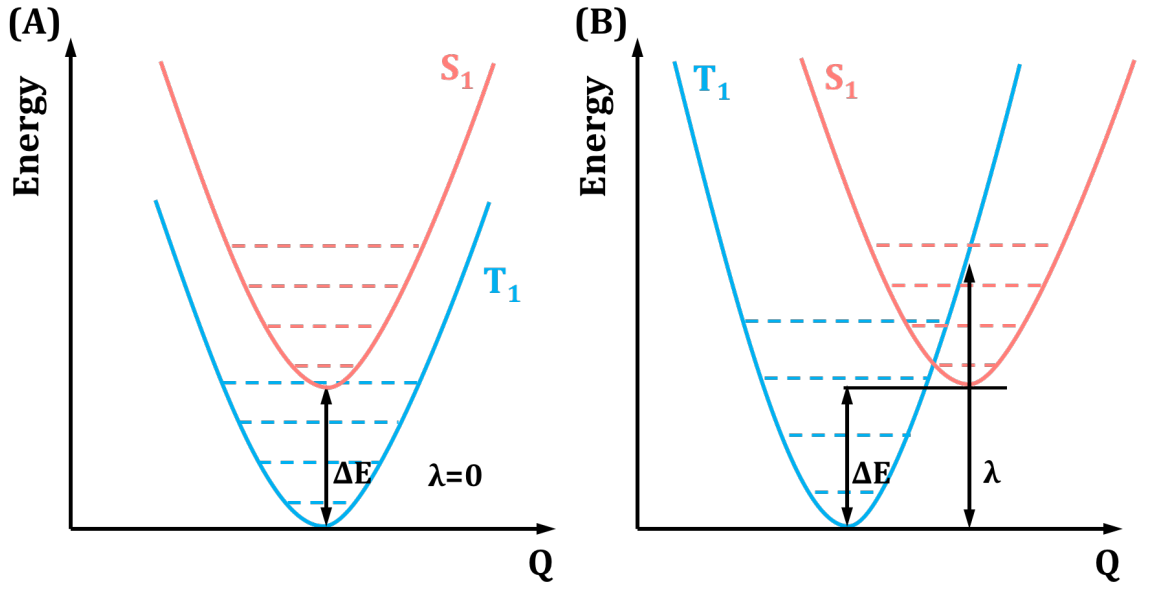

Fig. 2.7 The potential energy curves of S_1 and T_1 states for the case of (A) weak coupling and (B) strong coupling between two states. Figure adapted from references [51, 70].

2.3.5 Exciton interactions

Excitons are able to migrate and interact with each other, resulting in exciton-exciton annihilation. There are three types of exciton-exciton annihilations: (1) singlet-singlet annihilation, (2) singlet-triplet annihilation and (3) triplet-triplet annihilation (TTA). Annihilation of two singlets can be expressed as:

$$S_1^D + S_1^A \rightarrow S_0^D + S_n^A \rightarrow S_0^D + S_1^A + \text{phonons} \tag{2.31}$$

Annihilation of one singlet and one triplet can be expressed as:

$$S_1^D + T_1^A \rightarrow S_0^D + T_n^A \rightarrow S_0^D + T_1^A + \text{phonons} \tag{2.32}$$

where D and A represent donor and acceptor respectively. The situation is more complicated for triplet-triplet annihilation because the result is dependent on the spin values of the initial states. As discussed previously, interactions between two spin-half particles (fermions) leads to four spin angular momentum states with one singlet ($S = 0$) and three triplets ($S = 1$).

Triplet-triplet annihilation can be regarded as an interaction between four spin-half particles, resulting in 16 pure spin states with three spin configurations in total: two singlets (overall spin $S_{TT} = 0$), nine triplets ($S_{TT} = 1$) and five quintet states ($S_{TT} = 2$).[77]

$$T_1 + T_1 \rightarrow \begin{cases} S_n + S_0 \rightarrow S_1 + S_0 + \text{phonons} & S_{TT} = 0, \text{multiplicity} = 1 \\ T_n + S_0 \rightarrow T_1 + S_0 + \text{phonons} & S_{TT} = 1, \text{multiplicity} = 3 \\ Q_n + S_0 \rightarrow Q_1 + S_0 + \text{phonons} & S_{TT} = 2, \text{multiplicity} = 5 \end{cases} \tag{2.33}$$

However, even if quintet states are theoretically accessible, due to their significantly high energy, they are typically ignored.[78] Thus, triplet-triplet annihilation is described as the first two reactions. In the first reaction, two singlets are generated, one is at ground state S_0, the other is at higher singlet state S_n, which dissipates the additional energy by emission of phonons and decays back to S_1. This annihilation-produced singlet can emit fluorescence as normal singlets. However, its luminescence lifetime is longer as the formation of this singlet is restricted by the rate of the bimolecular process. Thus, fluorescence from these annihilation-produced singlets is described as P-type delayed fluorescence, distinguished from E-type delayed fluorescence due to TADF. TTA is feasible because the lifetime of triplet excitons is quite long (microseconds) compared to the nanosecond lifetime of singlet excitons even at low excitation densities.[79] TTA is generally considered as an energy loss and detrimental process in phosphorescence and TADF because the high-energy excitons are formed, which is likely to break carbon-carbon bond and causes materials degradation, especially for blue OLEDs due to higher photon energy. However, in some aromatic molecules, triplet fusion is efficient and it is able to harvest otherwise wasted triplets contributing to the total emission.[80–82]

2.4 Environmental effects on excited states and charge transfer

2.4.1 From single molecule to the condensed phase

The absorption and luminescence spectra of molecules vary with aggregation from single molecules in the gas phase, to the condensed phase, such as solid films. This can be attributed to the interactions with the surrounding environment, and there are several different effects. The first effect is from polarisation. The chromophore carries an electric dipole moment p_1, which is able to interact with the permanent or induced-dipoles of the adjacent molecules. Consequently, the potential energy of the chromophore is stabilised by the interaction energy

of the dipole moments. In a simplified picture, one can consider two dipoles with dipole moments p_1 and p_2 at an arbitrary orientation separated by the distance r, which is large compared to the size of the dipoles i.e. point dipole approximation. The electrostatic interaction energy is expressed as:

$$V = \frac{1}{4\pi\varepsilon_0} \frac{p_1 p_2 - 3(p_1\hat{\mathbf{r}})(p_2\hat{\mathbf{r}})}{r^3} \tag{2.34}$$

where $\hat{\mathbf{r}} = \mathbf{r}/r$ denotes the unit vector of the two dipoles. It is clear to see that the interaction energy increases with the dipole moments of the chromophores and depends on the distance r.

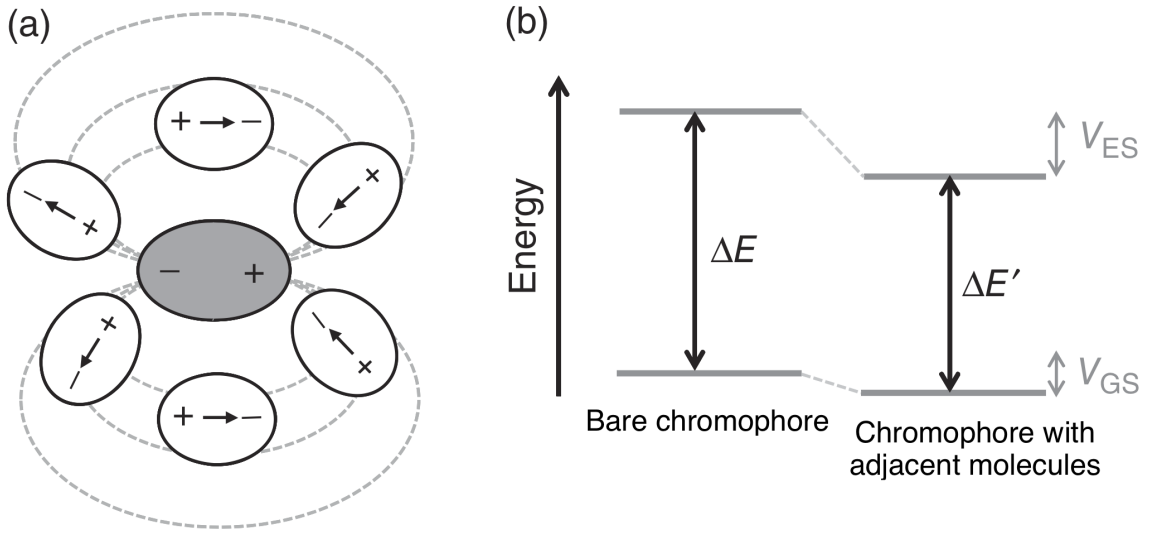

Fig. 2.8 Schematic illustrating the effect of van der Waals interactions between a chromophore and adjacent molecules. (a) The dipole moment of the chromophore, shown in gray, induces dipoles in adjacent molecules, shown in white, by electrostatic interaction. The dashed lines indicate the electrostatic field due to the chromophore's dipole. (b) The energy of the bare chromophore in its ground state, E_{GS}, and in its excited sate, E_{ES}, is reduced by the electrostatic interaction energy V. Figure adapted from reference [35].

When considering an ensemble of chromophores in the condensed phase, due to the superposition of different polarisation-induced energy shift, statistical effects need to be considered. The polarisation-induced energy shift depends on the distance and mutual orientation of chromophores and surrounding molecules. These parameters are randomly distributed in a disordered solid, such as amorphous film, resulting in a random distribution of energy shifts, the density of states (DOS) of which can be described by Gaussian distribution

centred around a mean value:

$$g(\varepsilon) = \frac{1}{\sqrt{2\pi}\sigma}\exp\left(-\frac{(\varepsilon-\varepsilon_0)^2}{2\sigma^2}\right) \tag{2.35}$$

where ε_0 is the mean energy, σ is the standard deviation. In contrast, for isolated chromophores in a dilute gas phase, density of states (DOS) is a δ-function and all chromophores have the same energy ε_{gas}. The mean energy ε_0 of a disordered condensed phase decreases from ε_{gas} by a mean polarisation-induced energy shift D', as illustrated in Fig 2.9.

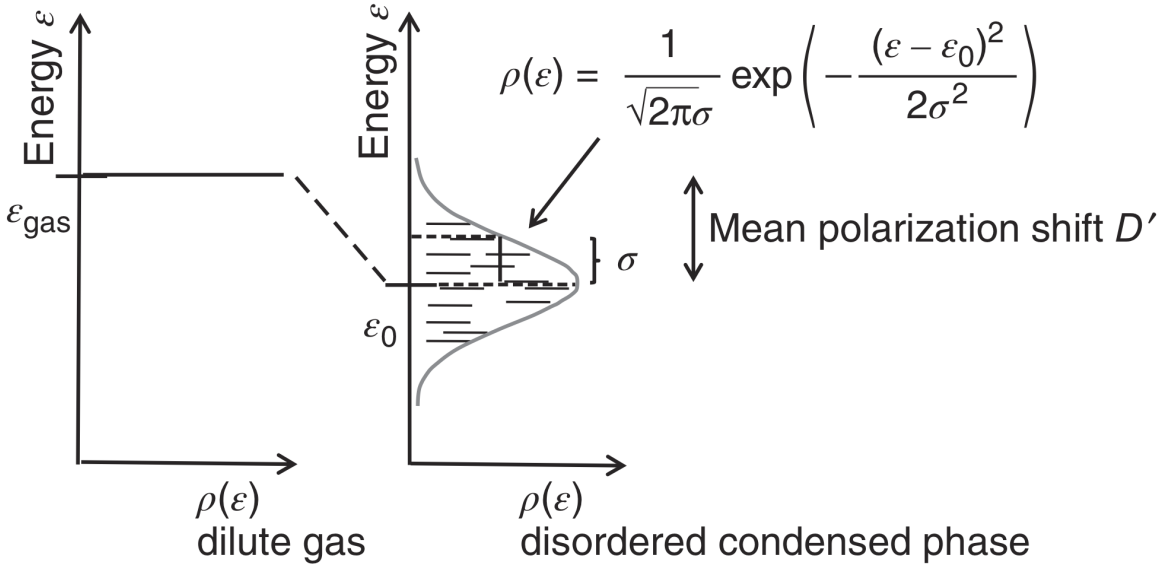

Fig. 2.9 Schematic illustrating the effect of polarization on the excited state energy levels ε of chromophores. In a dilute gas, the excited state energy is identical for all chromophores, resulting in a density of states (DOS) distribution that features a δ-function. In a disordered condensed phase, the chromophores experience a polarisation shift D' that varies statistically and leads to a Gaussian distribution of excited state energies centred around a mean value ε_0. Figure adapted from reference [35].

The polarisation effect discussed above is based on chromophores and stationary surrounding molecules. This applies to solid matrices, however, in the liquid state molecules are dynamic and able to reorient and move to maximise the dipole interaction and thus minimise the overall energy of the system "chromophore + surrounding molecules", which is known as the solvation process. When the chromophore is excited, the electronic polarisation of surrounding molecules happens on the same timescale, followed by geometric reorientation of these molecules and thus energetic relaxation. The same applies to the emission process. Emission occurs from the relaxed excited state and the surrounding molecules instantly change electronic distribution to stabilise the ground state dipole, followed by geometric

reorientation at longer timescale to reach the relaxed ground state energy. This timescale depends on the matrix rigidity. For organic solvents this is typically in the picosecond scale while for more viscous solvent it may become longer. The two excited state energies before and after solvent process and two ground state energies before and after solvent process form a four-level system, as illustrated in Fig 2.10. The process of solvation leads to an energy offset between the 0-0 transitions in absorption and emission, known as a Stokes' shift.

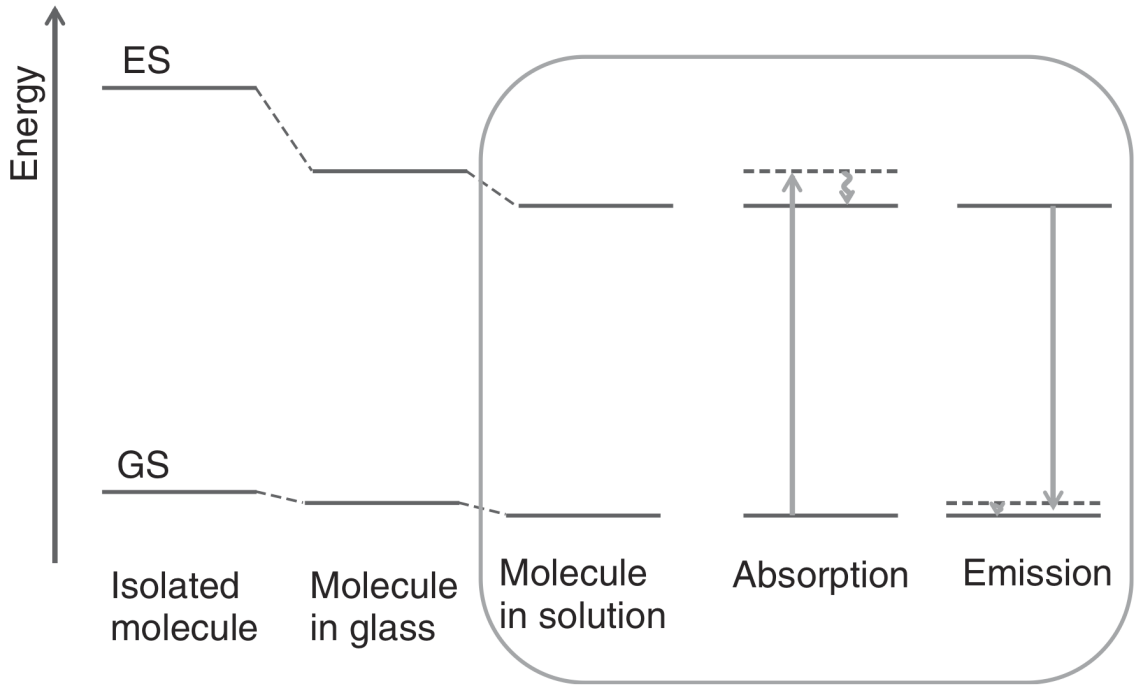

Fig. 2.10 Illustration of the energy shifts associated with solvation. Due to the effect of polarisation, ES and GS of molecule in glass are stabilised with respect to isolated molecule. The solvation process further stabilises the molecular energy in solution. For the absorption and emission, dotted lines denote the system "chromophore + surrounding molecules" energy before geometric reorientation, i.e. solvation, and solid lines denote energies after the solvation process, which form a four-level system. Figure adapted from reference [35].

A phenomenon arising from the solvation effect is solvatochromism, commonly seen in charge-transfer type molecules where the molecular dipole is large. Solvatochromism describes the significant change of absorption and emission energy and sometimes intensity corresponding to a change in medium polarity. Solvatochromism can be either positive or negative.[83] In the case of $\pi \rightarrow \pi^*$ transitions, the dipole moment of the molecule increases upon excitation, so a more polar or polarisable solvent will prefer to stabilise the excited state than the ground state. As a result, the energy gap between the ground and excited state is reduced and the absorption spectrum is red-shifted. This phenomenon is called positive

solvatochromism or a bathochromic shift. On the other hand, for molecules with $n \rightarrow \pi^*$ transitions, negative solvatochromism or a hypsochromic shift occurs in molecules whose dipole moment decreases in the excited state compared to the ground state, which stabilises the ground state energy in polar solvents, resulting in a blue-shifted absorption spectrum. The magnitude of this shift is determined by the change in molecule's dipole moment during the excitation, and solvent polarity.

2.4.2 Energy transfer process

In organic semiconductors, there are two energy transfer mechanisms for Frenkel excitons: long-range Förster resonance energy transfer (FRET) via Coulomb coupling (dipole-dipole interaction), and short-range Dexter energy transfer (DET) via exchange coupling. The rate for the energy transfer k_{ET} can be derived from Fermi's golden rule Eq. 2.13, and the electronic interaction energy is $\beta = |\langle \psi_f | \hat{H}' | \psi_i \rangle|$. The donor (D) and acceptor (A) molecule are considered as a combined system and two electrons are denoted as 1 and 2. The electronic interaction energy β can be expressed as:

$$\begin{aligned} 2\beta = &\langle \psi_D(1)\psi_A^*(2)|\hat{H}'|\psi_D^*(1)\psi_A(2)\rangle - \langle \psi_D(1)\psi_A^*(2)|\hat{H}'|\psi_D^*(2)\psi_A(1)\rangle \\ &- \langle \psi_D(2)\psi_A^*(1)|\hat{H}'|\psi_D^*(1)\psi_A(2)\rangle + \langle \psi_D(2)\psi_A^*(1)|\hat{H}'|\psi_D^*(2)\psi_A(1)\rangle \end{aligned} \quad (2.36)$$

In the first and last term, electrons remain on the same molecules before and after the interaction, which together constitute a coulomb term. In the second and third terms, electrons exchange between molecules and retain their status (ground or excited) before and after the interaction, which together constitute an exchange term. Thus, the equation can be written:

$$\beta = \beta^C - \beta^E \quad (2.37)$$

$$\begin{aligned} \beta^C = \langle \psi_D(1)\psi_A^*(2)|\hat{H}'|\psi_D^*(1)\psi_A(2)\rangle = &\langle \psi_{el,D}(1)\psi_{el,A}^*(2)|\hat{H}'|\psi_{el,D}^*(1)\psi_{el,A}(2)\rangle \\ &\cdot \langle \psi_{spin,D}(1)|\psi_{spin,D}^*(1)\rangle \cdot \langle \psi_{spin,A}^*(2)|\psi_{spin,A}(2)\rangle \end{aligned} \quad (2.38)$$

$$\begin{aligned} \beta^E = \langle \psi_D(1)\psi_A^*(2)|\hat{H}'|\psi_D^*(2)\psi_A(1)\rangle = &\langle \psi_{el,D}(1)\psi_{el,A}^*(2)|\hat{H}'|\psi_{el,D}^*(2)\psi_{el,A}(1)\rangle \\ &\cdot \langle \psi_{spin,D}(1)|\psi_{spin,A}(1)\rangle \cdot \langle \psi_{spin,A}^*(2)|\psi_{spin,D}^*(2)\rangle \end{aligned} \quad (2.39)$$

Förster resonance energy transfer (FRET) involves non-radiative energy transfer from the excited state donor to an acceptor through Coulomb interaction.[84, 85] If the donor and

acceptor size is small compared to their distance, it is sufficient to consider only the main dipole-dipole interaction. The energy transfer rate k_{FRET} is expressed as:

$$k_{FRET} \propto \frac{|\mu_D|^2 |\mu_A|^2}{R^6} \kappa^2 \tag{2.40}$$

where $|\mu_D|$ and $|\mu_A|$ are donor and acceptor transition dipole moments, κ is the orientation factor between $|\mu_D|$ and $|\mu_A|$, and R is the donor-acceptor distance. FRET relies on the close proximity of the donor and acceptor (D-A) and can only occur if the distance between donor and acceptor is less than approximately 10 nm.[86] In order for the spin-integral in β^C to be non-zero, spin multiplicity has to be the same for ground and excited states, and thus only singlets can be transferred through this mechanism.

Dexter energy transfer (DET) is a short-range exchange process in which two molecules (intermolecular) or two moieties of the same molecule (intramolecular) bilaterally exchange their electrons.[87] In order for the spin-integral in β^E to be non-zero, overlap between spin wavefunctions of donor and acceptor is required. The energy transfer rate k_{DET} is highly dependent on donor-acceptor distance R.[87]

$$k_{DET} \propto \exp(-\frac{2R}{L}) \tag{2.41}$$

where L is a constant related to the effective average radius of the donor and acceptor. The exchange process typically occurs at a distance shorter than 1 nm.[88–90] In Dexter energy transfer (DET), since electrons are exchanged between molecules, the process is not restricted by the spin-forbidden transition, which makes it feasible to transfer both singlets and triplets from donor to acceptor. The processes are summarised in Fig 2.11. It is clear that both Coulomb term and exchange term always contribute to the electronic interaction energy. However, at long distance regime, due to the short interaction distance of exchange term compared to Coulomb term, Förster transfer always dominates. If the distances is shorter than 1 nm, Dexter transfer is preferred given the exponential dependence on the distance.

2.4.3 Charge transfer process

If the interaction energy between transfer sites dominates over the energies due to dynamic or static disorder, charge transport occurs through a band where charge carriers delocalise. This band-like transport is commonly seen in inorganic semiconductors and some molecular crystals.[91] If energies due to dynamic and static disorder become significant, the delocalised wavefunctions in the transport band are interrupted and thus transport becomes incoherent

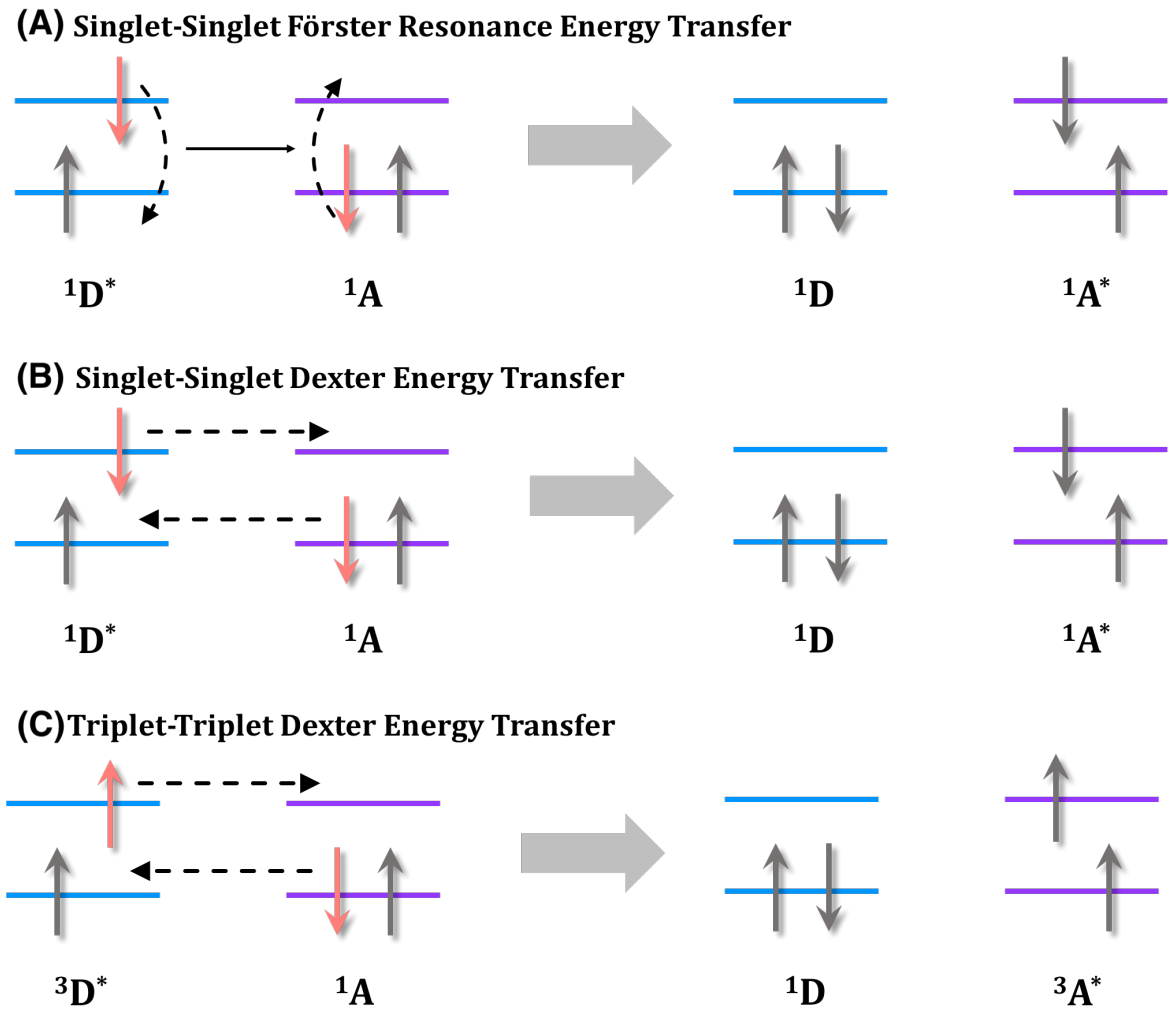

Fig. 2.11 (A) Diagram illustrating Förster resonance energy transfer (FRET) from a singlet donor to a singlet acceptor. (B) Diagram illustrating Dexter energy transfer (DET) from a singlet donor to a singlet acceptor. (C) Diagram illustrating Dexter Energy Transfer (DET) from a triplet donor to a triplet acceptor.

between individual sites, which is referred to as hopping motion. The same situation also applies to excitons. An exciton hopping in an amorphous ensemble of molecules can be described by the concept of a random walk model through a rough energy landscape. When a neutral exciton is generated at an arbitrary site within a density of states (DOS) distribution, initially energetic downwards hopping is a dominant process towards the energy tail and occasionally thermally activated upwards hopping is required for excitons to overcome intermediate energy barriers. Eventually, excitons reach a balanced quasi-equilibrium energy between downhill and thermally activated uphill jump. The process is illustrated in Fig 2.12. The mean quasi-equilibrium energy ε_∞ is calculated by the long-time limit of the statistical

average using Eq. 2.35 with $\varepsilon_0 = 0$:[35, 92, 93]

$$\varepsilon_\infty = \lim_{t\to\infty} \varepsilon(t) = \frac{\int_{-\infty}^{+\infty} \varepsilon g(\varepsilon)\exp(-\varepsilon/kT)d\varepsilon}{\int_{-\infty}^{+\infty} g(\varepsilon)\exp(-\varepsilon/kT)d\varepsilon} = -\frac{\sigma^2}{kT} \tag{2.42}$$

where σ is the standard deviation, k is the Boltzmann constant, and T is the temperature in Kelvin. In the random walk model, excitons occasionally overcome intermediate energy barriers via thermal activation. Upon lowering the temperature this becomes increasingly difficult. In the $T \to 0$ limit all jumps that require activation are frozen out. As a consequence, the luminescence lifetime of excitons elapses before excitons reach the quasi-equilibrium energy, resulting in a blueshift of steady-state luminescence at low temperature. This blueshift is specific for excitations that coupled by short-range interactions such as triplet excitons. For singlet excitons, long-range dipole coupling (Föster-type transfer) allows excitons to bypass a neighbouring barrier and transit to a lower energy site further away, so that the quasi-equilibrium energy is reached. Non-equilibrium diffusion is difficult to describe analytically except for 0 K, and can only be solved via Monte Carlo simulation.[94]

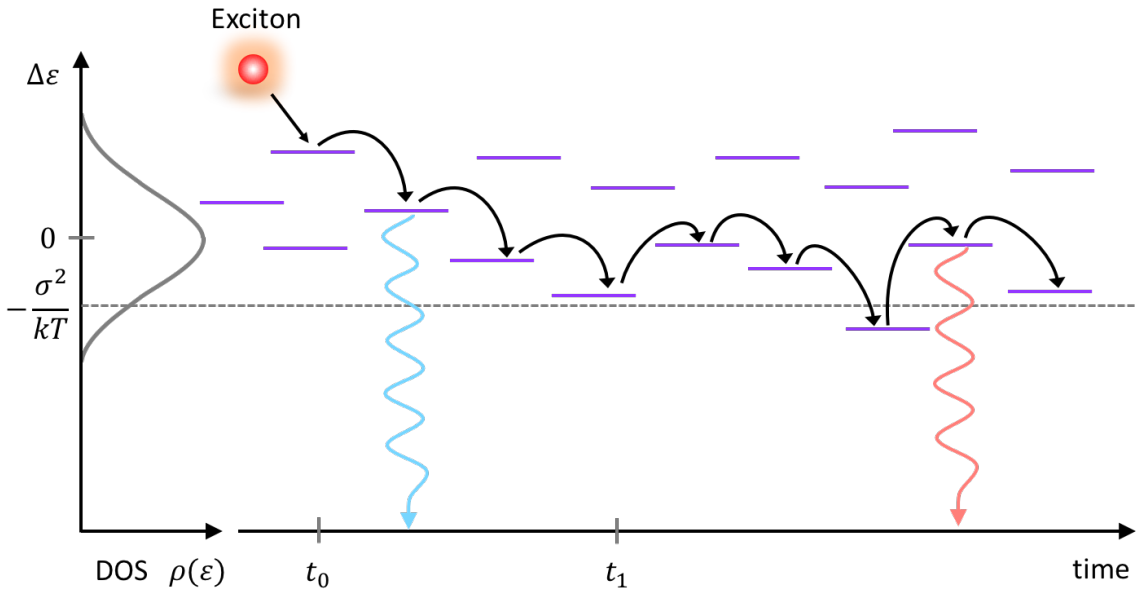

Fig. 2.12 Illustration of a charge carrier, generated at an arbitrary energy, that hops within a Gaussian DOS. The dotted horizontal line is the energy at which the charge carriers tend to equilibrate in the long time limit. Figure adapted from reference [92].

Marcus theory for charge transfer

Besides the long time limit of the hopping process, it is worth considering the charge or exciton transfer process between two sites, which was investigated in molecular crystals[95–97] and in solution[98, 99], both showing a similar mechanism. The charge carrier is localised in a transfer site due to dynamic disorder, and the charged molecule couples to the surrounding environment, which forms a polaron. The charge transfer is associated with a distortion of the molecule and the environment, which requires reorganisation energy λ. Therefore, the charge transfer process is thermally activated. The reorganisation energy consists of inner and outer contributions: $\lambda = \lambda_{inner} + \lambda_{outer}$. The inner reorganisation energy is associated with intramolecular distortion when a molecule becomes charged and the outer reorganisation energy is due to intermolecular displacement and polarisation. In a rigid organic solid where the inner reorganisation energy dominates, considering the charge transfer from molecule A to molecule B, the inner reorganisation energy is the sum of geometric relaxation energies for A and B: $\lambda_{inner} = E^A_{rel} + E^B_{rel} = 2E_{rel}$, as illustrated in Fig. 2.13 (B). When considering molecules A and B and the environment as a whole system, the potential energy minimum occurs at Q_i and Q_f for the initial and final state respectively, and the reorganisation energy is λ. Charge transfer occurs at the intersection of both potential energy curves, which can provided by an activation energy E_a due to thermal fluctuations. This is the key idea of Marcus theory. In general, the charge transfer rate given by Marcus theory is[35, 100–102]

$$W_{if} = \frac{2\pi}{\hbar} J_{if}^2 \sqrt{\frac{1}{4\pi k_B T \lambda}} \exp\left[-\frac{E_a}{k_B T}\right], \tag{2.43}$$

$$\text{with} \quad E_a = \frac{\lambda}{4}\left[1 + \frac{\Delta G^0}{\lambda}\right]^2 \tag{2.44}$$

where J_{if} is the electronic coupling between the initial state i and the final state f, E_a is the activation energy for the reaction, ΔG^0 is the variation of Gibbs free energy for the reaction. For charge transfer between identical molecules, $\Delta G^0 = 0$ and thus $E_a = \lambda/4$. When related to the geometric relaxation energy of the molecule, it gives $E_a = E_{rel}/2$.[103, 104] The relaxation energy can be calculated by adding contributions from each vibrational normal mode ω_j:[101, 105, 106]

$$E_{rel} = \sum_j \hbar \omega_j S_j \tag{2.45}$$

where S_j is the Huang-Rhys-parameter of the corresponding mode ω_j.

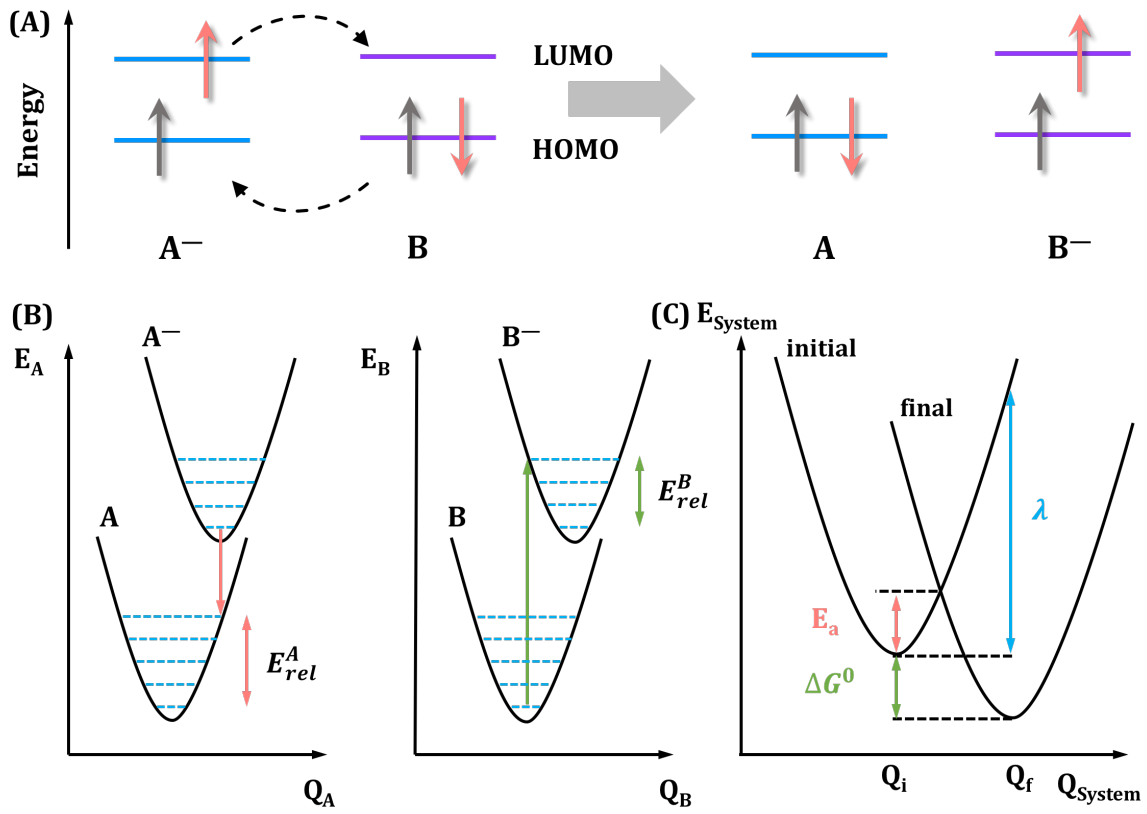

Fig. 2.13 (A) Frontier orbital representation of the triplet transfer mechanism as charge transfer. (B) The inner reorganisation energy consists of the geometric relaxation energies of molecule A and B: $\lambda_{inner} = E^A_{rel} + E^B_{rel} = 2E_{rel}$. E_{rel} is the energy related to the change from the equilibrium position of charged state to that of uncharged ground state. (C) The potential energy of the entire system (molecule A, B and surrounding molecules) versus a generalised configuration coordinate describing the entire system. The minimum of the initial and final state curve occurs at Q_i and Q_f. The reorganisation energy λ gives the difference in potential energy between Q_i and Q_f. Transfer happens either by thermal activation $E_a = \lambda/4$ at the intersection of potential curves or via quantum mechanically tunnelling. Figure adapted from reference [100].

Triplet exciton transfer

Triplet exciton diffusion within the density of states can be regarded as a series of triplet energy transfer processes. Each individual triplet transfer adopts the exchange mechanism, i.e. Dexter energy transfer, and thus involves the correlated exchange of two electrons under spin conservation, that is a double charge transfer. Therefore, triplet exciton transfer can be analysed in a similar approach as charger transfer. Firstly it is worth considering the regimes where triplet transfer occurs via adiabatic or non-adiabatic transport. The difference between the two regimes is demonstrated in Fig. 2.14.[102] For a two-site system, a charge carrier

transfers from one molecule to another, and the local fluctuation in the equilibrium position of the associated atoms can be described by two corresponding configuration coordinates (curves $E_{(+)}$ and $E_{(-)}$), which intersect at some point. For non-zero resonance electron coupling integral J between two sites, the degeneracy at the intersection point is replaced by a gap $\Delta E = 2J$ between two resulting generalised (collective) coordinates, see upper and lower solid curves. Therefore, the energy barrier E_a between two equilibrium positions decreases by the electronic coupling, noted as modified barrier height W_a'.

$$W_a' = E_a - J \tag{2.46}$$

If the electron coupling integral J is large, a charge carrier is able to instantaneously transport through the atoms and the whole system remains on the lower-energy surface, see Fig. 2.14 (A). This is the regime for adiabatic motion. However, if J is small the carrier cannot adapt to molecular vibrations, and non-adiabatic motion occurs. A carrier at the lower-energy surface of the first site reaches the upper-energy surface, followed by relaxing to an energetic minimum at the second site, see Fig. 2.14 (B). The rate describing the carrier transfer from site i to site j in the adiabatic regime for a disorder-free system is written as[102]

$$W_{ij} = \omega_0 \exp\left(-\frac{W_a'}{k_B T}\right) \tag{2.47}$$

where ω_0 is a characteristic frequency of optical or acoustic phonons, for example the high-energy modes observed in the vibrational progression of absorption and emission spectra or low-energy torsional modes. If J exceeds a critical value J_{cr}, $J > J_{cr}$, then $J \approx E_a$ and $W_a' \approx 0$, so that the transfer rate W_{ij} is weakly dependent on T. The critical value J_{cr} is given by[102]

$$J_{cr} = (E_a - J)^{1/4} \left(\frac{2k_B T}{\pi}\right)^{1/4} \left(\frac{\hbar\omega_0}{\pi}\right)^{1/2} \tag{2.48}$$

When considering non-adiabatic triplet transport, it is important to evaluate the jump rate W_{ij} at high and low temperatures.[96] For the high-temperature regime where $k_B T \gg \hbar\omega_0$, the jump rate can be expressed as[102]

$$W_{ij} = \frac{{J_0}^2}{\hbar}\sqrt{\frac{\pi}{4E_a k_B T}} \exp\left(-2\frac{r_{ij}}{L}\right) \exp\left[-\frac{E_a}{k_B T} - \frac{\varepsilon_j - \varepsilon_i}{2k_B T} - \frac{(\varepsilon_j - \varepsilon_i)^2}{16E_a k_B T}\right] \tag{2.49}$$

For the low-temperature regime, where $k_B T \ll \hbar\omega_0$, the jump rate can be expressed as[102]

$$W_{ij} = \nu_0 \exp\left(-2\frac{r_{ij}}{L}\right) \exp\left[-\frac{|\varepsilon_j - \varepsilon_i| + (\varepsilon_j - \varepsilon_i)}{2k_B T}\right] \tag{2.50}$$

where J_0 and ν_0 are related to the electronic coupling, E_a represents the activation energy for triplet transfer, r_{ij} is the intermolecular distance between sites i and j, L is the effective triplet localisation radius, and ε_i and ε_j are the energies of sites i and j. Eq. 2.49 is basically a Marcus expression which describes multiphonon hopping transport of triplet excitons. Phonons are involved not only to compensate the energy difference between sites, but also to overcome the energy barrier separating them.[101] Eq. 2.50 fits the Miller-Abrahams model where triplets transport via a single phonon tunnelling process between sites i and j with $\varepsilon_j > \varepsilon_i$.[107] The phonon now only provides the energy difference between sites. It should be noted that the activation energy E_a does not affect the transfer rate any more at low temperature.

The theoretical analyses above use the two-site transitions to approximate the energetic disorder. In order to conveniently compare the theoretical results with experimental data, effective-medium approximation (EMA) theory of non-adiabatic triplet transport is introduced to derive an expression for the effective triplet energy-transfer rate W_e in an energetically disordered system. The Eq. 2.49 and Eq. 2.50 can be written as

$$W_e = \frac{{J_0}^2}{\hbar}\sqrt{\frac{\pi}{4E_a k_B T}}\exp\left(-2\frac{a}{L}\right)\exp\left[-\frac{E_a}{k_B T}-\frac{1}{8}\left(\frac{\sigma}{k_B T}\right)^2\right] \tag{2.51}$$

describing the high-temperature regime where multiphonon energy-transfer mechanism is active, and

$$W_e = \nu_0\exp\left(-2\frac{a}{L}\right)\exp\left[-\frac{1}{2}\left(\frac{\sigma}{k_B T}\right)^2\right] \tag{2.52}$$

describing the low-temperature regime where single phonon tunnelling is active. a is an average intermolecular distance, and σ is the width of the Gaussian DOS distribution.

Optical electron transfer

Besides the thermally-induced electron transfer process discussed above, electron transfer can also be induced by optical transitions, i.e. absorption and emission. These two electron transfer processes are connected, as was developed by Hush[108] and Mullikin[109]. The semi-classical Mulliken-Hush model describes the absorption from the ground state to the charge-transfer (CT) state as[110]

$$\frac{A(\nu)}{\nu} = A_0\exp\left[-\frac{(E_{CT}^0+\lambda_{CT}-h\nu)^2}{4k_B T\lambda_{CT}}\right] \tag{2.53}$$

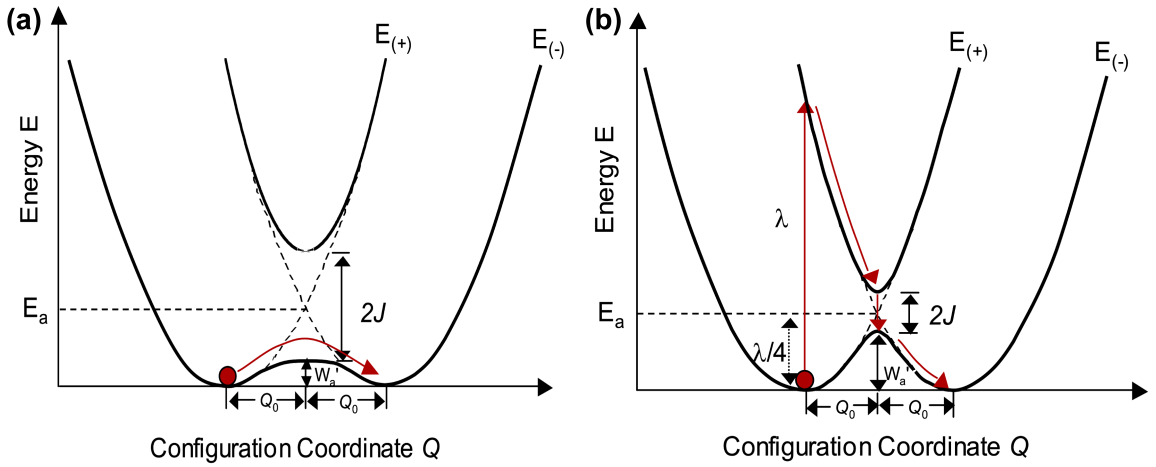

Fig. 2.14 Schematic representation of (A) adiabatic and (B) non-adiabatic transport in the configurational coordinates for a two-site system. The arrow indicates the path of the excited state. Figure adapted from reference [102].

$$E_{CT}^{a,max} = h\nu_{max} = E_{CT}^{0} + \lambda_{CT} \tag{2.54}$$

where $A(\nu)$ is the optical absorption intensity per donor-acceptor pair; ν is the transition frequency; A_0 is the exponential prefactor depending on the adiabatic transition dipole moment d_{CT}^{a}; h is Planck's constant; E_{CT}^{0} is the excitation energy of the relaxed CT state; λ_{CT} is the reorganisation energy; $E_{CT}^{a,max}$ is the energy at the maximum of the CT absorption; ν_{max} is the transition frequency at the maximum of the CT absorption. The potential energy surface diagram is shown in Fig. 2.15. The electronic coupling between the ground and CT states J_{CT-G}, is linked to the adiabatic transition dipole moment d_{CT}^{a} of the CT absorption band by the equation[110]

$$J_{CT-G} = \frac{d_{CT}^{a}}{\Delta d_{CT}} E_{CT}^{a,max} \tag{2.55}$$

where Δd_{CT} is the difference between the dipole moments of the adiabatic ground and CT states.

Similarly, the CT emission spectrum, in the semi-classical Mulliken-Hush model, is given by

$$\frac{I(\nu)}{\nu^3} = I_0 \exp\left[-\frac{(E_{CT}^{0} - \lambda_{CT} - h\nu)^2}{4k_B T \lambda_{CT}}\right] \tag{2.56}$$

where $I(\nu)$ is the optical-emission intensity and I_0 is the exponential prefactor.

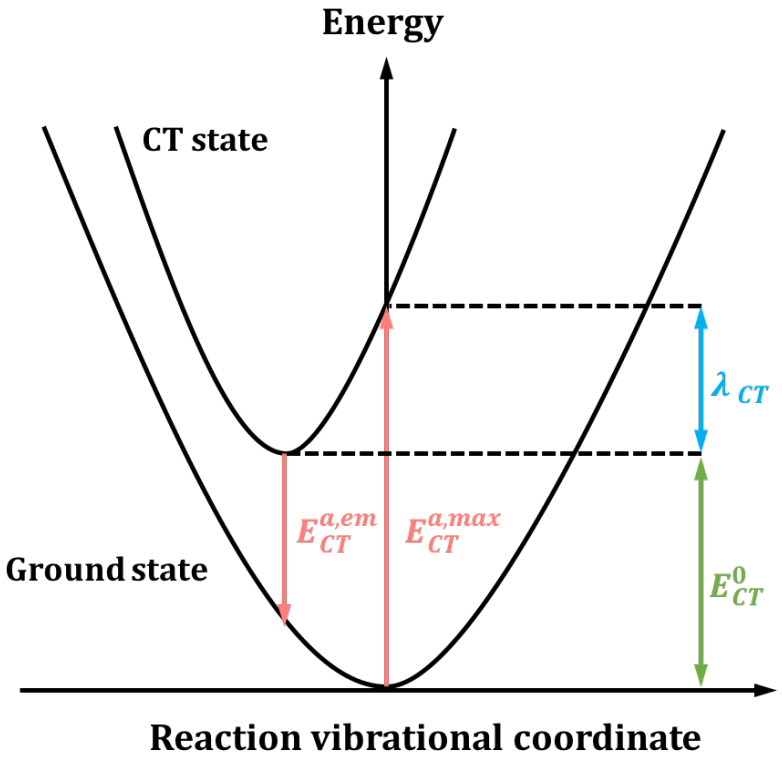

Fig. 2.15 Illustration of the adiabatic potential energy surfaces for the electronic charge-transfer (CT) and ground (G) states. λ_{CT} is the reorganisation energy; E_{CT}^{0} is the excitation energy of the relaxed CT state; $E_{CT}^{a,em}$ is the vertical transition from the CT state to the ground state; $E_{CT}^{a,max}$ is the energy at the maximum of the CT absorption. Figure adapted from reference [110].

Chapter 3

Experimental Methods

3.1 Introduction

This chapter describes the experimental methods employed in this thesis to obtain results presented in the following results and discussion chapters. It consists of four sections. The first section is sample preparation. The second section will introduce spectroscopy techniques, including steady-state absorption and luminescence spectroscopy, transient absorption spectroscopy, room-temperature and cryogenic time-resolved photoluminescence spectroscopy, Raman spectroscopy, and photoluminescence quantum efficiency measurements. The third section contains structural characterisation by X-ray diffraction. The fourth section will present computational methods using density functional theory calculations.

3.2 Sample preparation

Carbene-metal-amide family emitters are synthesised by collaborators in the Chemistry Department of the University of East Anglia (UEA) as reported in the literature.[32, 111, 112] Host molecules are supplied by Sigma Aldrich and Luminescence Technology Corp. The majority of the work presented in this thesis is focused on solution-processed thin films of organic molecules, either via spin cast or drop cast. For spin-cast films, host-guest thin films of different weight ratios or crystalline thin films (80 wt.% CMA1 in polyethylene oxide (PEO)) were made from chlorobenzene solution in 20 mg/mL concentration, heated overnight at 70 °C to dissolve. These well-mixed solutions (45 µL) were spun inside a nitrogen-filled glove box onto 13 mm pre-cleaned (ultrasonic in acetone and isopropanol followed by oxygen plasma for 10 min) spectrosil substrates at 1,200 r.p.m. for 40 s at room temperature to form thin films. Samples were stored in the nitrogen glovebox to minimise degradation. There

are several controllable parameters in the spin-coating process: composition of the solution, temperature, speed and time of spin. The thickness of the wet film has an inverse relationship to the spin speed and also depends on the solution concentration and viscosity.[113]

Drop-cast films are used for transient absorption spectroscopy due to higher optical density (OD), and for Raman spectroscopy and X-ray diffraction for better signal. Films were drop-cast from solution, 60 µL per film on 13 mm pre-cleaned spectrosil substrates heated to 70 °C for neat films and 120 °C for crystalline films. Films were made and kept in a glovebox. For transient absorption spectroscopy measurements, films are encapsulated using a glass slide and epoxy prior to being measured.

Solution samples in various solvents were prepared at 1 mg/mL in the nitrogen glovebox, deoxygenised and sealed in 1 mm path length QS grade quartz cuvettes.

3.3 Spectroscopy

3.3.1 Steady state absorption

A Shimadzu UV-3600 Plus spectrophotometer was employed to measure the steady-state absorbance of samples, which comprises three detectors: a PMT (photomultiplier tube) for the ultraviolet and visible regions and InGaAs and cooled PbS detectors for the near-infrared region. The wavelength range is from 185 to 3,300 nm with high resolution of 0.1 nm.

Working principle

The basic working principle is to detect the intensity of the light and compare with the decreased intensity after passing through the sample. The transmittance T is defined as the intensity of the light beam after transmitting through the sample, I_t, divided by the intensity of the measurement light beam I_0.

$$T = \frac{I_t}{I_0} \tag{3.1}$$

Sometimes it is more common to use the absorbance, *Abs*, also referred to as optical density (OD), which is given by:

$$Abs = \log_{10} \frac{1}{T} \tag{3.2}$$

The relationship between the absorbance *Abs*, and the concentration of solution C, is expressed in “Lambert-Beer law”, where ε is the molar extinction coefficient and L is the

optical path length.[114]

$$Abs = \varepsilon CL \tag{3.3}$$

3.3.2 Steady state photoluminescence

An Edinburgh Instruments FLS980 spectrofluorimeter was used to measure steady-state luminescence spectra. A R928P PMT detector was used in this experiment, with a wavelength range of 200 nm to 870 nm and a dark count rate of <50 cps (at -20 °C). The detector is operated in single photon counting mode. The PL spectra were collected from 350 nm to 650 nm at the resolution of 1 nm. Samples were excited by a 450 W xenon arc lamp. The light from the xenon arc is focused into the monochromator by using an off-axis ellipsoidal mirror.

3.3.3 Transient absorption spectroscopy

Transient absorption spectroscopy (TA) is a technique for studying short-time exciton dynamics (ps to ns time range and ns to µs time range), especially the intersystem crossing time (ISC) from singlet to triplet manifold in this thesis. TA measures the differential change in transmission of a sample before and after photoexcitation as a function of time, and thus TA probes the dynamics of the exciton population. TA data is typically expressed as differential transmission ($\Delta T/T$), which is defined in terms of the transmission with and without a pump pulse

$$\frac{\Delta T}{T} = \frac{T_{on} - T_{off}}{T_{off}} \tag{3.4}$$

where T denotes the intensity of the transmitted probe beam. A pump pulse is used for photoexciting the sample and "on" and "off" are controlled by a chopper. A probe pulse is used to measure the differential transmission over time and extract the information about the exciton population. In this way, $\Delta T/T$ is built up as function of wavelength (probe pulse) and time. The time resolution of the TA depends on the length of the pulses. The main laser used was a Spectra Physics Solstice Ti:Sapphire laser, outputting pulses of width 80 fs and a repetition rate of 1 kHz at 800 nm. The pump beam was frequency-doubled using a BBO to give 400 nm pulses. Excitation fluence was varied from 9-60 µJcm^{-2}. The probe beam was generated from the 800 nm fundamental using a noncollinear optical parametric amplifier (NOPA), built in-house. The probe was further split into a probe and reference, with only the probe beam overlapping with the pump on the sample. The pump-probe delay was controlled using a computer-controlled delay stage. A Hamamatsu G11608-512 InGaAs dual-line array detector was used to measure the transmitted probe and reference.

3.3.4 Time-resolved photoluminescence spectroscopy

Time-resolved photoluminescence spectra were measured by an electrically-gated intensified charge-coupled device (ICCD) camera (Andor iStar DH740 CCI-010) connected to a calibrated grating spectrometer (Andor SR303i). Samples were photoexcited by femtosecond laser pulses which were created by second harmonic generation (SHG) in a β-barium borate crystal from the fundamental source (wavelength = 800 nm, pulse width = 80 fs) of a Ti: Sapphire laser system (Spectra-Physics Solstice), at a repetition rate of 1 kHz. The photons from the laser pulses have a wavelength of 400 nm. A 425 nm long-pass filter was used to prevent scattered laser signal from entering the camera. Temporal evolution of the PL emission was recorded by stepping the ICCD gate delay with respect to the trigger pulse. The minimum gate width of the ICCD was 5 ns.

Working principle of intensified CCD cameras (ICCD)

Intensified CCD cameras are able to overcome the read noise limit by exploiting gain and also capable of achieving very fast gate times. The gating and amplification are achieved in the image intensifier tube. The image intensifier tube is composed of the photocathode, microchannel plate (MCP) and a phosphor screen and placed in a vacuum chamber. The properties of these components determine the performance of the device. The configuration of an image intensifier tube is illustrated in Fig. 3.1. The photocathode is coated on the inside surface of the output window and it captures the incident photons. When an incident photon striking the photocathode, a photoelectron is emitted and then accelerated towards the MCP by an applied electric field. The MCP is a thin disc (around 1 mm thickness) carved with a honeycomb of glass channels approximate 6-10 μm, each with a resistive coating. A high voltage is applied across the MCP to accelerate the photoelectron with high energy to one of the channels in the disc. Photoelectrons with high energy are able to release secondary electrons from the channel walls. These electrons experience acceleration similarly, resulting in a cloud of electrons departing from the MCP and amplifying the signal. Gains of 200 can be achieved easily. The degree of signal amplification/electron multiplication is governed by the gain voltage applied across the MCP which can be controlled in the camera.

The noise and hence the sensitivity of the ICCD depends on the image intensifier. The image intensifier amplifies the light signal so that the noise of the camera is not dominated by the CCD section. However, there still exists a dark current component originating from thermally generated charge in the photocathode which will also be amplified. A significant advantage of an ICCD camera over CCD is the optical shuttering properties. The image intensifier is capable of being operated as a very fast optical switch and capturing an optical

signal in a nanosecond. Depending on the negative or positive voltage applied, the intensifier can be gated on or off. The minimum time required to switch the intensifier from being off to on and then off again is defined as the minimum gate time. The minimum gate time is typically governed by various factors but principally by the structure of the photocathode and the electron gating circuitry. The minimum gate time of the ICCD used in this thesis is 5 ns.

Cryogenic photoluminescence measurements

Cryogenic steady-state and time-resolved photoluminescence measurements (10 K to 300 K) were carried out using an Oxford Instruments Optistat dynamic continuous flow cryostat with liquid helium coolant, and an ITC 502 S temperature control unit.

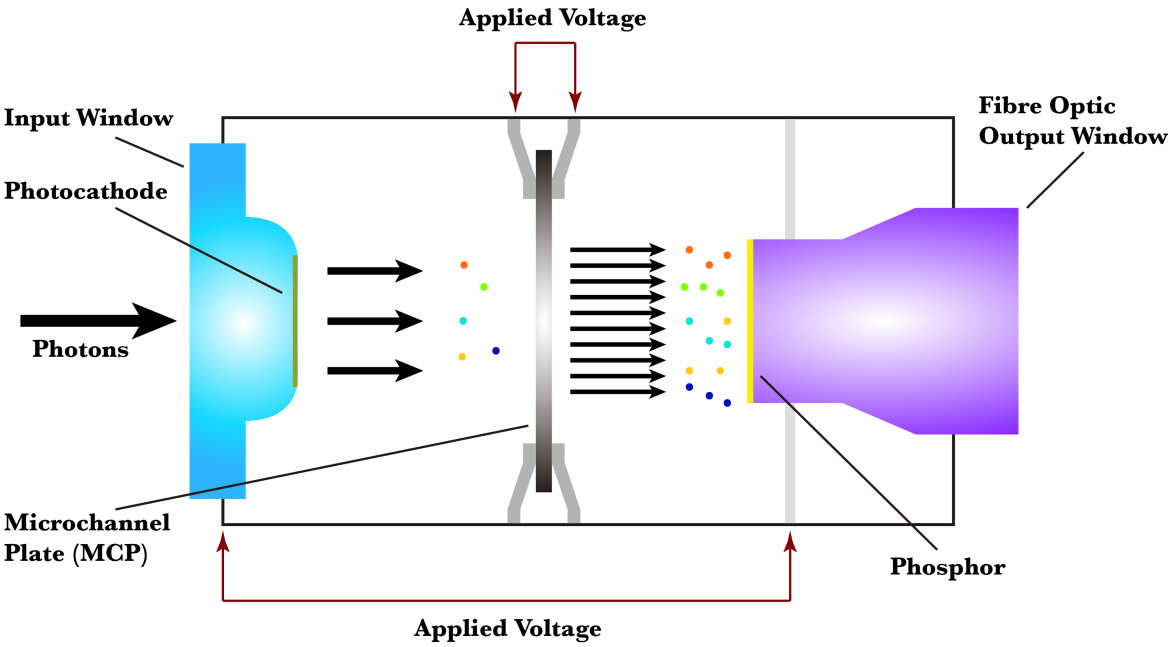

Fig. 3.1 Configuration and working principle of an image intensifier tube in an intensified CCD camera (ICCD). Colourful spots represent photoelectrons with different energies.

Characteristic luminescence lifetime

Lifetimes of up to 1 ms can be accurately measured in this experiment due to the 1 kHz repetition rate of the laser used. For non-exponential luminescence decays in the solid state, a characteristic lifetime rather than a monoexponential decay time is quoted. We choose the time taken for the delayed component to reach 63% (1-(1/e)) of the total emission integrated from 0 to 950 µs. This allows direct comparison to lifetimes extracted from monoexponential

decays as this is the fraction of total emission which has been emitted after one time constant of a monoexponential decay.

3.3.5 Raman spectroscopy

Raman spectroscopy, based on the process of Raman scattering, is employed to detect vibrations in molecules and provide information on chemical structures and physical forms. Sample preparation is relatively simple and is compatible with different physical states, for instance, as solids, liquids or vapours, in different temperature states, in bulk, as microscopic particles, or as surface layers, which makes Raman spectroscopy quite versatile and widely used. The nature of the Raman effect is based on the inelastic scattering of electromagnetic radiation. During this interaction, energy is transferred between the incoming photons and the molecular vibrations and thus the scattered photons have different energies to the incoming photons. Smekal[115] firstly hypothesised the inelastic scattering of light and the phenomenon was experimentally confirmed by Raman and Krishnan[116]. Afterwards, the phenomenon was named as Raman spectroscopy. In this thesis, Raman measurements were conducted by back-scattering (HORIBA T64000) a 640 nm (CW diode) laser. Spectra were collected between 13 and 1770 cm^{-1} where the CCD detector (HORIBA Synapse Open-Electrode) has a monotonically increasing quantum efficiency of between 0.43 and 0.50. Acquisitions employed a 100× optical objective and used minimal necessary laser intensity to avoid laser damage. Drop-cast film samples were measured in air at room-temperature.

Raman scattering

When light interacts with matter, the incoming photons may be absorbed, scattered, or may not interact with the material and pass through it. For scattering, the energy of the photon is not required to match the difference between two energy levels of the molecule. In Raman scattering, the light interacts with the molecule and polarises the electron cloud around the nuclei to form a temporary state called a “virtual state”, which is not stable so the photon is re-radiated quickly. If only the electron cloud is distorted in scattering, the photons will be scattered with very small frequency changes as the electrons are considerably light compared to nuclei. The scattering process is considered as elastic scattering, called Rayleigh scattering for molecules. However, if nuclear motion (ΔQ) is involved during scattering, energy will be transferred either from the incoming photon to the molecule, or from the molecule to the scattered photons. This scattering is inelastic and the energy of the scattered photon differs from that of the incident photon by one vibrational unit, which is Raman scattering. It should be noted that Raman scattering is an inherently weak process with only one in every

$10^6 - 10^8$ photons scattering in this way[117]. The intensity of Raman scattering is defined by the equation[117]

$$I = Kl\alpha^2\omega^4 \tag{3.5}$$

where K consists of constants, l is the laser power, ω is the frequency of the incident radiation, and α is the polarisability of the electrons in the molecule. However, sensitivity can be achieved with modern lasers and microscopes by employing very high power densities, but it could result in other problems such as sample degradation and fluorescence. The process can be expressed mathematically because the distortion of electron cloud is directly related to the induced dipole moment. Under the external electrical field $\vec{E}$, only considering the first order component, the induced dipole moment $\vec{p}$ is simplified to

$$\vec{p} = \alpha \cdot \vec{E} \tag{3.6}$$

where the polarisability α is a tensor which is dependent on the shape and dimensions of the chemical bond. As chemical bonds vary during vibrations, the polarisability is dependent on the vibrations of the molecule, i.e. the normal coordinate Q of the molecule. The relationship can be expressed as a Taylor series[118]

$$\alpha = \alpha_0 + \sum_k \left(\frac{\partial \alpha}{\partial Q_k}\right)_0 \cdot Q_k + \frac{1}{2}\sum_{k,l}\left(\frac{\partial^2 \alpha}{\partial Q_k \partial Q_l}\right)_0 \cdot Q_k \cdot Q_l + \ldots \tag{3.7}$$

where Q_k and Q_l are the normal coordinates corresponding to the kth and lth normal vibration with vibrational frequencies ν_k and ν_l. In a first approximation, only the first two terms are maintained. Thus, considering the nth normal vibration, Eq.3.7 is simplified to

$$\alpha_n = \alpha_0 + \alpha_n' \cdot Q_n \tag{3.8}$$

with α_n' the derivative of the polarisability tensor with respect to the normal coordinate Q_n under equilibrium conditions. Light can be considered as an oscillating electric field, with the electric field vector $\vec{E}$ at the moment t is described as

$$\vec{E} = \vec{E_0} \cdot \cos(2\pi \cdot \nu_0 \cdot t) \tag{3.9}$$

Combining Eq. 3.6 3.7 and 3.9, the induced dipole moment can be expressed as a function of the vibrational frequencies of the molecule ν_n and incident radiation ν_0

$$\vec{p} = \vec{p}(\nu_0) + \vec{p}(\nu_0 + \nu_n) + \vec{p}(\nu_0 - \nu_n) \tag{3.10}$$

The first term represents the elastic scattering, i.e. Rayleigh scattering: the frequency of the induced dipole moment is the same as the incident radiation. The second and third term correspond to the inelastic scattering, Raman scattering. Second term is called anti-Stokes scattering with higher energy of scattered radiation compared to the incident radiation, while the third term, Stokes scattering, represents lower frequency. Three different scattering processes are illustrated in Fig. 3.2. Usually, the intensity in a Raman spectrum is plotted as a function of wavenumber ω, expressed in cm^{-1}, representing the frequency shift of scattered light ν_m from the incident light ν_0.

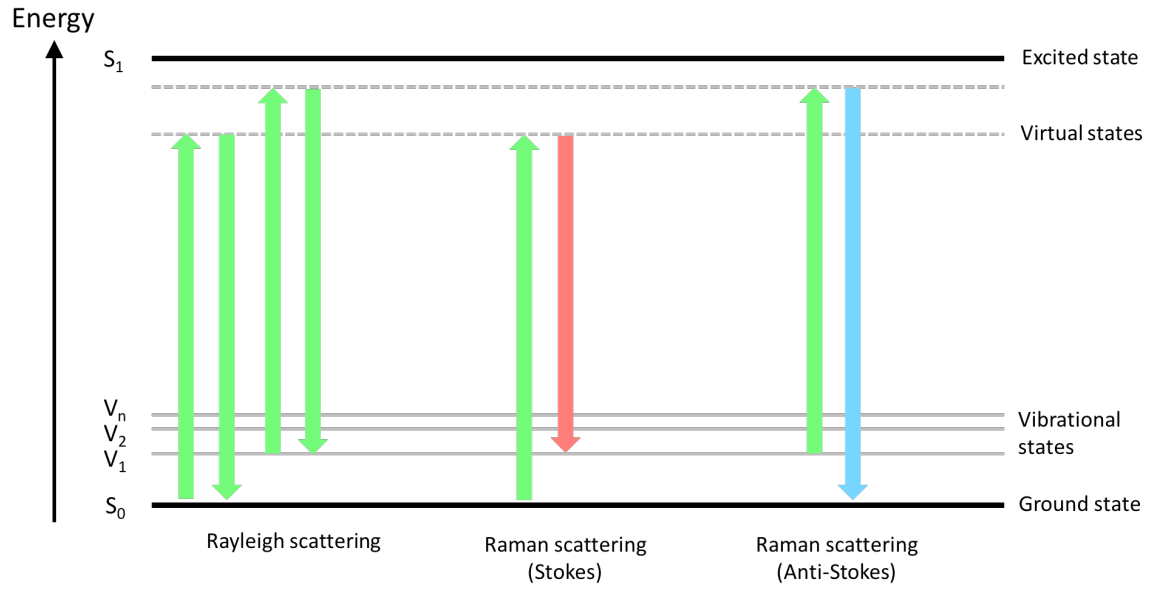

Fig. 3.2 Jablonski diagram of Rayleigh scattering, Stokes Raman scattering and Anti-stokes Raman scattering.

The basic selection rule

The basic selection rule is that Raman scattering originates from the change in polarisability of the molecule, which can be expressed as:

$$\alpha'_k = \left(\frac{\partial \alpha}{\partial Q_k}\right)_0 \neq 0 \tag{3.11}$$

Based on this selection rule[118], it is possible to determine whether a vibration is Raman (change in polarisability during the vibration) or infrared active (change in permanent dipole moment during vibration). For complex molecules, quantum mechanics and group theory

must be applied to determine vibrations. However, at a simple level, the selection rule means that symmetric vibrations will lead to the most intense Raman scattering.

3.3.6 Photoluminescence quantum efficiency measurement

Photoluminescence quantum efficiency (PLQE) is considered to be an important value for a sample, either solution or thin film as it limits the electroluminescent efficiency of devices. The photoluminescence quantum efficiency η is defined as

$$\eta = \frac{\text{number of photons emitted}}{\text{number of photons absorbed}} \tag{3.12}$$

PLQE is relatively straightforward to measure in solution as the emission is usually assumed to be isotropic. However, for thin films, emission usually shows anisotropy, which could be the result of the anisotropic distribution of chromophores. Wave-guiding effects also change the angular distribution of the emission. In order to circumvent mapping out the angular distribution, an integrating sphere is used to measure thin-film samples. An integrating sphere is a hollow sphere, the inner surface of which is coated with diffusively reflective materials (typically barium sulfate), and the light can be assumed to be isotropically distributed over the interior surface. An optical fibre connected to the sphere is used to transfer the signal to a CCD spectrometer. A baffle coated with barium sulfate is placed in front of the optical fibre to prevent direct illumination of the optical fibre.

Working principle

The experimental setup is illustrated in Fig. 3.3. According to the method proposed by de Mello et al.[119], there are three separate measurements. For the first measurement, shown in (A), laser is shone into the empty sphere and only laser signal is detected. For the second measurement, shown in (B), sample is placed inside the sphere with the laser directed to the sphere wall. For the third measurement, shown in (C), sample is placed inside the sphere and directly illuminated by the laser beam.

In the measured spectra, the area under the laser signal is proportional to unabsorbed light, noted as L. The area under the emission signal is proportional to emission light, noted as P. The total amount of laser shone on the sample consists of two contributions: the first is the laser directly and locally hitting the sample; the second is the diffuse-reflected laser from the wall subsequently hitting the entire sample surface. In experiment (B), the fraction of laser absorbed by the sample is noted as μ. In experiment (C), laser first directly hits the sample and the fraction absorbed is denoted as A. A fraction $(1-A)$ is either scattered or

reflected to the interior sphere surface, and a fraction μ is reabsorbed by the sample. Two equations can be written:

$$L_B = L_A(1-\mu) \tag{3.13}$$

$$L_C = L_A(1-A)(1-\mu) \tag{3.14}$$

$$A = \left(1 - \frac{L_C}{L_B}\right) \tag{3.15}$$

In experiment (B), the total detected photons are given by $L_B + P_B$. In experiment (C), the total detected photons can be divided into two contributions: the contribution of scattered laser light $(1-A)\cdot(L_B+P_B)$; and the contribution of light emitted from the sample after direct absorption $\eta L_A A$, which give the equation

$$L_C + P_C = (1-A)(L_B+P_B) + \eta L_A A \tag{3.16}$$

Combining Eq. 3.15 and 3.16, PLQE η can be expressed as:

$$\eta = \frac{P_C - (1-A)P_B}{L_A A} \tag{3.17}$$

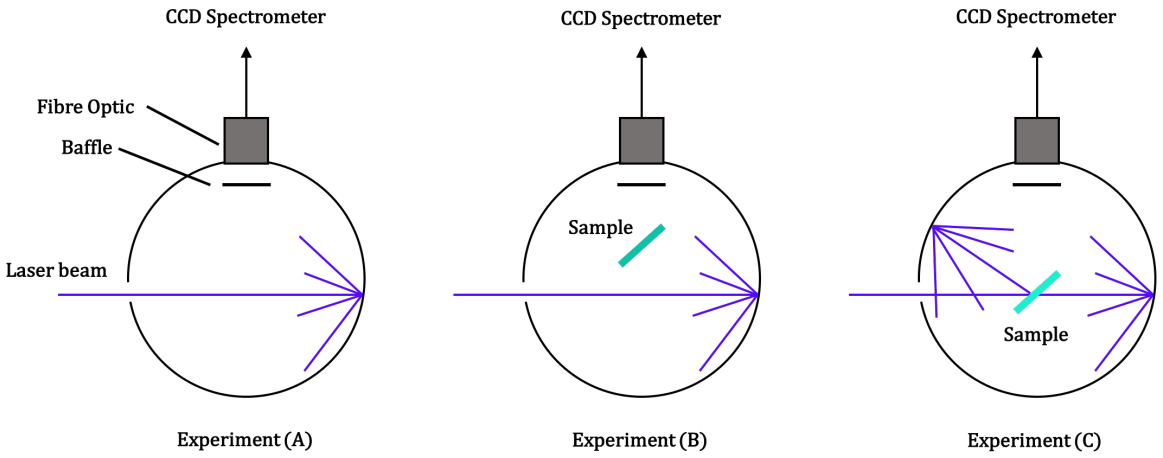

Fig. 3.3 Illustration of three configurations of PLQE measurements: (A) the empty measurement; (B) laser beam indirectly strikes the sample; (C) laser beam directly strikes the sample. Figure adapted from reference [119].

3.4 Structural characterisation

3.4.1 X-ray diffraction

X-rays are electromagnetic radiation with wavelength roughly between 0.1 Å and 100 Å, which is close to the interatomic distances in a crystal. Therefore, X-rays are convenient to examine the crystal structures by diffraction. X-ray diffraction is a direct tool to identify crystalline and amorphous states. For crystals, it is also used to identify different phases, cell parameters, orientation, crystallite size and other structural parameters. X-ray diffraction was performed using a Bruker X-ray D8 Advanced diffractometer with Cu K$\alpha_{1,2}$ radiation (λ=1.541 Å). Spectra were collected with an angular range 2θ of 6° to 30° and the angular resolution $\Delta\theta$ = 0.046°. Measurement were conducted on drop-cast films.

Working principle

When reaching the sample, incident X-ray will either be transmitted or scattered by the electrons of the atoms in the material. Crystal information can be analysed from the peaks formed when scattered X-rays interfere constructively. Constructive interference requires that the path-length difference between two X-rays is an integer number n of wavelength λ, and combine to a new wave with a larger amplitude. Fig. 3.4 (A) illustrates the two parallel X-rays scatter from two adjacent planes in crystal. The total path difference is

$$\text{Total path difference} = 2d_{hkl}\sin\theta \tag{3.18}$$

For constructive interference,

$$n\lambda = 2d_{hkl}\sin\theta \tag{3.19}$$

which is Bragg's Law.[120] The angle between the transmitted and the Bragg diffracted beams is always equal to 2θ due to the geometry of the Bragg condition, as shown in Fig. 3.4 (B).

3.5 Computation

3.5.1 Density functional theory calculations

The main idea of density functional theory (DFT) is that the energy of an electronic system can be expressed in terms of the electron probability density $\rho(\vec{r})$. $\rho(\vec{r})$ denotes the total electron density at a particular point $\vec{r}$ in space. The electronic energy E is thus as a function

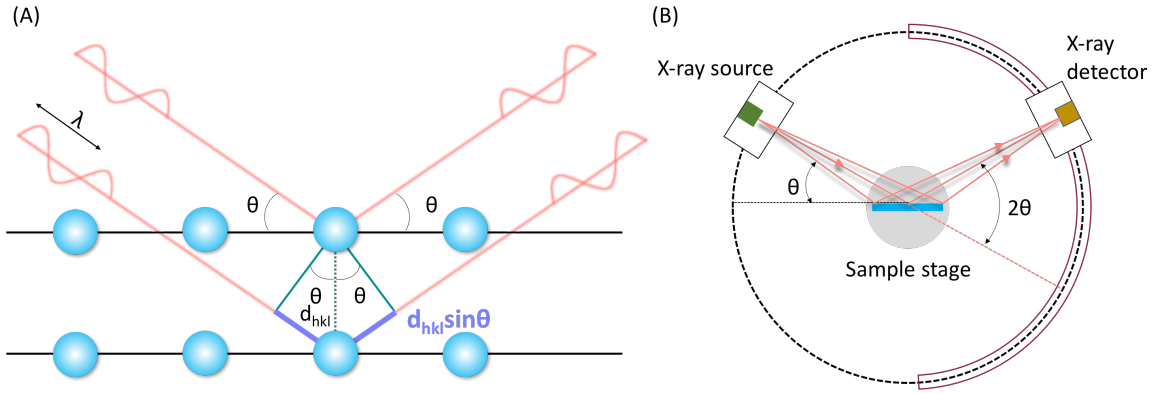

Fig. 3.4 (A) Bragg's law for constructive interference of two parallel X-rays after diffracting from two adjacent crystal planes. (B) Geometry of the Bragg condition in experimental situations. It is 2θ that is measured by the X-ray detector.

of the electron density $E(\rho)$. For a given function $\rho(\vec{r})$, there is a single corresponding energy.[34] The expression of electronic energy includes four terms: (1) the kinetic energy of the electrons; (2) electron-nucleus attraction; (3) the Coulomb interaction between the total charge distribution at $\vec{r}_1$ and $\vec{r}_2$; (4) the exchange-correlation energy of the system, which is a function of the density. However, the exchange-correlation energy has no exact analytical form and numerous methods have been developed for obtaining approximate forms for the functional. The main source of errors in DFT usually comes from the approximate nature of this exchange-correlation functional. The DFT calculation is performed in the following steps: (1) guess the electron density ρ, typically by using a superposition of atomic densities. Use approximate form for the exchange-correlation energy; (2) an initial set of electron spatial orbitals can be solved; (3) this set of orbitals is then used to compute an improved electron density; (4) iterate the process until the density and exchange-correlation energy have converged to within some tolerance, and then compute the electronic energy. Electron orbitals can also be expressed in terms of a set of basis functions multiplied by some coefficients. A variety of exchange-correlation functionals and basis functions have been developed for use in DFT calculations.

DFT calculations of static electric dipole moments of organic host molecules in this thesis employed the "ORCA" package[121] with the B3LYP hybrid functional[122, 123] and 6-31G basis set.[124] The B3LYP/6-31G* functional/basis combination has been widely used for organic molecules, and it performs well optimising ground-state geometries.[125, 126] Calculations were performed by several steps: (1) estimate the three-dimensional geometry from the chemical structure which is expected to be close to the real equilibrium geometry; (2) run a optimisation calculation where all degrees of freedom, including bond lengths,

angles and dihedral angles are able to adjust to reach the minimum of the free energy surface; (3) check the calculation is convergent and the output geometry is reasonable; (4) use the optimised geometry to calculate static electric dipole moment.

Chapter 4

Non-Chemical Control of Triplet Emission in Donor-Bridge-Acceptor Organometallics

4.1 Abstract

Carbene-metal-amides (CMAs) are a promising family of donor–bridge–acceptor molecular charge-transfer (CT) emitters for organic light-emitting diodes. A universal approach is demonstrated to tune the energy of their CT emission. A blueshift of up to 210 meV is achievable in the solid state via dilution in a polar host matrix. The origin of this shift has two components: constraint of thermally-activated triplet diffusion, and electrostatic interactions between guest and polar host. This allows the emission of mid-green CMA archetypes to be tuned to sky blue without chemical modifications. Monte Carlo simulations based on a Marcus-type hopping rate successfully reproduce the concentration- and temperature-dependent triplet diffusion process, revealing a substantial shift in the ensemble density of states in polar hosts. In gold-bridged CMAs, this shift does not lead to a significant change in luminescence lifetime, thermal activation energy, reorganisation energy, or intersystem crossing rate. These discoveries offer new insight into coupling between the singlet and triplet manifolds in CMA materials, revealing a dominant interaction between states of CT character. The same approach is employed using materials which have been chemically modified to alter the energy of their CT state directly, shifting the emission of sky-blue chromophores into the practical blue range.

This work was published as Environmental Control of Triplet Emission in Donor-Bridge-Acceptor Organometallics - Jiale Feng, Lupeng Yang, Alexander S. Romanov, Jirawit

Ratanapreechachai, Antti-Pekka M. Reponen, Saul T. E. Jones, Mikko Linnolahti, Timothy J. H. Hele, Anna Köhler, Heinz Bässler, Manfred Bochmann, Dan Credgington. Advanced Functional Materials, 2020, 30(9), 1908715.

All the below work was carried out by myself except where stated. Lupeng Yang carried out the Monte Carlo simulation code development. Dr. Alexander S. Romanov performed the molecular design and synthesis. Jirawit Ratanapreechachai carried out the solution steady-state absorption, photoluminescence, and PLQE measurements. Antti-Pekka M. Reponen carried out the transient absorption measurements. Dr. Timothy J. H. Hele contributed the molecular symmetry discussions. Prof. Mikko Linnolahti carried out the quantum chemical calculations for CMA1. Prof. Anna Köhler and Prof. Heinz Bässler assisted in design and interpretation of Monte Carlo simulations.

4.2 Introduction

Thin-film organic light-emitting diodes (OLEDs) have developed into a flourishing commercial industry in the last few decades. In 1987, Tang and Van Slyke demonstrated first 'sandwich structure' OLED utilising fluorescent emission from spin-singlet states.[16] Second-generation phosphorescent OLEDs utilising emission from spin-triplet states, developed a decade later, exhibit high efficiency and significant synthetic tuneability, making them the current best candidates for lighting and display technologies.[22] However, efficient deep blue OLEDs remain one of the key challenges limiting their broader application, due to low quantum efficiency and short operational lifetime.[52] Within this sphere, a new class of donor-bridge-acceptor carbene-metal-amide (CMA) emitters has been developed that exhibit high electroluminescence quantum efficiency at high brightness and rapid (sub-microsecond) harvesting of triplet states.[32] Short emission lifetime is critical for preventing bimolecular exciton annihilation reactions, which are implicated in efficiency roll-off and reduced operational stability.[127, 128] CMA emitters exhibit flexible molecular design with low synthetic complexity[111, 112, 129–131] and benign solid state interactions.[132, 133] Their combination of low exchange energy and high spin-orbit coupling occupies a space between traditional phosphorescent emitters and more recently developed thermally-activated delayed-fluorescence compounds, leading to significant interest in their underlying emission mechanism.[133–136]

The archetype of the family, CMA1, is a mid-green emitter both in solution and in amorphous thin film. However, unlike many other triplet-harvesting organic and organometallic archetypes, CMA materials exhibit three features which allow additional routes to tune emission characteristics: (1) significant geometric flexibility, allowing tuning of excited state

energies through control of geometry, (2) large negative absorption solvatochromism due to a significant electrostatic dipole in the ground state, (3) lack of concentration quenching, allowing flexibility in host:dopant ratio and host choice.

This chapter discusses how the emission of CMA1 can be tuned by utilising intermolecular interactions with a variety of host materials to both restrict triplet diffusion and shift the density of excited states. The result is that the photoluminescence peak of CMA1 can be increased in energy by 210 meV, into the blue colour range, without altering its chemical structure. We determine that static electrostatic interactions are one of the most important parameters for these composites while for general TADF type emitters, influence of the host always redshifts the emission due to dynamic polarisability.[57, 137–139] Despite the significant change in emission energy achieved, we find that the low activation energy for delayed emission and short room-temperature emission lifetimes are preserved. We use these new experimental findings to test current quantum-chemical descriptions of CMA emission, and provide a better understanding of its mechanism. We go on to show that this approach extends to other gold CMA complexes across the visible spectrum, allowing the emission energy for each to be tuned over a 150-200 meV range.

4.3 Results and Discussion

4.3.1 The CMA1 molecule

The chemical structure of CMA1 is illustrated in Fig. 4.1(A). In the ground state S_0, the CAAC group is relatively electron deficient, while the amide is electron rich, creating a ground-state electrostatic dipole moment of order 15 Debye aligned along the C-Au-N axis, hereafter taken as the z-axis of the molecule.[135] This large ground-state dipole is unusual for organic donor-acceptor type emitters and is the key factor utilised to achieve large luminescence blueshift. The HOMO and LUMO of CMA1, calculated by density functional theory (DFT) utilising the hybrid MN15 functional with the def2-TZVP basis set are presented in Fig. 4.1(B). The HOMO resides primarily on the amide, and the LUMO on the carbene. Of order 3.0/11.4% of the electron density in the HOMO/LUMO resides on the metal, with largest contributions from the $5d_{yz}/5p_y$ atomic orbitals, respectively, where the carbazole is taken to lie in the $x-z$ plane. Excitation from S_0 to S_1 is dominated by a HOMO-LUMO transition (natural transition orbitals comprise 98% HOMO-LUMO), which spans the metal bridge and has significant charge-transfer (CT) character, shifting electron density back from the amide to the carbene group. This reduces the electrostatic dipole to approximately 5 D and reverses its sign.[32, 140]

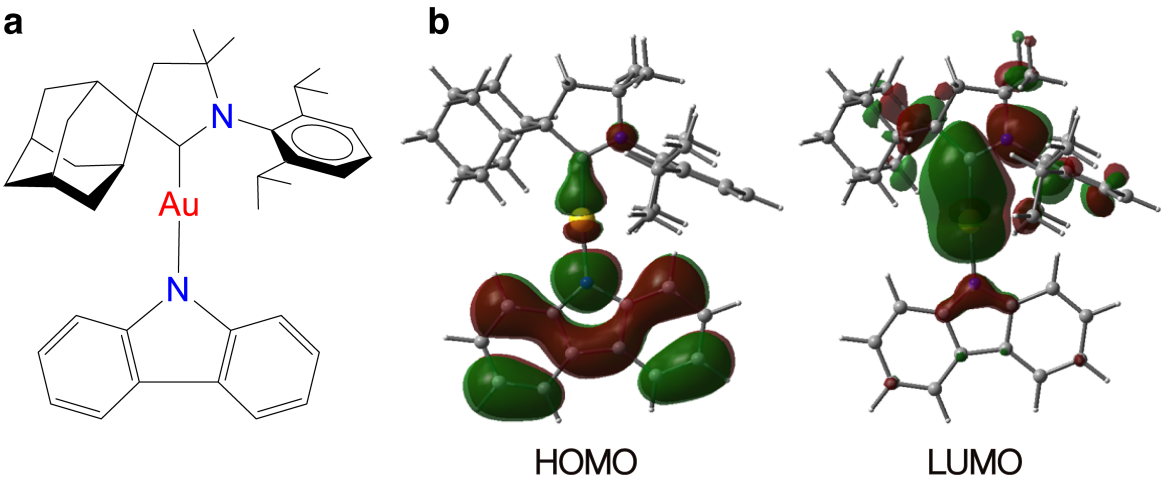

Fig. 4.1 (A) Chemical structure of CMA1. (B) HOMO and LUMO wavefunctions of CMA1 from DFT calculations, red/green corresponds to positive/negative sign of wavefunctions. The calculations were performed by Prof. Mikko Linnolahti.

In addition to direct absorption to the singlet CT state, optical absorption spectra of CMA1 show features related to ligand-centred excitations of the carbene and amide groups (Fig. 4.2). For CMA1, the photoexcited CT singlet crosses to the triplet manifold within around 5 ps, with subsequent unstructured emission on sub-microsecond timescales.[32] The steady-state emission peak is around 520 nm (green region) in neat film at 300 K, see Fig. 4.3, with a Stokes' shift of 795 meV (measured peak-to-peak). The large Stokes' shift has been assigned in previous reports to a combination of fast vibrational relaxation followed by torsional relaxation from a coplanar to a twisted geometry, which narrows the S_1-S_0 energy gap.[140]

In solution, the CT band of CMA1 exhibits large negative absorption solvatochromism, consistent with the ordering of polar solvents around the large ground-state dipole, stabilising S_0 and destabilising S_1.[135] Emission shows weak positive solvatochromism, consistent with much weaker ordering of solvent around the smaller S_1 dipole, see Fig. 4.4 and 4.5. In neat thin film, the CT absorption band is broader and peaks at 388 nm, between the values in toluene (407 nm) and dichloromethane (385 nm) solutions.

4.3.2 Dopant concentration and role of diffusion for CMA1 in PVK host

We first examine the effect of host on emission energy in the absence of significant electrostatic interactions. Poly(9-vinylcarbazole) (PVK) is a common polymer host material for solution-processed OLEDs, possessing relatively low polarity.[141] Efficient CMA1:PVK

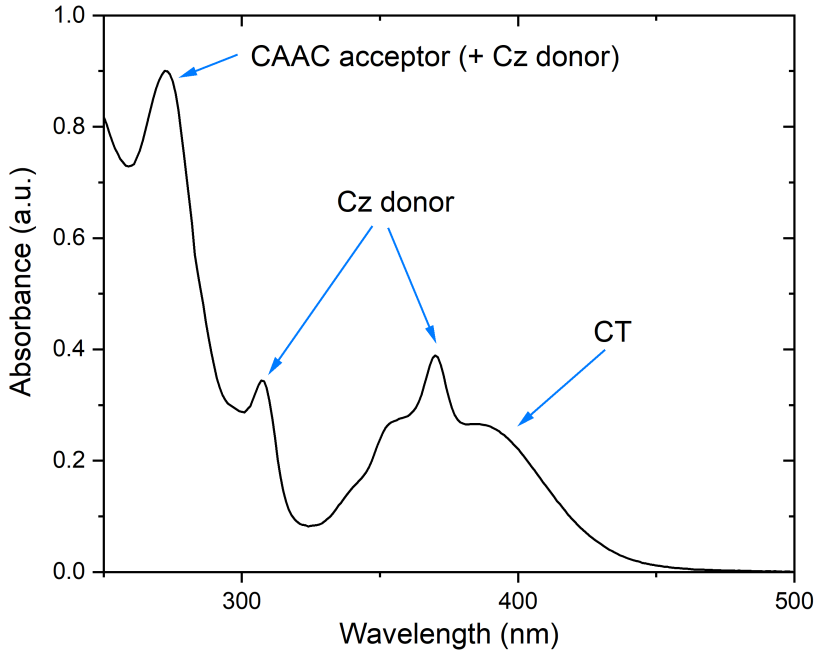

Fig. 4.2 Optical steady state absorption spectrum of CMA1 neat thin film. The film was spun from chlorobenzene solution (20 mg/mL) in a nitrogen glovebox. Vibronic progressions related to ligand-centred excitations of carbazole donor (Cz), CAAC acceptor, and the unstructured direct absorption to the S_1 CT state are labelled.

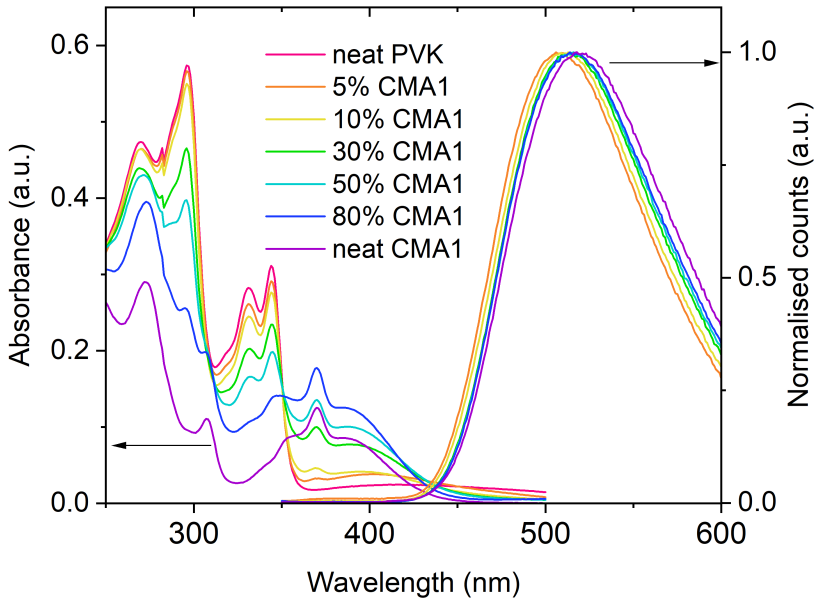

Fig. 4.3 Steady state absorption and photoluminescence of CMA1 in PVK host at different concentrations. Films were spun from chlorobenzene solution (20 mg/mL) in a nitrogen glovebox. Excitation wavelength is 350 nm.

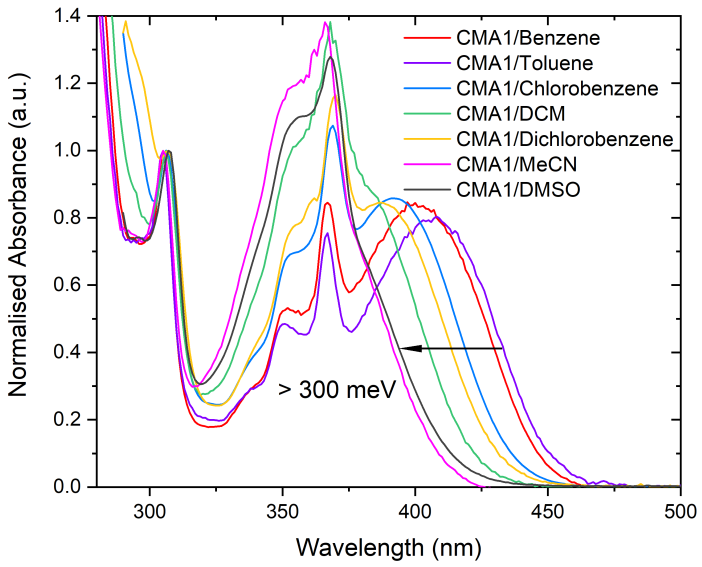

Fig. 4.4 Steady state absorption spectra of CMA1 in various solvents at 300 K. Concentration is 1 mg/mL for all solutions. Spectra were normalised with respect to the carbazole absorption peak at around 305 nm. CT absorption peak blue shifts when increasing the solvent polarity, by over 300 meV for this solvent range. This figure was produced by Jirawit Ratanapreechachai.

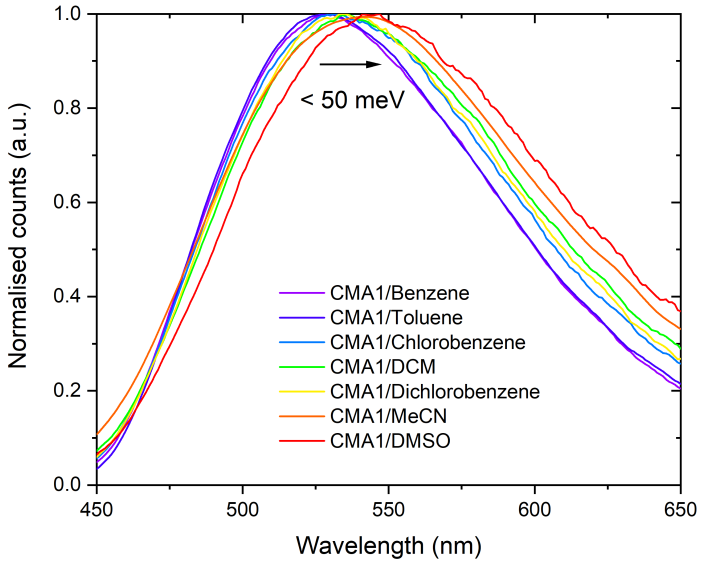

Fig. 4.5 Steady state photoluminescence spectra of CMA1 in various solvents at 300 K. Concentration is 1 mg/mL for all solutions. Spectra were normalised with respect to their maximum. Emission peak position is weakly affected by solvent polarity, with shift smaller than 50 meV over this solvent range. Excitation wavelength is 350 nm. This figure was produced by Jirawit Ratanapreechachai.

solution-processed OLEDs were previously reported, using a CMA1 concentration of 20% by weight.[32] Fig. 4.3 presents the steady state absorption and photoluminescence spectra of CMA1 doped in to PVK host at concentrations from 100% (neat CMA1) to 5% by weight, representing the range of dopant concentrations over which efficient OLED devices have been shown to be achievable.[132] The absorption of CMA1 in PVK is dominated by parasitic host absorption and a weak scattering tail, which obscures the exact CMA1 absorption edge. PL data are more revealing; when decreasing the concentration of CMA1 in the host-guest composite from 100% to 5%, the position of the steady-state photoluminescence peak energy blue-shifts by approximately 60 meV, from 2.39 to 2.45 eV. Photoluminescence quantum efficiency (PLQE) of these films ranges from 67% to 94%, calculated using the de Mello method.[119] The luminescence lifetime of CMA1 in host remains relatively constant with concentration, varying from 0.97 µs to 1.04 µs between 100% and 5% concentration, see Fig. 4.6. These values are tabulated in Table 4.1.

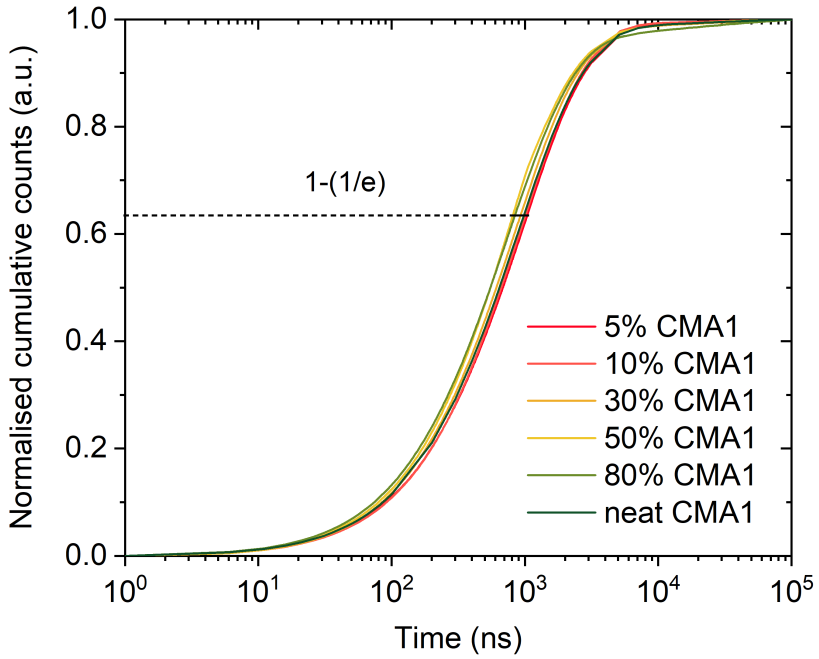

Fig. 4.6 Room temperature emission integral of CMA1 and PVK composites, with 1-(1/e) labelled as the characteristic luminescence lifetime.

Fig. 4.7 presents time-resolved PL peak energy as a function of time for different concentrations at room temperature. Spectral migration is observed over the lifetime of the excited state, with migration rate dependent on dopant concentration. The spectral relaxation shifts on a logarithmic time scale with increasing concentration. This implies that the diffusion process takes place via the dopant, and via an electronic coupling between dopants that depends on distance, such as a Dexter-type transfer for triplets.[142] At high

CMA1 in PVK	Luminescence Lifetime (ns)	PLQE
5% CMA1	1040	67%
10% CMA1	1000	75%
30% CMA1	920	76%
50% CMA1	850	94%
80% CMA1	840	81%
100% CMA1	970	80%

Table 4.1 Luminescence lifetime and photoluminescence quantum efficiency (PLQE) of CMA1 in PVK host varying concentrations from 5 wt.% to neat CMA1 films. Luminescence lifetime was measured in vacuum with sample excited by 400 nm laser. Luminescence lifetime was determined by the time when the emission reaches 1-(1/e) of the total time-integrated emission, see 4.6. Errors on lifetime are around 50 ns. PLQE was measured in a nitrogen environment in an integrating sphere with sample excited by 405 nm laser of 1 mW power. PLQE was calculated based on the de Mello method.

dopant concentration, the peak position saturates to a constant value at long times. At low dopant concentration, migration is too slow for saturation to be observed before PL becomes undetectable.

Migration rates for both high and low concentration are reduced at low temperature, shown in Fig. 4.8 and Fig. 4.9 and steady state PL peak energies blue shift with decreasing temperature. The luminescence rate of CMA1 in PVK is strongly thermally activated above 120 K, increasing by nearly two orders of magnitude between 10 K and 300 K, with characteristic activation energy of 72 meV for 10% CMA1 and 76 meV for 80% CMA1, see Fig. 4.10 and Fig. 4.11. The total time-integrated luminescence increases with the same activation energy (Fig. 4.12), indicating that thermal activation is primarily of the radiative triplet decay rate. Calculations from thermally activated decay rates are shown in Eq. 4.1 and Eq. 4.2. The observed temperature dependence is consistent with the diffusion of triplet excitons, for example as reported in neat films of poly(*p*-phenylene) type conjugated polymers.[92]

$$k_{decay} = k_r + k_{nr} = k_{r0}\exp\left(-\frac{E_{A1}}{k_B T}\right) + k_{nr0}\exp\left(-\frac{E_{A2}}{k_B T}\right) \tag{4.1}$$

$$PL_{total} \propto \text{PLQE} \propto \frac{k_r}{k_r + k_{nr}} \propto \frac{k_{r0}\exp\left(-\frac{E_{A1}}{k_B T}\right)}{k_{r0}\exp\left(-\frac{E_{A1}}{k_B T}\right) + k_{nr0}\exp\left(-\frac{E_{A2}}{k_B T}\right)} = PL_0\exp\left(-\frac{E_{A3}}{k_B T}\right) \tag{4.2}$$

where k_{decay} is the total decay rate of excitons, k_r is the radiative decay rate of excitons, k_{nr} is the non-radiative decay rate of excitons, k_{r0} is the radiative decay rate constant, k_{nr0} is

the non-radiative decay rate constant, E_{A1} is the activation energy for the radiative decay, E_{A2} is the activation energy for the non-radiative decay, PL_{total} is the total time-integrated emission, PL_0 is the total time-integrated emission constant, E_{A3} is the activation energy for the total photoluminescence, k_B is the Boltzmann constant, and T is the temperature in Kelvin. Since we do not expect a significant temperature dependence of the excitation rate in the steady-state PL experiment, the total PL is assumed to follow the PLQE. For CMA1, the activation energies yielded from the PL decay and the total PL are quite close, so we can assume that the non-radiative decay rate varies little with temperature, and we denote this rate as a constant c. Since the total PL drops by two orders of magnitude between high and low temperatures, we require that c is significantly larger than the the value of the radiative decay rate k_r at low temperatures but significantly smaller than the value of k_r at high temperatures.

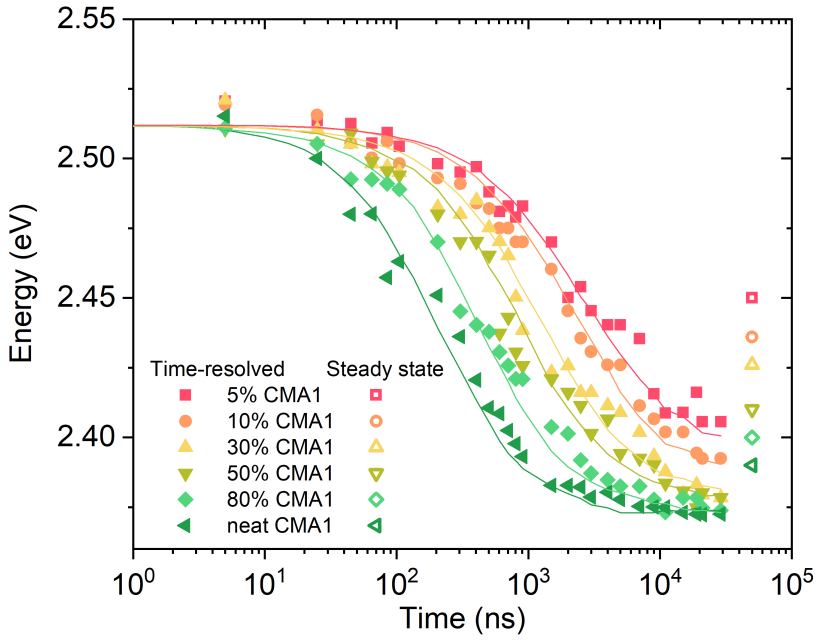

Fig. 4.7 Room temperature time resolved PL peak energy of CMA1 in PVK at different concentrations to track the spectral diffusion. Lines are results of Monte Carlo simulation. Monte Carlo simulation was assisted by Lupeng Yang.

We model this behaviour by considering that spectral migration occurs via triplet diffusion through a disordered density of emitter states, as described by Movaghar et al.[93] By applying a Monte Carlo simulation of 3D triplet diffusion, we find that a Dexter-type dependency of hopping probability on intermolecular distance reproduces the observed concentration-dependent migration rate, with the long-time saturation of peak position occurring where triplets are able to relax to the tail of their density of states. We find that a fixed density of states for all concentrations is sufficient to model the trend observed,

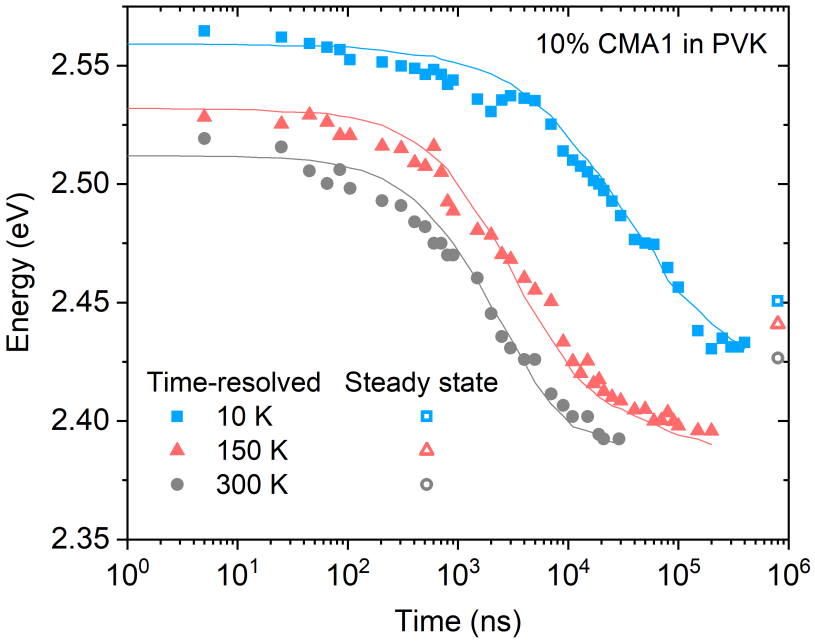

Fig. 4.8 Cryogenic time resolved PL peak position of 10% CMA1 in PVK at 10 K, 150 K, and 300 K. Lines are results of Monte Carlo simulation. Monte Carlo simulation was assisted by Lupeng Yang.

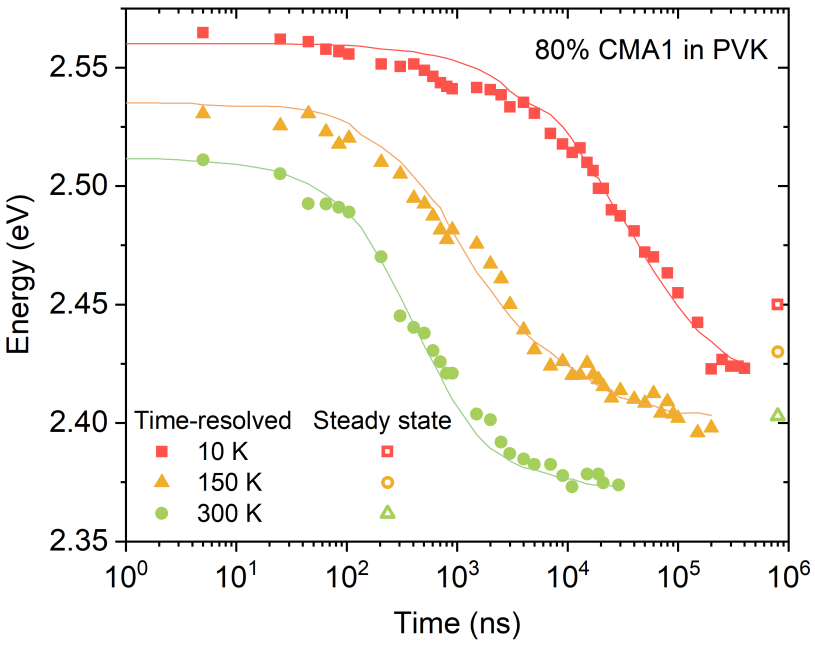

Fig. 4.9 Cryogenic time resolved PL peak position of 80% CMA1 in PVK at 10 K, 150 K, and 300 K. Lines are results of Monte Carlo simulation. Monte Carlo simulation was assisted by Lupeng Yang.

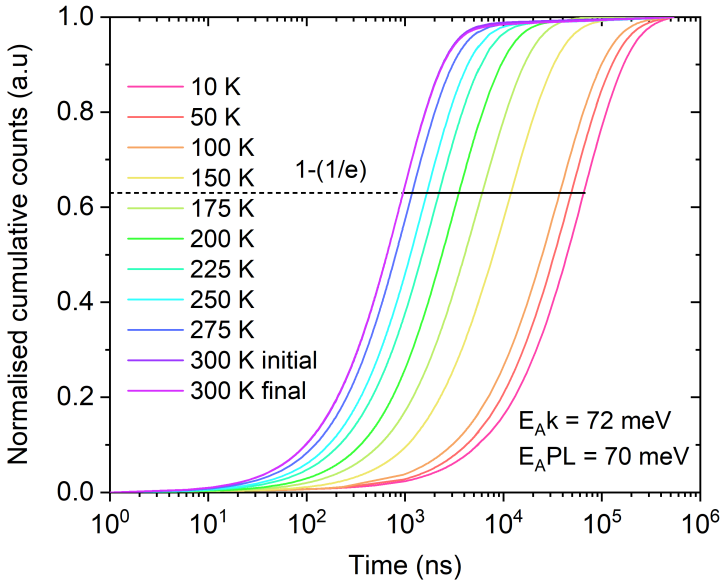

Fig. 4.10 Cryogenic emission integral of 10% CMA1 in PVK with 1-(1/e) labelled as the characteristic luminescence lifetime. “Initial" data taken at 300 K before cooling the film to 10 K, “Final” data upon warming back to 300 K after low-temperature measurements. Two activation energies are labelled, E_Ak is extracted from the PL decay rate against temperature, and E_APL is extracted from the integrated PL intensity against temperature.

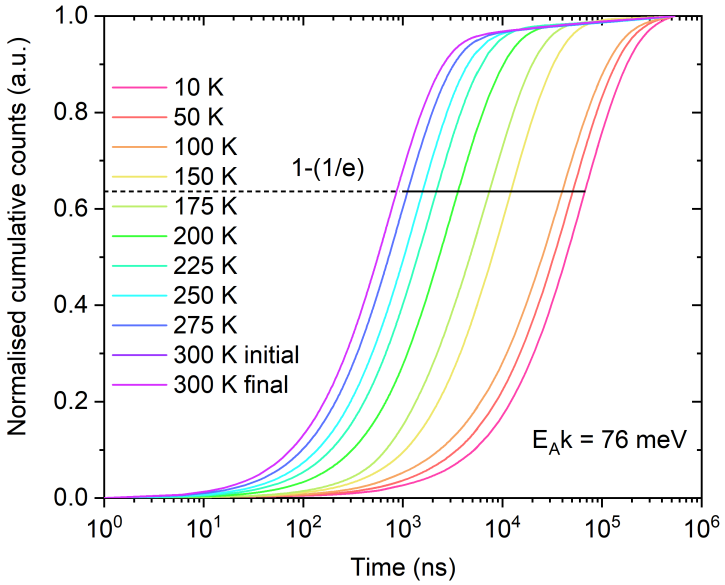

Fig. 4.11 Cryogenic emission integral of 80% CMA1 in PVK with 1-(1/e) labelled as the characteristic luminescence lifetime. “Initial" data taken at 300 K before cooling the film to 10 K, “Final” data upon warming back to 300 K after low-temperature measurements. The activation energy E_Ak is extracted from the PL decay rate against temperature.

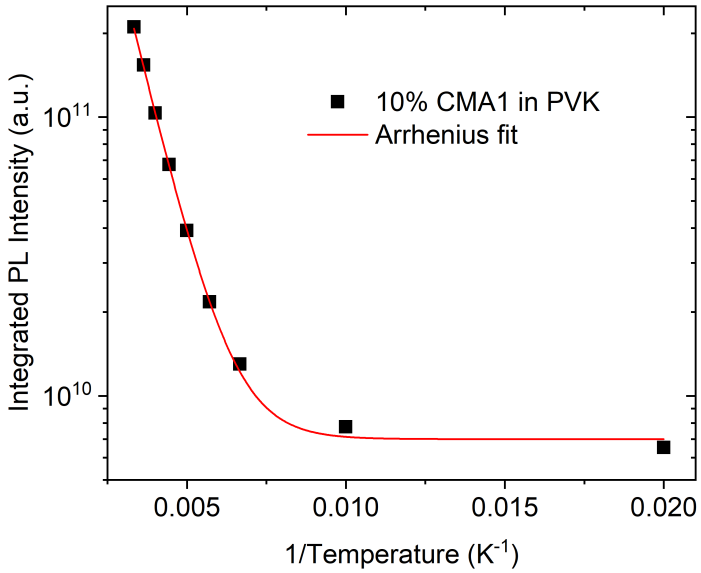

Fig. 4.12 Integrated PL intensity plotted against temperature of 10% CMA1 in PVK. The integrated PL intensity is thermally activated and can be fitted by the Arrhenius equation. The activation energy extracted from the integrated PL intensity E_APL = 70 meV.

see Table 4.2. Moreover, we find that a Marcus-type activated hopping probability (Eq. 2.49 and Eq. 2.51) is required to reproduce the observed temperature dependence.[100] By fitting the experimental data, we extract a characteristic reorganisation energy λ of 240 meV, corresponding to an activation energy of $E_a = \lambda/4 = 60$ meV. We note that the trend observed cannot be reproduced using a Miller-Abrahams type hopping probability, which does not account for reorganisation.[92] Emission is in general from a non-equilibrium ensemble of triplet excited states, with restriction of triplet diffusion able to tune emission energy over a small (60 meV) range. Only at high dopant concentration and higher temperatures are photoexcited triplets able to relax to a quasi-equilibrium energy in the tail of the density of states within their emission lifetime.[35] Note that the steady state emission energy reflects the weighted time-integrated signal so that it contains contributions from across the DOS. At quasi-equilibrium in solid films, PL peak energies are within ~10 meV of those observed in low polarity solvents (benzene, toluene), which we take as evidence that the tail of the density of states represents molecules close to the fully-relaxed S_1 geometry. The blueshift in steady state PL at decreased temperature results from the larger reduction in diffusion rate than the decrease in emission rate.

To explore the generality of this effect, Fig. 4.13 presents the dependence of steady state luminescence peak energy on CMA1 concentration for a range of polymer and small molecule host materials with high triplet energies, deposited as thin films from solution. For all hosts lacking a significant permanent electric dipole, calculated by DFT (B3LYP/6-31G**), a

CMA1 in PVK (300 K)	Mean energy (eV)	Deviation σ (eV)
5% CMA1	2.427	0.048
10% CMA1	2.427	0.048
30% CMA1	2.427	0.048
50% CMA1	2.427	0.048
80% CMA1	2.427	0.048
100% CMA1	2.427	0.048

Table 4.2 Mean energy and standard deviation of density of states (DOS) input in Monte Carlo simulations of CMA1 in PVK concentration series at 300 K. These parameters correspond to the simulations in Fig. 4.7, with triplet states concentration being the only variable. The spectral diffusion becomes slower upon the dilution of CMA1, however, the relaxation stays relatively constant as the concentration changes from 100% to 5%. Note that as the concentration approaches 0, the simulation result quickly becomes a horizontal line.

CMA1 in PVK (cryo)	Mean energy (eV)	Deviation σ (eV)
10% CMA1 (10 K)	2.490	0.048
10% CMA1 (150 K)	2.445	0.048
80% CMA1 (10 K)	2.485	0.048
80% CMA1 (150 K)	2.450	0.048

Table 4.3 Mean energy and standard deviation of density of states (DOS) input in Monte Carlo simulations of 10% and 80% CMA1 in PVK at 10 K and 150 K. These parameters correspond to the simulations in Fig. 4.8 and Fig. 4.9. As temperature reaches 0 K, the excitation becomes trapped and the simulation energy approaches a constant.

universal blue-shift is observed as concentration decreases, very close in magnitude to that observed in PVK. We interpret this as evidence that triplet diffusion between guest emitters is primarily limited by emitter spacing, and relatively insensitive to the nature of the intervening host. We likewise infer that molecular relaxation on the timescales of triplet emission plays only a minor role.

By contrast, we observe an additional shift in host molecules exhibiting permanent electric dipole moments, specifically bis(N-carbazolyl)benzene (mCP) with 1.4 D; bis[3,5-di(9H-carbazol-9-yl)phenyl]diphenylsilane (SimCP2) with 2.37 D; 9-(3-(9H-carbazol-9-yl)phenyl)-3-(diphenylphosphoryl)-9H-carbazole (mCPPO1) with 3.91 D and diphenyl-4-triphenylsilylphenyl-phosphine oxide (TSPO1) with 4.1 D.

Chemical structures, electric dipole moments and steady state photoluminescence spectra of these hosts are shown in Fig. 4.15 and Fig. 4.14. PS is polystyrene. Steady state luminescence energy increases markedly compared to non-polar host matrices for mCP and TSPO1,

with the trend of PL in mCP host consistent with that observed in electroluminescence by Conaghan et al.[132] The effect for larger host molecules SimCP2 and mCPPO1 is less pronounced. To understand the origin of this phenomenon, we focus on TSPO1, which produces the largest magnitude shift in this set.

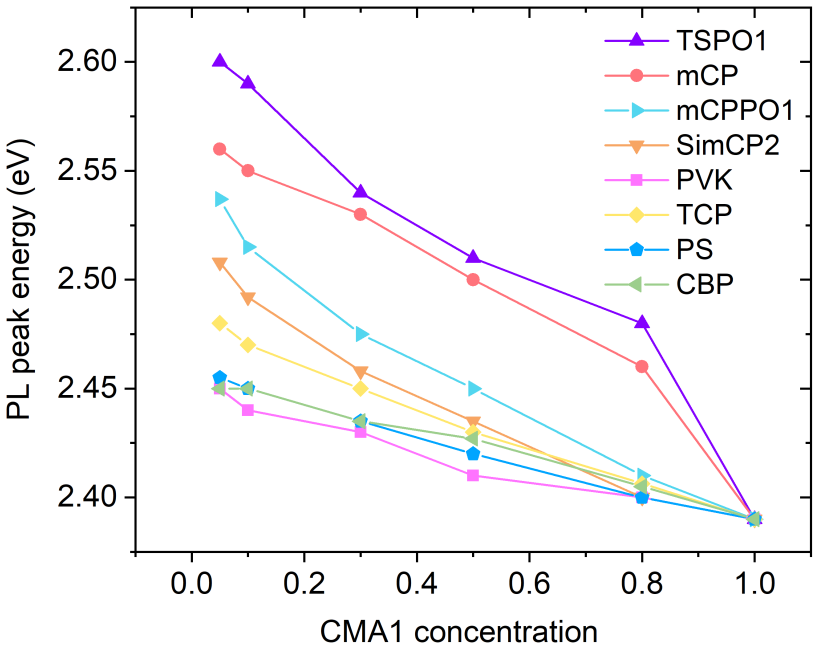

Fig. 4.13 Steady state PL peak energy of CMA1 in a range of hosts varying weight concentrations from 100% to 5%.

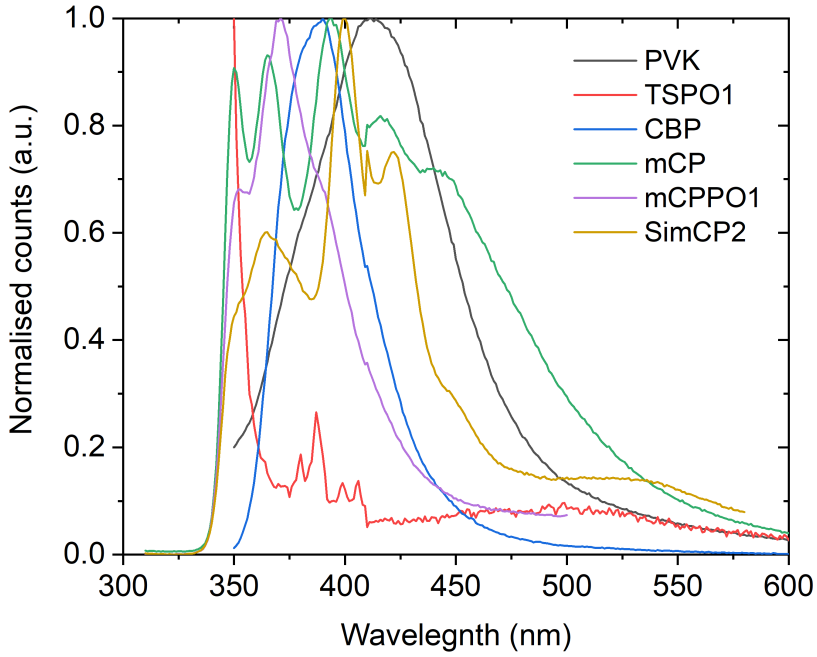

Fig. 4.14 Steady state photoluminescence of various hosts in solid thin films. The films were spun from chlorobenzene solutions (20 mg/mL) in a nitrogen glovebox and measured by photoluminescence spectrometer, excited at 325 nm. The PL spectra of neat host molecules show that the blue shifted PL in host-guest composite films are from the guest emission, not from the host.

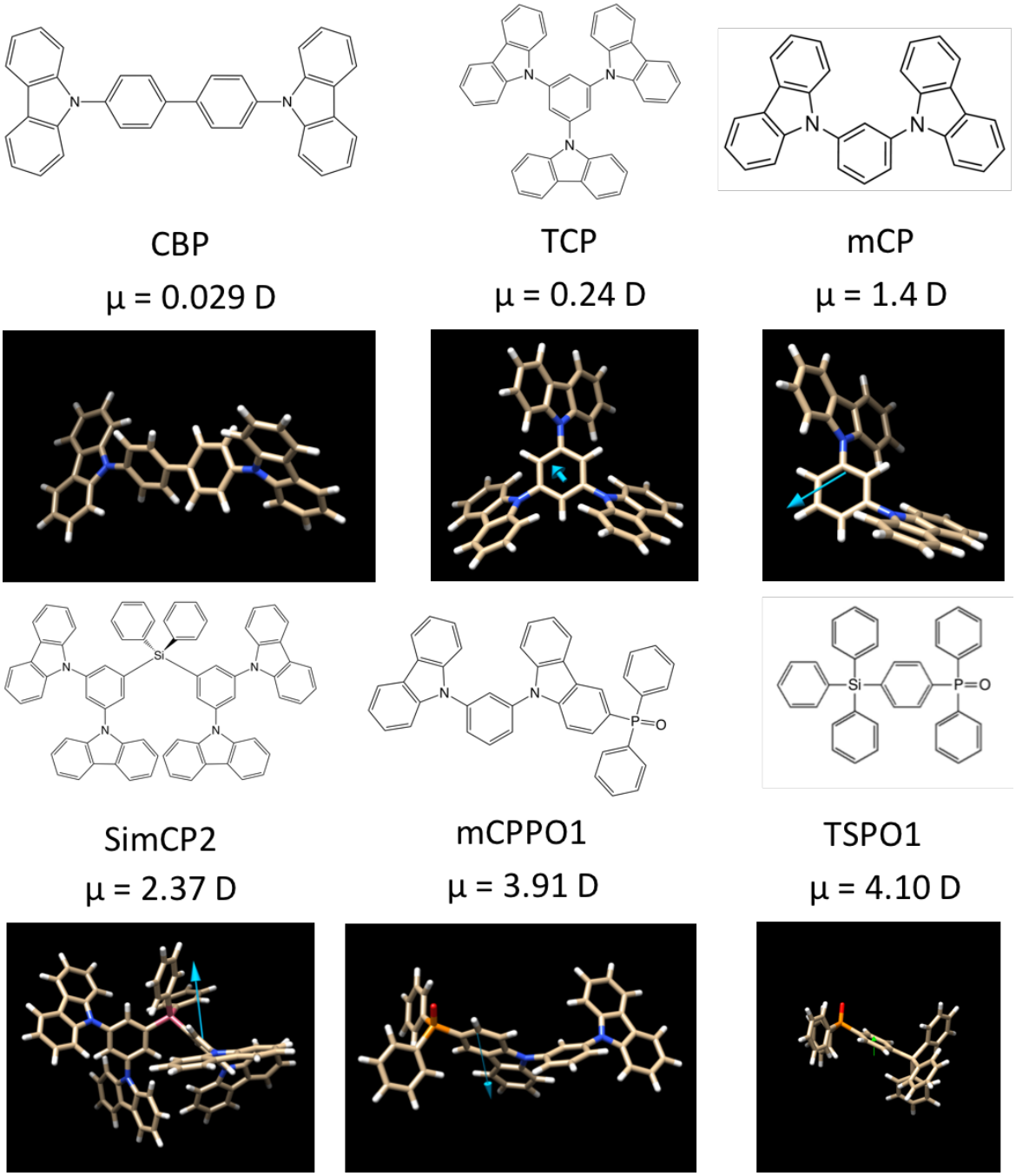

Fig. 4.15 Chemical structures and electric dipole moments of various small-molecule hosts. 4,4'–bis(N-carbazolyl)biphenyl (CBP); 1,3,5-Tris(N-carbazolyl)benzene (TCP); 1,3-bis(N-carbazolyl)benzene (mCP); bis[3,5-di(9H-carbazol-9-yl)phenyl]diphenylsilane (SimCP2); 9-(3-(9H-carbazol-9-yl)phenyl)-3-(diphenylphosphoryl)-9H-carbazole (mCPPO1); diphenyl-4-triphenylsilylphenyl-phosphine oxide (TSPO1). Molecular geometries and static dipole moments were calculated by DFT (B3LYP/6-31G**) with arrows indicating orientation of calculated dipole moments.

4.3.3 Organic polar molecule hosts and role of electrostatic interactions

Steady state absorption and photoluminescence spectra of CMA1 in TSPO1 host at various concentrations are shown in Fig. 4.16. As for PVK, the absorption of CMA1 in TSPO1 is dominated by parasitic host absorption and a weak scattering tail, which renders the exact absorption edge difficult to resolve. However, photoluminescence peak position shows a large blue shift compared to nonpolar hosts, from 2.39 eV for neat CMA1 films to 2.6 eV for 5:95 wt.% CMA1:TSPO1 films. PLQEs of these films are around 65% to 80%. Luminescence lifetime increases slightly from 0.97 µs (neat film) to 1.4 µs (5% CMA1), see Fig. 4.17 and Table 4.4. Low-temperature luminescence lifetime of 10% CMA1 in TSPO1 increases by approximately a factor of 50, from 1.3 µs at 300 K to 65 µs at 10 K, see Fig. 4.18. The same trend is seen at higher concentration; luminescence lifetime increases from 1.02 µs at 300 K to 66 µs at 10 K for 80% CMA1 in TSPO1 (Fig. 4.19). The activation energies extracted from the PL decay rate of 10% and 80% CMA1 in TSPO1 host are 79 meV and 77 meV, which are close to the values for PVK-hosted samples. Integrated PL intensity against temperature of 10% CMA1 in TSPO1 also yields the same activation energy as extracted from the PL decay rate, indicating that thermal activation still contributes primarily to the radiative triplet decay rate as shown in Fig. 4.20.

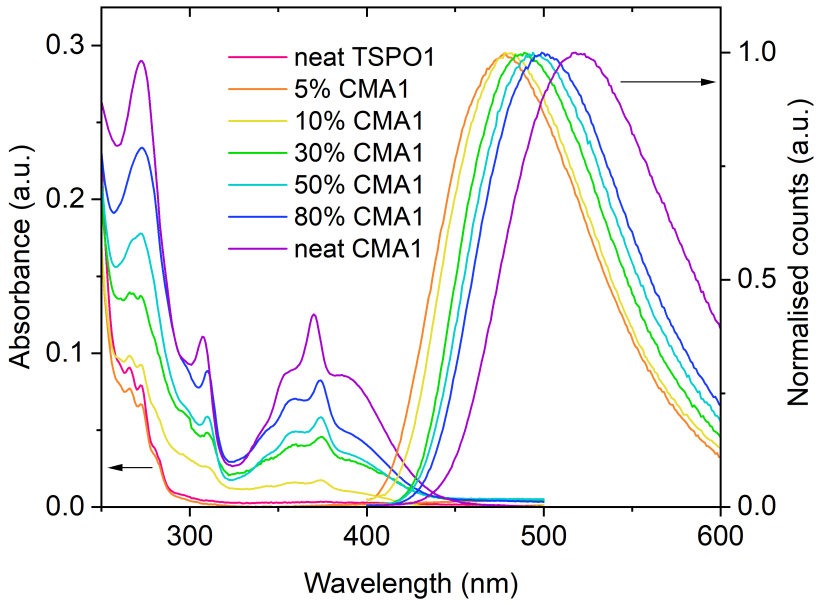

Fig. 4.16 Steady state absorption and photoluminescence of CMA1 in TSPO1 host at different concentrations. Excitation wavelength is 350 nm.

CMA1 in TSPO1	Luminescence Lifetime (ns)	PLQE
5% CMA1	1400	65%
10% CMA1	1330	72%
30% CMA1	1190	78%
50% CMA1	1180	70%
80% CMA1	1010	75%
100% CMA1	970	80%

Table 4.4 Luminescence lifetime and photoluminescence quantum efficiency (PLQE) of CMA1 in TSPO1 host varying concentrations from 5 wt.% to neat CMA1 films. Luminescence lifetime was measured in vacuum with sample excited by 400 nm laser. Luminescence lifetime was determined by the time when the emission reaches 1-(1/e) of the total time-integrated emission, see Fig. 4.17. PLQE was measured in a nitrogen environment in an integrating sphere with sample excited by 405 nm laser of 1 mW power. PLQE was calculated based on the de Mello method.

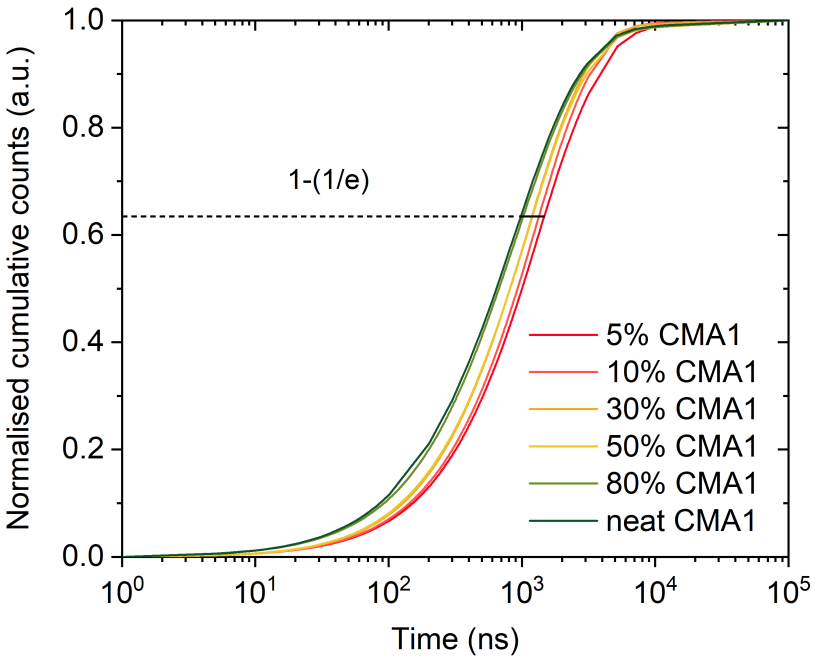

Fig. 4.17 Room temperature emission integral of CMA1 and TSPO1 composites, with 1-(1/e) labelled as the characteristic luminescence lifetime.

Monte Carlo modelling of concentration- and temperature-resolved emission spectra (Fig. 4.21, 4.22, 4.23) reveal that this shift has two components. The first is a thermally activated spectral migration, consistent with triplet diffusion via an activated hopping process, with characteristic reorganisation energy $\lambda = 240$ meV, the same as that observed for CMA1:PVK films. However, we are unable to reproduce the trend observed assuming a fixed density of

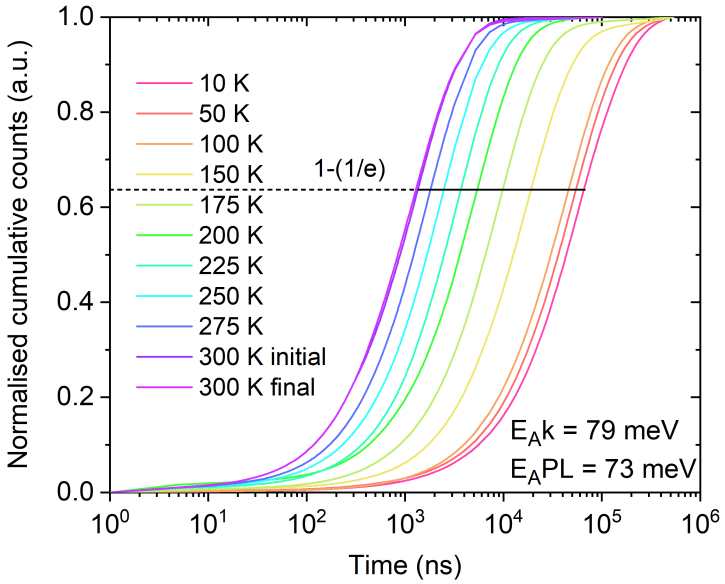

Fig. 4.18 Cryogenic emission integral of 10% CMA1 in TSPO1 with 1-(1/e) labelled as the characteristic luminescence lifetime. “Initial" data taken at 300 K before cooling the film to 10 K, “Final” data upon warming back to 300 K after low-temperature measurements. Two activation energies are labelled, E_Ak is extracted from the PL decay rate against temperature, and E_APL is extracted from the integrated PL intensity against temperature.

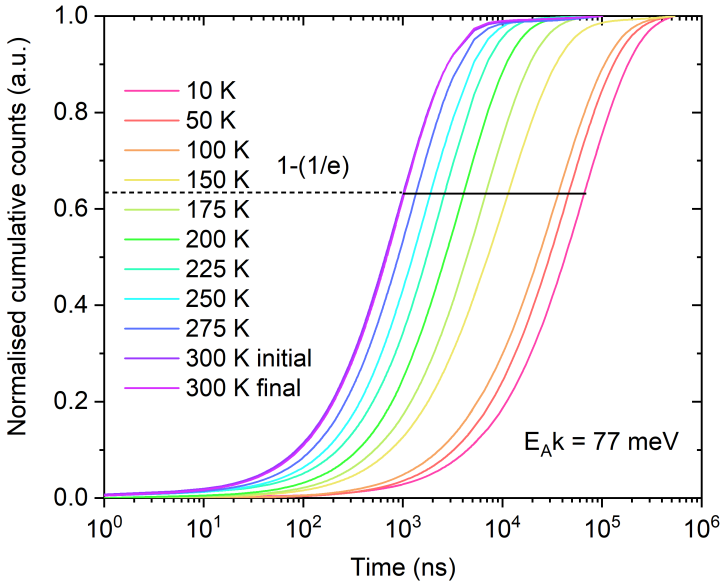

Fig. 4.19 Cryogenic emission integral of 80% CMA1 in TSPO1 with 1-(1/e) labelled as the characteristic luminescence lifetime. “Initial" data taken at 300 K before cooling the film to 10 K, “Final” data upon warming back to 300 K after low-temperature measurements. The activation energy E_Ak is extracted from the PL decay rate against temperature.

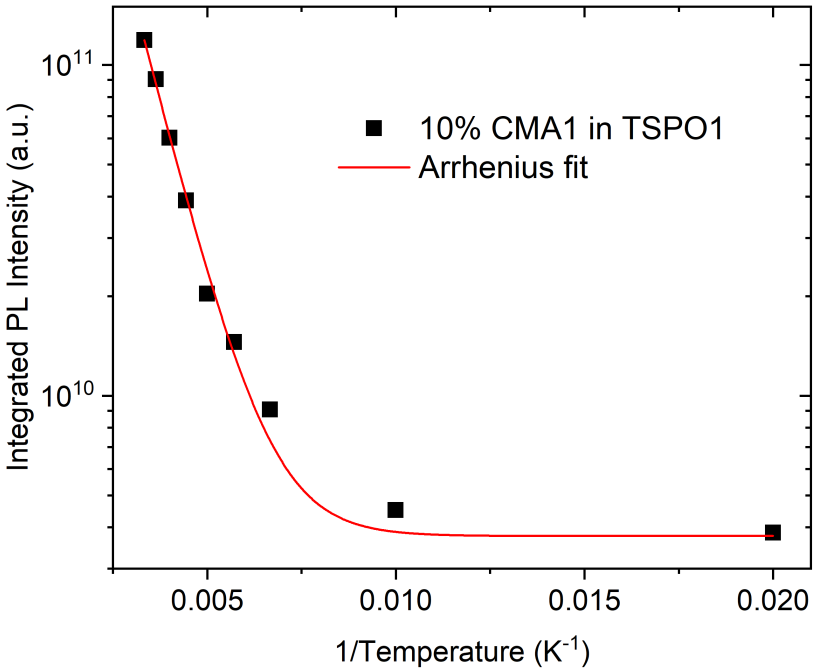

Fig. 4.20 Integrated PL intensity plotted against temperature of 10% CMA1 in TSPO1. The integrated PL intensity is thermally activated and can be fitted by the Arrhenius equation. The activation energy extracted from the integrated PL intensity E_APL = 73 meV.

states. Instead, the mean energy of the Gaussian density of states varies with concentration, shifting up by 113 meV between neat film and 5% concentration at 300 K. At the same time, the distribution narrows by 25 meV. By examining the low-temperature spectral diffusion for both high and low concentration, see Fig. 4.22 and 4.23, it is clear that this effect becomes more pronounced at low temperature, shifting the PL spectra to higher energy. Parameters for Monte Carlo simulations are tabulated in Table 4.5 and 4.6.

CMA1 in TSPO1 (300 K)	Mean energy (eV)	Deviation σ (eV)
5% CMA1	2.540	0.023
10% CMA1	2.528	0.028
30% CMA1	2.515	0.036
50% CMA1	2.504	0.042
80% CMA1	2.490	0.044
100% CMA1	2.427	0.048

Table 4.5 Mean energy and standard deviation of density of states (DOS) input in Monte Carlo simulations of CMA1 in TSPO1 concentration series at 300 K. In contrast to the table above, both the Gaussian mean energy and width vary for different concentrations. These parameters correspond to the simulations in Fig. 4.21.

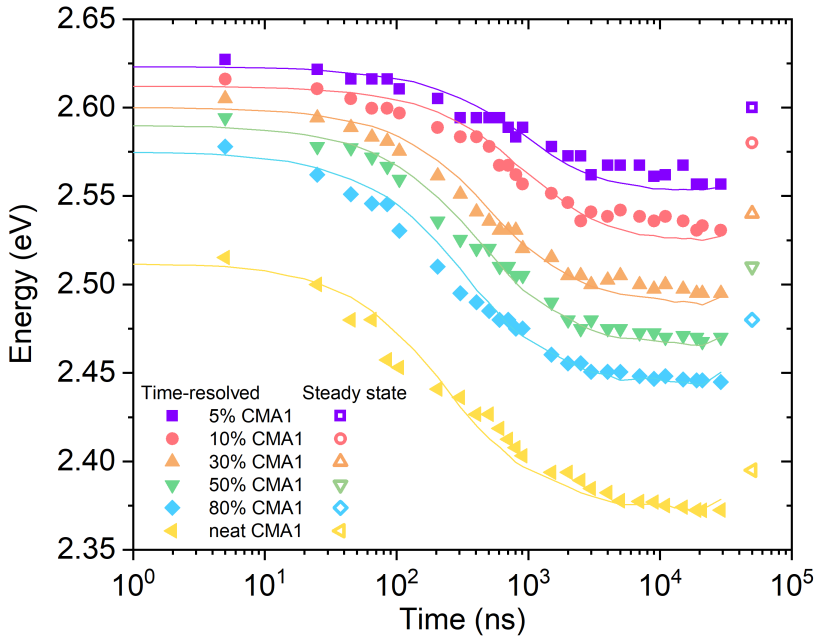

Fig. 4.21 Room-temperature time-resolved PL peak energy of CMA1 in TSPO1 at different concentrations to track the spectral diffusion. Lines are results of Monte Carlo simulation. Monte Carlo simulation was assisted by Lupeng Yang.

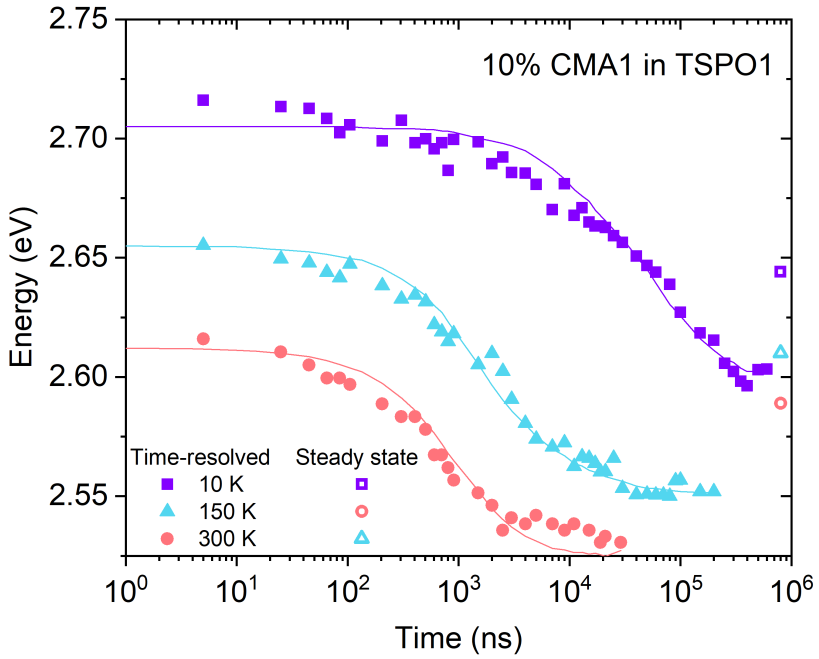

Fig. 4.22 Cryogenic time resolved PL peak position of 10% CMA1 in TSPO1 at 10 K, 150 K, and 300 K. Lines are results of Monte Carlo simulation. Monte Carlo simulation was assisted by Lupeng Yang.

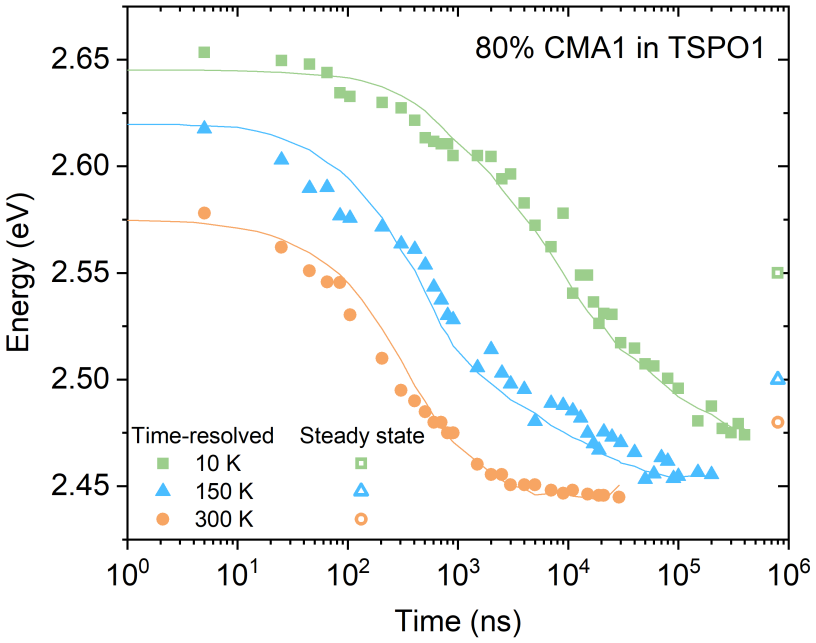

Fig. 4.23 Cryogenic time resolved PL peak position of 80% CMA1 in TSPO1 at 10 K, 150 K, and 300 K. Lines are results of Monte Carlo simulation. Monte Carlo simulation was assisted by Lupeng Yang.

CMA1 in TSPO1 (cryo)	Mean energy (eV)	Deviation σ (eV)
10% CMA1 (10 K)	2.620	0.028
10% CMA1 (150 K)	2.569	0.028
80% CMA1 (10 K)	2.558	0.044
80% CMA1 (150 K)	2.528	0.044

Table 4.6 Mean energy and standard deviation of density of states (DOS) input in Monte Carlo simulations of 10% and 80% CMA1 in TSPO1 at 10 K and 150 K. These parameters correspond to the simulations in Fig. 4.22, and Fig. 4.23. As temperature reaches 0 K, the excitation becomes trapped and the simulation energy approaches a constant.

PXRD measurement indicates very little evidence of crystallisation of CMA1 in these TSPO1 composites (Fig. 4.24), though at low CMA1 concentration, weak host crystallisation features are observed. We therefore propose that the energetic shift is due to an electrostatic interaction between the large ground state electric dipole moment of CMA1 with the smaller host dipoles, leading to orientation of the latter during deposition. Previous work by Dos Santos et al. also showed that polar matrix is able to influence molecular conformation and shifts the energy of CT states.[143] The effect is increased at low temperature, which we interpret as a reduction in thermal disorder. This solid-state solvatochromism leads to a stabilisation of the ground state, and a destabilisation of the excited state, as is observed

in liquid solution. Unlike in solution, upon excitation the host dipoles are much less able to reorient, preserving the increased energetic splitting between the ground and excited states. As for low-polarity hosts, this is consistent with diffusion, rather than intramolecular relaxation, dominating spectral relaxation in the solid state. Consistent with this, we find no correlation with measured glass transition temperatures (which are > 100 °C for all hosts) or with molecular weight. An additional effect is the apparent narrowing of the density of states in the MC model, which requires some explanation. We consider that this is most likely an effect of the microstructure of low-concentration TSPO1 blends. The appearance of a weak TSPO1 crystallisation signal suggests an inhomogeneous local microstructure, which might reduce access to the full DOS and manifest as such a narrowing.

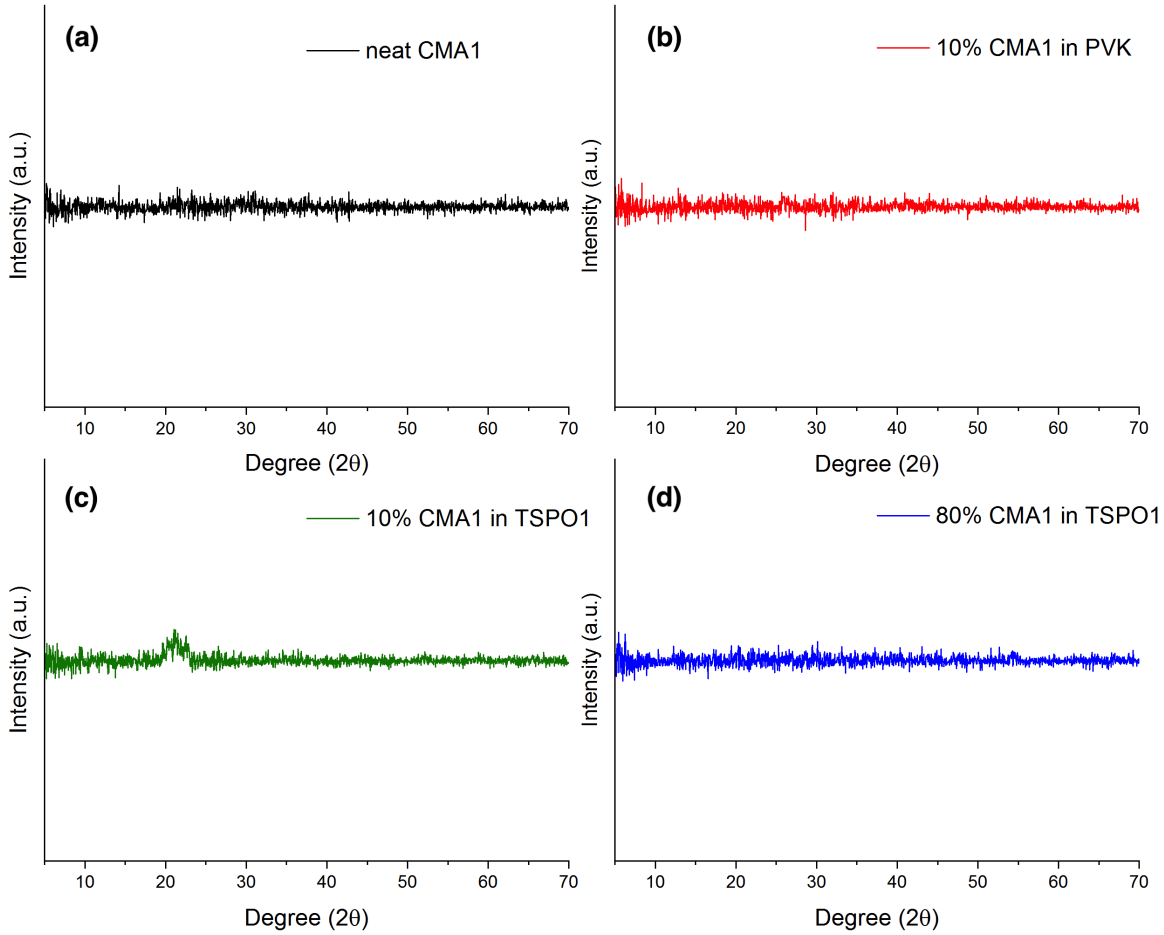

Fig. 4.24 PXRD patterns of: (a) neat CMA1; (b) 10 wt.% CMA1 in PVK; (c) 10 wt.% CMA1 in TSPO1; (d) 80 wt.% CMA1 in TSPO1 thin films. The intensity of X-ray scatter is presented on the same scale. The films were spun from chlorobenzene solutions (20 mg/mL) in a nitrogen glovebox. The feature around 20°in panel (c) is from TSPO1 host.

We thus conclude that of the 210 meV blue shift in steady-state luminescence observed between neat and dilute CMA1, approximately 60 meV arises from suppressed triplet diffusion and 150 meV arises from an electrostatic host-guest interaction. In addition to providing a mechanism by which emission peak energy may be controlled over a meaningful range, solid-state solvatochromism offers a means to tune the relative energies of excited states with differing charge-transfer character, and probe the underlying mechanism of triplet harvesting.

4.3.4 Coupling mechanism for triplet harvesting

Initial TD-DFT calculations of CMA1 using the PBE0 functional and def2-TZVP basis set, when referenced to experimental energies, suggested torsion leads to a crossing of the lowest singlet and triplet energies.[32] However, TD-DFT calculations using the more accurate MN15 functional, which does not suffer from the underestimation typical for TD-DFT reveal a different picture, predicting a significantly greater destabilisation of S_0 by torsion, and a reduced stabilisation of S_1, see Fig. 4.25, such that both the $S_1 - S_0$ and $T_1 - S_0$ energy gaps reduce as dihedral angle increases.[112] This is consistent with the combined DFT and multireference configuration interaction calculations of Föller and Marian, who find that while the S_1 state is stabilised to a greater extent than T_1 by contributions from doubly-excited configurations, this is insufficient in most circumstances to invert the spin states.[135] This work also concluded that T_1 phosphorescence borrows oscillator strength from S_2, and that coupling between S_1 and T_1 is spin-vibronic in nature. Subsequent work by Penfold et al. considered couplings from S_1 to the lowest three excited triplet states and two nuclear degrees of freedom: torsion around the Au–N bond and the stretching mode of the same bond with the molecule in the relaxed S_1 geometry.[134] This work concluded that indirect SOC (i.e. $S_1 - T_n - T_1$) mediated by torsional motion may influence the rate of triplet harvesting. Taffet et al. in examining the structurally related Cu(I) analogue CMA2 concluded that ISC was likely most effective in a sterically constrained coplanar configuration, relying on a breaking of planar symmetry by distortion of the C-Cu-N central axis to allow coupling between S_1 and T_1.[136]

The underlying process coupling the T_1 state to the singlet manifold is therefore unclear. We use the experimental results above to provide new insight to this question. While charge-transfer (CT) excited states show significant negative absorption solvatochromism, excited states localised to the donor and acceptor ligands (“LE” states) are insensitive to environmental polarisability, see Fig. 4.4 and 4.5. Upon dilution in TSPO1 host, the peak-to-peak energy difference between the lowest-lying emissive triplet localised to the carbazole donor (2.9 eV) (Fig. 4.26) and the CT triplet decreases from 510 meV to 300 meV. A similar

analysis considering the shift in high-energy edge gives a range 190 meV to around 0 meV. Despite being brought substantially closer to resonance with the localised triplets, increased CT energy leads to a slight *increase* in emission lifetime, and no meaningful change in activation energy is observed (Fig. 4.28). We also find that excited state lifetime depends very weakly on whether or not a given excited molecule is structurally relaxed, with lifetime in dilute solid comparable to lifetime in dilute solution, see Table 4.7. Intersystem crossing (ISC) time measured using transient absorption spectroscopy is likewise insensitive to the increased CT energy, and is constant at around 5 to 6 ps, see Fig. 4.29.

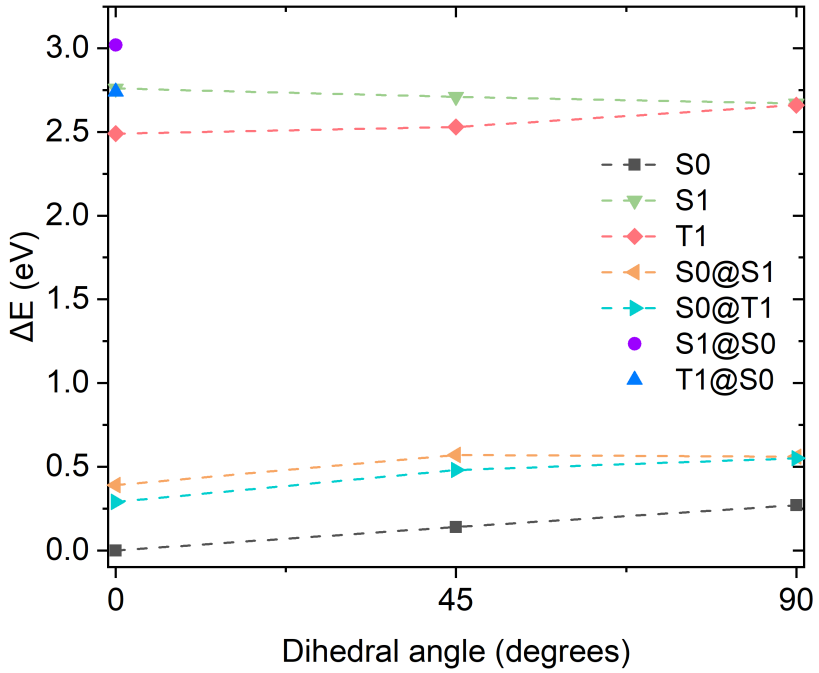

Fig. 4.25 Energy diagram for CMA1 with various orientation between the planes of CAAC carbene and carbazole: planar (0°), twisted (45°) and rotated (90°). S_0 stands for ground state geometry; S_1 and T_1 are relaxed geometries for S_1 and T_1 excited states; $S_0@S_1$ stands for S_0 ground state with geometry of S_1 excited state; $S_0@T_1$ stands for S_0 ground state with geometry of T_1 excited state; $S_1@S_0$ stands for S_1 excited state with geometry of S_0 ground state; $T_1@S_0$ stands for T_1 excited state with geometry of S_0 ground state. All S_0 were calculated with DFT and excited states were calculated with time-dependent DFT (TD-DFT) using the MN15/def2-TZVP method. The energies were calculated by Prof. Mikko Linnolahti.

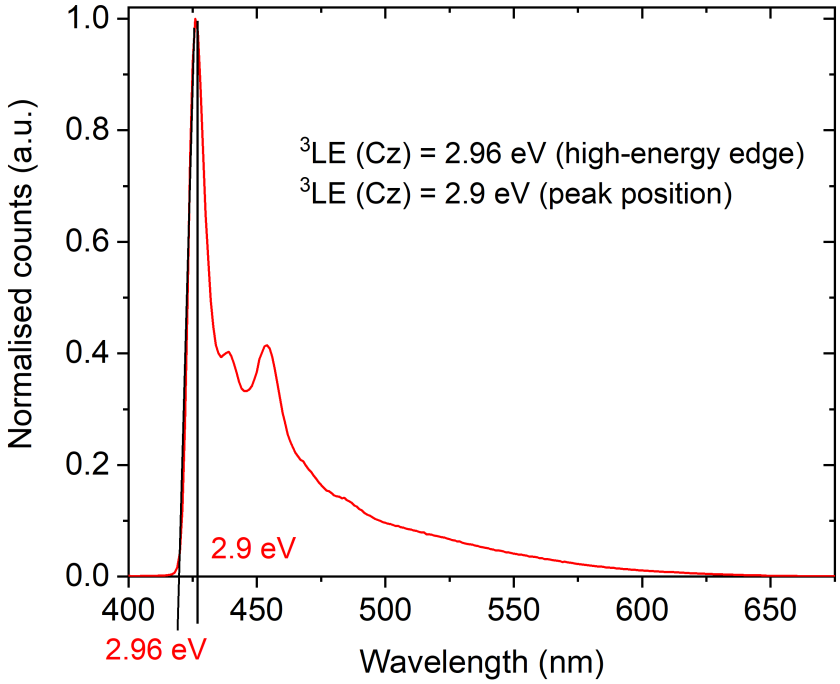

Fig. 4.26 Steady state photoluminescence of CMA1 in 2-MeTHF glass at 77 K. Structured PL is from the triplet localised to the carbazole donor (^{3}Cz). The reason is that, at room temperature, i.e. fluid solution, the polar 2-MeTHF glass molecules are able to organise around the large dipole moment of CMA1 to stabilise the ground state. However, at 77 K, the solvent molecules are frozen and rigid, which destabilises the CT excited states and thus shifts the energies higher than that of the carbazole triplet state (^{3}Cz).[130, 131] Solution was deoxygenated and sealed in a cuvette. Concentration is 1 mg/mL. The excitation wavelength is 350 nm. The spectrum was measured by Dr. Alex Romanov.

CMA1 in solvent	Luminescence Lifetime (ns)	PLQE
CMA1 in tol	1250	98%
CMA1 in CB	1100	98%
CMA1 in DCB	1000	95%
CMA1 in DMSO	1050	77%

Table 4.7 Luminescence lifetime and photoluminescence quantum efficiency (PLQE) of CMA1 in different solvents (1 mg/mL) deoxygenated and sealed in cuvettes. Luminescence lifetime was measured under 400 nm laser. Luminescence lifetime was determined by the time when the emission reaches 1-(1/e) of the total time-integrated emission. PLQE was measured in an integrating sphere with sample excited by 405 nm laser of 1 mW power. PLQEs were calculated based on the de Mello method. The values were measured by Jirawit Ratanapreechachai.

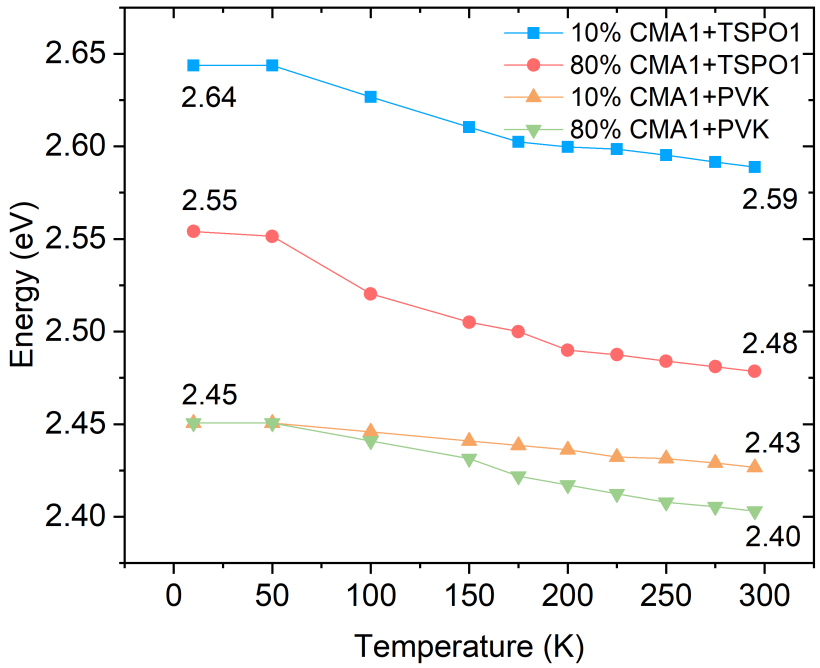

Fig. 4.27 Steady state PL peak energy of 10% and 80% concentration of CMA1 in TSPO1 and PVK host at different temperatures. PL blueshifts when decreasing the temperature.

CMA1 composites	Estimated intersystem crossing (ISC) time (ps)
5 wt.% CMA1:TSPO1 25 µW	5.6
5 wt.% CMA1:TSPO1 50 µW	5.6
5 wt.% CMA1:TSPO1 100 µW	5.6
5 wt.% CMA1:TSPO1 170 µW	5.3
3 wt.% CMA1:TSPO1 160 µW	5.5

Table 4.8 Estimated intersystem crossing (ISC) time extracted from Fig. 4.29.

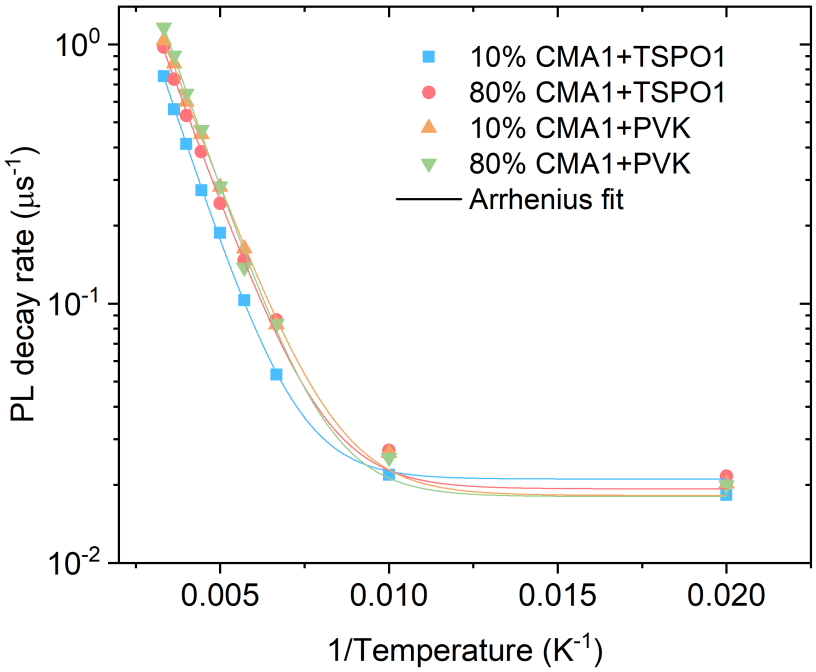

Fig. 4.28 PL decay rate of 10% and 80% concentration of CMA1 in TSPO1 and PVK at different temperatures as a function of 1/Temperature. PL decay rate is the reciprocal of characteristic luminescence lifetime from cryogenic emission integral. The fitted curves yield activation energies: E_Ak (10% CMA1 + TSPO1) = 79 meV, E_Ak (80% CMA1 + TSPO1) = 77 meV, E_Ak (10% CMA1 + PVK) = 72 meV, E_Ak (80% CMA1 + PVK) = 76 meV.

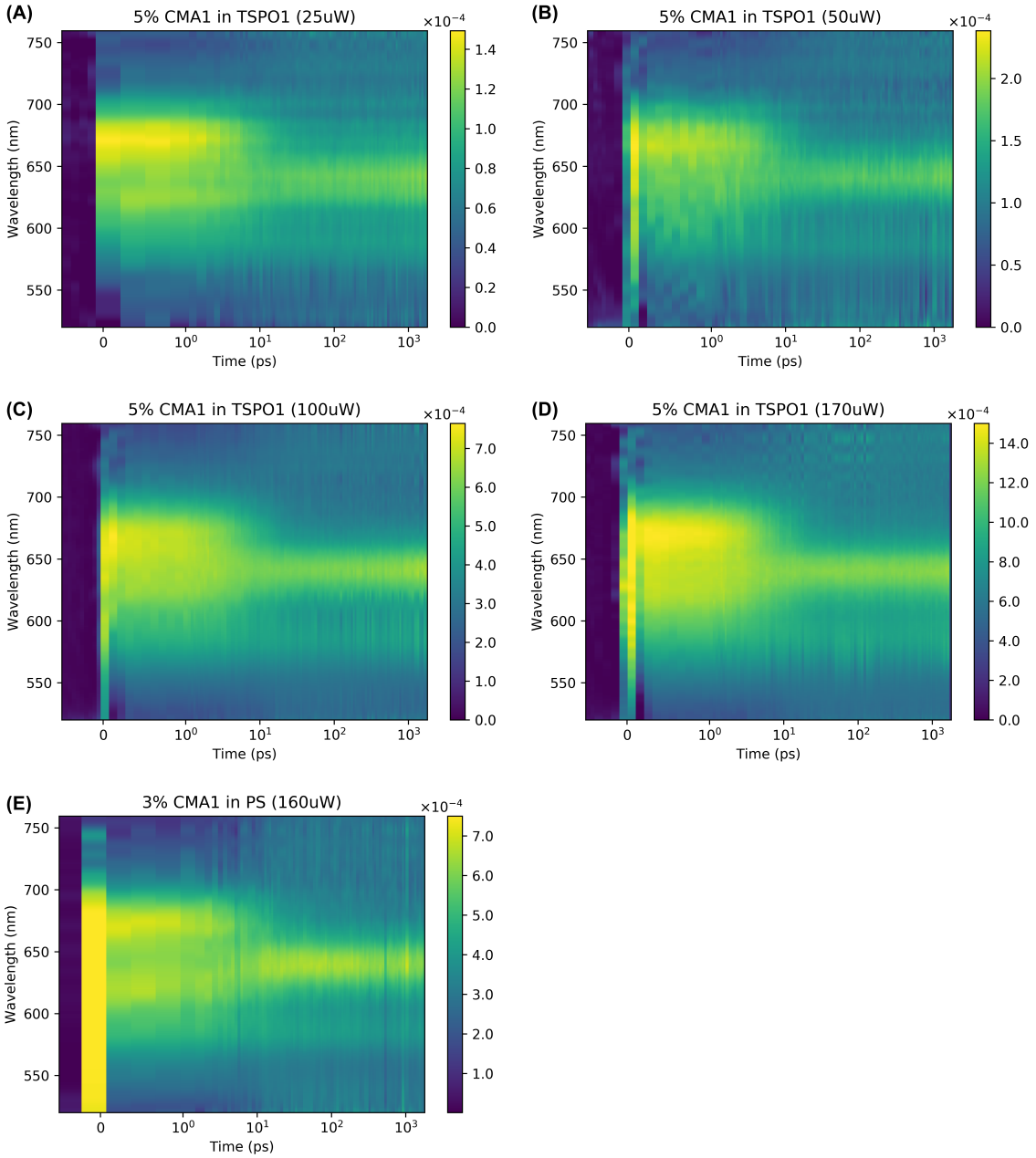

Fig. 4.29 (a) - (d) Transient absorption (TA) colour map of 5 wt.% CMA1 in TSPO1 films under various pump power, 25 µW, 50 µW, 100 µW, and 170 µW; (e) 3 wt.% CMA1 in polystyrene film under 160 µW pump power. The initial excited state absorption associated with singlet is located at 680 nm, which fades away at early times around 5 to 6 ps. The narrower peak located at 645 nm is associated with triplet, which exists at longer timescale. The intersystem crossing (ISC) time of each sample is estimated by the crossover of singlet and triplet kinetics, and is summarised in Table 4.8. These transient absorption (TA) measurements were performed by Antti Reponen.

To establish a framework for interpreting these observations, we consider a simplified version of the chromophore which has C_{2v} symmetry[144], with reference to molecular orbital calculations summarised in Fig. 4.30, Fig. 4.31 and Table 4.9. From an examination of symmetry arguments, the locally excited carbazole state ($\approx$ HOMO to LUMO+3) transforms as A_1 in the C_{2v} point group, the same irrep as the S_1 and T_1 states. In C_{2v} the molecular rotations (and therefore the SOC operator) transform as all irreps except A_1. When the CMA chromophore is completely planar or twisted at 90 degrees (both of which correspond to approximate C_{2v} symmetry), there can therefore be no direct SOC between S_1 and T_1, and nor can there be any indirect SOC via the Cz(LE) state (referred to as LE_1).

Since there can be no direct coupling (and therefore RISC) in this idealised picture, further coupling has to be included in the model. One possibility is mixing via higher-lying states which transform as irreps other than A_1. The ligand-centred state corresponding to $\approx$ HOMO-3 to LUMO (referred to as LE_2) transforms as B_2 and therefore its triplet form can mix with S_1. Similarly, the state formed by a predominantly HOMO-1 to LUMO transition is predominantly of CT character (referred to as CT_2) and transforms as B_1, thus its triplet form can interact with S_1 via SOC. In order for LE_2 and CT_2 to mix with T_1 there would need to be vibronic symmetry breaking, for LE_2 a B_2 mode and for CT_2 a B_1 mode. It is impossible to state for certain without calculation which of these interactions is stronger or more likely to contribute to SOC and therefore delayed fluorescence. However, the insensitivity of the photophysics to the energy of the CT states relative to the LE states suggests that the interaction could be via CT_2, which will be perturbed by electrostatic environment similarly to S_1.

In addition, upon descending from C_{2v} (the symmetry of the model chromophore) to C_s (the symmetry of the actual chromophore) B_1 descends to A'; as does A_1, whereas A_2 and B_2 descend to A". This suggests that in the reduced symmetry of the true chromophore then CT_2 may be more able to couple with T_1 than LE_2. While these arguments consider interactions via the triplet forms of LE_2 and CT_2, similar arguments also hold for interactions via the singlet forms, though this is in reality less likely due to larger energy separation. An alternative mechanism for coupling to occur between states of CT character could be vibronically allowed SOC, particularly since calculation suggests emission may result from a configuration involving twisting around the carbene-metal-amide bond.[145] In a partially twisted geometry (between 0 and 90 degrees) the idealised chromophore descends in symmetry to C_2 (and the full chromophore to C_1), and S_1 and T_1 descend from A_1 to A. In this lower symmetry R_z also transforms as A, meaning that in the twisted geometry there could be direct SOC between S_1 and T_1, facilitating emission. This would also be consistent with the relative insensitivity of emission rate to host polarisability, since the $S_1 - T_1$ energy

gap is likely to be similar in range of host environments. We find little experimental evidence for beneficial coupling to LE states within energy range explored, which agrees with the "interference" effect predicted by Penfold et al.[134] This picture contrasts with several models for organic donor-acceptor emitters, where direct $S_1 - T_1$ coupling is assumed to be very weak and emission requires spin-vibronic coupling to LE triplets.[59, 146] Character tables for point group C_{2v}, C_s and C_1 are summarised in Table 4.10, 4.11, 4.12.

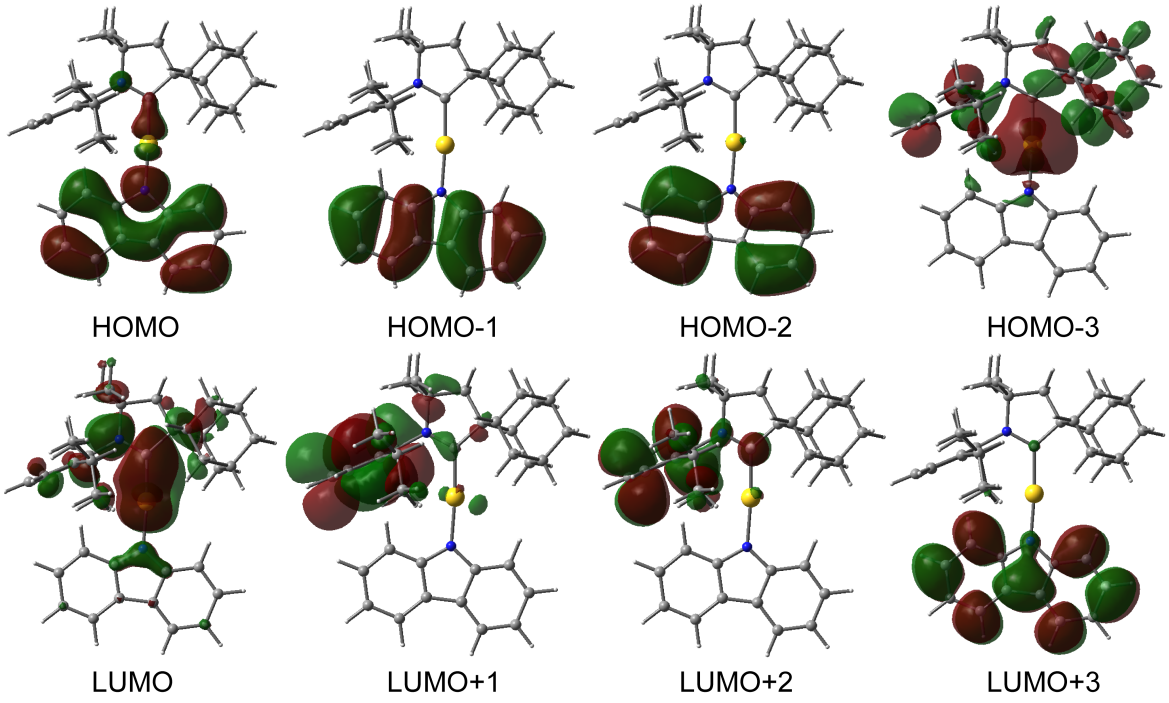

Fig. 4.30 Molecular orbitals of CMA1 from DFT calculations, red/green corresponds to positive/negative sign of wavefunctions. The calculations were performed by Prof. Mikko Linnolahti.

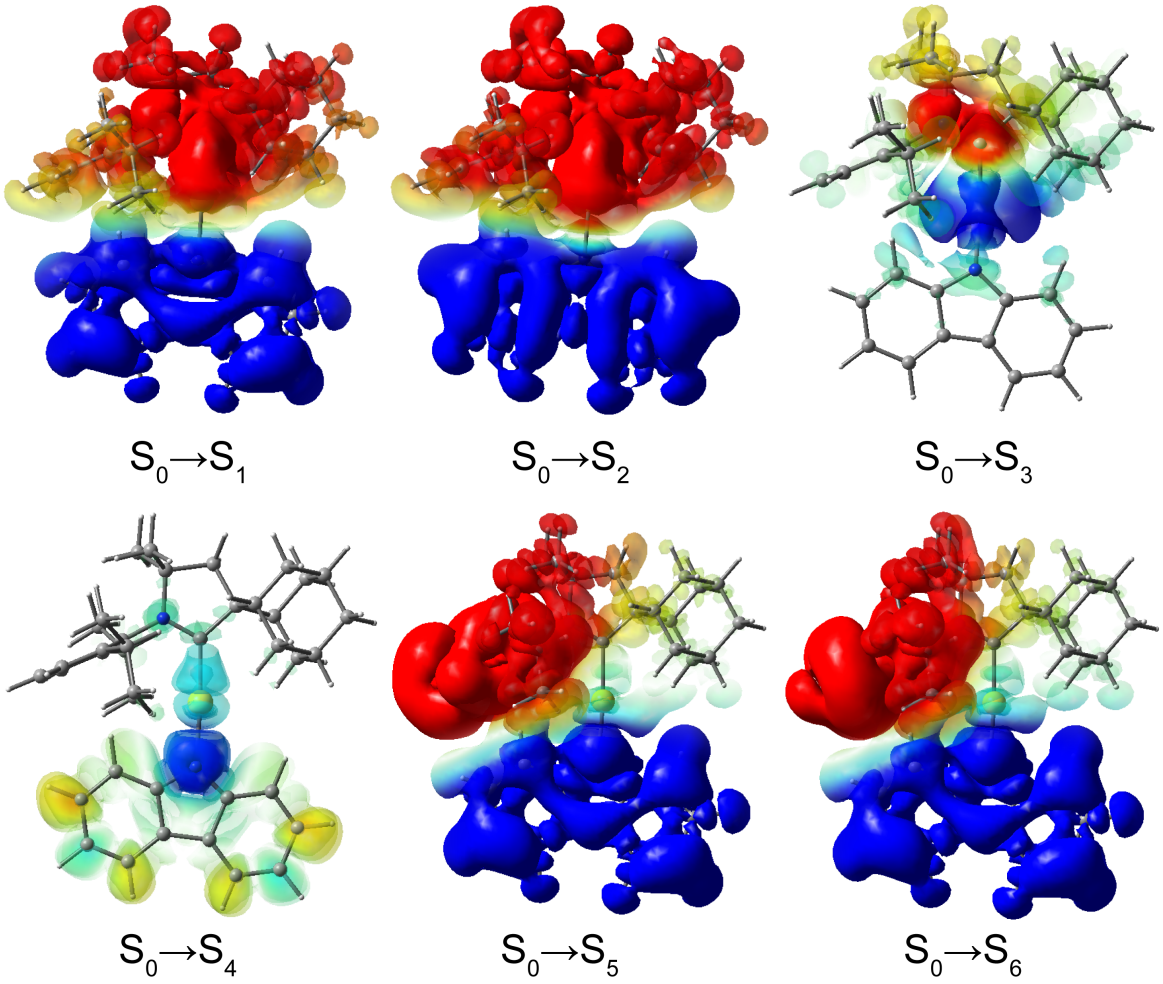

Fig. 4.31 Charge transfer upon excitation, from blue region to red region. Orbital contributions to vertical excitations are summarised in Table 4.9. The calculations were performed by Prof. Mikko Linnolahti.

State	Energy (eV)	Main contributions	Oscillator strength	HONTO	LUNTO
S_1	3.02	H→L 98%	0.1556	≈HOMO	≈LUMO
S_2	3.68	H-1→L 99%	0.0004	≈HOMO-1	≈LUMO
S_3	3.93	H-3→L 91% H-6→L 2%	0.0033	≈HOMO-3	≈LUMO
S_4	3.94	H→L+3 91% H-1→L+7 4% H→L+1 3%	0.0490	≈HOMO	≈LUMO+3
S_5	4.03	H→L+1 95% H→L+3 3%	0.0035	≈HOMO	≈LUMO+1
S_6	4.17	H→L+2 98%	0.0026	≈HOMO	≈LUMO+2

Table 4.9 Orbital contributions to vertical excitations ($S_0 \rightarrow S_1$ - S_6). The calculations were performed by Prof. Mikko Linnolahti.

C_{2v}	E	$C_2(z)$	$\sigma_v(xz)$	$\sigma_v(yz)$	Linear functions, rotations	Molecular states
A_1	+1	+1	+1	+1	z	S_1, T_1, Cz(LE)
A_2	+1	+1	-1	-1	R_z	$\hat{H}_{SO}$
B_1	+1	-1	+1	-1	x, R_y	CT_2, $\hat{H}_{SO}$
B_2	+1	-1	-1	+1	y, R_x	LE_2, $\hat{H}_{SO}$

Table 4.10 Character table for point group C_{2v}.[34]

C_s	E	σ_h	Linear functions, rotations	Molecular states
A'	+1	+1	x, y, R_z	S_1, T_1, CT_2
A"	+1	-1	z, R_x, R_y	LE_2

Table 4.11 Character table for point group C_s.[34]

C_1	E	Linear functions, rotations	Molecular states
A	+1	x, y, z, R_x, R_y, R_z	S_1, T_1, $\hat{H}_{SO}$

Table 4.12 Character table for point group C_1.[34]

4.3.5 Extension to other CMAs

This strategy for emission tuning and photophysical exploration does not rely on a particular emitter choice, the same approach can be extended to tune the emission of other charge-transfer emitters with a large ground-state dipole moment. In particular, we apply the same approach to emitters from the CMA family across the visible spectrum. Fig. 4.32 presents thin-film photoluminescence peak energies for CMA1 and structurally-related gold-bridged analogues: (CAAC)Au(3,6-di-tBucarbazole) (CMA4), (CAAC)Au(6-(tert-butyl)-3-(trifluoromethyl)-9H-carbazole) (CMA5), (CAAC)Au(10,11-dihydrodibenz[b,f]azepin-5-ide) (CMA6) embedded in the TSPO1 host. We observe a universal blue shift of PL peak energies as concentration is reduced, with similar magnitude to that of CMA1, around 200 meV.

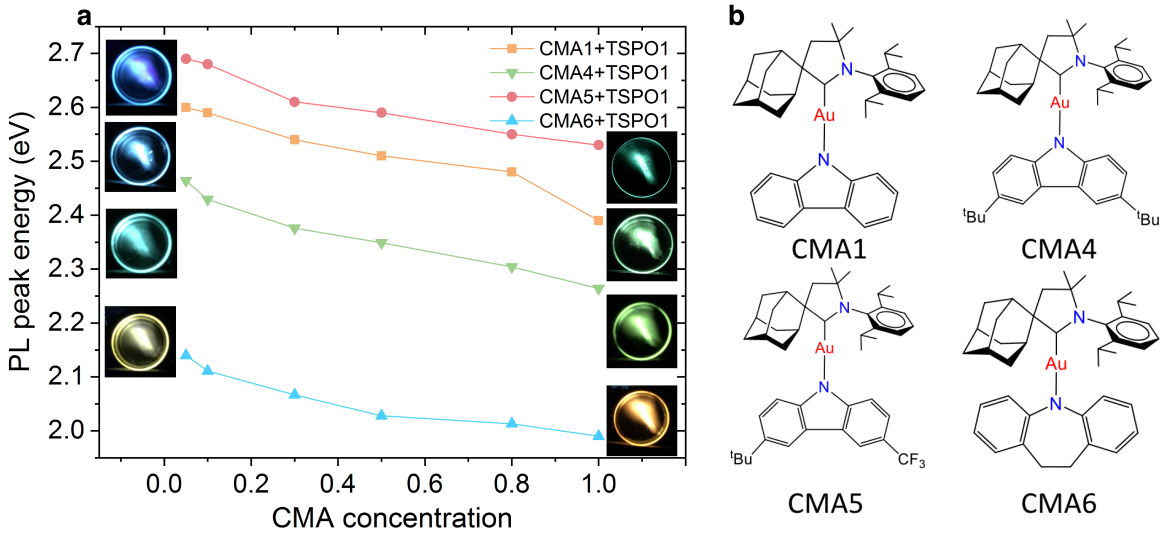

Fig. 4.32 (A) Dependence of PL peak energy of various CMAs on the doping concentration in TSPO1 host. Photographs show photoluminescence of neat CMA1, CMA4, CMA5, and CMA6 and 5% weight concentration of CMAs in TSPO1 thin films under UV illumination. (B) Chemical structures of CMA1, CMA4, CMA5 and CMA6.

4.4 Conclusions

In summary, we have demonstrated a physical approach to modulate the CT triplet energy in a donor-bridge-acceptor type organometallic emitter CMA1. The CT energy can be tuned by around 200 meV via thermally activated diffusion and electrostatic interactions with host molecules. This shift leads to no meaningful change in intersystem crossing rate, slightly increased luminescence lifetime, and no significant change in thermal activation energy. The energy relaxation process was studied by Monte Carlo simulations, which show that

triplet diffusion can account for the experimental trends if modelled as a Marcus-type rate equation and the mean energy and width of the density of states responds to the variations of host-guest electrostatic interactions. We infer that structural relaxation is hindered in the solid state as we see little evidence for large-amplitude structural relaxation or host reorganisation occurring during the excited state lifetime. Tuning of CT energy provides an experimental approach to probe the triplet harvesting mechanism and the coupling between the T_1 and S_1 states. We find that for CMA1 there is likely to be no direct spin-orbit coupling between charge transfer states (S_1 and T_1) and ligand-centred excited states localised to the carbazole, as they transform as the same irrep. However, higher-lying CT states (for example LUMO-1 to HOMO) can interact with S_1 and T_1. From the insensitivity of CMA1 photophysics to CT energy, we suggest that CT$-$CT coupling contributes more significantly than CT$-$LE coupling, offering a design rule for the realisation of rapid triplet emission. We go on to show that solid-state solvatochromism may be applied to a range of gold-bridged CMAs, achieving a universal blue shift around 200 meV. Such an approach should be directly transferrable to other charge-transfer emitters with large permanent dipole moment, allowing host-guest interactions as a tool to tune electroluminescence in OLED devices over a significant range.

Chapter 5

Influence of Nuclear Reorganisation and Polarisation on Crystalline Carbene-Metal-Amide Photoemitters

5.1 Abstract

The nature of carbene-metal-amide (CMA) photoluminescence in the solid state is explored through spectroscopic and quantum-chemical investigations on a representative Au-centred molecule. The crystalline phase offers well-defined coplanar geometries, enabling the link between molecular conformations and photophysical properties to be unravelled. We show that a combination of restricted torsional distortion and molecular electronic polarisation blueshift the charge-transfer emission by around 400 meV in the crystalline versus the amorphous phase, through energetically raising the less-polar S_1 state relative to S_0. This blueshift brings the lowest charge-transfer states very close to the localised carbazole triplet state, whose structured emission is observable at low temperature in the polycrystalline phase. Moreover, we discover that the rate of intersystem crossing and emission kinetics are unaffected by the extent of torsional distortion. We conclude that more coplanar triplet equilibrium conformations control the photophysics of CMAs.

This work was published as Carbene-Metal-Amide Polycrystalline Materials Feature Blueshifted Energy yet Unchanged Kinetics of Emission - Jiale Feng, Elliot J. Taffet, Antti-Pekka M. Reponen, Alexander S. Romanov, Yoann Olivier, Vincent Lemaur, Lupeng Yang, Mikko Linnolahti, Manfred Bochmann, David Beljonne, Dan Credgington. Chemistry of Materials, 2020, 32, 4743-4753.

All the below work was carried out by myself except where stated. Dr. Elliot J. Taffet, Prof. Yoann Olivier, Dr. Vincent Lemaur, and Prof. David Beljonne performed the quantum-chemical simulations. Lupeng Yang carried out the Monte Carlo simulation code development. Dr. Alexander S. Romanov performed the molecular design and synthesis. Antti-Pekka M. Reponen carried out the solution transient absorption measurements.

5.2 Introduction

Carbene-metal-amides (CMA) are a large family of organometallic donor-bridge-acceptor emitters that are promising candidates for thin-film light-emitting diodes.[32, 129–131, 147, 148] CMA1, as the archetype of this group of molecules, employs a cyclic (alkyl)(amino) carbene (CAAC) acceptor and a carbazole (Cz) donor bridged by a gold (Au) atom, showing high photoluminescence quantum efficiency (80-90%) from states involving electron transfer from donor to acceptor, good chemical stability and fast intersystem crossing.[32, 129–131, 147, 148] The σ-donating nature of the carbene ligand leads to a large permanent electrostatic dipole moment in the ground state. Photoluminescence mainly occurs via the triplet charge-transfer (CT) state and is thermally activated, with characteristic activation energy around 70-80 meV and sub-microsecond characteristic emission lifetime in both solution-processed and sublimed devices at 300 K.[32, 132]

CMA1, in common with many CMA materials, exhibits an energetic minimum in the ground state with donor and acceptor ligands approximately coplanar, while the excited singlet minimum of the isolated molecule occurs when donor and acceptor ligands are approximately orthogonal [32, 112, 134, 135, 140], indicative of twisted-intramolecular-charge-transfer (TICT) character. A range of emission energies and conformations are therefore accessible between the ground-state and excited-state minima, because in the solid state the molecules encounter different steric and dielectric environments. Significant differences in the photophysics are hence expected when varying the environment of the molecules, as increasing torsion angle leads to reductions in oscillator strength, exchange energy and molecular symmetry.[149–151] The search for next-generation electroluminescent materials requires that we understand the impact of these changes, in order to design materials with “ideal” photophysical characteristics. Such material design is predicated on resolving the interplay between emitter conformation and environmental embedding, which is the issue motivating this investigation.

Multiple models now exist for how torsional motion impacts triplet emission in TADF materials in general, and CMAs in particular. Föller and Marian suggested that coupling between S_1 and T_1 is dependent on molecular geometry, and at 300 K is spin-vibronic

in nature, while low-temperature phosphorescence involves direct spin-orbit coupling via an S_2 state.[135] Further calculations by Penfold et al. concluded that indirect SOC (i.e. $S_1-T_n-T_1$) assisted by torsional motion impacts the rate of triplet harvesting.[134] Taffet et al. found from multireference orbital-optimisation calculations that despite the fact that torsional motion is able to narrow the charge-transfer S_1-T_1 energy gap, a concomitant decrease in oscillator strength and spin-orbit coupling occurs. They concluded that the distortion of the carbene carbon-metal-amide nitrogen central axis followed by carbene carbon-nitrogen bond stretching facilitates intersystem crossing (ISC).[136] Current models of thermally-activated emission in organic materials suggest that orthogonal D-A groups are a necessary requirement for CT emission, and experimental evidence exists that restriction of torsional motion leads to a degradation in performance.[151, 152]

Here we realise an experimental method to achieve polycrystalline thin films of CMA materials, allowing the link between geometry and photophysics to be probed directly by experiment. We find that torsional restriction together with molecular polarisation significantly blueshift the photoluminescence. In spite of this emission-energy blueshift, emission kinetics remain constant across material phases, a phenomenon we ascribe to the partially twisted nature of the triplet geometric optimum that remains accessible under conditions of frustrated nuclear reorganisation. On the other hand, the excited state singlet potential is modified significantly by crystallisation, such that its energetic minimum lies proximal to that of the nearly coplanar triplet. Thus, crystallisation pushes the density of emissive states closer to that of phosphorescent, carbazole-based, triplets. The photophysical behaviour, in turn, is largely unchanged in the solid state, dominated by the kinetics of spin crossover at more coplanar conformations associated with the relaxed triplet.

Consequently, we find a constant activation energy for delayed luminescence. We interpret this as corresponding to the exchange energy at a partially twisted triplet geometry. Thus, while the absolute value of emission energy is dependent on the environment, the relative energy between the lowest-lying singlet and triplet states, the exchange splitting, is determined by molecular conformation, and it is this splitting which primarily influences radiative triplet decay. Experimental spectroscopy and quantum chemistry are reconciled under the physical picture that constrained torsional distortion leads to a singlet minimum-energy conformation resembling that of the triplet, which appears unperturbed by the solid-state environment.

5.3 Results and Discussion

5.3.1 Thin-film crystallisation

Although single crystals and crystalline powders offer well-defined geometries, they are typically optically thick and difficult to assess using thin-film characterisation techniques and unsuitable for incorporation into devices and device-like thin films. We therefore first describe a method to produce thin films of crystallised CMA1 hosted in a plasticising poly(ethyleneoxide) (PEO) matrix. PEO is a polar matrix with average dipole moment per repeat unit of around 1 D at 25 °C.[153] A range of PEO variants with weight-average molecular weight (Mw) from 2,000 to 8,000,000 Da were explored. The glass transition temperatures for PEO in this range of polymerisation are all below 0 °C, allowing it to act a thin-film plasticiser at ambient temperature.[154] For the structural and photophysical characterisation detailed below, we employed PEO with Mw of 100,000 Da since spin-cast films offer appropriate optical density (O.D.) for photophysical characterisations. Qualitatively similar results were obtained for all Mw in this range. CMA1 was mixed at 80 wt.% in PEO in chlorobenzene solution (20 mg/mL). Spin coating at 1,200 rpm for 40 seconds on fused quartz substrates (spectrosil) resulted in thin films exhibiting green photoluminescence. Upon annealing on a hotplate at 120 °C for 1 min, photoluminescence progressively shifts to the blue, with conversion to the blue-emitting phase essentially complete after 20 seconds at 120 °C, see Fig. 5.1. No regions of residual green emission are observed.

Fig. 5.2 presents the XRD pattern of as-cast and annealed CMA1 thin films. As-cast samples exhibit little diffraction signal, and we consider these to comprise largely amorphous material. After annealing, samples show strong diffraction peaks at 8.2°, 8.7°and 10.3°which match with diffraction peaks assigned to the (002), (100) and (101) planes in polycrystalline powder samples.[32] The crystalline phase corresponds to a largely coplanar geometry close to the ground-state minimum (torsion angle of 20°) with alternating head-to-tail alignment of CMA molecules. The PEO matrix also shows partial crystallisation after annealing, with two peaks at 19.2°and 23.4°as reported in literature and assigned to the (120) planes and overlapping reflections from the (032), ($\bar{1}$32), (112), ($\bar{2}$12), ($\bar{1}$24), ($\bar{2}$04), and (004) planes.[155–158] We thus consider that the soft, polar, PEO environment enables nucleation and growth of CMA crystals to create a thin film of polycrystalline CMA1 embedded in an optically inert PEO matrix. Crystallisation can also be induced in other matrices under harsher experimental conditions and/or over longer times, as detailed in Table 5.1. We will henceforth refer only to CMA1 crystallised within a PEO matrix.

Non-resonant Raman spectra of as-cast and annealed CMA1:PEO samples are shown in Fig. 5.3. Since the molecular species are identical, spectral differences represent changes

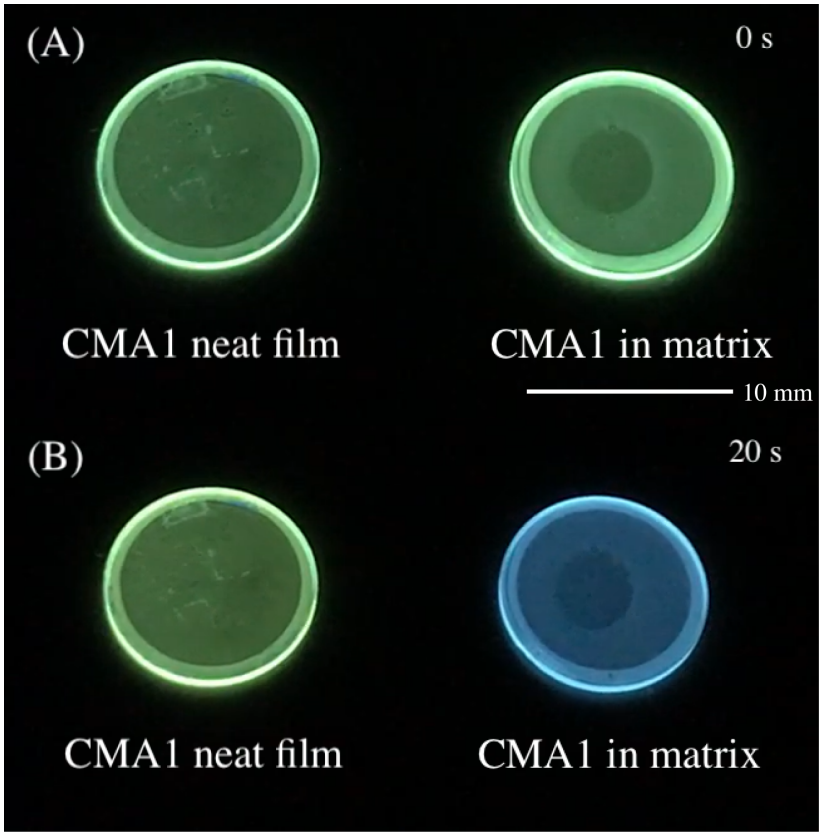

Fig. 5.1 Pictures show the crystallisation of 80 w.t% CMA1 in polymer matrix PEO(100,000) (right), for comparison with neat CMA1 thin film (left). Two films are placed on the hotplate at 120 °C and under UV light. (A) is taken before crystallisation, at 0 s; (B) is taken when the crystallisation is complete, at 20 s.

CMA1 composites	Annealing condition
Neat CMA1	175 °C, 10 min
80 wt.% CMA1 in PVK	225 °C, 10 min
80 wt.% CMA1 in PS	200 °C, 10 min
80 wt.% CMA1 in PVA	175 °C, 10 min
80 wt.% CMA1 in PEO	120 °C, 20 s

Table 5.1 Annealing conditions for crystallisation in different CMA1:polymer composites. PVK: poly(vinylcarbazole); PS: polystyrene; PVA: poly(vinylalcohol); PEO: poly(ethyleneoxide).

in vibrational freedom within different forms. Low-frequency rotation between donor and acceptor is revealed at low Raman shift peaks ($< 200\ cm^{-1}$), which sharpen significantly in the crystalline phase. We interpret this as a decrease in conformational disorder associated with crystallisation. Just as important as the conformational restriction is the dynamic polarisation

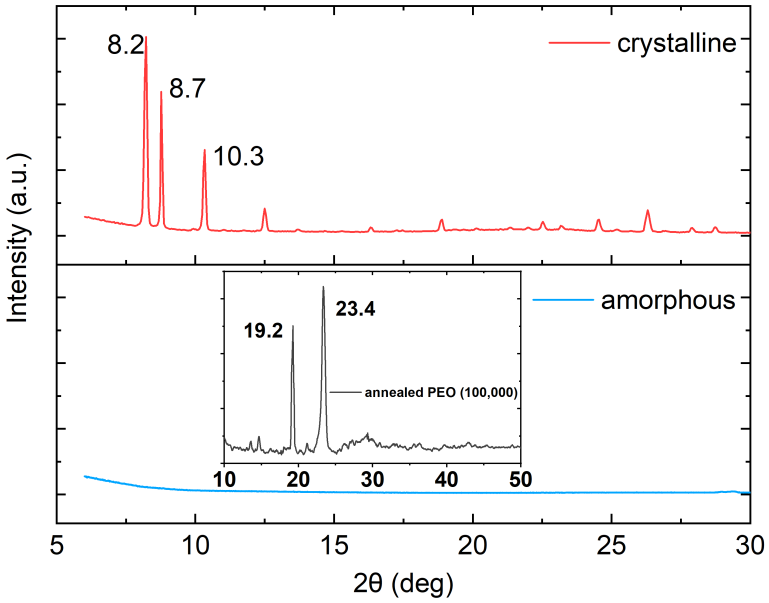

Fig. 5.2 X-ray diffraction of crystalline and amorphous CMA1. Three distinct peaks appear at 8.2°, 8.7°and 10.3°. The inset shows weak crystallisation of annealed PEO(100,000) with two peaks at 19.2°and 23.4°.

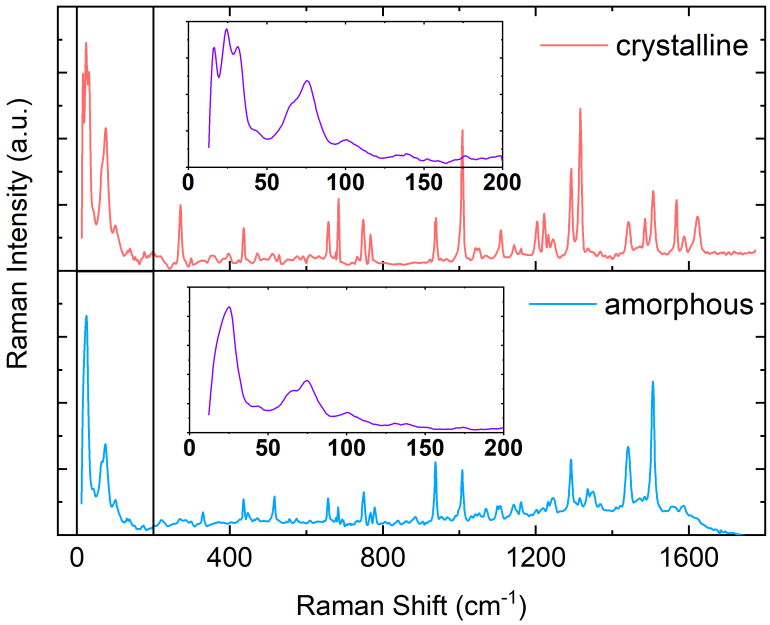

Fig. 5.3 Raman spectra of crystalline and amorphous CMA1. Raman shift below 200 cm^{-1} is magnified. Films were drop cast from CMA1 chlorobenzene solution (20 mg/mL) mixing with 20 wt.% PEO (Mw 100,000 Da) in a nitrogen glovebox, followed by annealing at 120 °C for 1 min to crystallise.

conferred by the induced dipoles of surrounding CMA1 molecules in the solid state. The unique environment conferred by crystallisation manifests in Raman intensity reduction of the carbene-nitrogen bond-stretching mode ($\sim$1500 cm^{-1}), complemented by enhancement of the carbene bending modes at $\sim$1000 and $\sim$1300 cm^{-1}. As such, the environment non-trivially influences the molecular polarisability tensor, meaning that considerations of molecular relaxation must be coupled with considerations of the surrounding environment.

5.3.2 Steady-state spectroscopy investigations

Fig. 5.4 presents the steady-state absorption and photoluminescence (PL) spectra of amorphous and crystallised CMA1 thin films, and CMA1 in toluene solution. The broad absorption peak at around 390 nm for films and 405 nm for solution represents direct excitation to the singlet charge-transfer (CT) state while higher-energy peaks are associated with CAAC/Cz locally excited (LE) states and their vibronic progressions: 370 nm (short-axis-polarised Cz transition), 305 nm (long-axis-polarised Cz transition), and 270 nm (transitions from both CAAC acceptor and Cz donor).

In the crystalline phase, the oscillator strengths of intraligand transitions at 305 nm and 270 nm are highly suppressed. This is consistent with the short-axis-polarised Cz singlet at 370 nm transition inheriting oscillator strength from the linear on-axis anti-alignment of CMA1 dipoles in this phase. In addition, the CT absorption feature narrows, consistent with a reduction in both conformational and electrostatic disorder leading to a narrower density of states (DOS). The photoluminescence peak of CMA1 in toluene solution is around 525 nm, in amorphous film around 520 nm, and in crystallised film 450 nm. The crystalline phase therefore exhibits a substantial blueshift of 400 meV relative to the toluene solution and 370 meV relative to the amorphous film. This blueshifted emission in the crystalline phase was also observed in other organic emitters.[159] The Stokes shift, measured from CT absorption to CT emission, which represents twice the reorganisation energy induced by conformational relaxation from S_1 to S_0 in a harmonic picture of potential energy surfaces, decreases from 0.7 eV in solution to 0.44 eV in crystal. This implies smaller structural changes in the crystal during the excited-state relaxation process. The emission spectrum of crystalline material shows negligible contribution from the green-emitting amorphous phase. The photoluminescence quantum efficiency (PLQE) of crystallised thin film is 55%.

5.3.3 Time-resolved spectroscopy investigations

Fig. 5.5 shows the room temperature time-resolved photoluminescence peak energy and integrated emission with time. The energy offset between the amorphous and crystalline CMA1

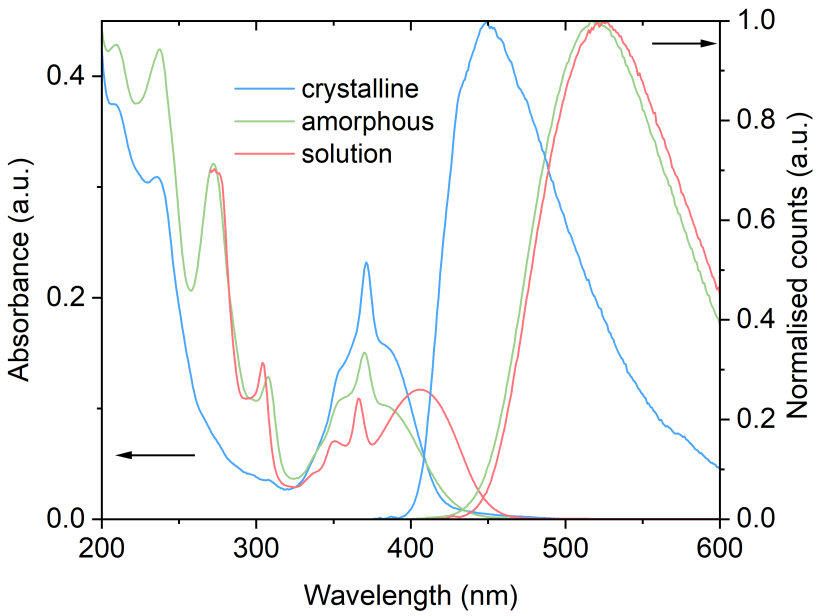

Fig. 5.4 Steady-state absorption and normalised photoluminescence spectra of CMA1 in toluene solution (1 mg/mL), amorphous and crystalline CMA1 thin films. Excitation wavelength is 350 nm.

is large, around 350 meV before 4 µs, beyond which PL of the crystalline sample rapidly redshifts to an amorphous-like emission energy. We interpret this as a small contribution to emission from remnant non-crystalline CMA1 that might be initially photoexcited, leading to a long-lived tail in cumulative counts after 4 µs. The long lifetime of this emission implies that molecular conformations exist in the amorphous sample that are detrimental to rapid triplet harvesting, and that these are absent in the purely crystalline phase.

Fig. 5.6 presents the normalised emission kinetics. By monoexponential fitting to the blue region (5 ns – 4000 ns) in emission kinetics, a luminescence lifetime of 1.05 µs is yielded for crystalline CMA1 at room temperature, and 0.79 µs for the amorphous phase. By comparison, emission kinetics in deoxygenated toluene solution are monoexponential with lifetime 1.1 µs. Energy relaxation to a quasi-equilibrium within the DOS is observed for solid samples, with the degree of relaxation smaller for crystalline CMA1 (around 93 meV compared to 136 meV in amorphous films, see Fig. 5.5. This indicates a narrower DOS for crystalline films, consistent with absorption and Raman spectroscopy. A broad excited-state DOS may originate from both variations in molecular conformation, and from the relative polarisation of the environment around individual chromophores, which varies with their separation and relative orientation.[133] In amorphous films, these parameters are randomly distributed, resulting in a Gaussian distribution of polarisation-induced energy shifts.

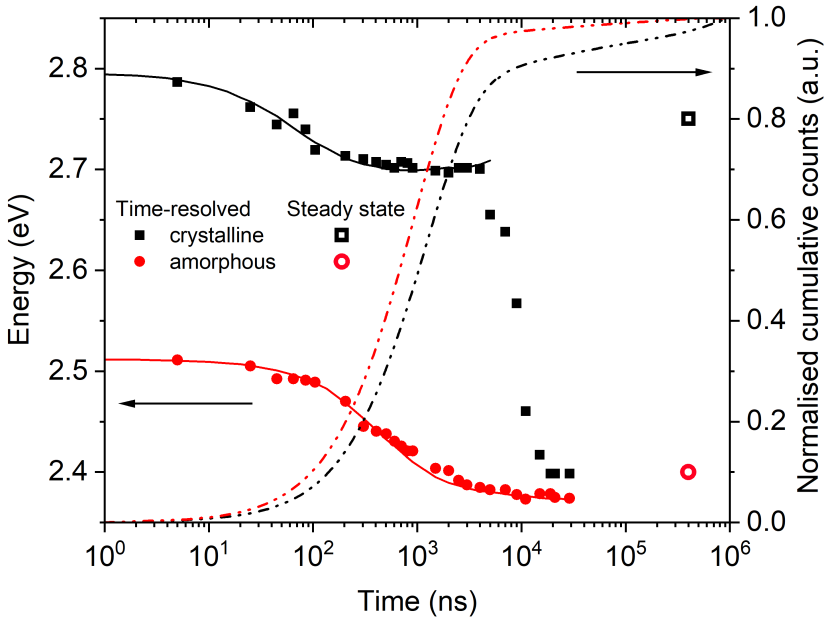

Fig. 5.5 Room temperature time-resolved photoluminescence peak energy of amorphous and crystalline CMA1 to track the spectral diffusion. Solid lines are results of Monte Carlo simulation. Dotted lines are room temperature emission integral.

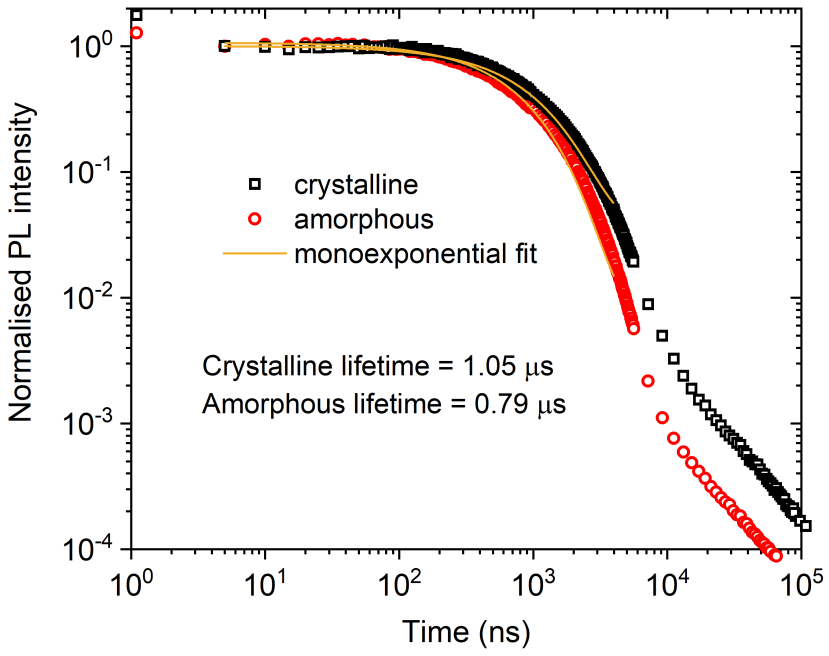

Fig. 5.6 Normalised delayed emission kinetics with monoexponential fits to crystalline and amorphous CMA1 within the 5 – 4000 ns time range. Lifetimes of 1.05 μs and 0.79 μs are yielded respectively for the crystalline and amorphous phases.

At low temperature, characteristic luminescence lifetimes (taken for cumulative emission to reach 63% (1-(1/e)) of the total) increase by approximately a factor of 50 for both crystalline and amorphous CMA1, from 1.6 µs to 94.2 µs for crystalline and 0.97 µs to 60.2 µs for amorphous samples at 10 K, see Fig. 5.7 and Fig. 5.8. The activation energies extracted from an Arrhenius fit to PL decay rate of both samples are similar, 65 meV and 69 meV, as shown in Fig. 5.9. This value agrees nicely with the computed exchange splitting of 71 meV at the CMA1 triplet optimised geometry from state-averaged multireference orbital optimisation. Note that the characteristic activation energies inferred from the integrated PL intensity show a lower value for the crystallised sample of 42 meV compared to 68 meV for the amorphous sample, indicating an interplay between thermally activated radiative and nonradiative decay rates for the crystalline sample.

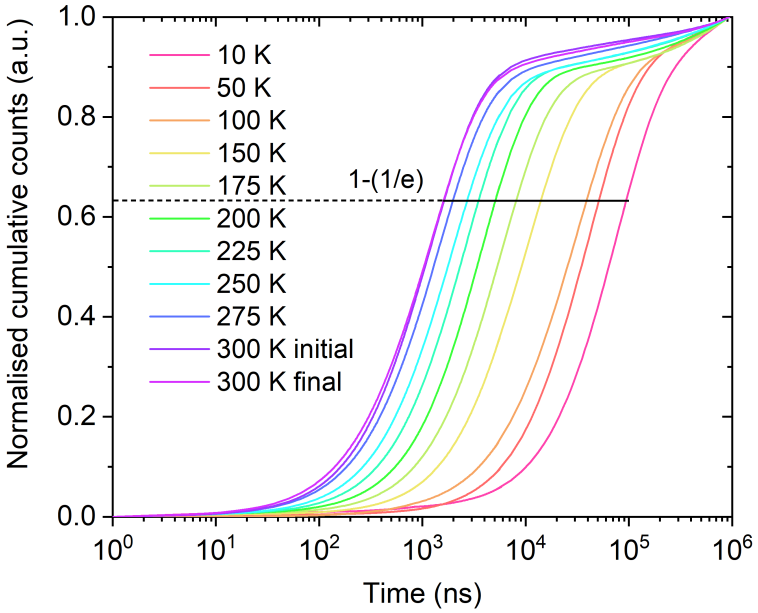

Fig. 5.7 Cryogenic emission integral of crystalline CMA1 film at a temperature series with 1-(1/e) labelled as the characteristic luminescence lifetime. “Initial” data taken at 300 K before cooling the film to 10 K, “Final” data upon warming back to 300 K after low-temperature measurements. Extracted PL decay rates correspond to the data points in Fig. 5.9.

PL from the CT state blueshifts with decreasing temperature, consistent with a narrowing of the thermally broadened DOS toward coplanar conformers, a reduction in electrostatic disorder due to thermal motion, and arrested spectral relaxation, see Fig. 5.10. Below 150 K, the blueshift of the CT state in crystalline material uncovers structured emission, which we assign to phosphorescence from triplets localised to the carbazole ligand, see Fig. 5.11. By comparison to structured phosphorescence observed in frozen MeTHF (Fig. 4.26), we estimate the localised carbazole triplet energy to be approximately 2.95 eV above the ground

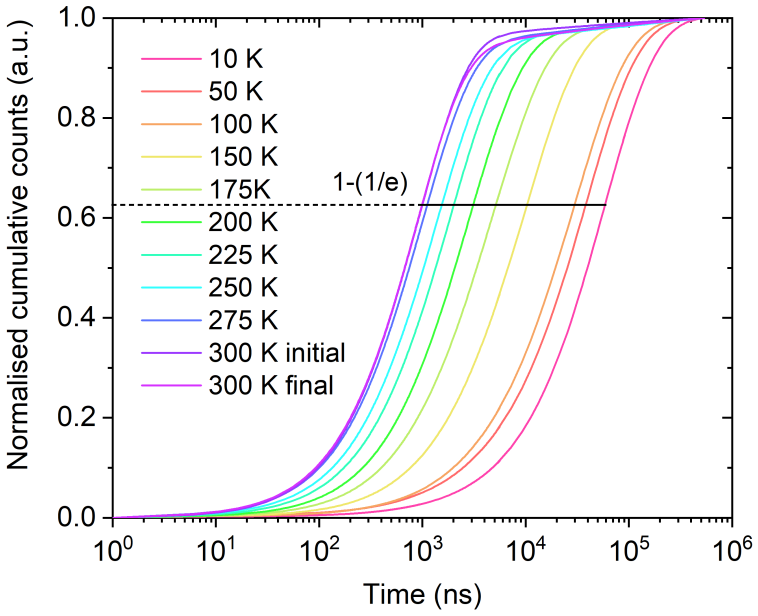

Fig. 5.8 Cryogenic total emission integral of neat amorphous CMA1 film at a temperature series with 1-(1/e) labelled as the characteristic luminescence lifetime. "Initial" data taken at 300 K before cooling the film to 10 K, "Final" data upon warming back to 300 K after low-temperature measurements. Extracted PL decay rates correspond to the data points in Fig. 5.9.

state. By contrast, in amorphous CMA1, the carbazole triplet cannot be accessed from the relaxed CT state, and no structured emission is observed even at low temperature, see Fig. 5.12. The presence of parasitic emission from the localised carbazole triplet precludes direct comparison of CT phosphorescence rates between crystalline and amorphous samples.

Turning to triplet dynamics, the spectral migration shown in Fig. 5.5 and Fig. 5.10 is modelled by considering a Monte Carlo simulation of 3D triplet diffusion through a Gaussian density of states, as described by Movaghar et al.[93] To reproduce the trends observed, the width of the amorphous-phase DOS (48 meV) is found to be larger than for the crystalline phase (30 meV), as expected. A Marcus-type activated hopping probability (Eq. 2.49 and Eq. 2.51 [100]) is required to reproduce the observed temperature dependence, and yields a lower characteristic reorganisation energy (λ) of 140 meV for transport in the crystalline phase, corresponding to an activation energy of $E_a = \lambda/4 = 35$ meV, compared to 240/60 meV in the amorphous phase. The input for the Monte Carlo simulation is tabulated in Table 5.2.

Fig. 5.13 (a), (b), and (c) present the transient absorption (TA) spectra of CMA1 in toluene (1 mg/mL), neat amorphous CMA1 film, and crystalline CMA1 picosecond-nanosecond time scales. Consistent with previous analyses, we assign the early-time photo-induced absorption (PIA) feature to photogenerated singlets, and the later-time PIA feature to triplets formed

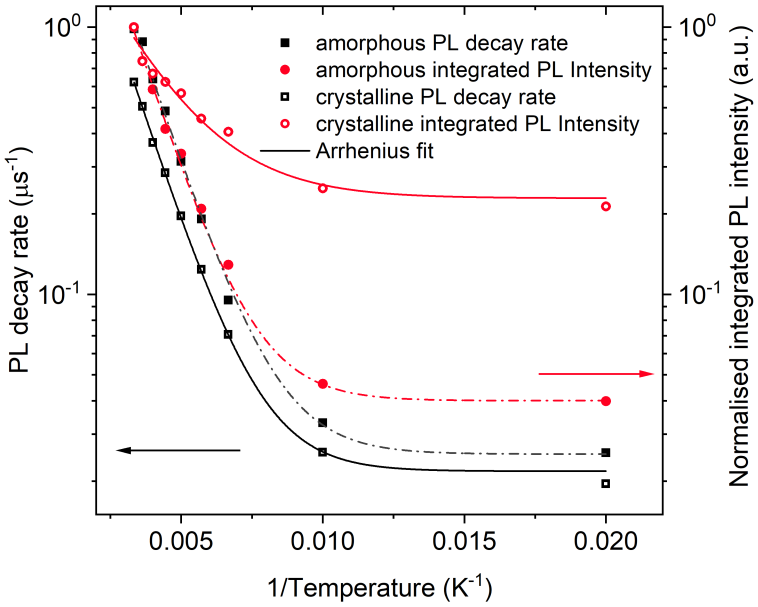

Fig. 5.9 PL decay rate and integrated PL intensity of crystalline and amorphous CMA1 at different temperatures as a function of 1/Temperature. PL decay rate is the reciprocal of characteristic luminescence lifetime from the cryogenic emission integral. Fitting an Arrhenius-type model to the data (lines) yields activation energies: E_Ak (crystalline) = 65 meV, E_APL (crystalline) = 42 meV, E_Ak (amorphous) = 69 meV, E_APL (amorphous) = 68 meV.

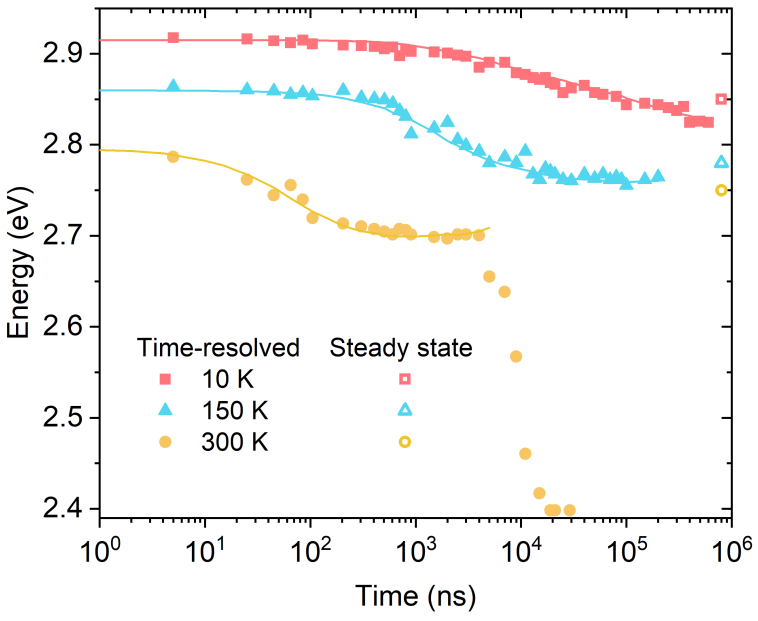

Fig. 5.10 Cryogenic time-resolved PL peak position of crystalline CMA1 at 10 K, 150 K, and 300 K. Lines are results of Monte Carlo simulation.

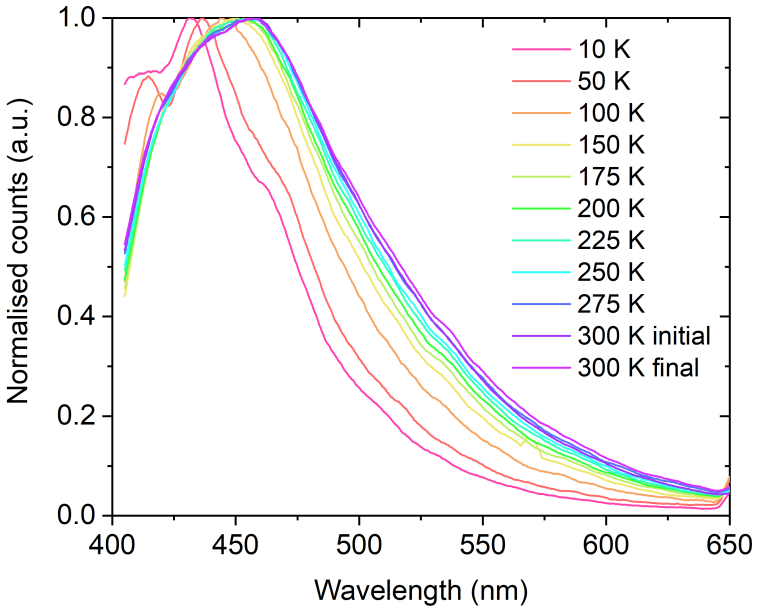

Fig. 5.11 Temperature dependent steady-state photoluminescence of crystalline CMA1 film. "Initial" data taken at 300 K before cooling the film to 10 K, "Final" data upon warming back to 300 K after low-temperature measurements. Laser excitation is at 400 nm, below which the spectra were cut off. In order to uncover structured localised emission, the 425-nm long-pass filter was not applied.

Samples (Temperature)	Mean energy (eV)	Deviation σ (eV)
Amorphous CMA1 (300 K)	2.427	0.048
Crystalline CMA1 (300 K)	2.703	0.03
Crystalline CMA1 (150 K)	2.773	0.03
Crystalline CMA1 (10 K)	2.828	0.03

Table 5.2 Mean energy and deviation of density of states (DOS) input in Monte Carlo simulations of amorphous CMA1 at 300 K, and crystalline CMA1 at 300 K, 150 K and 10 K. These parameters correspond to the simulation in Fig. 5.5 and Fig. 5.10.

following intersystem crossing.[32] In solution, the edge of a stimulated emission can also be observed, which shares kinetics with the singlet. The energy and oscillator strength of PIAs in this spectral range vary in each phase. Fig. 5.13 (d) and Fig. 5.14 show the normalised decomposed singlet and triplet kinetics in each phase. The intersystem crossing (ISC) time of each sample is estimated from the crossover of singlet and triplet kinetics and is found to be identical, within experimental error, at around 5 ps in all phases.

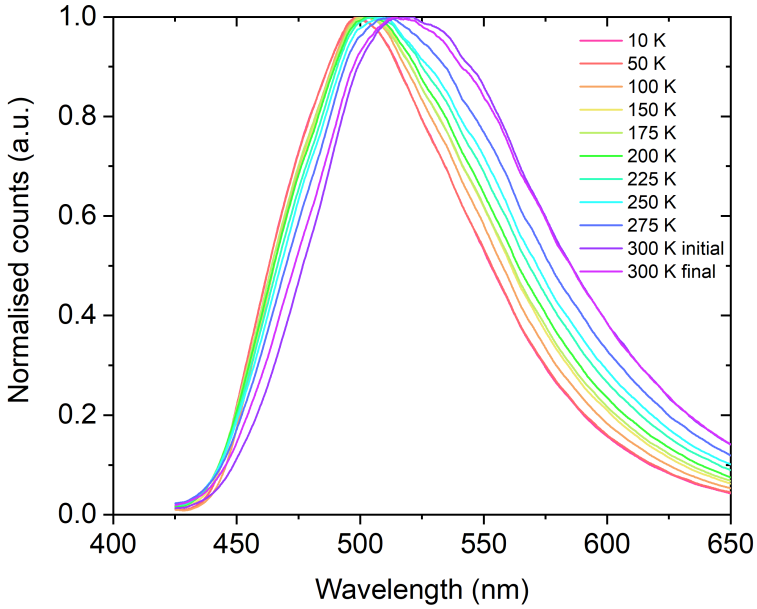

Fig. 5.12 Temperature dependent steady-state photoluminescence of neat amorphous CMA1 film. “Initial” data taken at 300 K before cooling the film to 10 K, “Final” data upon warming back to 300 K after low-temperature measurements. Laser excitation is at 400 nm and the 425-nm long-pass filter was applied.

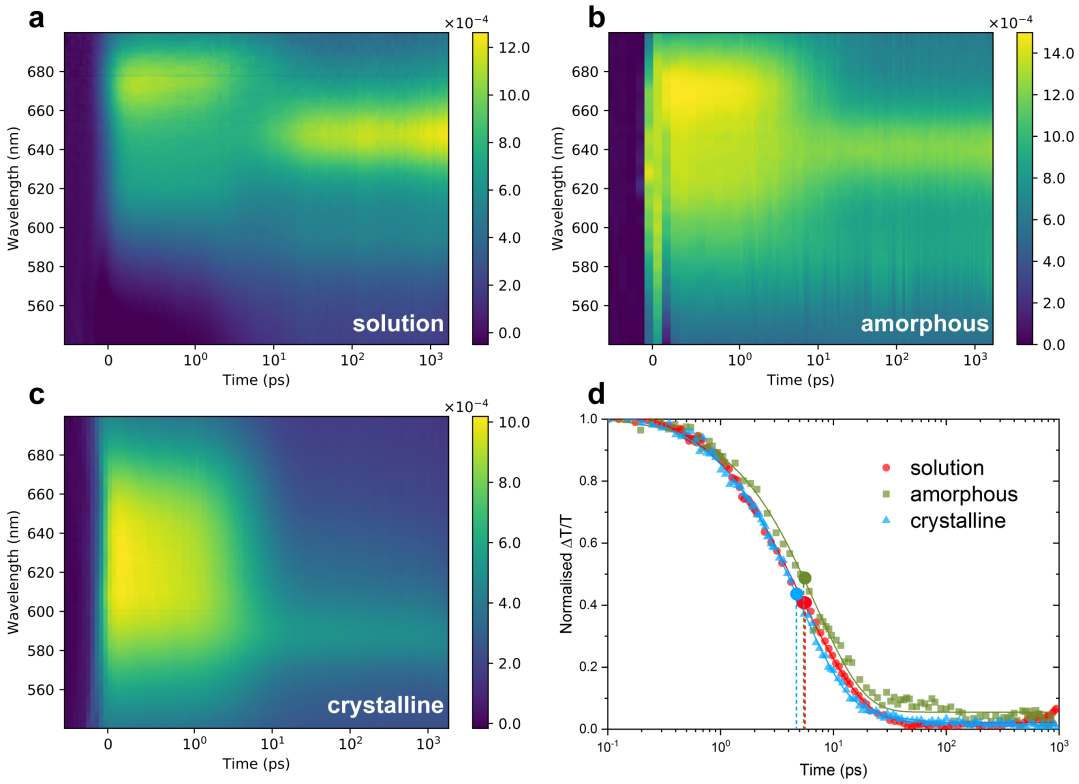

Fig. 5.13 Room temperature transient absorption spectra of (a) CMA1 in toluene at 1 mg/mL, (b) neat amorphous CMA1 film, and (c) crystalline CMA1 film on picosecond-nanosecond time scales. The intensity is shown in ΔT/T, the fractional change in transmission. Samples were pumped at 400 nm under 120 µW pump power for films and 100 µW for solution. (d) presents the normalised decomposed singlet kinetics of solution, amorphous and crystalline phases. The intersystem crossing time of each sample is estimated by the crossover of singlet and triplet kinetics labelled by spots, around 5 ps for all samples. Solid lines are a guide to the eye. The triplet growth kinetic is not included for clarity. Full kinetics are shown in Fig. 5.14. The solution TA experiment was performed by Antti Reponen.

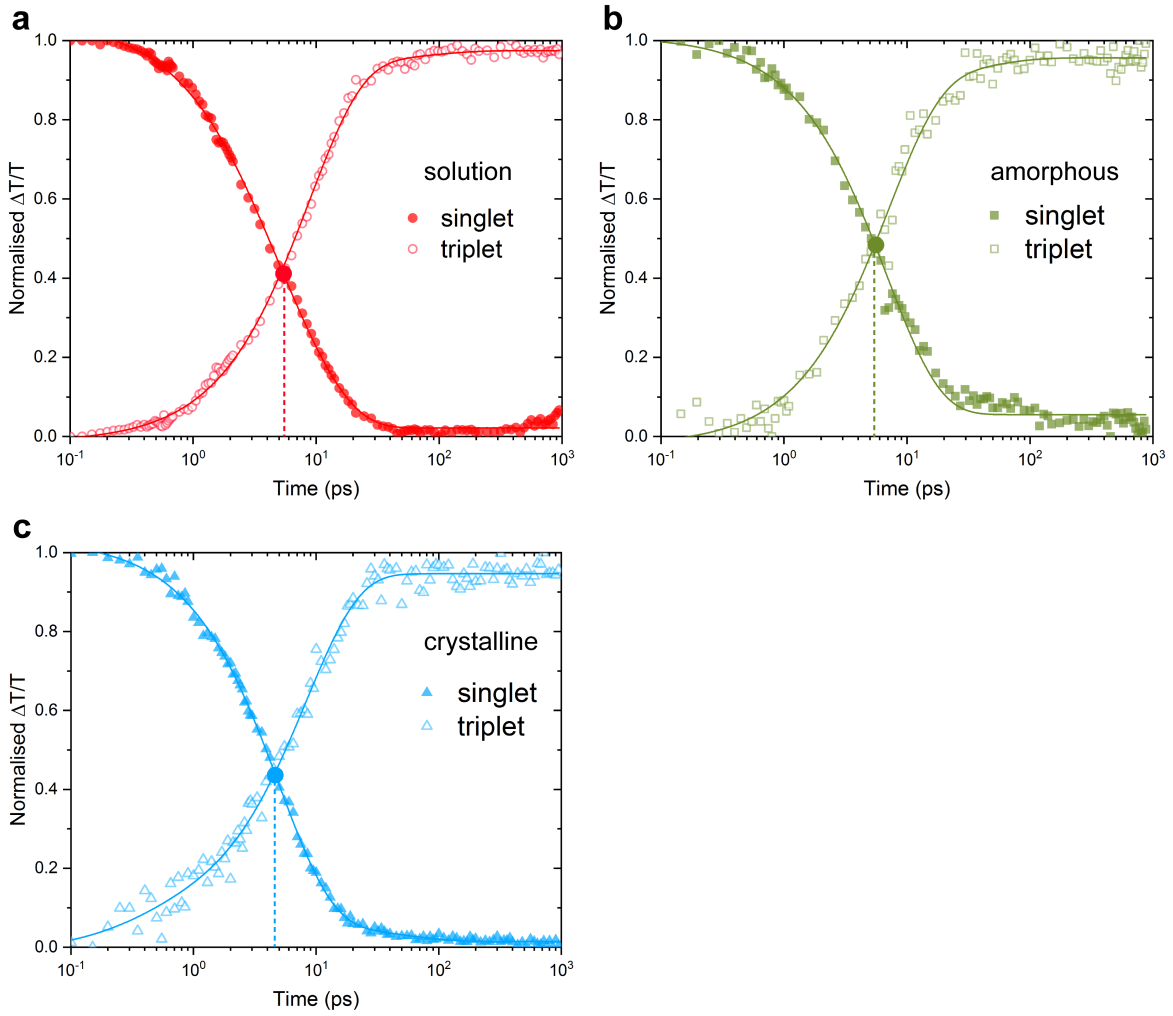

Fig. 5.14 Kinetics of singlet and triplet species deconvoluted from transient absorption spectra in Fig. 5.13 of (a) CMA1 in toluene (1 mg/mL), (b) neat amorphous CMA1 drop-cast film, and (c) crystalline CMA1 drop-cast film. Singlet and triplet species are both normalised. Solid lines are a guide to the eye. The intersystem crossing (ISC) time of each sample is estimated by the crossover of singlet and triplet kinetics labelled by spots, around 5 ps for all samples. Spectral deconvolution is achieved by isolating co-varying regions of the TA spectra by iterative application of a genetic algorithm (GA). The full details of this approach is described in reference.[160, 161] Singular value decomposition of the TA maps reveal two dominant components. As such, the genetic algorithm was restricted to find two independent time-varying species. The solution TA experiment was performed by Antti Reponen.

5.3.4 Computational simulations

To understand these results, we turn to quantum-chemical simulations of the CMA1 crystal environment. The crystal environment constitutes long-range order with intermolecular packing representative of a thermodynamic minimum-energy configuration of ground-state molecules, which can be approximated as a cluster of molecules with relative orientation determined by the crystal structure. We therefore consider a cluster with an embedded CMA1 molecule flanked on either side of a one-dimensional array by anti-aligned CMA1 dipoles and packed in other dimensions by neighbouring molecules in the cell as shown in Fig. 5.15. Incorporating this environment of molecules leads to physical hindrance of intramolecular torsion (a classical effect) and electronic polarisation of the excitations (a quantum effect) in the embedded CMA1 molecule, combining to blueshift the $S_1 - S_0$ transition energy, as described below.

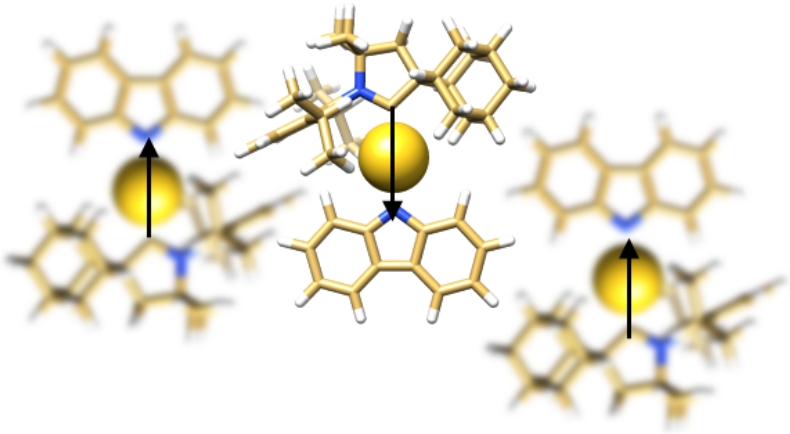

Fig. 5.15 Illustration of a molecular cluster used to simulate the crystal environment where an embedded CMA1 molecule is flanked on either side of a one-dimensional array by anti-aligned CMA1 dipoles and packed in other dimensions by neighbouring molecules in the cell. The simulation was performed by Dr. Elliot Taffet.

Conformational frustration in the crystal

S_1-state geometry optimisation was performed either in the vacuum phase or in the crystalline environment. In the latter case, an embedding Quantum-Mechanics/Molecular-Mechanics (QM/MM) scheme was applied to account for possible frustration effects in the solid. The geometry optimisations alone suggest that photoluminescence blueshifting may be due in part to hampered nuclear reorganisation, restricted intramolecular torsion caused by the steric hindrance within the CMA1 crystalline cluster. While full rotation to an orthogonal

torsional angle is predicted for a single-molecule S_1 state optimisation in the gas phase, a retention of effective coplanarity (around 20°torsional angle) is instead obtained for the S_1 geometry of CMA1 in its simulated cluster environment. Frustrated torsion manifests as a stagnation of the S_1-T_1 energy gap following bond stretching within the initial optimisation steps leading to the converged geometry. Thus, the energetic stabilisation initially appears equivalent in the crystal and vacuum phases before diverging upon activation of torsional modes in the vacuum, which relaxes the S_1 (^{1}CT) state to the point of effective degeneracy with the T_1 (^{3}CT) state. This is in contrast to the finite, albeit small, S_1-T_1 energy gap retained throughout crystal-phase S_1 optimisation. Moreover, the oscillator strength remains non-negligible in the minimum-energy conformation of the crystal S_1 state. In contrast, the oscillator strength is diminished to essentially zero following torsion in the vacuum optimisation. Ultimately, the (simulated) loss of additional reorganisation energy from the suppressed torsional degrees of freedom raises the S_1 energy relative to that of S_0/T_1 at an emissive geometry featuring enhanced S_1-S_0 oscillator strength.

Electronic polarisation in the crystal

Due to a more pronounced dipole moment in the ground-state electronic configuration, the polarisation energy from the surrounding CMA1 environment also leads to blueshifted emission. The polarisation energy was simulated in molecular clusters extracted from the crystalline phase and a full quantum-chemical model was adopted, combining the Tamm-Dancoff-Approximate Time-Dependent Density Functional Theoretical (TDA-DFT) framework with a long-range asymptotically correct LC-ω-PBE tuned DFT functional.[162–164] It is indeed critical to include the dynamic (electronic) polarisation response of the 'solute' to the varying ground- or excited-state charge distribution of the surrounding 'solvent' and this requires either a polarisable classical force-field or a full quantum treatment, which is preferred here. The TDA-DFT/LC-ω-PBE results in Table 5.3 agree with experiment on two major fronts. First, the emission-energy result in the vacuum phase (1.92 eV, 646 nm) bounds the experimental dilute-solution emission energy from below, understandable in light of the destabilising effect a polarisable solvent has on emission relative to having no polarisable environment at all. Second, the computed blueshift in the crystal emission energy (2.84 eV, 436 nm) of 0.92 eV positions the crystal emission spectrum within the blue colour range as observed experimentally.

System/Geometry	Emission energy (eV)	Emission energy (nm)	Emission colour
Crystal / S_1	2.84	436	Dark blue
Vacuum / S_1	1.92	646	Reddish orange

Table 5.3 Emission Energy and colour in the simulated crystal phase compared to vacuum at the TDA(LC-ω-PBE/def2-SVP) level of theory. The simulation was performed by Dr. Elliot Taffet.

The amorphous phase

In between the crystal and solution results is the amorphous-phase emission peak energy that can be thought of as emission from an ensemble of rotamers due to the conformational disorder inherent to kinetic, rather than thermodynamic, control of this phase. Here, force-field Molecular Dynamics (MD) simulations were used to sample the conformational space explored by the molecules in a completely amorphous solid. Room-temperature MD simulations suggest that the molecules can adopt a broad distribution of torsion angles in the ground state, directly reflecting the inhomogeneous environment and lower density of the amorphous phase ($\sim$1.37 g/cm^3, compared to 1.53 g/cm^3 in the crystal). Excited-state geometric relaxation was performed considering the limiting cases of either orthogonal or coplanar orientations. The corresponding lower and upper bounds of the broadened S_1 amorphous-phase emission can then be straightforwardly ascertained by considering spherical clusters of physically reasonable density surrounding a central embedded molecule constrained to that conformation. The simulation results indicate that these extrema, computed to be at 2.38 eV for the orthogonal orientation and 2.76 eV for the coplanar orientation, fill the gap between the solution- and crystal-phase emission peak energies. The slightly smaller transition energy (2.76 v.s 2.84 eV) obtained for the planar molecule in the amorphous versus crystalline films provides a direct measure for the reduced electrostatic stabilisation associated with the lower density in the amorphous phase. From these simulations, it is apparent that a combination of geometric (conformational) control and enhanced polarisation energy in the ordered crystalline phase lead to the most pronounced photoluminescence blueshift. We note that the extent of polarisation-induced S_1-S_0 energetic blueshift determines the viability of S_1-T_{Cz} population transfer, where T_{Cz} is the carbazole-centred LE triplet state, since polarisation pushes the S_1 state closer in energy to the marginally affected locally excited triplet that represents T_2 in the quantum-chemical calculations.

Energy landscape for direct and reverse intersystem crossing

Nuclear reorganisation in the crystalline singlet excited state (a 21.5°out-of-plane twist) is found to differ negligibly from that in the crystalline/vacuum triplet excited state (19.5°/26.5°) due to torsional restriction. In other words, the potential minimum of S_1 is pushed closer to that of T_1 in the crystalline phase (averting decreased direct S_1-T_1 spin-orbit coupling). A triplet reorganisation energy for exciton diffusion λ=0.1 eV, taken as half the excitation-energy difference of S_0-T_1 at the ground-state and excited-state geometries, is recovered. This value is in agreement with the experimental result of 0.14 eV and is an anticipated underestimation, given the outstanding nuclear reorganisation in T_1 that is not considered from minimising S_1. It should be mentioned that this reorganisation energy is attributable mostly to intramolecular bond-stretching modes that are active in all environments. Moreover, when considered alongside the similar activation energies measured for crystal-phase and amorphous-phase emission, this result strongly suggests that complete torsional distortion to achieve the largest reorganisation energy of 0.4 eV (as computed for S_1 at the orthogonal minimum-energy geometry) is not necessary for TADF.

Furthermore, not only is such a large-amplitude change in the torsion angle not required but it is also very much undesired, as the direct spin-orbit coupling (SOC) matrix element $\langle S_1|\hat{H}_{SO}|T_1\rangle$ driving RISC is substantial ($\sim$4 cm^{-1}) at the close-to-planar triplet geometry[165, 166], which possesses relatively low symmetry, but decreases by a factor $\sim$20 in the higher symmetry orthogonal configuration[136], in line with theoretical prediction.[133, 144] This dramatic reduction in direct S_1-T_1 SOC is fully consistent with El-Sayed's rule and the fact that the states involved should have different spatial wavefunctions for the total (angular plus spin) momentum to be conserved. This turns out to be the case in the sterically constrained solid-state environments but would not be the case for fully twisted molecules. We thus conclude that a partial twist on the triplet potential leads to reverse intersystem crossing without an energetic spin-state inversion, in line with the theoretical prediction by Föller, Marian and Penfold.[134, 135]

The T_1 reorganisation energy, computed to be 0.1 eV, not only leads to a narrower energy gap between the relaxed T_1 state of the embedded molecule and neighbouring molecular triplets, thereby facilitating triplet diffusion, but also leads to a narrowed gap between the relaxed S_1 state and the T_{Cz} carbazole triplet on the same embedded molecule. As such, we propose a bifurcation of S_1 population into T_1 and T_{Cz} population at the relaxed crystalline S_1 geometry, as summarised in Fig. 5.16. Frustrated nuclear reorganisation and molecular polarisation lead to an S_1 computed emission energy of 2.84 eV, 0.17 eV above the T_1 state (2.67 eV) and 0.26 eV below the T_{Cz} state (3.10 eV). As thermally activated delayed fluorescence in the crystal suggests that a $\sim$0.2 eV energy gap can be surmounted, the likely

reason for isolated T_{Cz} emission in the crystal is kinetic trapping stemming from constrained coplanarity. At the limit of completely hampered torsional distortion, quantum-chemical calculations suggest that T_{Cz} phosphorescence may appear spectrally "uncovered" below the S_1 emission energy. This T_{Cz} state is a local excitation polarised along the carbazole long axis, leading to a large exchange splitting from the ∼305 nm singlet excitation in the solid state.

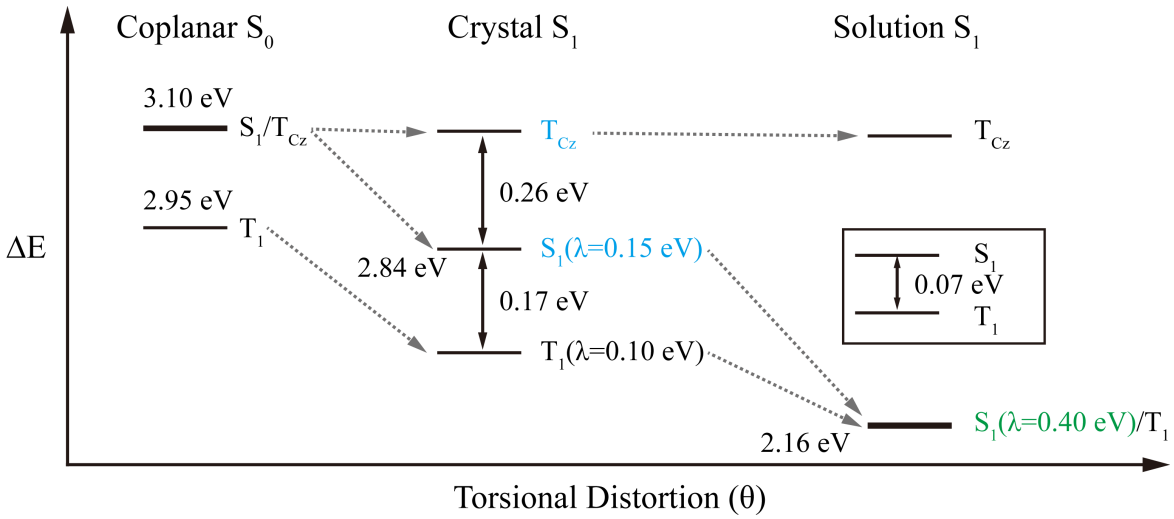

Fig. 5.16 Summary of CMA1 phase-dependent photophysics. At the coplanar S_0 geometry (identical for solution and solid phases), S_1 and T_{Cz} are quasidegenerate, while at the solution S_1 geometry (featuring complete torsional distortion), S_1 and T_1 are quasidegenerate. While the 0.4-eV reorganisation energy of S_1 in solution leads to a large energy gap with respect to the negligibly changed (< 0.1 eV) T_{Cz} state, the smaller 0.15-eV reorganisation energy of the partially rotated S_1 in the crystal leads to a 0.26-eV energy gap with respect to T_{Cz} that is comparable to the T_1-S_1 energy gap of 0.17 eV at this geometry. The state labels have been coloured to reflect the emission energy ranges from these states, where observed experimentally. The inset details the results from multireference orbital optimisation for the non-solid-phase (solution) T_1 geometry of CMA1 in isolation. The values were calculated by Dr. Elliot Taffet.

5.4 Conclusions

In summary, we developed a method to crystallise CMA1 compounds in-situ using a polar, low glass-transition-temperature matrix and achieved nearly complete crystallisation of the entire thin film. Consequently, we are able to explore the impact of molecular geometry in a controlled manner, contrasting intersystem crossing and emission from constrained coplanar geometries with the behaviour of relaxed rotamers. We find that in the crystalline phase,

energetic disorder and the reorganisation energy for triplet diffusion are reduced. Crystallisation also leads to significantly blue-shifted charge-transfer emission. At low temperature, this shift is sufficient to allow observation of structured emission from triplets localised on the carbazole ligand. We explore these results using QM/MM calculations and find that a combination of restricted torsional relaxation and enhanced electrostatic interactions lead to the modification of the ^{1}CT potential such that a more coplanar conformation is computed to be the equilibrium geometry, resulting in a blueshifted emission peak energy. Because quantum-chemical calculations suggest that the thermal activation energy for CT emission in the absence of spectral migration may be attributed to the exchange energy pushing S_1 above T_1 at a more coplanar triplet geometric optimum, the activation energy is not appreciably altered by material phase, that is, spin crossover does not rely on inter-ligand twisting to orthogonality. Similarly, while photo-induced absorption spectra in crystalline, amorphous and solution phases are distinct, the rate of intersystem crossing appears unaffected by the S_1 equilibrium conformation. We therefore infer that the fairly constant activation energy derived from temperature-dependent photoluminescence spectroscopy reflects the fixed exchange splitting inherent to an unmodified, more coplanar T_1 conformational distribution.

Remarkably, we find that at 300 K, emission rates from coplanar crystalline materials are very similar to those observed in the amorphous phase and in isolated, relaxed molecules in solution, despite a 400 meV difference in CT energy. Torsional distortion, in turn, insignificantly impacts the photophysics of TADF organometallics. The real impact comes from an incompletely twisted S_1 distribution of conformers that stabilises T_1, leading to spin-orbit-coupling kinetics that are uniform across CMA1 molecules in different material phases.

Chapter 6

Influence of the Heavy Atom Effect on the Photophysics of Carbene-Metal-Amide Light Emitters

6.1 Abstract

The effect of the heavy metal atom on the photophysics of coinage metal-bridged CMAs is explored through spectroscopical investigations to reveal the coupling mechanism responsible for the communication between the singlet and triplet manifolds. The photophysical properties do not reflect expected trends based upon the heavy atom effect as both direct (^{1}CT$-^3$CT) coupling and spin-vibronic coupling via a local triplet state ^{3}LE are present. The direct ^{1}CT$-^3$CT coupling is the weakest for CMA(Ag), making the spin-vibronic pathway via the ^{3}LE(Cz) state important and the properties more sensitive to the CT$-$LE energy gap than for the Au and Cu-bridged analogues. The measured activation energy represents the exchange energy of the CT state and decreases in an order of CMA(Cu)>CMA(Au)>CMA(Ag), which is also closely related to the C-M-N bond length. These findings reveal that less interference between the CT and LE states and the minimisation of exchange energy are required for developing efficient CMA complexes.

This work was submitted as the manuscript Influence of the Heavy Atom Effect on the Photophysics of Carbene-Metal-Amide Emitters - Jiale Feng, Antti-Pekka M. Reponen, Alexander S. Romanov, Mikko Linnolahti, Manfred Bochmann, Neil Greenham, Thomas Penfold, Dan Credgington.

All the below work was carried out by myself except where stated. Dr. Thomas Penfold and Prof. Mikko Linnolahti performed the quantum-chemical calculations. Dr. Alexander S.

Romanov performed the molecular design and synthesis. Antti-Pekka M. Reponen helped with measuring the CMA(Cu) transient absorption spectrum.

6.2 Introduction

Carbene-metal-amides (CMAs) are a promising family of organometallic donor-bridge-acceptor photoemitters with potential for use in highly efficient light-emitting diodes. The prototype of this family firstly reported in the literature[32] employs a cyclic (alkyl)(amino)carbene (CAAC) acceptor and a carbazole (Cz) donor bridged by a coinage metal atom. Gold-bridged CMA emitters have been investigated in detail,[32, 132, 148, 167] and the other two coinage metals, Cu and Ag-bridged CMAs have also been demonstrated in OLED devices.[112, 130, 131, 136] However, the influence of spin-orbit coupling (SOC) provided primarily by the two-coordinate d^{10} coinage metal has not been explored experimentally. We have previously shown that direct SOC between singlet and triplet charge-transfer (CT) states is implicated in gold-bridged coinage metal variants,[133] in contrast with many prevailing models for SOC in organic TADF archetypes.[57, 59, 168, 169] Here we explore the influence of the heavy atom effect on the emission kinetics of CMAs.

We have shown that the charge-transfer (CT) states of gold-bridged CMAs can be shifted by around 210 meV relative to the ligand-centred locally-excited (LE) states through electrostatic interactions with host molecules in a solid matrix.[133] We use this method for tuning the CT$-$LE energy gap to provide a direct experimental probe of the coupling mechanism in these coinage metal-bridged CMAs.

We find that the strength of direct SOC between ^{1}CT$-^3$CT reduces in the order CMA(Cu) > CMA(Au) > CMA(Ag) as a result of both decreased d-orbital contribution to the HOMO and LUMO and the decreased heavy metal effect. However, the spin-vibronic coupling between ^{3}CT and ^{1}CT via an intermediate state localised in the ligand (^{3}LE) does not vary significantly among the coinage metal CMAs. Spin-vibronic coupling become more important as the direct SOC strength drops, making the photophysical properties of CMA(Ag) very sensitive to the CT$-$LE energy gap. In contrast, for CMA(Au) and CMA(Cu), we find that the direct SOC between CT states remains the dominant effect, with activation energies insensitive to the CT energy.

6.3 Results and discussion

6.3.1 Coinage metal CMA molecules

The chemical structures of coinage metal CMAs are illustrated in Fig. 6.1. The highest occupied molecular orbital (HOMO) and the lowest unoccupied molecular orbital (LUMO) of three CMAs are shown in Fig. 6.2, calculated by density functional theory (DFT) utilising the hybrid MN15 functional with the def2-TZVP basis set. For all three CMAs, a large ground-state electrostatic dipole moment of around 15 D aligned along the carbene carbon (C)-metal (M)-amide nitrogen (N) axis is observed arising from the electron-deficient CAAC group and the electron-rich Cz group. Natural transition orbitals (NTO) of the S_0 to S_1 excitation are 98% HOMO-to-LUMO transition. The S_1 state therefore has significant charge-transfer (CT) character, shifting electron density back from the amide to the carbene group. This reduces the electrostatic dipole moment to around 5 D and reverses its sign.[32, 140] This unusually large ground-state dipole and decreased excited state dipole are critical for upshifting the CT energy and probing the coupling mechanism of intersystem crossing (ISC).[133]

The bond length between the carbene carbon and the amide nitrogen C-M-N differs between three metal atoms, with silver-bridged CMA possessing the longest bond (4.099 Å) and thus the smallest HOMO/LUMO overlap, compared to 3.980 Å in CMA(Au) and 3.773 Å in CMA(Cu).

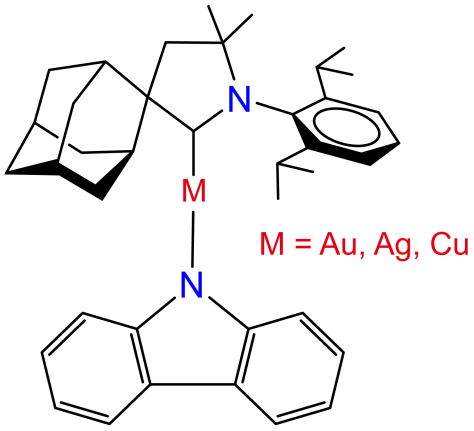

Fig. 6.1 Chemical structure of coinage metal bridged carbene-metal-amide (CMA) photoemitters.

The steady-state absorption spectra of all three emitters in toluene show similarities as shown in Fig. 6.3: direct absorption to the singlet CT state at around 400 nm and ligand-centred excitations of carbene and amide groups at shorter wavelength. The strength of the CT band decreases in the order CMA(Au) > CMA(Cu) > CMA(Ag). CMA(Au) has a

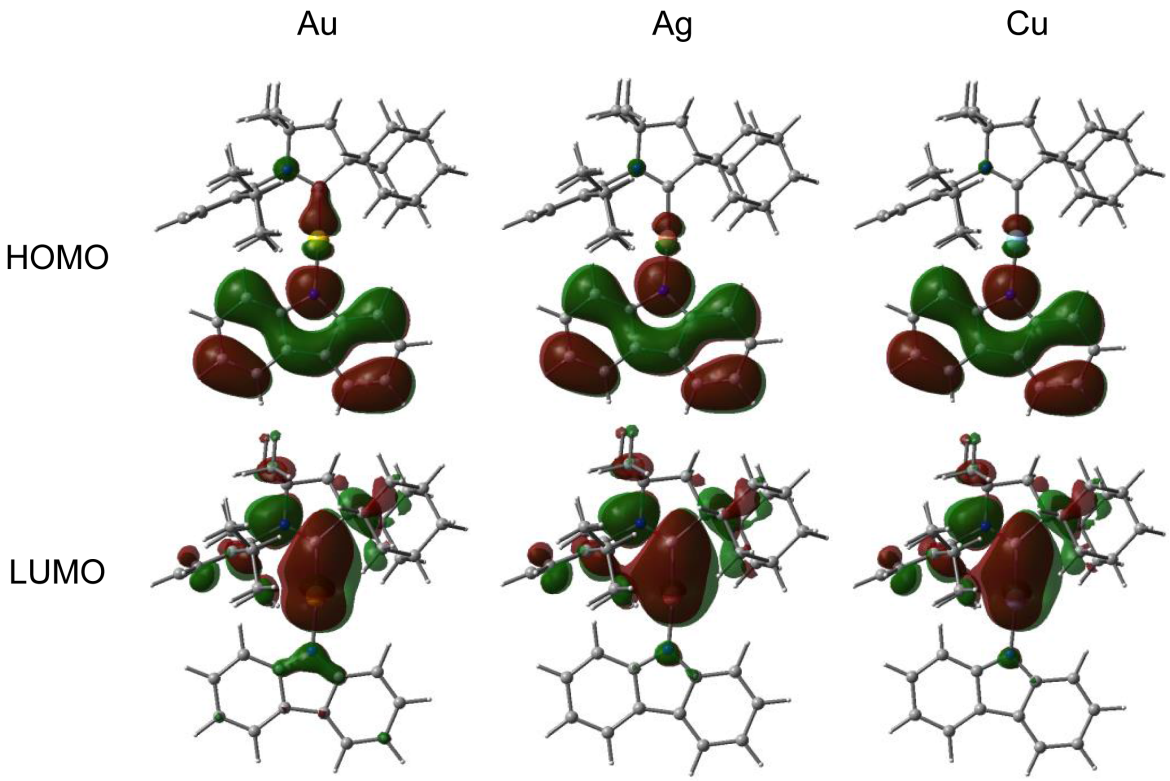

Fig. 6.2 Highest occupied molecular orbital (HOMO) and lowest unoccupied molecular orbital (LUMO) wavefunctions of coinage-metal-bridged CMAs from DFT calculations (MN15 functional/def2-TZVP basis set), red/green corresponds to positive/negative sign of wavefunctions. The calculations were performed by Prof. Mikko Linnolahti.

larger oscillator strength than CMA(Cu).[170] However, the CT band for CMA(Ag) is the weakest because it possesses the longest C-M-N distance, and as a result also a shallower torsional potential around the M-N bond, which makes it easier for CMA(Ag) to become distorted from the co-planar geometry. The increased distance and angle between the donor and acceptor reduces their overlap and thus simultaneously the oscillator strength for the transition.[170] Fig. 6.4 shows that the steady-state emission peaks of CMA(Au), CMA(Ag), and CMA(Cu) in toluene are around 528 nm, 544 nm, and 515 nm respectively at 300 K. These are all broad unstructured spectra consistent with emission from a CT state.

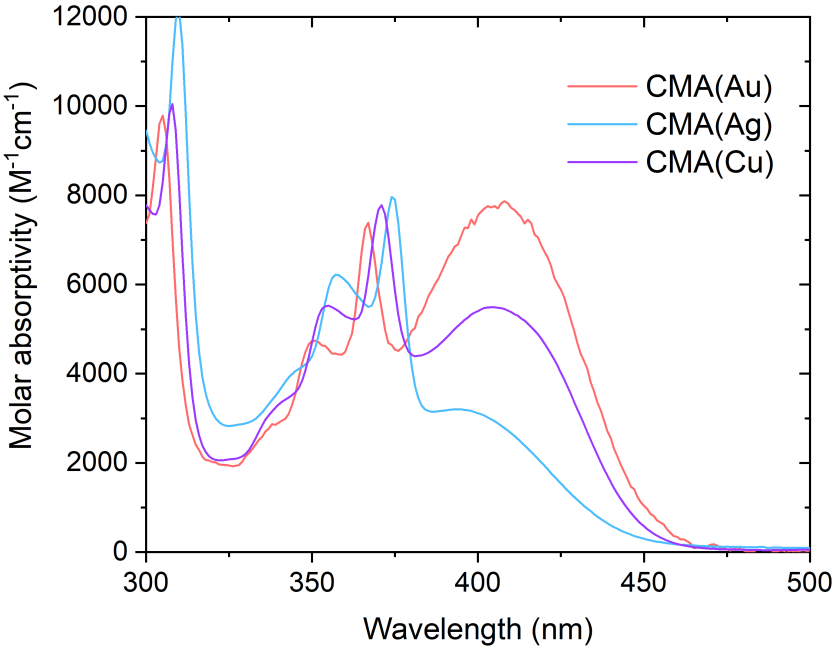

Fig. 6.3 Steady-state molar absorptivity spectra of CMA(Au), CMA(Ag), and CMA(Cu) in toluene at 300 K. Density is 0.5 mg/mL for all solutions. Molar concentration of CMA(Au) is 6.75 $\times 10^{-4}$ M, CMA(Ag) is 7.68 $\times 10^{-4}$ M and CMA(Cu) is 8.23 $\times 10^{-4}$ M. The spectra were measured by Heather Goodwin.

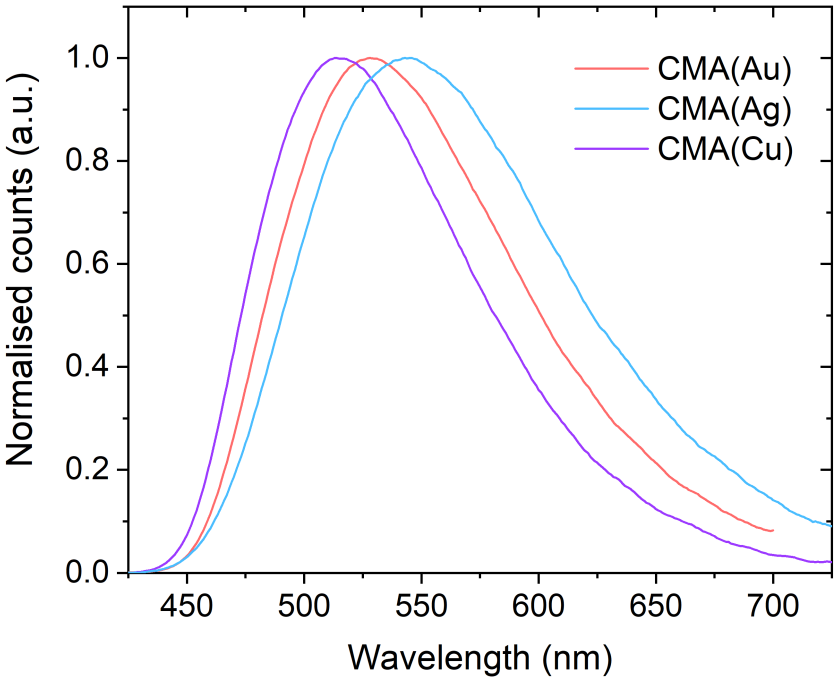

Fig. 6.4 Steady-state photoluminescence spectra of CMA(Au), CMA(Ag), and CMA(Cu) in toluene at 300 K. Density is 0.5 mg/mL for all solutions. Excitation wavelength is 400 nm. The spectra were measured by Heather Goodwin.

6.3.2 Intersystem crossing rate of coinage metal CMAs in a non-polar solid-state matrix

To understand the effect of the metal on the excited state properties of the CMAs, we first measure the intersystem crossing (ISC) time using transient absorption (TA) spectroscopy of dilute solid films, shown in Fig. 6.5. We have previously shown that in both solid state and solution,[32, 133, 170] direct photoexcitation of the CT band for CMA materials populates a short-lived (ps) CT singlet state, which converts to a long-lived (ns-µs) species that shares kinetics with CT emission. We assign this long-lived species to the CT triplet, and consider the interconversion to represent ISC between CT states. Decomposition of the TA maps reveals two dominant independent time-varying species, which are assigned to short-lived singlets and long-lived triplets. The intersystem crossing time is estimated by the crossover of singlet and triplet kinetics, and shown in Fig. 6.5d and 6.6. The ISC time is 6.0 ps for CMA(Au), 32.2 ps for CMA(Ag), and 3.7 ps for CMA(Cu). These solid state measurements contrast with longer ISC times for CMA(Cu) and CMA(Ag) previously reported in dilute solution.[170] In the solid state, ISC is constrained to occur in the photoexcited ground-state geometry for which a coplanar arrangement of the donor and acceptor is preferred, while in solution, ISC occurs during or after relaxation towards the relaxed S_1 geometry (donor and acceptor close to orthogonal).[134, 170] The trend and timescales in dilute solid state are consistent with recent computational results which demonstrated that the rate of ISC for CMA(Ag) was the slowest as SOC between the ^{1}CT$-^3$CT states was smallest, 2.58 cm^{-1}.[170] Moreover, the rapid ISC predicted for CMA(Cu) when compared with the other coinage metal bridges in a similar environment is likewise reproduced.

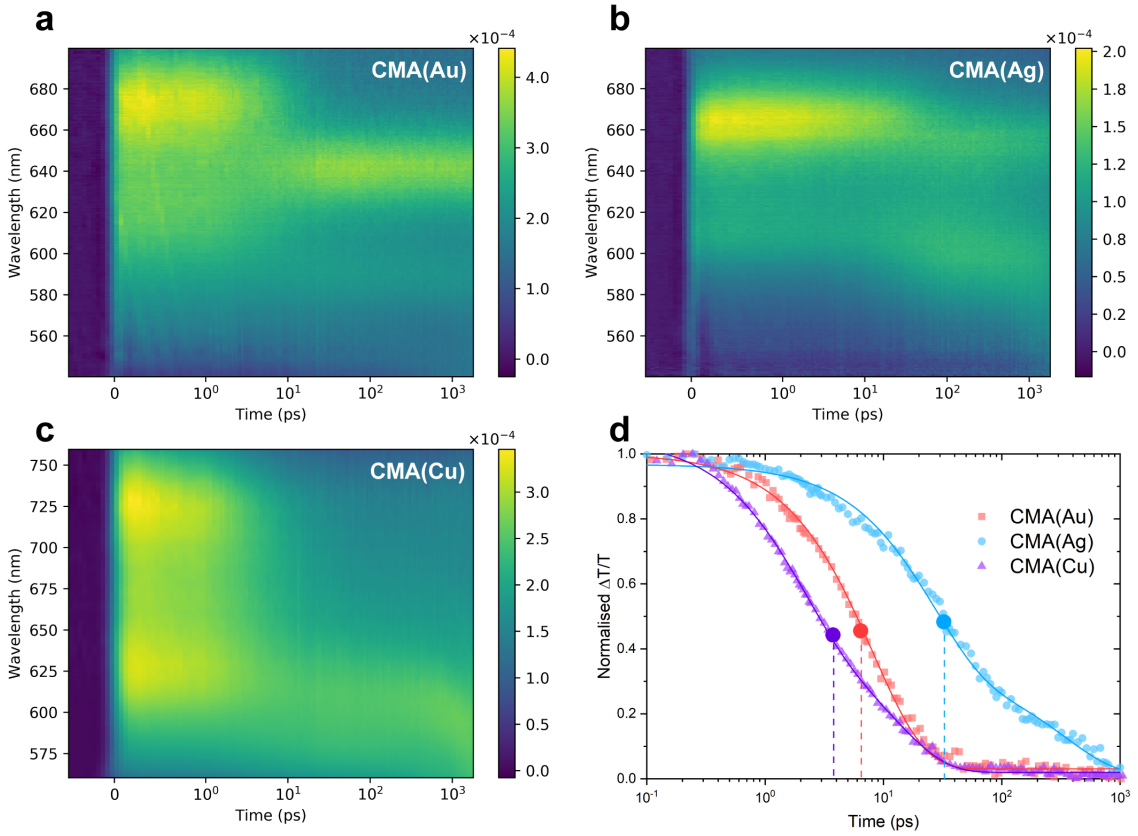

Fig. 6.5 Room temperature transient absorption spectra of (a) 5 wt.% CMA(Au) in PS thin film, (b) 5 wt.% CMA(Ag) in PS thin film, and (c) 5 wt.% CMA(Cu) in PS thin film on picosecond-nanosecond time scales. The intensity is shown in ΔT/T, the fractional change in transmission. Samples were pumped at 400 nm under 50 µW average pump power. (d) presents the normalised decomposed singlet kinetics of CMA(Au), CMA(Ag), and CMA(Cu). The intersystem crossing time of each sample is estimated by the crossover of singlet and triplet kinetics labelled by spots, around 6.0 ps for CMA(Au), 32.2 ps for CMA(Ag), and 3.7 ps for CMA(Cu). Solid lines are a guide to the eye. The triplet growth kinetics is not included for clarity. Full kinetics are shown in Fig. 6.6. Spectral decomposition is achieved by isolating co-varying regions of the TA spectra by iterative application of a genetic algorithm (GA). The full details of this approach is described in references[160, 161]. Singular value decomposition of the TA maps reveals two dominant components. As such, the genetic algorithm was restricted to find two independent time-varying species.

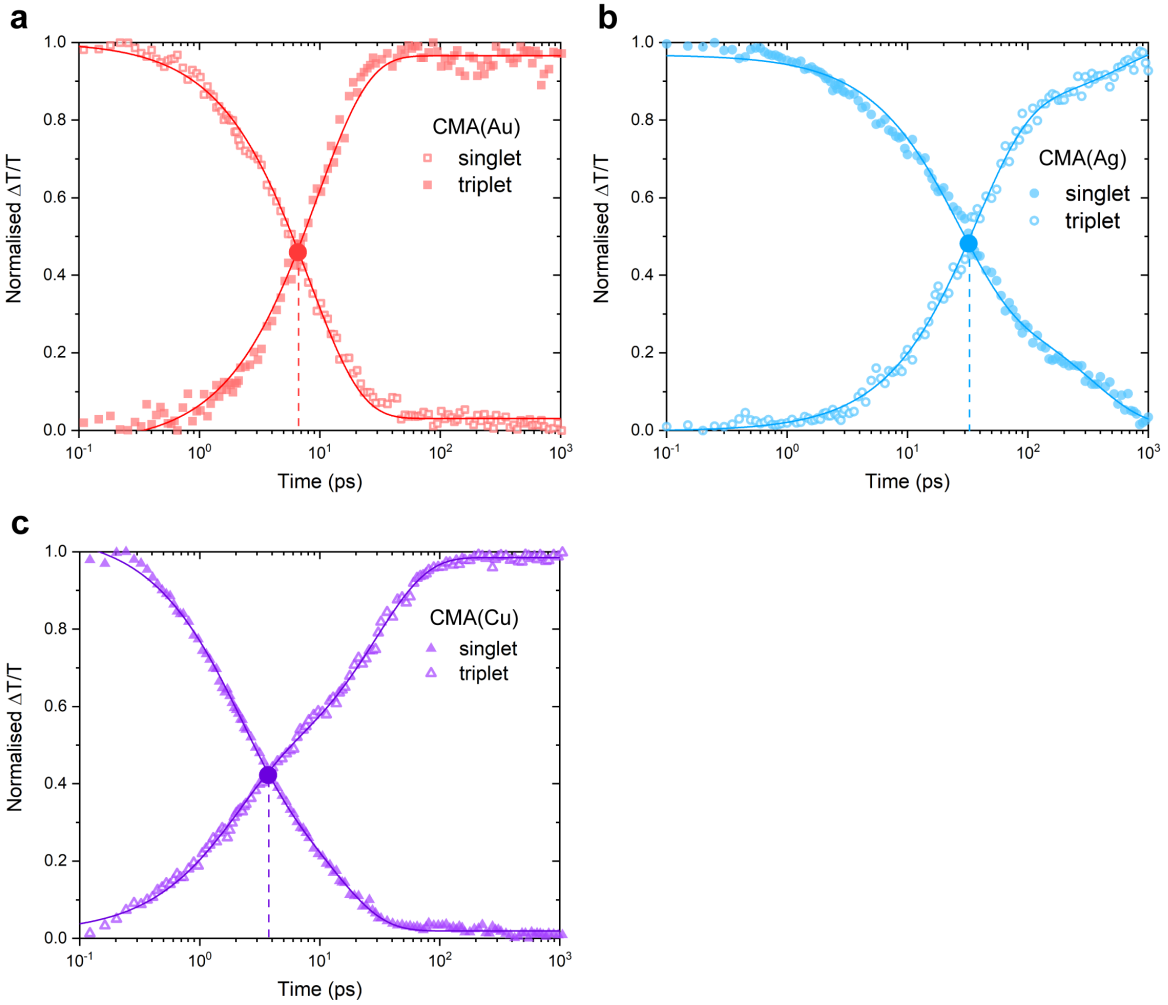

Fig. 6.6 Kinetics of singlet and triplet species decomposed from transient absorption spectra in Fig. 6.5 of (a) 5 wt.% CMA(Au) in PS thin film, (b) 5 wt.% CMA(Ag) in PS thin film, and (c) 5 wt.% CMA(Cu) in PS thin film on picosecond-nanosecond time scales. Singlet and triplet species are both normalised. Solid lines are a guide to the eye. The intersystem crossing (ISC) time of each sample is estimated by the crossover of singlet and triplet kinetics labelled by spots, around 6.0 ps for CMA(Au), 32.2 ps for CMA(Ag), and 3.7 ps for CMA(Cu). Spectral decomposition is achieved by isolating co-varying regions of the TA spectra by iterative application of a genetic algorithm (GA). The full details of this approach is described in reference[160, 161]. Singular value decomposition of the TA maps reveal two dominant components. As such, the genetic algorithm was restricted to find two independent time-varying species.

6.3.3 Photophysical characterisations of coinage metal CMAs in a non-polar solid-state matrix

We first examine doping the emitters in polystyrene (PS), which is considered an electronically and electrostatically inert matrix for photophysical investigations,[171] and therefore will not exert a strong influence on the CMA emitters or shift the CT state energy. Fig. 6.7, Fig. 6.8 and Fig. 6.9 present the steady-state absorption and photoluminescence (PL) spectra of CMA(Cu), CMA(Ag), and CMA(Au) doped into PS host at concentrations from 100% (neat film) to 5% by weight. PL spectra gradually blueshift on dilution, by around 70 meV for CMA(Au), 75 meV for CMA(Cu) and 87 meV for CMA(Ag), which is interpreted as dilution limiting diffusional relaxation through the disordered density of states.[133] The luminescence lifetime of coinage metal CMAs remains relatively constant against concentration in host, with CMA(Ag) the fastest (0.65 ± 0.05 µs), CMA(Cu) the slowest (2.62 ± 0.06 µs), and CMA(Au) in between (1.02 ± 0.05 µs), see Fig. 6.10, Fig. 6.11 and Fig. 6.12. Lifetimes at all concentrations are tabulated in Table 6.1. Note that the dependence of these luminescence lifetimes on bridge atomic number contrasts with that of the ISC times measured using TA. The luminescence rate of all three CMAs in PS is strongly temperature dependent. The cryogenic steady state PL of CMA(Cu) and CMA(Au) remains unstructured, see Fig. 6.13 and Fig. 6.14. We interpret this as indicating that in PS matrix PL primarily arises from CT emission for these compounds at all temperatures. The only difference upon cooling is a slight blueshift in the steady-state PL, which we interpret as due to the restriction of triplet diffusion at low temperature.[133] The luminescence lifetime increases by a factor of 50 for CMA(Au)[133] and 15 for CMA(Cu) at 10 K compared to 300 K. The thermal activation energy extracted from the temperature dependent PL decay rate is of CT emission for CMA(Cu) around 103 meV and CMA(Au) around 75 meV in PS.[133]

In contrast, for the silver-bridged CMA, shown in Fig. 6.16 and Fig. 6.17, the emission spectrum transforms below 150 K and structured emission consistent with triplets localised on the carbazole ligand ^{3}LE(Cz) (shown in Fig. 6.18) appears and begins to compete with the unstructured CT emission in the steady state PL. This drastically increases the luminescence lifetime by a factor of 700 at 10 K compared to 300 K, as ^{3}LE(Cz) is only very weakly dipole-coupled to the electronic ground state.

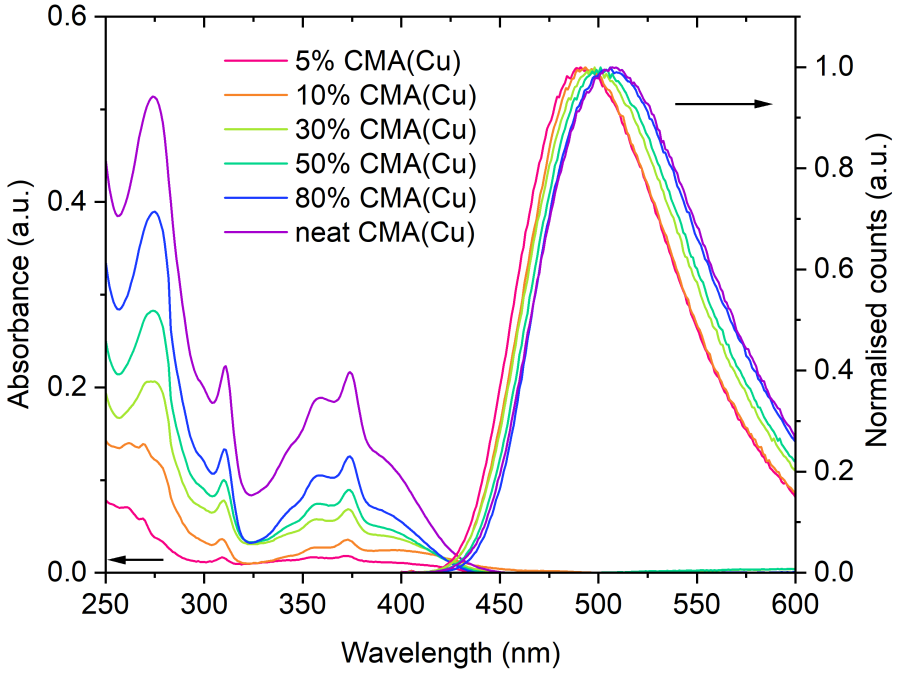

Fig. 6.7 Steady-state absorption and photoluminescence of CMA(Cu) in PS host at different concentrations. Excitation wavelength is 350 nm.

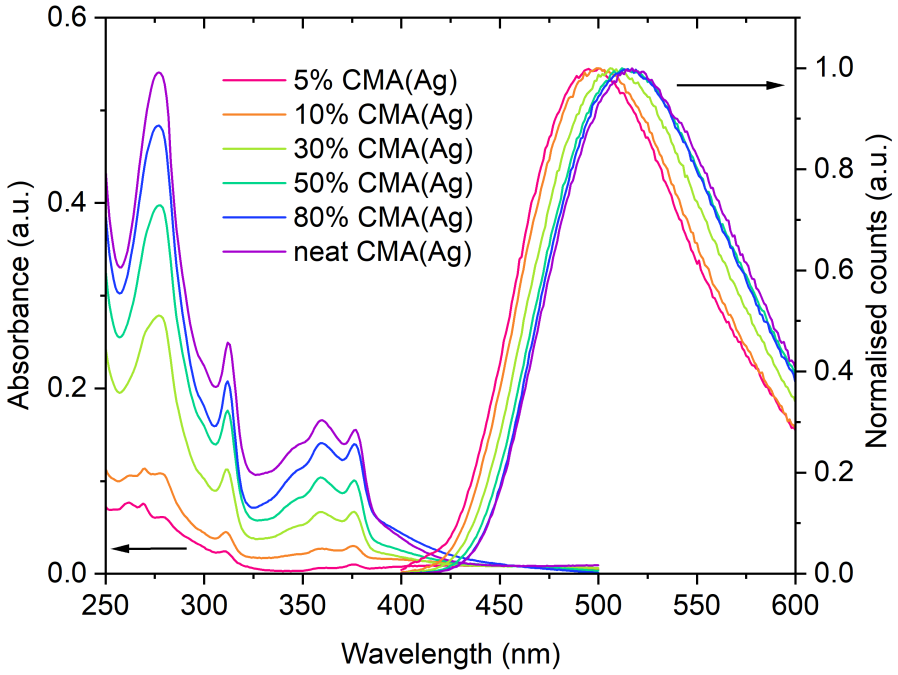

Fig. 6.8 Steady-state absorption and photoluminescence of CMA(Ag) in PS host at different concentrations. Excitation wavelength is 350 nm.

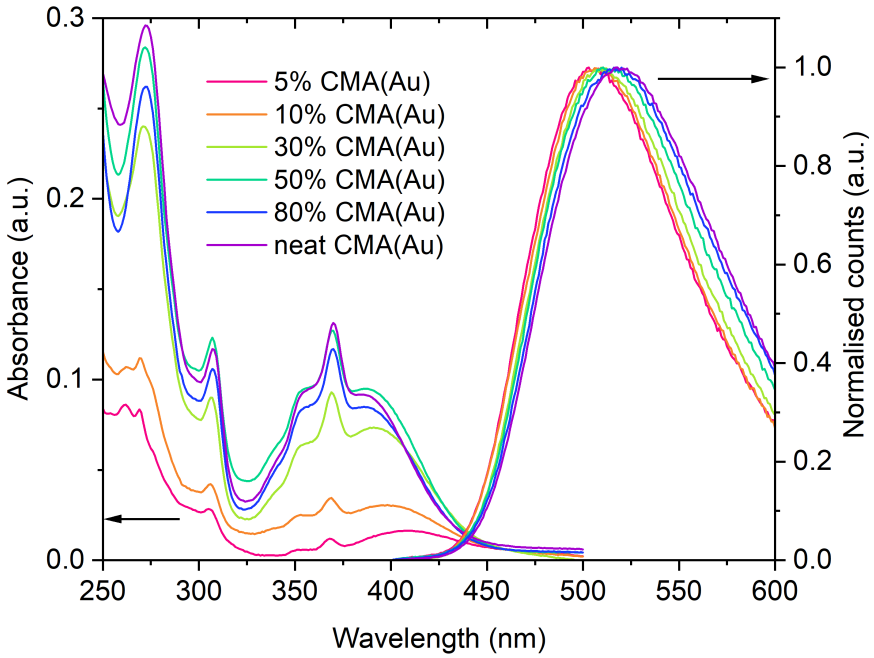

Fig. 6.9 Steady-state absorption and photoluminescence of CMA(Au) in PS host at different concentrations. Excitation wavelength is 350 nm.

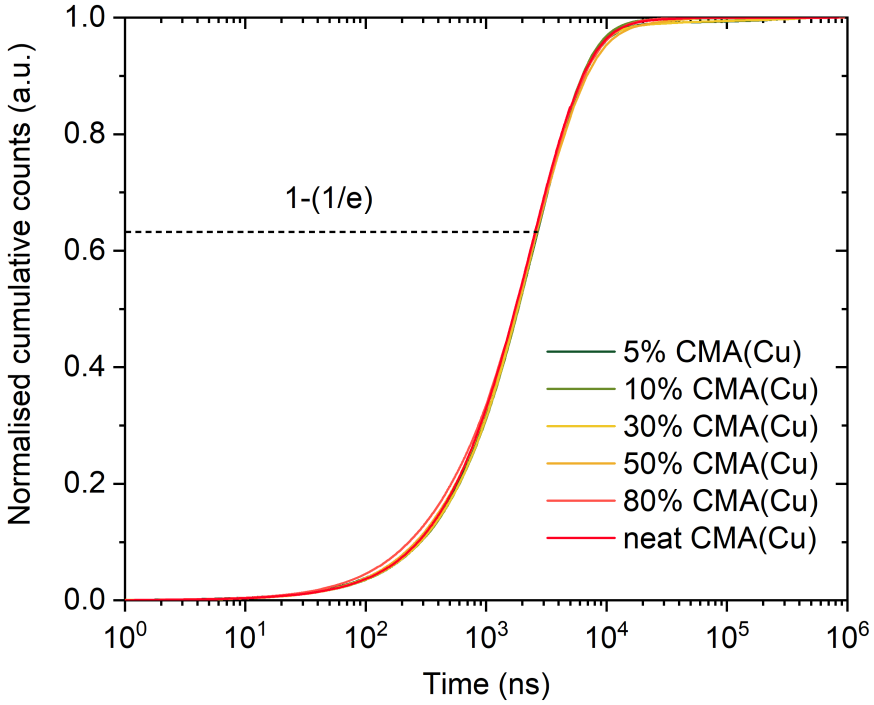

Fig. 6.10 Room temperature emission integral of CMA(Cu) in PS composites, with 1-(1/e) labelled as the characteristic luminescence lifetime.

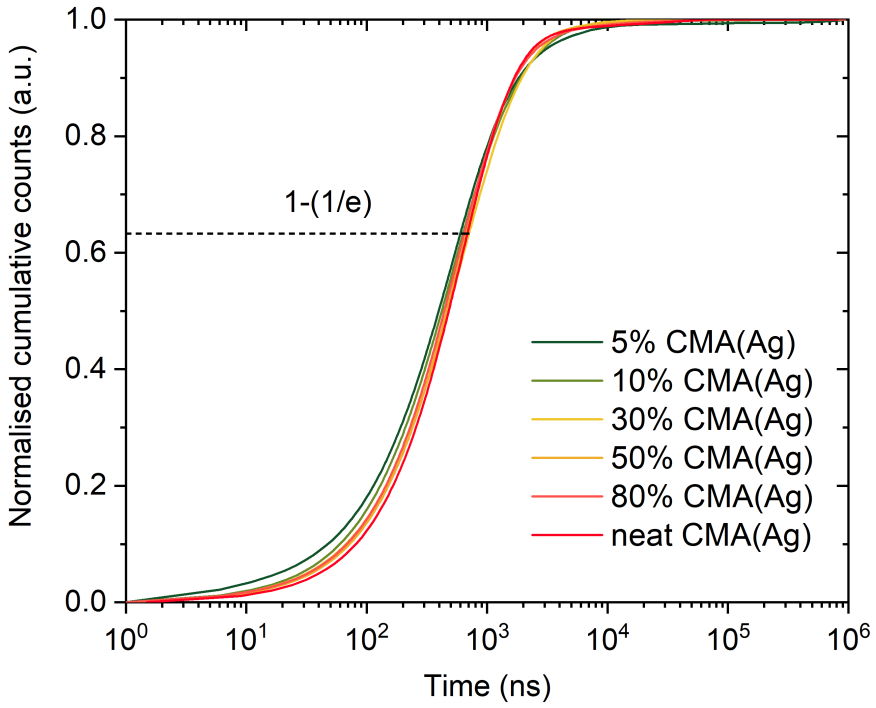

Fig. 6.11 Room temperature emission integral of CMA(Ag) in PS composites, with 1-(1/e) labelled as the characteristic luminescence lifetime.

Luminescence lifetime (ns)	CMA(Au)	CMA(Ag)	CMA(Cu)
5% CMA in PS	1069	598	2675
10% CMA in PS	1035	630	2658
30% CMA in PS	1050	707	2630
50% CMA in PS	1003	673	2634
80% CMA in PS	1067	644	2578
Neat film	970	685	2550

Table 6.1 Luminescence lifetime of CMA(Au), CMA(Ag), and CMA(Cu) in PS host varying concentrations from 5 wt.% to neat CMA films. Luminescence lifetime was measured in vacuum with sample excited by 400 nm laser. Luminescence lifetime was determined by the time when the emission reaches 1-(1/e) of the total time-integrated emission.

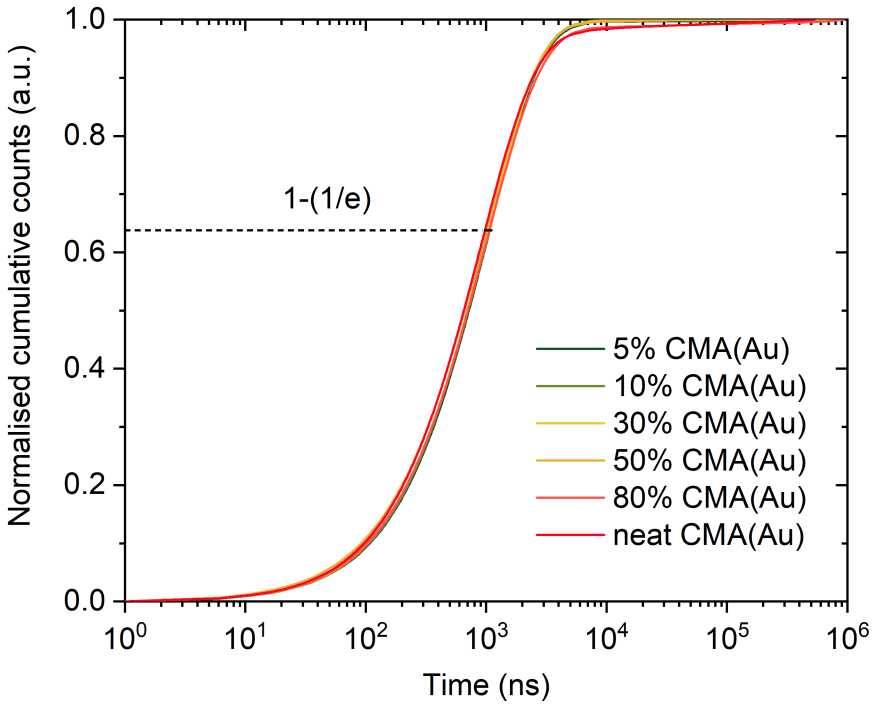

Fig. 6.12 Room temperature emission integral of CMA(Ag) in PS composites, with 1-(1/e) labelled as the characteristic luminescence lifetime.

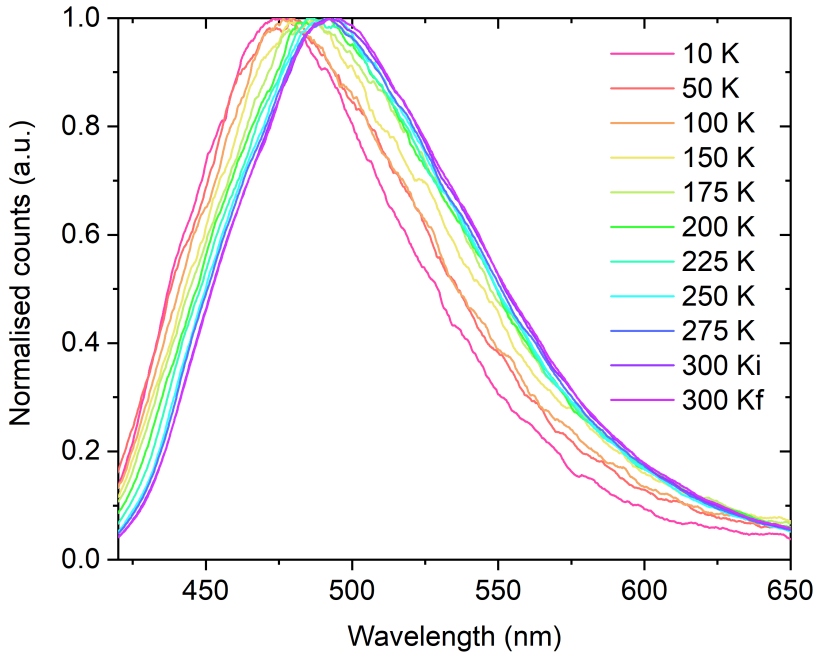

Fig. 6.13 Temperature dependent steady-state photoluminescence of 10% CMA(Cu) in PS thin film. "Initial" data taken at 300 K before cooling the film to 10 K, "Final" data upon warming back to 300 K after low-temperature measurements. Excitation wavelength is 400 nm.

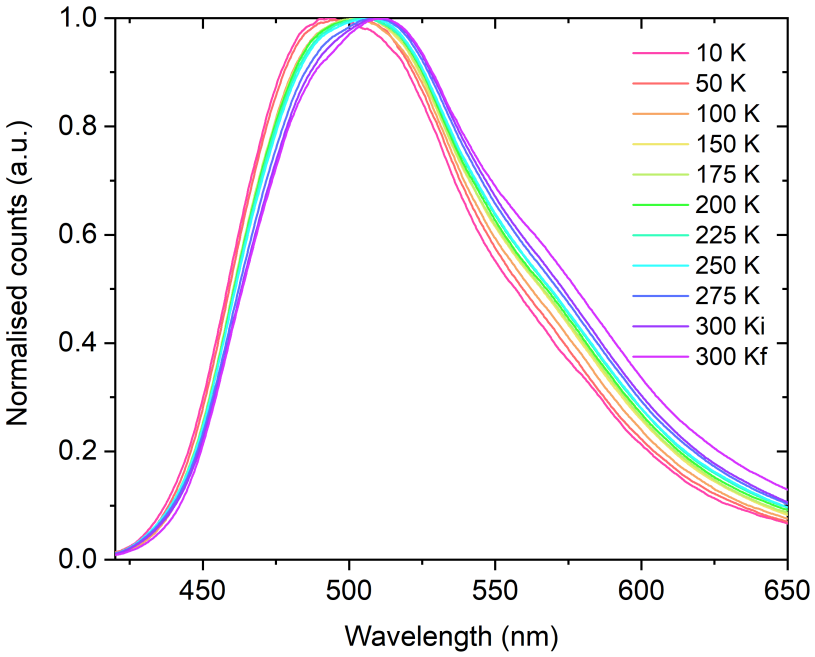

Fig. 6.14 Temperature dependent steady-state photoluminescence of 10% CMA(Au) in PS thin film. "Initial" data taken at 300 K before cooling the film to 10 K, "Final" data upon warming back to 300 K after low-temperature measurements. Excitation wavelength is 400 nm.

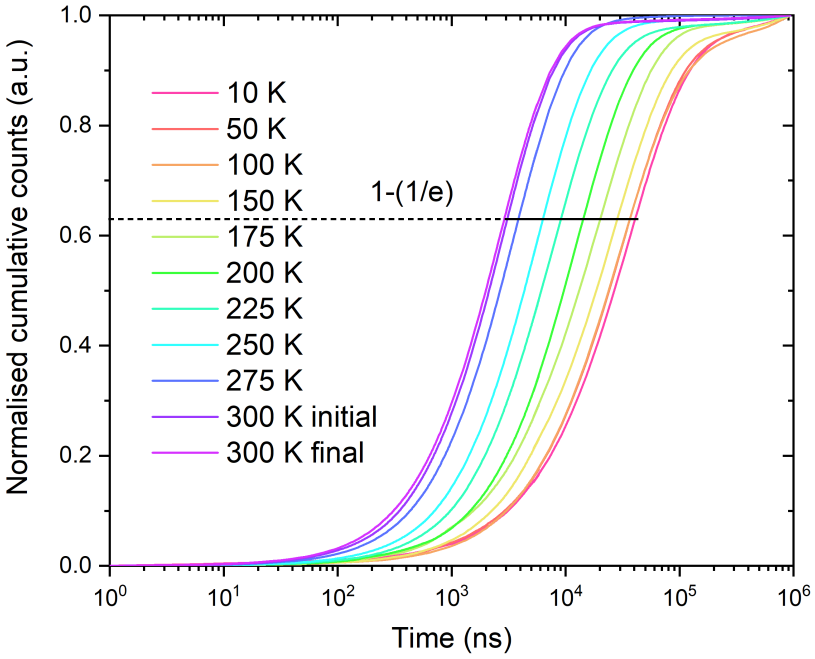

Fig. 6.15 Cryogenic emission integral of 10% CMA(Cu) in PS with 1-(1/e) labelled as the characteristic luminescence lifetime. "Initial" data taken at 300 K before cooling the film to 10 K, "Final" data upon warming back to 300 K after low-temperature measurements.

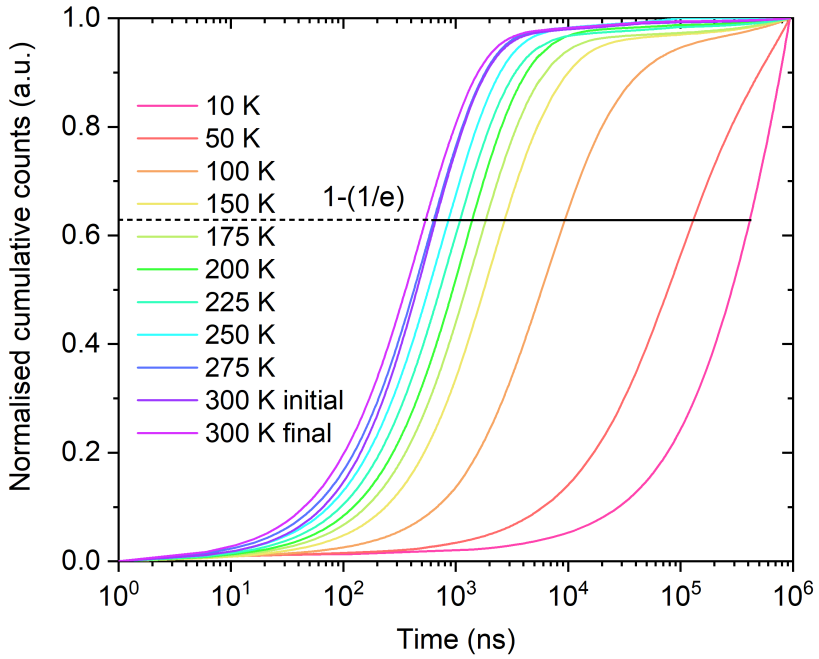

Fig. 6.16 Cryogenic emission integral of 10% CMA(Ag) in PS with 1-(1/e) labelled as the characteristic luminescence lifetime. "Initial" data taken at 300 K before cooling the film to 10 K, "Final" data upon warming back to 300 K after low-temperature measurements.

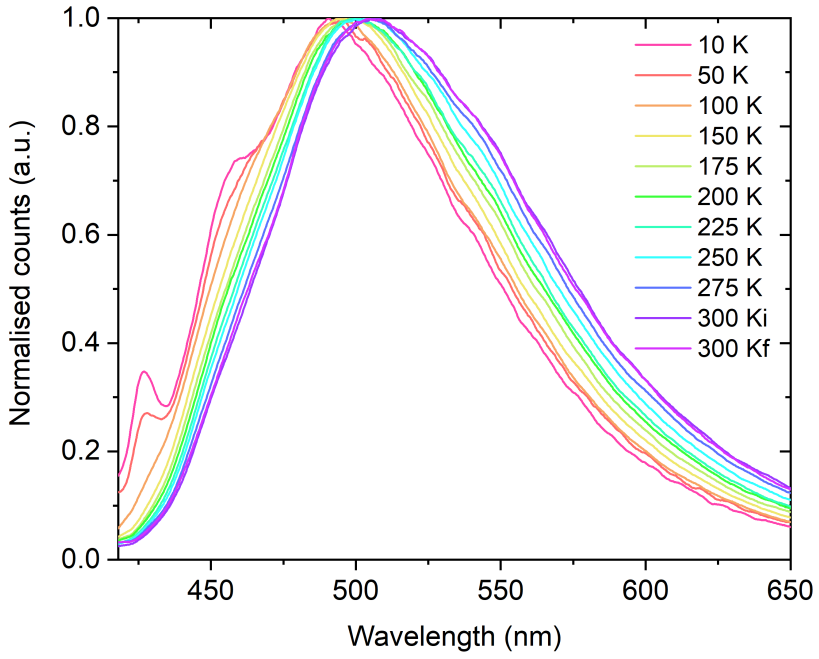

Fig. 6.17 Temperature dependent steady-state photoluminescence of 10% CMA(Ag) in PS thin film. "Initial" data taken at 300 K before cooling the film to 10 K, "Final" data upon warming back to 300 K after low-temperature measurements. Excitation wavelength is 400 nm.

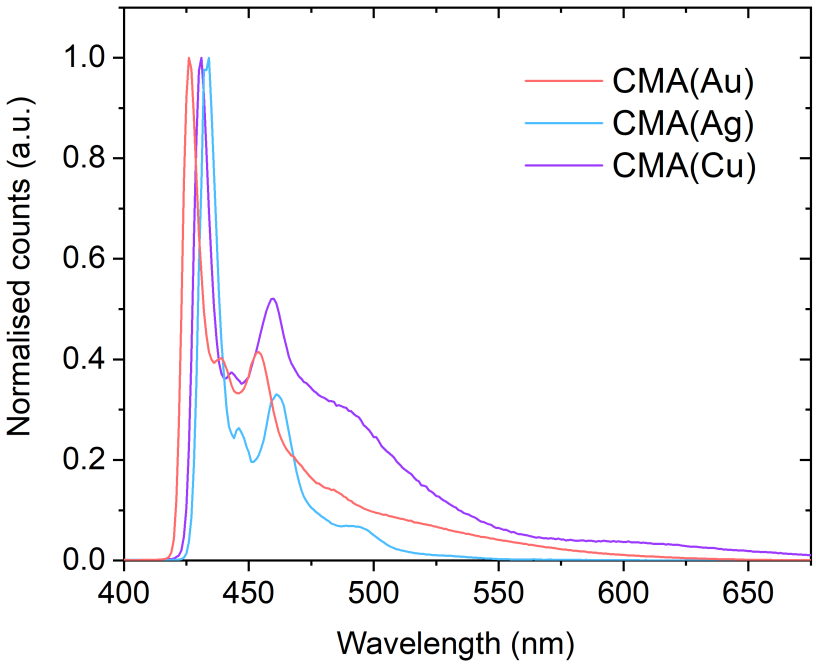

Fig. 6.18 Steady-state photoluminescence of CMA(Au), CMA(Ag), and CMA(Cu) in 2-MeTHF at 77 K. Structured PL is from the triplet localised to the carbazole donor (Cz), denoted as ^{3}LE(Cz). Solutions were deoxygenated and sealed in cuvette. Concentration is 1 mg/mL for all solutions. The peak position is 426 nm, 433 nm, 430 nm for CMA(Au), CMA(Ag), and CMA(Cu) respectively. Excitation wavelength is 350 nm. The spectra were measured by Dr. Alex Romanov.

6.3.4 Photophysical characterisations of coinage metal CMAs with the presence of strong solid-state electrostatic interactions

We have previously shown that strong electrostatic interactions between the CMA emitters and polar host molecules are able to upshift the CT state energies relative to the triplets localised to the carbazole donor ^{3}LE(Cz).[133] The small-molecule host diphenyl-4-triphenylsilyl-phenyl-phosphine oxide (TSPO1) with a large permanent electric dipole moment of 4.1 D is a suitable candidate.[133] Steady state absorption and photoluminescence spectra of CMA(Cu), CMA(Ag), and CMA(Au) in TSPO1 host at various concentrations are shown in Fig. 6.19, Fig. 6.20 and Fig. 4.16, where large PL blueshift is observed: 134 meV, 161 meV, and 210 meV for Cu, Ag and Au-bridged CMA respectively when decreasing the doping concentration from neat films to 5 wt.% CMAs:TSPO1 composite films. In contrast to PS, the luminescence lifetime increases 2.4 times for CMA(Cu) from 2.566 µs (neat film) to 6.156 µs (5%), 7.6 times for CMA(Ag) from 0.598 µs (neat film) to 4.564 µs (5%), and 1.4 times for CMA(Au) from 0.97 µs (neat film) to 1.4 µs (5%), see Fig. 6.21, Fig. 6.22 and Fig. 4.17. These values are tabulated in Table 6.2.

Fig. 6.23 shows the time-resolved emission peak position of CMA(Cu) in TSPO1 as a function of concentration, where the redshift is due to the energy relaxation via the triplet diffusion in the density of states (DOS) of CT state, similar to that previously observed for CMA(Au).[133] By contrast, the emission peak position of CMA(Ag) blueshifts with time at doping concentrations below 50 wt.%, see Fig. 6.24. The reason is that ^{3}CT states with higher energy in the density of states are closer in energy to the ^{3}LE(Cz). Mixing between the CT and ^{3}LE(Cz) prolongs the overall luminescence lifetime since the emission rate from the ^{3}LE(Cz) state is much lower than that of the CT state. The ^{3}CT DOS is energetically broad, and since lower-energy CT triplets mix less with ^{3}LE(Cz), they are observed to emit at earlier times. This admixed PL becomes clearer at low temperature due to the thermally-activated nature of CT emission.

On cooling, the luminescence lifetime of 10% CMA(Cu) in TSPO1 increases by approximately a factor of 7.3, from 6.4 µs at 300 K to 46.8 µs at 10 K, see Fig. 6.25. Low-temperature steady state PL shows that the photoluminescence is still predominantly of CT character above 150 K, but below this, structured features begin to emerge, as shown in Fig. 6.26. The activation energies extracted from the PL decay rate of 10% and 80% CMA(Cu) in TSPO1 host are 103 meV and 105 meV, which are in good agreement with value of 102 meV yielded from 10% CMA(Cu) in PS, see Fig. 6.27. However, activation energies yielded from the integrated PL intensity against temperature are lower than those from the PL decay rate: 70 meV (10% CMA(Cu) in TSPO1), 65 meV (80% CMA(Cu) in TSPO1) and 74 meV (10% CMA(Cu) in PS), see Fig. 6.29. In this case, the key difference between the two

measurements is that the former incorporates non-radiative decay processes, indicating that the non-radiative decay rate in CMA(Cu) has a significant thermally activated component, in contrast to CMA(Au)[133] and consistent with typically lower photoluminescence and electroluminescence quantum efficiency measured at ambient temperature.[32, 129] However, activation energy does not change with the ^{3}CT$-^3$LE(Cz) energy gap, and we thus infer that ^{3}LE(Cz) is not significantly involved in the intersystem crossing in CMA(Cu).

At low temperature, the luminescence lifetime of 10% CMA(Ag) in TSPO1 increases by a factor of 275, from 1.7 µs at 300 K to 466 µs at 10 K, see Fig. 6.30. Low-temperature steady state PL shows a distinct transition from mainly unstructured CT emission to the emission dominated by the structured features from the ^{3}LE(Cz) state (see Fig. 6.18) below 150 K, see Fig. 6.31. This simultaneously transforms the shape of emission integral at low temperature. The emission spectra evolve significantly over time, with unstructured CT emission on ns timescales, and long-lived, higher-energy ^{3}LE(Cz) emission on µs timescales. Spectral evolution over time for 10% CMA(Ag) in TSPO1 at 10 K is shown in Fig. 6.32. In contrast to CMA(Au) and CMA(Cu), the activation energies yielded from the PL decay rate for CMA(Ag) are dependent on the ^{3}CT$-^3$LE(Cz) energy gap: 39 meV for 10% CMA(Ag) in PS, 40 meV for 80% CMA(Ag) in TSPO1 and 114 meV for 10% CMA(Ag) in TSPO1, see Fig. 6.33. While we consider the former two measurements to represent the thermal activation in the absence of significant interference of a nearby ^{3}LE(Cz) state, consistent with other reports,[130] the latter measurement represents a regime with strong interference between CT and ^{3}LE(Cz) states. For CMA(Ag), the integrated PL intensity does not show a simple thermally-activated growth, which indicates that non-radiative decay in CMA(Ag) is significantly thermally activated. This is consistent with the relatively low luminescence quantum efficiency and electroluminescence quantum efficiency reported for Ag compounds vs Au analogues.[112, 130]

Luminescence lifetime (ns)	CMA(Au)	CMA(Ag)	CMA(Cu)
5% CMA in TSPO1	1400	4530	8236
10% CMA in TSPO1	1330	3359	7262
30% CMA in TSPO1	1190	3280	4693
50% CMA in TSPO1	1180	1729	4216
80% CMA in TSPO1	1010	1062	3758
Neat film	970	685	2550

Table 6.2 Luminescence lifetime of CMA(Au), CMA(Ag), and CMA(Cu) in TSPO1 host varying concentrations from 5 wt.% to neat CMA films. Luminescence lifetime was measured in vacuum with the sample excited by 400 nm laser. Luminescence lifetime was determined by the time when the emission reaches 1-(1/e) of the total time-integrated emission.

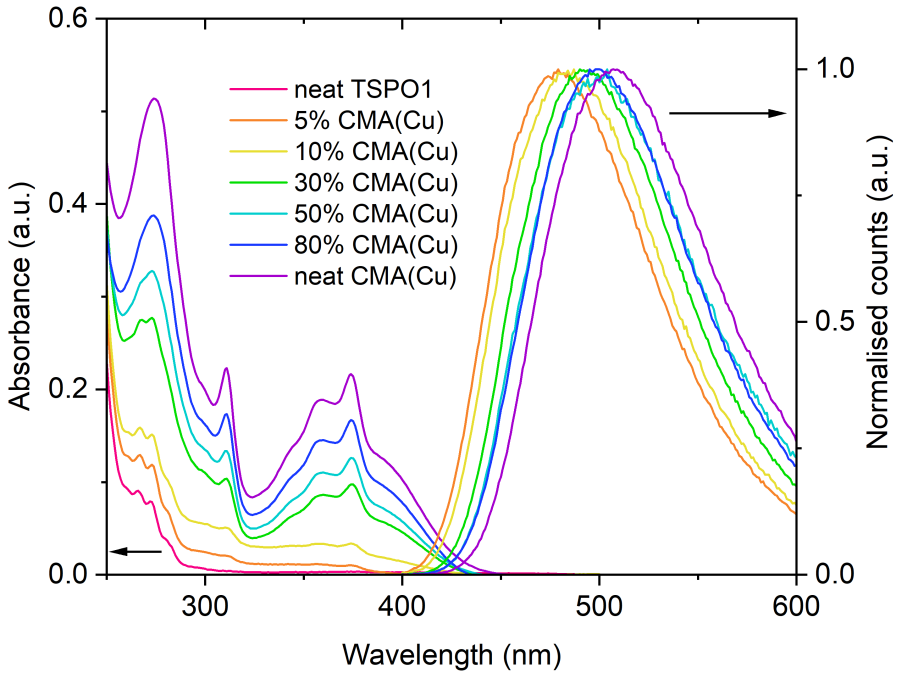

Fig. 6.19 Steady-state absorption and photoluminescence of CMA(Cu) in TSPO1 host at different concentrations. Excitation wavelength is 350 nm.

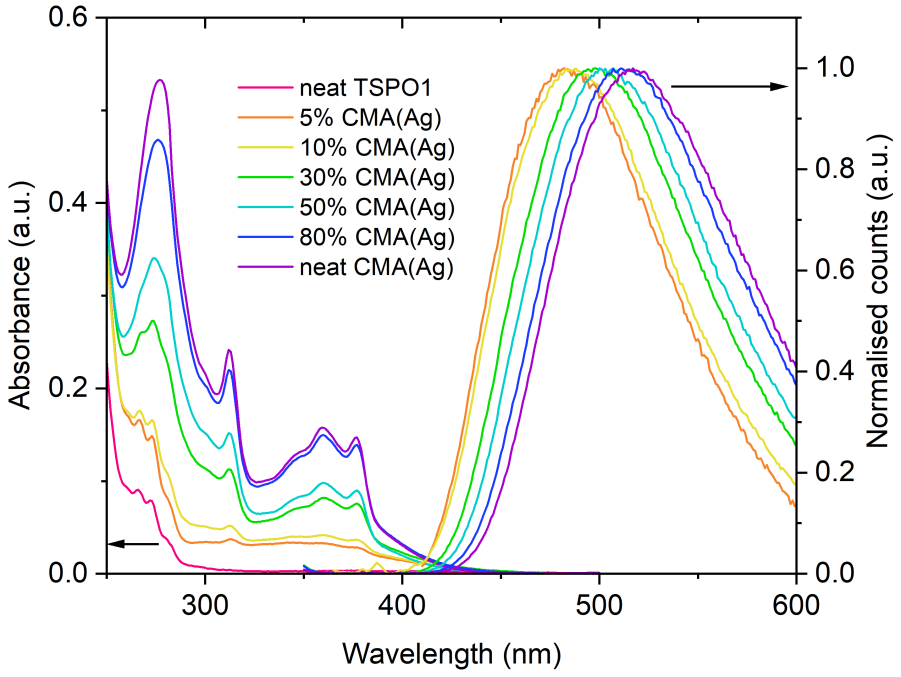

Fig. 6.20 Steady-state absorption and photoluminescence of CMA(Ag) in TSPO1 host at different concentrations. Excitation wavelength is 350 nm.

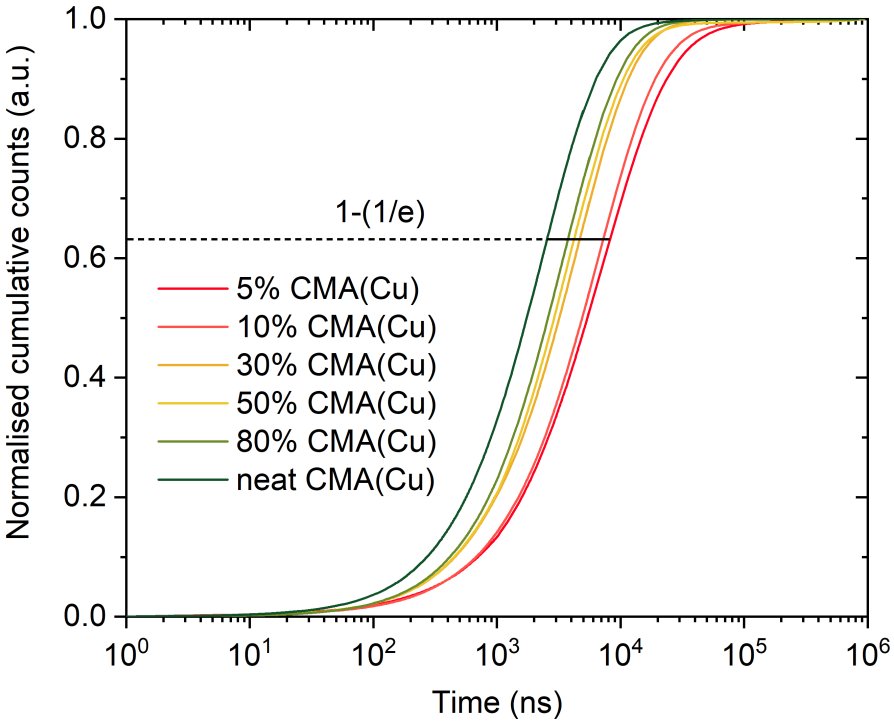

Fig. 6.21 Room temperature emission integral of CMA(Cu) in TSPO1 composites, with 1-(1/e) labelled as the characteristic luminescence lifetime.

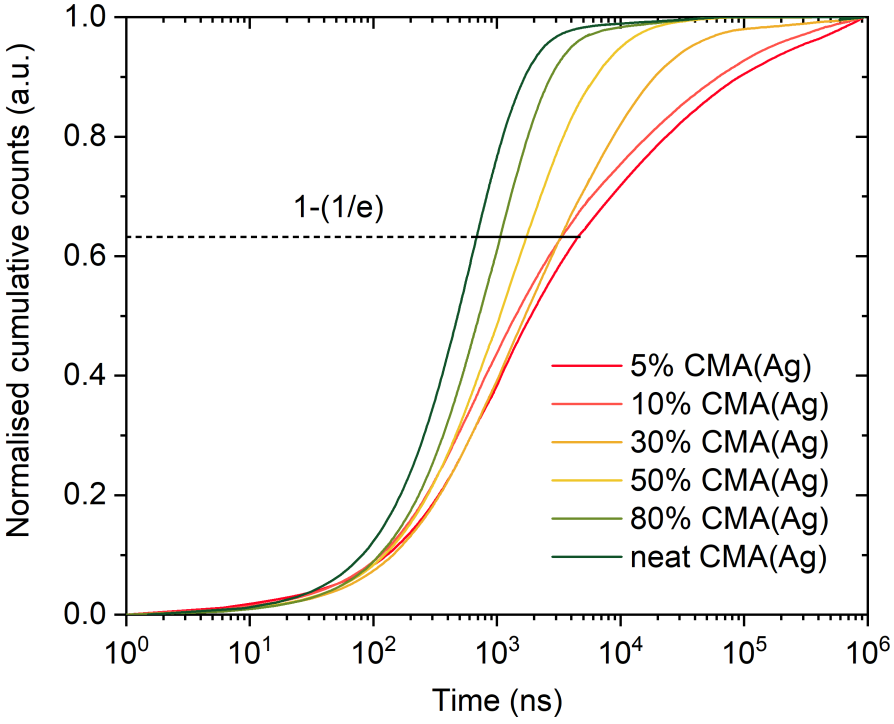

Fig. 6.22 Room temperature emission integral of CMA(Ag) in TSPO1 composites, with 1-(1/e) labelled as the characteristic luminescence lifetime.

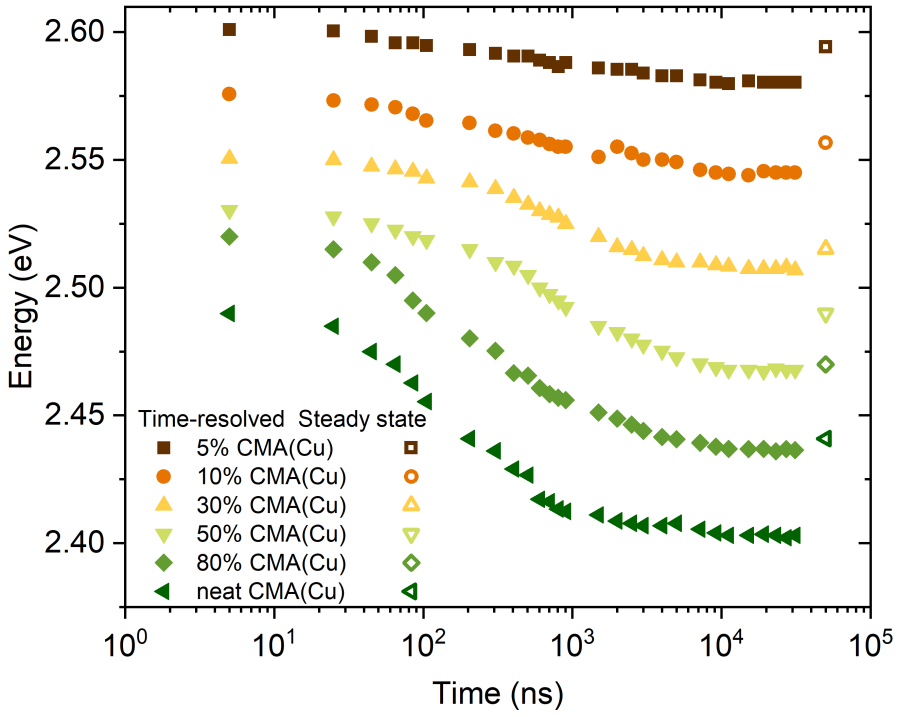

Fig. 6.23 Room temperature time-resolved PL peak energy of CMA(Cu) in TSPO1 at different concentrations to track the spectral diffusion.

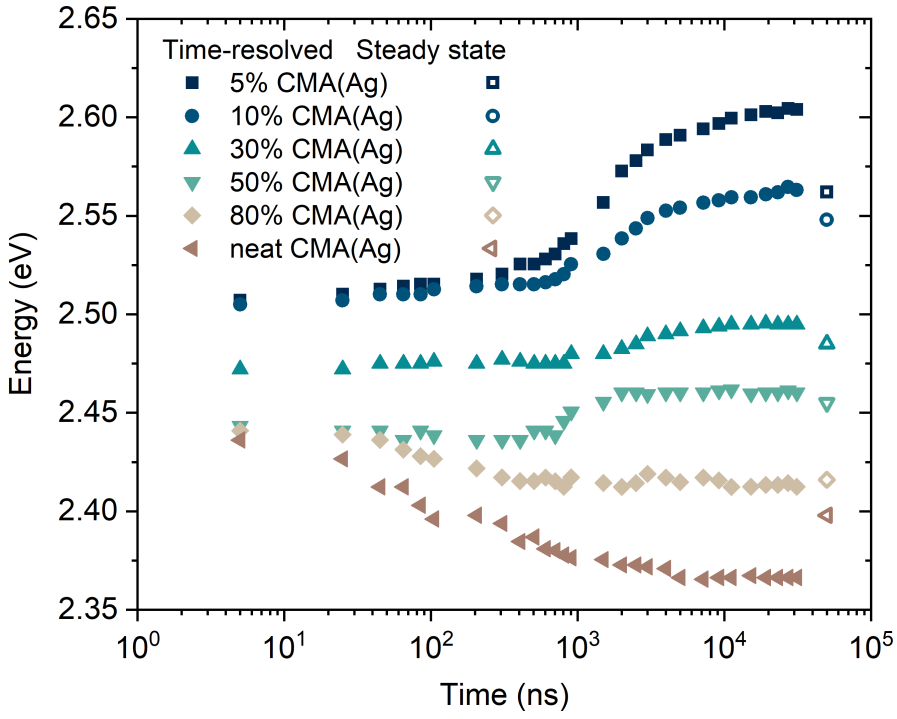

Fig. 6.24 Room temperature time-resolved PL peak energy of CMA(Ag) in TSPO1 at different concentrations to track the spectral diffusion.

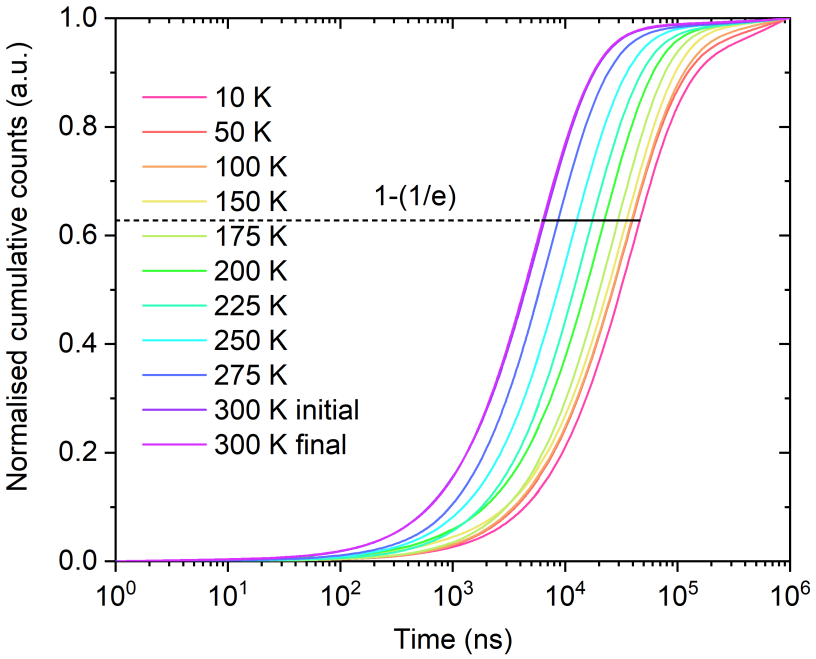

Fig. 6.25 Cryogenic emission integral of 10% CMA(Cu) in TSPO1 with 1-(1/e) labelled as the characteristic luminescence lifetime. "Initial" data taken at 300 K before cooling the film to 10 K, "Final" data upon warming back to 300 K after low-temperature measurements.

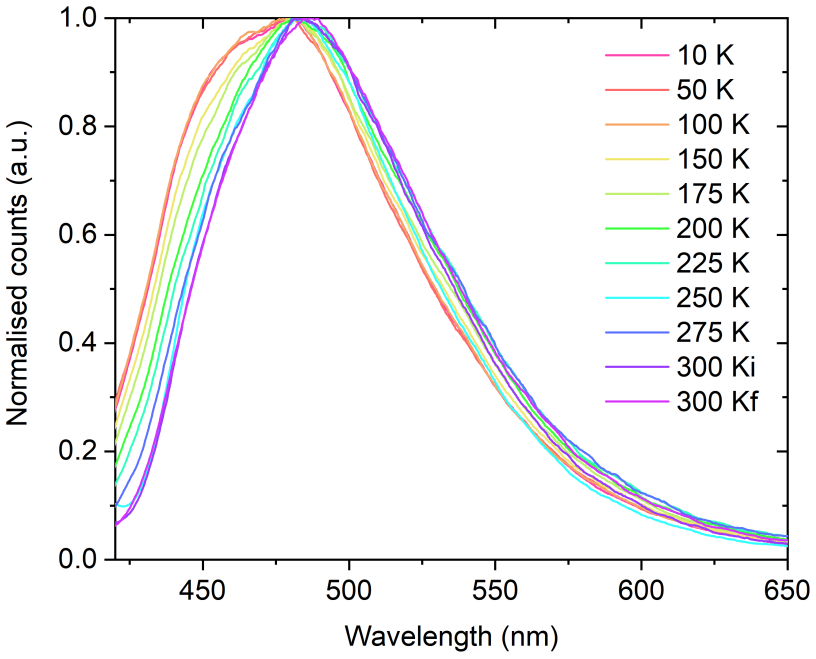

Fig. 6.26 Temperature dependent steady-state photoluminescence of 10% CMA(Cu) in TSPO1. "Initial" data taken at 300 K before cooling the film to 10 K, "Final" data upon warming back to 300 K after low-temperature measurements. Excitation wavelength is 400 nm.

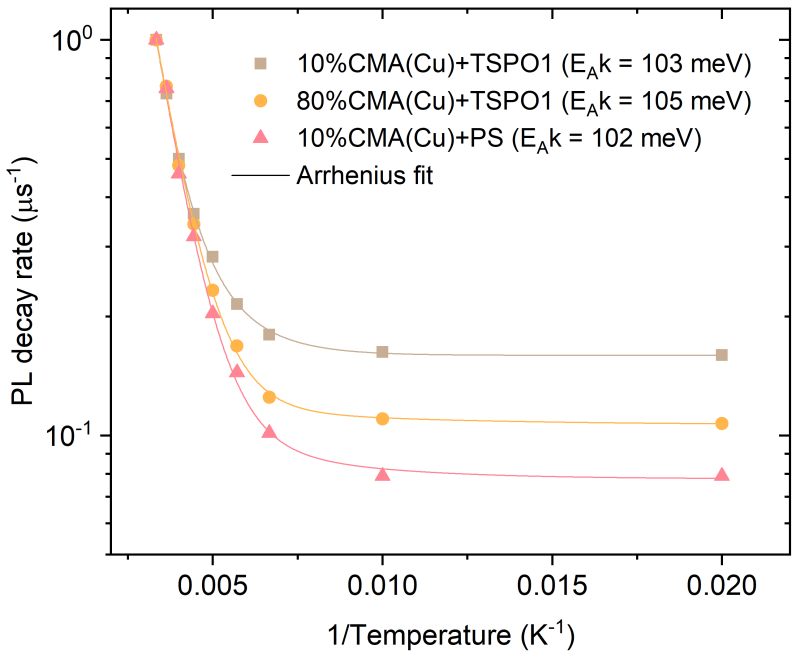

Fig. 6.27 PL decay rate of 10% and 80% concentration of CMA(Cu) in TSPO1 and 10% in PS at different temperatures as a function of 1/Temperature. PL decay rate is the reciprocal of the characteristic luminescence lifetime from the cryogenic emission integral. The activation energies E_Ak are yielded from the Arrhenius fit.

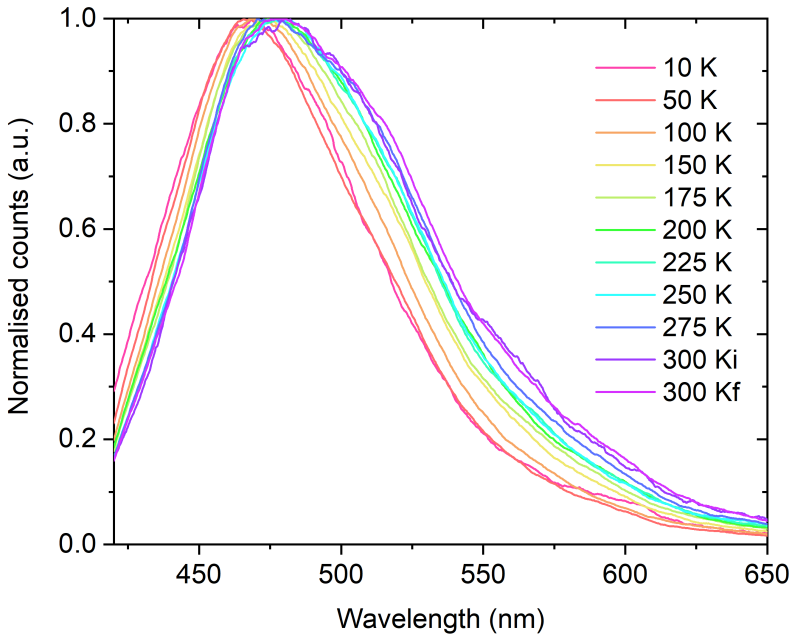

Fig. 6.28 Temperature dependent steady-state photoluminescence of 10% CMA(Au) in TSPO1. "Initial" data taken at 300 K before cooling the film to 10 K, "Final" data upon warming back to 300 K after low-temperature measurements. Excitation wavelength is 400 nm.

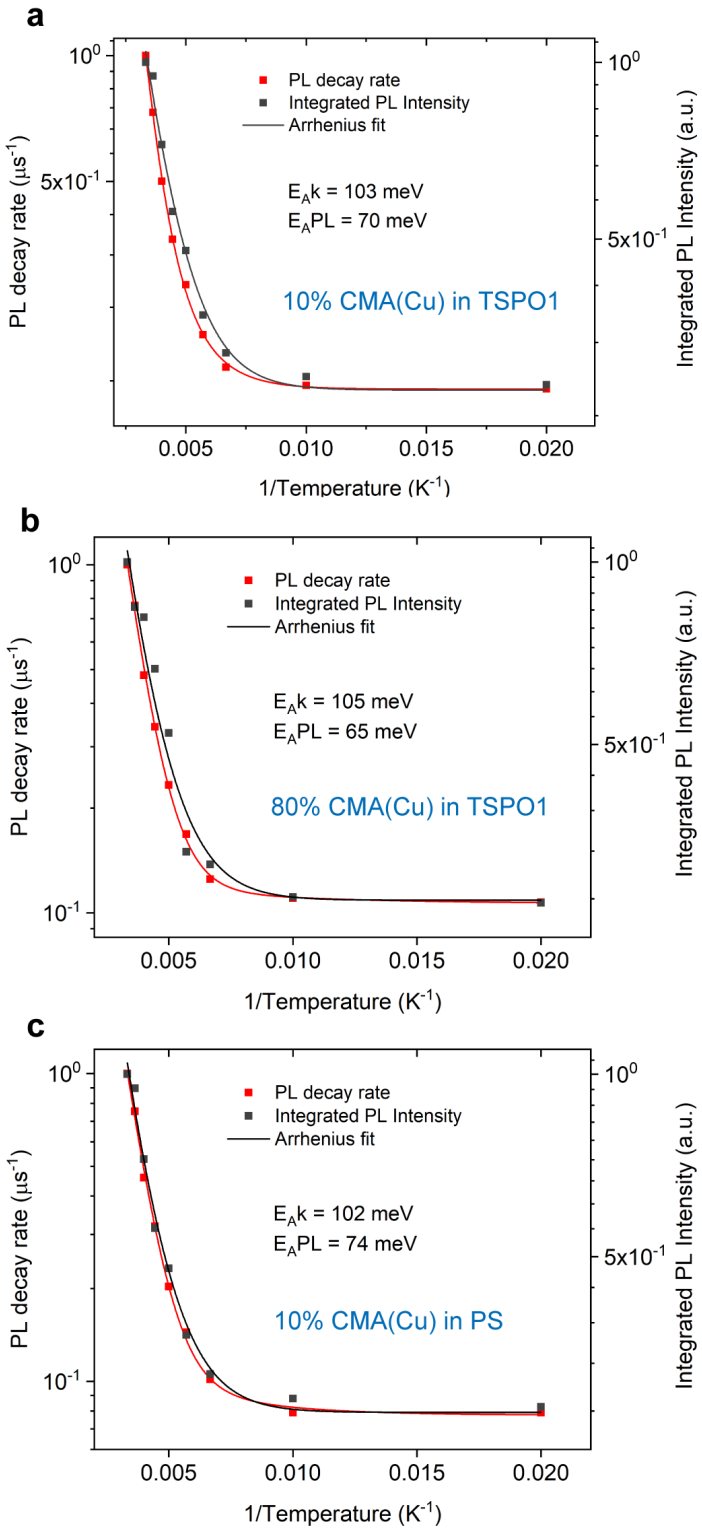

Fig. 6.29 PL decay rate and integrated PL intensity plotted against temperature of 10% and 80% CMA(Cu) in TSPO1 host and 10% CMA(Cu) in PS host. Both the PL decay rate and the integrated PL intensity are thermally activated and can be fitted by the Arrhenius equation. For 10% CMA(Cu) in TSPO1: the activation energy extracted from the PL decay rate E_Ak=103 meV and the activation energy extracted from the integrated PL intensity E_APL=70 meV. For 80% CMA(Cu) in TSPO1: E_Ak=105 meV and E_APL=65 meV. For 10% CMA(Cu) in PS: E_Ak=102 meV and E_APL=74 meV.

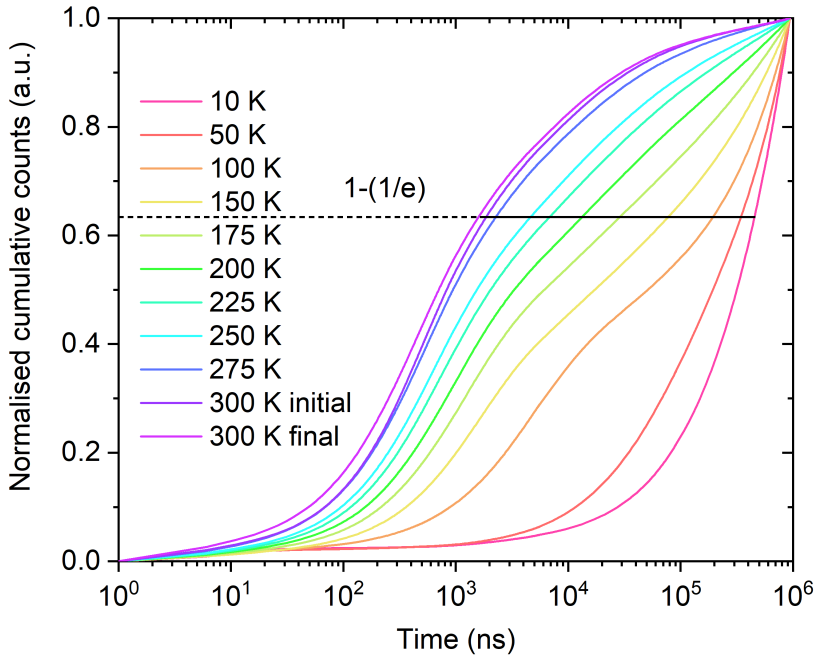

Fig. 6.30 Cryogenic emission integral of 10% CMA(Ag) in TSPO1 with 1-(1/e) labelled as the characteristic luminescence lifetime. "Initial" data taken at 300 K before cooling the film to 10 K, "Final" data upon warming back to 300 K after low-temperature measurements.

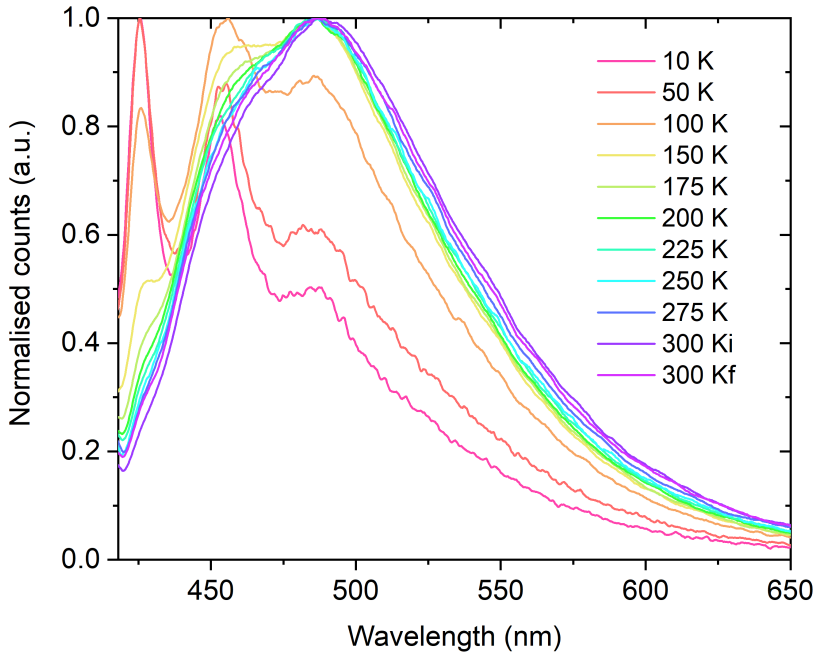

Fig. 6.31 Temperature dependent steady-state photoluminescence of 10% CMA(Ag) in TSPO1. "Initial" data taken at 300 K before cooling the film to 10 K, "Final" data upon warming back to 300 K after low-temperature measurements. Excitation wavelength is 400 nm.

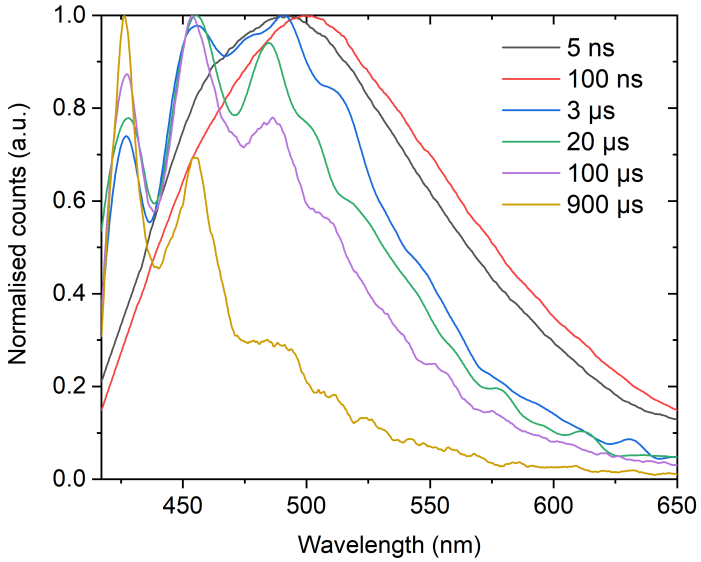

Fig. 6.32 Time-resolved photoluminescence spectra of 10% CMA(Ag) in TSPO1 at 10 K. After initial photoexcitation (noted as time zero) by a 400 nm laser. Unstructured early-time emission (5 ns and 100 ns) is from the charge-transfer (CT) state, which is thermally activated and the redshifted emission is due to energy relaxation within the density of states. Emission rate from CT state is highly suppressed at low temperature so the long-lived locally-excited carbazole triplets ^{3}LE(Cz) dominate the emission at longer time (3 µs, 20 µs, 100 µs and 900 µs).

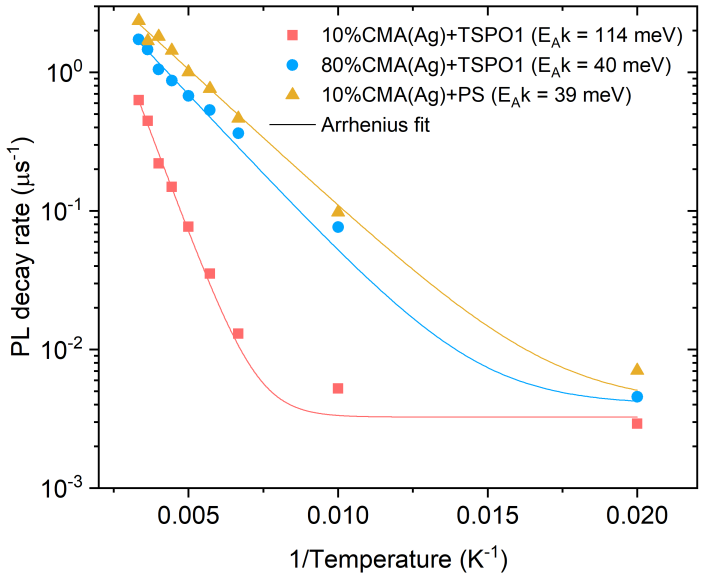

Fig. 6.33 PL decay rate of 10% and 80% concentration of CMA(Ag) in TSPO1 and 10% in PS at different temperatures as a function of 1/Temperature. PL decay rate is the reciprocal of characteristic luminescence lifetime from cryogenic emission integral. The activation energies E_Ak are yielded from the Arrhenius fit.

6.3.5 Discussion of the luminescence mechanism of the coinage metal CMAs

In the previous sections, we have presented the effect of the coinage metal and host molecules on the excited state properties of coinage metal-bridged CMA complexes. We find that the intersystem crossing (ISC) and triplet harvesting in coinage metal CMAs do not follow the trend expected for the heavy atom effect. The ISC rate is quantitively consistent with the quantum dynamics simulations of Penfold et al. with a trend of CMA(Cu) > CMA(Au) > CMA(Ag) observed.[170] CMA(Cu) exhibits a higher rate than CMA(Au) due to its stronger direct ^{1}CT$-^3$CT coupling, resulting from the larger metal d-orbital contribution to the lowest lying CT excited states in CMA(Cu). The spin-orbit coupling matrix elements (SOCMEs) are dominated by an internal effect concerning the character of the states involved in the transition as outlined in the El-Sayed rules,[63] rather than the external heavy atom effect.[51, 134, 170, 172] CMA(Ag) has the smallest SOCMEs 2.58 cm^{-1} because the metal *d*-orbitals mix weakly to the lowest lying CT states similar to Au, and the external heavy atom effect of Ag further reduces the size of the SOCMEs.[170] Given the weak coupling strength between two CT states, recent work states that in order to achieve effective ISC in CMA(Ag), coupling to an intermediate state localised to the donor or acceptor ligands ("LE" states) is preferred.[170]

For each CMA, electrostatic interactions with the host are shown to blueshift the CT states. However, the LE states discussed in the previous paragraph are insensitive to interactions with the environment, which consequently alters the CT$-$LE energy gap. In principle while both the ^{3}LE(CAAC) and ^{3}LE(Cz) states,[170] could play a role, the former appears energetically inaccessible in practice. However,^{3}LE(Cz) is observed in some cases, such as CMA(Ag) in TSPO1. The activation energy is consistent for all CT states for CMA(Au) and CMA(Cu), and for CMA(Ag) where ^{3}LE(Cz) emission is not observed. The emission process, which we take to be analogous with organic TADF, requires thermal mixing of ^{3}CT with ^{1}CT.[25, 45] We interpret the activation energies measured therein to correspond to the energy barrier for this process. CMA(Cu) exhibits the highest energy barrier, of 100 meV, CMA(Au) an intermediate barrier (70 meV) and CMA(Ag) the lowest energy barrier (40 meV). The energy barriers and thus the shortest luminescence lifetime of CMA(Ag) agree with the findings by Thompson and coworkers.[130] These energy scales correspond to the value ΔE_{ST} commonly reported in the organic TADF literature.[25, 28, 46, 60] However, where ^{3}CT and ^{3}LE(Cz) are close proximity, the nature of the energy barrier changes, and we interpret this as the energy required to escape a local ^{3}LE(Cz) and access states in the ^{3}CT manifold – similar to the type-III TADF model in the current literature,[59, 168] but with the important caveat that it is ^{1}CT$-^3$CT coupling which provides the luminescence pathway. The interference

from the ^{3}LE(Cz) state greatly increases the luminescence lifetime of CMA(Ag) whereas for CMA(Au) and CMA(Cu) where the direct coupling between CT states is strong the ^{3}LE(Cz) state is not significantly involved in ISC.

For all compounds, ISC occurs on the picosecond timescale and is therefore not a rate-limiting step for emission, and indeed there is little correlation between the ISC and luminescence rates. Instead, our data supports the hypothesis that it is access to molecular configurations that permits mixing of ^{1}CT and ^{3}CT which represents the rate-limiting step. Accessing such configurations is easier in CMA(Ag), owing to its flatter ground and excited state potential along torsional degree of freedom[170] allowing the highest radiative rates. By contrast, despite showing stronger SOC, CMA(Cu) shows low radiative rates due to its higher activation energy. The correlation between C-M-N bond length and activation energy, with the former influencing HOMO-LUMO overlap, suggests that activation energy is closely related to the exchange energy of the CT state. Longer, more flexible, bonds, may also play a part in allowing easier reorganisation, but may also contribute to nonradiative decay. The activation energy therefore represents the energy of an internal reorganisation of the CT state, for instance by altering its symmetry, and in most cases, it does not represent the energy needed to access a discrete state of different quantum mechanical character.

6.4 Conclusions

In conclusion, we have investigated the heavy atom effect on the coinage-metal bridged CMAs to reveal its influence on the intersystem crossing and luminescence mechanism. We find that the photophysical properties do not reflect expected trends based upon the heavy atom effect as both direct (^{1}CT$-^3$CT) coupling and spin-vibronic coupling via a local triplet state ^{3}LE(Cz) are present. The combination of the small contribution from the Ag d-orbitals to the lowest-lying CT states and lighter metal atom renders the weakest direct ^{1}CT$-^3$CT coupling for CMA(Ag) and thus the slowest ISC rate, making the spin-vibronic coupling more important and the photophysical properties more sensitive to the CT$-$LE energy gap than the Au and Cu-bridged analogues. The activation energy measured from photoluminescence spectroscopy stays relatively constant for all CT states for CMA(Au), CMA(Cu) and for CMA(Ag) where ^{3}LE(Cz) is not significantly involved. We infer the activation energy represents the thermal energy required for mixing the ^{3}CT and ^{1}CT states for luminescence. However, where the CT$-$LE gap is diminished, strong interference from ^{3}LE(Cz) state makes the spin-vibronic coupling dominant in CMA(Ag) and strongly retards the emission rate.

The development of CMA complexes for high efficiency OLEDs, which rely on high radiative decay rates and high luminescence quantum efficiency, therefore requires the removal of parasitic local triplet states close to the CT energy and the minimisation of exchange energy. In this respect, the design rules for such a compound echo those initially developed for organic TADF compounds, before the concept of spin-vibronic coupling between states of different character was introduced as an appropriate model.

Chapter 7

Conclusions and Outlook

This thesis presents three main investigations into the effects of solid-state intermolecular interactions on the triplet excitons in a new family of organometallic light emitters, carbene-metal-amides (CMAs). The motivation is to understand the electrostatic effects on the energy landscape, the link between molecular conformations and photophysical properties, and the triplet harvesting mechanism, by employing various spectroscopy techniques, structural characterisations, and simulations. This chapter will first summarise the key findings and then discuss future work worth investigating in the field.

7.1 Influence of triplet diffusion and electrostatic interactions

Chapter 4 investigates the triplet diffusion process and the effects of electrostatic interactions on the excited states, especially the CT states, of gold-bridged CMA1 emitters. The approach of shifting the CT state is then utilised to probe the ISC mechanism in CMA1. CMA1 emitters hosted by non-polar PVK and polar TSPO1 molecules were examined, in order to compare the photophysics without/with the presence of strong electrostatic interactions. Contributions from both thermally activated diffusion and electrostatic interactions upshift the CT energy by around 200 meV. However, this blueshift results in no significant change in intersystem crossing rate, slightly increased luminescence lifetime, and no significant change in thermal activation energy. The experimentally obtained energy relaxation process can be reproduced by Monte Carlo simulations, where triplet diffusion within the density of states can be modelled by using a Marcus-type hopping rate. The mean energy and width of the density of states changes as the host-guest electrostatic interactions are varied. The energies of locally-excited states are relatively insensitive to the electrostatic interactions.

Therefore, the tunability of the CT-LE energy gap provides an experimental approach to probe the triplet harvesting mechanism and the coupling between the T_1 and S_1 states. By examining the molecular symmetry, there is likely to be no direct spin-orbit coupling between charge transfer states (S_1 and T_1) and ligand-centred excited states localised to the carbazole, since they transform as the same irrep. However, some higher-lying CT states, for example LUMO-1 to HOMO are able to interact with S_1 and T_1. From the experimental evidence that CMA1 photophysics is insensitive to the CT energy, it is reasonable to suggest that CT−CT coupling plays a more important role than CT−LE coupling, opening up a design rule for the realisation of rapid triplet emission. This solid-state solvatochromism can be generalised to a range of gold-bridged CMAs, universally blueshifting the emission by around 200 meV. This approach should be directly transferrable to other charge-transfer type emitters possessing large permanent dipole moment, allowing host-guest interactions to be used as a tool to tune electroluminescence in OLED devices over a significant range into the blue spectral region without chemical modifications to the emitters.

7.2 Influence of nuclear reorganisation and polarisation

Chapter 5 investigates the link between the molecular conformation and photophysical behaviour of CMA1 by developing a new method to crystallise CMA1 as thin films using a polar, low glass-transition temperature matrix. Since previous investigations of CMAs and broader TADF-type emitters mainly centred around the amorphous phase and solution phase where molecules are free to relax, crystallisation provides constrained coplanar geometries of the emitters, so that the conformation-photophysics link can be explored in a controlled manner. In the crystalline phase, energetic disorder of the density of states and the reorganisation energy for triplet diffusion decrease. Charge-transfer emission of the crystalline phase greatly blueshifts by around 400 meV compared to the amorphous phase. At low temperature, this large shift, and thus decreased CT−LE energy gap, allows the structured emission from triplets localised on the carbazole ligand to be uncovered. Quantum-chemical calculations find that a combined effect of restricted torsional relaxation and enhanced electrostatic interactions modifies the ^{1}CT potential, rendering a more coplanar conformation as the equilibrium geometry and a blueshifted emission peak energy. The thermal activation energy derived from temperature-dependent photoluminescence spectroscopy is fairly constant across different materials phases, which, as calculations suggest, can be attributed to the exchange energy between S_1 and T_1 at an unmodified, more coplanar triplet geometric optimum. While the photo-induced absorption spectra in crystalline, amorphous and solution phases are distinct, the rate of intersystem crossing appears unaffected by the S_1 equilibrium

conformation, which suggests that the spin crossover does not rely on inter-ligand twisting to orthogonality. Surprisingly, at 300 K, emission rates from coplanar crystalline materials are close to those measured in the amorphous phase and in isolated, relaxed molecules in solution, despite a 400 meV shift in CT energy. Torsional distortion does not significantly impact the photophysics of TADF organometallics. The photophysics is largely determined by the more coplanar T_1 state, which is accessible in different materials phases and thus renders a uniform spin-orbit-coupling kinetics. The effect of polarisation is consistent with the host-guest electrostatic interactions investigated in Chapter 4. Since CMA1 possesses a large ground-state dipole moment, closed-packed crystalline phase yields a large polarisation energy, which largely blueshifts the charge-transfer emission.

7.3 Influence of the heavy atom effect

Chapter 6 investigates the heavy atom effect on the coinage-metal bridged CMAs to reveal its influence on the intersystem crossing and luminescence mechanism. We find that the photophysical properties do not reflect expected trends based on the heavy atom effect as both direct (^{1}CT$-^3$CT) coupling and spin-vibronic coupling via a local triplet state ^{3}LE(Cz) are present. The combination of the small contribution from the Ag d-orbitals to the lowest-lying CT states and the lighter metal atom gives the weakest direct ^{1}CT$-^3$CT coupling for CMA(Ag) and thus the slowest ISC rate, making the spin-vibronic coupling more important and the photophysical properties more sensitive to the CT$-$LE energy gap than the Au and Cu-bridged analogues. The activation energy measured by photoluminescence spectroscopy stays relatively constant for all CT states for CMA(Au), CMA(Cu) and for CMA(Ag) where ^{3}LE(Cz) is not significantly involved. We infer the activation energy represents the thermal energy required for mixing the ^{3}CT and ^{1}CT states for luminescence. However, where the CT$-$LE gap is diminished, strong interference from ^{3}LE(Cz) state makes the spin-vibronic coupling dominant in CMA(Ag) and greatly retards the emission rate. The development of CMA complexes for high efficiency OLEDs, which rely on high radiative decay rates and high luminescence quantum efficiency, therefore requires the removal of parasitic local triplet states close to the CT energy and the minimisation of exchange energy. In this respect, the design rules for such a compound echo those initially developed for organic TADF compounds before the concept of spin-vibronic coupling between states of different character was introduced as an appropriate model.

7.4 Outlook and concluding remarks

Understanding and managing the coupling mechanism between the singlet and triplet excitons are of significant importance in organic semiconductors. In the context of light-emitting organic molecules, breakthrough of manipulating the triplet excitons revolutionises the field and realises broader commercial applications of displays and lightings, from the fluorescence-type emitters, to the phosphorescence-type emitters, to the TADF-type emitters, and to the hybrid-type CMA emitters. While the workhorse molecules employed in this thesis are mainly gold-bridge CMAs and the two silver- and copper-bridged analogues, these three serve as the archetypes of almost all CMA-type emitters and the effects of solid-state interactions are universally observed. For example, Using highly-polar hosts are able to shift the original sky-blue electroluminescence in OLED devices into deep-blue spectral region while preserving high efficiency and stability.[132, 167] The dual effects of heavy metal atoms and the ligand-centred molecular orbitals in these organometallic compounds provides multiple channels for intersystem crossing, thereby opening up new possibilities for molecular design.

We note that while all experiments in this thesis were focused on the CMA-type emitters, the effects of solid-state interactions are not specific and limited to the CMAs.[61, 138] The methods and findings developed here can be extended to the wider context of all-organic emitters. There are still some remaining questions to answer, for example, which vibrational modes in a CMA-type or generally a TADF-type molecule are most relevant to the efficient ISC, and non-radiative loss mechanisms in inefficient emitters. Arguments in the literature also centre around whether flexible molecular conformation is beneficial or detrimental to the ISC.[136, 173, 174] Time-resolved vibrational spectroscopy is a suitable technique to potentially investigate these questions, which probes the dynamic information about the geometries of molecules in the excited states and allows one to relate the structural dynamics to the dynamics of excited species.[174]

Furthermore, spin-sensitive techniques such as transient electron paramagnetic resonance (EPR) spectroscopy are useful in detecting and determining the nature of paramagnetic excited states, such as triplet excitons. This is particularly attractive for studying organic electronics as predominantly triplet excitons are formed after excitation.[175] Compared with optical spectroscopy, EPR allows us to directly probe triplet states by detecting the resonances between the triplet sublevels. Since the triplet sublevel populations are sensitive to the molecular geometry as well as the triplet precursor state, EPR spectroscopy is able to reveal the underlying ISC mechanism.[145] Paramagnetic states with higher spin multiplicity can also be assigned, such as the quintet states from two coupled triplets after singlet fission.[176] EPR spectroscopy is also particularly useful in examining the (de)localisation

of triplet excitons in organic semiconductors and connecting it to the electronic structure, molecular conformation, and environmental effects such as solid-state interactions. In TADF emitters, this helps to distinguish between LE and CT states which can support the information obtained from the optical spectroscopy, although EPR has not yet been employed to study TADF solid-state interactions.

In summary, the work described in this thesis contributes to the management of triplet excitons via solid-state interactions in organic light emitters, highlighting the diffusion process, the electrostatic interactions with surrounding molecules, the link between molecular conformations and photophysical properties, and heavy-atom effects. These findings open up new research avenues in the control of triplet-singlet upconversion for optoelectronic applications.

References

[1] R. H. Friend, R. W. Gymer, A. B. Holmes, J. H. Burroughes, R. N. Marks, C. Taliani, D. D. C. Bradley, D. A. Dos Santos, J. L. Bredas, M. Logdlund, and W. R. Salaneck. Electroluminescence in conjugated polymers. *Nature*, 397(6715):121–128, 1999.

[2] Christoph J. Brabec. Organic photovoltaics: Technology and market. *Solar Energy Materials and Solar Cells*, 83(2-3):273–292, 2004. ISSN 09270248.

[3] B. Crone, A. Dodabalapur, Y. Y. Lin, R. W. Filas, Z. Bao, A. LaDuca, R. Sarpeshkar, H. E. Katz, and W. Li. Large-scale complementary integrated circuits based on organic transistors. *Nature*, 403(6769):521–523, 2000. ISSN 00280836.

[4] Zachary B. Henson, Klaus Müllen, and Guillermo C. Bazan. Design strategies for organic semiconductors beyond the molecular formula. *Nature Chemistry*, 4(9): 699–704, 2012. ISSN 17554330.

[5] Yirang Im, Mounggon Kim, Yong Joo Cho, Jeong A. Seo, Kyoung Soo Yook, and Jun Yeob Lee. Molecular Design Strategy of Organic Thermally Activated Delayed Fluorescence Emitters. *Chemistry of Materials*, 29(5):1946–1963, 2017. ISSN 15205002.

[6] Yan Qian, Xinwen Zhang, Dianpeng Qi, Linghai Xie, Bevita K. Chandran, Xiaodong Chen, and Wei Huang. Thin-film organic semiconductor devices: from flexibility to ultraflexibility. *Science China Materials*, 59(7):589–608, 2016. ISSN 2095-8226.

[7] P. E. Burrows, G. Gu, V. Bulović, Z. Shen, S. R. Forrest, and M. E. Thompson. Achieving full-color organic light-emitting devices for lightweight, flat-panel displays. *IEEE Transactions on Electron Devices*, 44(8):1188–1203, 1997. ISSN 00189383.

[8] Fei Guo, Andre Karl, Qi-Fan Xue, Kai Cheong Tam, Karen Forberich, and Christoph J Brabec. The fabrication of color-tunable organic light-emitting diode displays via solution processing. *Light: Science & Applications*, 6(11):e17094–e17094, 2017. ISSN 2047-7538.

[9] Shumeng Wang, Xingdong Wang, Bing Yao, Baohua Zhang, Junqiao Ding, Zhiyuan Xie, and Lixiang Wang. Solution-Processed Phosphorescent Organic Light-Emitting Diodes with Ultralow Driving Voltage and Very High Power Efficiency. *Scientific Reports*, 5(July):1–9, 2015. ISSN 20452322.

[10] Amin Salehi, Chen Dong, Dong Hun Shin, Liping Zhu, Christopher Papa, Anh Thy Bui, Felix N. Castellano, and Franky So. Realization of high-efficiency fluorescent

organic light-emitting diodes with low driving voltage. *Nature Communications*, 10 (1):1–9, 2019. ISSN 20411723.

[11] Hajime Nakanotani, Takahiro Higuchi, Taro Furukawa, Kensuke Masui, Kei Morimoto, Masaki Numata, Hiroyuki Tanaka, Yuta Sagara, Takuma Yasuda, and Chihaya Adachi. High-efficiency organic light-emitting diodes with fluorescent emitters. *Nature Communications*, 5(May):1–7, 2014. ISSN 20411723.

[12] A. Bernanose, M. Comte, and P. Vouaux. A new method of emission of light by certain organic compounds. *J. Chim. Phys*, 50:64–68, 1953.

[13] A. Bernanose. Electroluminescence of organic compounds. *J. Appl. Phys*, 6:S54–S55, 1955.

[14] M. Pope, H. P. Kallmann, and P. Magnante. Electroluminescence in Organic Crystals. *The Journal of Chemical Physics*, 38:2042, 1963.

[15] W. Helfrich and W. G. Schneider. Recombination radiation in anthracene crystals. *Physical Review Letters*, 14(7):229–231, 1965. ISSN 00319007.

[16] C. W. Tang and S. A. Vanslyke. Organic electroluminescent diodes. *Applied Physics Letters*, 51(12):913–915, 1987. ISSN 00036951.

[17] R. H. Friend, J. H. Burroughes, D. D. C. Bradley, A. R. Brown, R. N. Marks, K. Mackay, P. L. Burns, and A. B. Holmes. Light-emitting diodes based on conjugated polymers. *Nature*, 347:539–541, 1990. ISSN 0028-0836.

[18] D. Braun and A. J. Heeger. Visible light emission from semiconducting polymer diodes. *Applied Physics Letters*, 58(18):1982–1984, 1991. ISSN 00036951.

[19] S. Matthew Menke, Richard H. Friend, and Dan Credgington. *The WSPC Reference on Organic Electronics: Organic Semiconductors*. World Scientific, 2016.

[20] A. W. Grice, D. D.C. Bradley, M. T. Bernius, M. Inbasekaran, W. W. Wu, and E. P. Woo. High brightness and efficiency blue light-emitting polymer diodes. *Applied Physics Letters*, 73(5):629–631, 1998. ISSN 00036951.

[21] Y. Yang, Q. Pei, and A. J. Heeger. Efficient blue polymer light-emitting diodes from a series of soluble poly(paraphenylene)s. *Journal of Applied Physics*, 79(2):934–939, 1996. ISSN 00218979.

[22] M. A. Baldo, D. F. O'Brien, Y. You, A. Shoustikov, S. Sibley, M. E. Thompson, and S. R. Forrest. Highly efficient phosphorescent emission from organic electroluminescent devices. *Nature*, 395(6698):151–154, 1998.

[23] Tissa Sajoto, Peter I Djurovich, Arnold B Tamayo, Jonas Oxgaard, William A Goddard, and Mark E Thompson. Temperature Dependence of Blue Phosphorescent Cyclometalated Ir (III) Complexes. *Journal of the American Chemical Society*, 131 (18):9813–9822, 2009.

[24] M. Baldo, S. Lamansky, P. E. Burrows, M. E. Thompson, and S. R. Forrest. Very high-efficiency green organic light-emitting devices based on electrophosphorescence. *Applied Physics Letters*, 75(1):4, 1999.

[25] Hiroki Uoyama, Kenichi Goushi, Katsuyuki Shizu, Hiroko Nomura, and Chihaya Adachi. Highly efficient organic light-emitting diodes from delayed fluorescence. *Nature*, 492(7428):234–238, 2012.

[26] C. A. Parker and C. G. Hatchard. Triplet-singlet emission in fluid solutions. Phosphorescence of eosin. *Transactions of the Faraday Society*, 57:1894–1904, 1961. ISSN 00147672.

[27] Andrzej Maciejewski, Marian Szymanski, and Ronald P. Steer. Thermally activated delayed S1 fluorescence of aromatic thiones. *Journal of Physical Chemistry*, 90(23): 6314–6318, 1986. ISSN 00223654.

[28] Hironori Kaji, Hajime Suzuki, Tatsuya Fukushima, Katsuyuki Shizu, Katsuaki Suzuki, Shosei Kubo, Takeshi Komino, Hajime Oiwa, Furitsu Suzuki, Atsushi Wakamiya, Yasujiro Murata, and Chihaya Adachi. Purely organic electroluminescent material realizing 100% conversion from electricity to light. *Nature Communications*, 6(May): 8476, 2015.

[29] Jun-ichi Nishide, Hajime Nakanotani, Yasuhide Hiraga, and Chihaya Adachi. High-efficiency white organic light-emitting diodes using thermally activated delayed fluorescence. *Applied Physics Letters*, 104(23):233304, 2014. ISSN 0003-6951.

[30] Qisheng Zhang, Daniel Tsang, Hirokazu Kuwabara, Yasuhiro Hatae, Bo Li, Takehiro Takahashi, Sae Youn Lee, Takuma Yasuda, and Chihaya Adachi. Nearly 100% internal quantum efficiency in undoped electroluminescent devices employing pure organic emitters. *Advanced Materials*, 27(12):2096–2100, 2015. ISSN 15214095.

[31] Ye Tao, Kai Yuan, Ting Chen, Peng Xu, Huanhuan Li, Runfeng Chen, Chao Zheng, Lei Zhang, and Wei Huang. Thermally activated delayed fluorescence materials towards the breakthrough of organoelectronics. *Advanced Materials*, 26(47):7931–7958, 2014. ISSN 15214095.

[32] Dawei Di, Alexander S. Romanov, Le Yang, Johannes M. Richter, Jasmine P.H. Rivett, Saul Jones, Tudor H. Thomas, Mojtaba Abdi Jalebi, Richard H. Friend, Mikko Linnolahti, Manfred Bochmann, and Dan Credgington. High-performance light-emitting diodes based on carbene-metal-amides. *Science*, 2017.

[33] Wolfgang Demtröder. *Atoms , Molecules and Photons An Introduction to Atomic-, Molecular- and Quantum-Physics*. Springer, 2010. ISBN 9783642102974.

[34] Peter Atkins and Ronald Friedman. *Molecular quantum mechanics*. Oxford university press, 2005.

[35] Anna Köhler and Heinz Bässler. *Electronic Processes in Organic Semiconductors-An Introduction*. Wiley-VCH, 2015.

[36] I.G. Hill, A Kahn, Z.G. Soos, and R.A. Pascal, Jr. Charge-separation energy in films of π-conjugated organic molecules. *Chemical Physics Letters*, 327(3-4):181–188, 2000.

[37] Lewis J Rothberg and Andrew J Lovinger. Status of and prospects for organic electroluminescence. *Journal of Materials Research*, 11(12):3174–3187, 1996.

[38] M. a. Baldo, D. F. O'Brien, and S. R. Forrest. Excitonic singlet-triplet ratio in a semiconducting organic thin film. *Physical Review B*, 60(20):14422–14428, 1999.

[39] Tetsuo Tsutsui. Progress in Electroluminescent Devices Using Molecular Thin Films. *MRS Bulletin*, 22(6):39–45, 1997. ISSN 08837694.

[40] Bodo H. Wallikewitz, Dinesh Kabra, Simon Gélinas, and Richard H. Friend. Triplet dynamics in fluorescent polymer light-emitting diodes. *Physical Review B - Condensed Matter and Materials Physics*, 85(4):22–25, 2012.

[41] M. Segal, M. Baldo, R. Holmes, S. Forrest, and Z. Soos. Excitonic singlet-triplet ratios in molecular and polymeric organic materials. *Physical Review B*, 68(7):1–14, 2003.

[42] J. S. Wilson, N. Chawdhury, M. R A Al-Mandhary, M. Younus, M. S. Khan, P. R. Raithby, A. Köhler, and R. H. Friend. The energy gap law for triplet states in pt-containing conjugated polymers and monomers. *Journal of the American Chemical Society*, 123(38):9412–9417, 2001.

[43] A. Köhler and D. Beljonne. The Singlet–Triplet Exchange Energy in Conjugated Polymers. *Advanced Functional Materials*, 14(1):11–18, 2004.

[44] A. Köhler and H. Bässler. Triplet states in organic semiconductors. *Materials Science and Engineering R: Reports*, 66(4-6):71–109, 2009.

[45] Qisheng Zhang, Bo Li, Shuping Huang, Hiroko Nomura, Hiroyuki Tanaka, and Chihaya Adachi. Efficient blue organic light-emitting diodes employing thermally activated delayed fluorescence. *Nature Photonics*, 8(March):1–7, 2014.

[46] Shuzo Hirata, Yumi Sakai, Kensuke Masui, Hiroyuki Tanaka, Sae Youn Lee, Hiroko Nomura, Nozomi Nakamura, Mao Yasumatsu, Hajime Nakanotani, Qisheng Zhang, Katsuyuki Shizu, Hiroshi Miyazaki, and Chihaya Adachi. Highly efficient blue electroluminescence based on thermally activated delayed fluorescence. *Nature materials*, 14(3):330–6, 2015.

[47] Peter K.H. Ho, Ji Seon Kim, Nir Tessler, and Richard H. Friend. Photoluminescence of poly(p-phenylenevinylene)-silica nanocomposites: Evidence for dual emission by Franck-Condon analysis. *Journal of Chemical Physics*, 115(6):2709–2720, 2001.

[48] Jenny Clark, Carlos Silva, Richard H. Friend, and Frank C. Spano. Role of intermolecular coupling in the photophysics of disordered organic semiconductors: Aggregate emission in regioregular polythiophene. *Physical Review Letters*, 98(20):1–4, 2007.

[49] Shunsuke Sasaki, Gregor P. C. Drummen, and Gen-ichi Konishi. Recent advances in twisted intramolecular charge transfer (TICT) fluorescence and related phenomena in materials chemistry. *J. Mater. Chem. C*, 4(14):2731–2743, 2016.

[50] Gleb Baryshnikov, Boris Minaev, and Hans Ågren. Theory and Calculation of the Phosphorescence Phenomenon. *Chemical Reviews*, 117(9):6500–6537, 2017. ISSN 15206890.

[51] Thomas J. Penfold, Etienne Gindensperger, Chantal Daniel, and Christel M. Marian. Spin-Vibronic Mechanism for Intersystem Crossing. *Chemical Reviews*, page acs.chemrev.7b00617, 2018.

[52] Jaesang Lee, Hsiao-Fan Chen, Thilini Batagoda, Caleb Coburn, Peter I Djurovich, Mark E Thompson, and Stephen R Forrest. Deep blue phosphorescent organic light-emitting diodes with very high brightness and efficiency. *Nature materials*, 15(October):1–8, 2015.

[53] Hisahiro Sasabe, Jun Ichi Takamatsu, Takao Motoyama, Soichi Watanabe, Gerhard Wagenblast, Nicolle Langer, Oliver Molt, Evelyn Fuchs, Christian Lennartz, and Junji Kido. High-efficiency blue and white organic light-emitting devices incorporating a blue iridium carbene complex. *Advanced Materials*, 22(44):5003–5007, 2010.

[54] Hirohiko Fukagawa, Takahisa Shimizu, Hiromu Hanashima, Yoshichika Osada, Mitsunori Suzuki, and Hideo Fujikake. Highly efficient and stable red phosphorescent organic light-emitting diodes using platinum complexes. *Advanced Materials*, 24(37): 5099–5103, 2012.

[55] D. Beljonne, Z. Shuai, G. Pourtois, and J. L. Bredas. Spin-orbit coupling and intersystem crossing in conjugated polymers: A configuration interaction description. *Journal of Physical Chemistry A*, 105(15):3899–3907, 2001. ISSN 10895639.

[56] A. C. Albrecht. Vibronic-spin-orbit perturbations and the assignment of the lowest triplet state of benzene. *The Journal of Chemical Physics*, 38(2):354–365, 1963. ISSN 00219606.

[57] T. J. Penfold, F. B. Dias, and A. P. Monkman. The theory of thermally activated delayed fluorescence for organic light emitting diodes. *Chemical Communications*, 54 (32):3926–3935, 2018. ISSN 1364548X.

[58] J. Gibson and T. J. Penfold. Nonadiabatic coupling reduces the activation energy in thermally activated delayed fluorescence. *Physical Chemistry Chemical Physics*, 19 (12):8428–8434, 2017. ISSN 14639076.

[59] Marc K. Etherington, Jamie Gibson, Heather F. Higginbotham, Thomas J. Penfold, and Andrew P. Monkman. Revealing the spin-vibronic coupling mechanism of thermally activated delayed fluorescence. *Nature Communications*, 7:1–7, 2016. ISSN 20411723.

[60] Kenichi Goushi, Kou Yoshida, Keigo Sato, and Chihaya Adachi. Organic light-emitting diodes employing efficient reverse intersystem crossing for triplet-to-singlet state conversion. *Nature Photonics*, 6(4):253–258, 2012.

[61] Vygintas Jankus, Przemyslaw Data, David Graves, Callum McGuinness, Jose Santos, Martin R. Bryce, Fernando B. Dias, and Andrew P. Monkman. Highly efficient TADF OLEDs: How the emitter-host interaction controls both the excited state species and electrical properties of the devices to achieve near 100% triplet harvesting and high efficiency. *Advanced Functional Materials*, 24(39):6178–6186, 2014.

[62] Ayataka Endo, Keigo Sato, Kazuaki Yoshimura, Takahiro Kai, Atsushi Kawada, Hiroshi Miyazaki, and Chihaya Adachi. Efficient up-conversion of triplet excitons into a singlet state and its application for organic light emitting diodes. *Applied Physics Letters*, 98(8):10–13, 2011.

[63] M. A. El-Sayed. Spin-orbit coupling and the radiationless processes in nitrogen heterocyclics. *The Journal of Chemical Physics*, 38(12):2834–2838, 1963. ISSN 00219606.

[64] Sei Yong Kim, Won Ik Jeong, Christian Mayr, Young Seo Park, Kwon Hyeon Kim, Jeong Hwan Lee, Chang Ki Moon, Wolfgang Br??tting, and Jang Joo Kim. Organic light-emitting diodes with 30% external quantum efficiency based on a horizontally oriented emitter. *Advanced Functional Materials*, 23(31):3896–3900, 2013. ISSN 1616301X.

[65] Jong-Kwan Bin, Nam-Sung Cho, and Jong-In Hong. New host material for high-performance blue phosphorescent organic electroluminescent devices. *Advanced materials*, 24(21):2911–5, 2012. ISSN 1521-4095.

[66] Guomeng Li, Dongxia Zhu, Tai Peng, Yu Liu, Yue Wang, and Martin R. Bryce. Very high efficiency orange-red light-emitting devices with low roll-off at high luminance based on an ideal host-guest system consisting of two novel phosphorescent iridium complexes with bipolar transport. *Advanced Functional Materials*, 24(47):7420–7426, 2014. ISSN 16163028.

[67] Christel M. Marian. Mechanism of the Triplet-to-Singlet Upconversion in the Assistant Dopant ACRXTN. *Journal of Physical Chemistry C*, 120(7):3715–3721, 2016. ISSN 19327455.

[68] W. Siebrand. Radiationless transitions in polyatomic molecules. I. Calculation of Franck-Condon factors. *The Journal of Chemical Physics*, 46(2):440–447, 1967. ISSN 00219606.

[69] G. W. Robinson and R. P. Frosch. Theory of electronic energy relaxation in the solid phase. *The Journal of Chemical Physics*, 37(9):1962–1973, 1962.

[70] Robert Englman and Joshua Jortner. The energy gap law for radiationless transitions in large molecules. *Molecular Physics*, 18(2):285–287, 1970.

[71] G. W. Robinson and R. P. Frosch. Electronic excitation transfer and relaxation. *The Journal of Chemical Physics*, 38(5):1187–1203, 1963.

[72] Hiroki Noda, Xian Kai Chen, Hajime Nakanotani, Takuya Hosokai, Momoka Miyajima, Naoto Notsuka, Yuuki Kashima, Jean Luc Brédas, and Chihaya Adachi. Critical role of intermediate electronic states for spin-flip processes in charge-transfer-type organic molecules with multiple donors and acceptors. *Nature Materials*, 18(10): 1084–1090, 2019. ISSN 14764660.

[73] Takuya Hosokai, Hiroyuki Matsuzaki, Hajime Nakanotani, Katsumi Tokumaru, Tetsuo Tsutsui, Akihiro Furube, Keirou Nasu, Hiroko Nomura, Masayuki Yahiro, and Chihaya Adachi. Evidence and mechanism of efficient thermally activated delayed fluorescence promoted by delocalized excited states. *Science Advances*, 3(May):1–10, 2017.

[74] Dae Hyeon Kim, Anthony D'Aléo, Xian Kai Chen, Atula D.S. Sandanayaka, Dandan Yao, Li Zhao, Takeshi Komino, Elena Zaborova, Gabriel Canard, Youichi Tsuchiya, Eunyoung Choi, Jeong Weon Wu, Frédéric Fages, Jean Luc Brédas, Jean Charles Ribierre, and Chihaya Adachi. High-efficiency electroluminescence and amplified spontaneous emission from a thermally activated delayed fluorescent near-infrared emitter. *Nature Photonics*, 12(2):98–104, 2018. ISSN 17494893.

[75] Julien Eng, Jerry Hagon, and Thomas James Penfold. D-A3 TADF emitters: The role of the density of states for achieving faster triplet harvesting rates. *Journal of Materials Chemistry C*, 7(41):12942–12952, 2019. ISSN 20507526.

[76] Paloma L. dos Santos, Jonathan S. Ward, Daniel G. Congrave, Andrei S. Batsanov, Julien Eng, Jessica E. Stacey, Thomas J. Penfold, Andrew P. Monkman, and Martin R. Bryce. Triazatruxene: A Rigid Central Donor Unit for a D–A3 Thermally Activated Delayed Fluorescence Material Exhibiting Sub-Microsecond Reverse Intersystem Crossing and Unity Quantum Yield via Multiple Singlet–Triplet State Pairs. *Advanced Science*, 5(6):1–9, 2018. ISSN 21983844.

[77] Andrew J. Musser and Jenny Clark. Triplet-Pair States in Organic Semiconductors. *Annual Review of Physical Chemistry*, 70(1):323–351, 2019. ISSN 0066-426X.

[78] Bernhard Dick and Bernhard Nickel. Accessibility of the lowest quintet state of organic molecules through triplet-triplet annihilation; an indo ci study. *Chemical Physics*, 1983.

[79] E. Engel, K. Leo, and M. Hoffmann. Ultrafast relaxation and exciton-exciton annihilation in PTCDA thin films at high excitation densities. *Chemical Physics*, 325(1): 170–177, 2006.

[80] D. Y. Kondakov, T. D. Pawlik, T. K. Hatwar, and J. P. Spindler. Triplet annihilation exceeding spin statistical limit in highly efficient fluorescent organic light-emitting diodes. *Journal of Applied Physics*, 106(12), 2009.

[81] Chien Jung Chiang, Alpay Kimyonok, Marc K. Etherington, Gareth C. Griffiths, Vygintas Jankus, Figen Turksoy, and Andy P. Monkman. Ultrahigh efficiency fluorescent single and bi-layer organic light emitting diodes: The key role of triplet fusion. *Advanced Functional Materials*, 23(6):739–746, 2013.

[82] Hirohiko Fukagawa, Takahisa Shimizu, Noriyuki Ohbe, Shizuo Tokito, Katsumi Tokumaru, and Hideo Fujikake. Anthracene derivatives as efficient emitting hosts for blue organic light-emitting diodes utilizing triplet-triplet annihilation. *Organic Electronics: physics, materials, applications*, 13(7):1197–1203, 2012.

[83] Shalini Nigam and Sarah Rutan. Principles and Applications of Solvatochromism. *Focal Point*, 55(11):362–370, 2001.

[84] Th Forster. Energiewanderung und Fluoreszenz. *Die Naturwissenschaften*, 5:166–175, 1946.

[85] Th Forster. Zwischenmolekulare Energiewanderung und Fluoreszenz. *Annalen der Physik*, 2:55–57, 1948.

[86] L Stryer. Fluorescence Energy Transfer as a Spectroscopic Ruler. *Annual Review of Biochemistry*, 47(1):819–846, 1978.

[87] D. L. Dexter. A Theory of Sensitized Luminescence in Solids. *The Journal of Chemical Physics*, 21(5):836–850, 1953.

[88] Hellen C. Ishikawa-Ankerhold, Richard Ankerhold, and Gregor P.C. Drummen. Advanced fluorescence microscopy techniques-FRAP, FLIP, FLAP, FRET and FLIM, 2012.

[89] John F. Callan, A. Prasanna De Silva, and David C. Magri. Luminescent sensors and switches in the early 21st century. *Tetrahedron*, 61(36):8551–8588, 2005.

[90] Carlos Lodeiro and Fernando Pina. Luminescent and chromogenic molecular probes based on polyamines and related compounds. *Coordination Chemistry Reviews*, 253 (9-10):1353–1383, 2009.

[91] Wilhelm Warta and Norbert Karl. naphthalene: High, electric-field-dependent. *Physical Review B*, 32(2):1172–1182, 1985.

[92] Sebastian T. Hoffmann, Stavros Athanasopoulos, David Beljonne, Heinz Bässler, and Anna Köhler. How do triplets and charges move in disordered organic semiconductors? A Monte Carlo study comprising the equilibrium and nonequilibrium regime. *Journal of Physical Chemistry C*, 116(31):16371–16383, 2012.

[93] B. Movaghar, M. Grünewald, B. Ries, H. Bässler, and D. Würtz. Diffusion and relaxation of energy in disordered organic and inorganic materials. *Physical Review B*, 33(8):5545–5554, 1986.

[94] B. Movaghar, B Ries, and M. Grunewald. Diffusion and relaxation of energy in disordered systems: Departure from mean-field theories. *Physical Review B*, 34(8), 1986.

[95] T Holstein. Studies of polaron motion: Part II. The "small" polaron. *Annals of Physics*, 389:343–389, 1959.

[96] David Emin. Phonon-assisted transition rates I. Optical-phonon-assisted hopping in solids. *Advances in Physics*, 24(3):305–348, 1975.

[97] I G Austin and N F Mott. Advances in Physics Polarons in crystalline and non-crystalline materials Polarons in Crystalline and Non-crystalline Materials. *Advances in Physics*, 8732, 1969.

[98] Rudolph A. Marcus. Electron Transfer Reactions in Chemistry: Theory and Experiment (Nobel Lecture). *Angewandte Chemie International Edition in English*, 32(8): 1111–1121, 1993.

[99] R. A. Marcus. On the theory of oxidation-reduction reactions involving electron transfer. I. *The Journal of Chemical Physics*, 24(5):966–978, 1956.

[100] Anna Köhler and Heinz Bässler. What controls triplet exciton transfer in organic semiconductors? *Journal of Materials Chemistry*, 21(12):4003–4011, 2011.

[101] Lekshmi Sudha Devi, Mohammad K. Al-Suti, Carsten Dosche, Muhammad S. Khan, Richard H. Friend, and Anna Köhler. Triplet energy transfer in conjugated polymers. I. Experimental investigation of a weakly disordered compound. *Physical Review B - Condensed Matter and Materials Physics*, 78(4):1–8, 2008.

[102] Ivan I. Fishchuk, Andrey Kadashchuk, Lekshmi Sudha Devi, Paul Heremans, Heinz Bässler, and Anna Köhler. Triplet energy transfer in conjugated polymers. II. A polaron theory description addressing the influence of disorder. *Physical Review B - Condensed Matter and Materials Physics*, 78(4):1–8, 2008.

[103] V. Coropceanu, J. Cornil, D. A. Filho, Y. Olivier, R. Silbey, and J.-L. Bredas. Charge transport in organic semiconductors. *Chem. Rev.*, 312:1–65, 2007.

[104] Jean Luc Bredas, David Beljonne, Veaceslav Coropceanu, and Jérŏme Cornil. Charge-transfer and energy-transfer processes in π-conjugated oligomers and polymers: A molecular picture. *Chemical Reviews*, 104(11):4971–5003, 2004.

[105] Heinz Bässler and Bernd Schweitzer. Site-selective fluorescence spectroscopy of conjugated polymers and oligomers. *Accounts of Chemical Research*, 32(2):173–182, 1999.

[106] D. Beljonne, H. F. Wittmann, A. Köhler, S. Graham, M. Younus, J. Lewis, P. R. Raithby, M. S. Khan, R. H. Friend, and J. L. Brédas. Spatial extent of the singlet and triplet excitons in transition metal-containing poly-ynes. *Journal of Chemical Physics*, 105(9):3868–3877, 1996.

[107] Allen Miller and Elihu Abrahams. Impurity conduction at low concentrations. *Physical Review*, 120(3):745–755, 1960. ISSN 0031899X.

[108] N. S. Hush. Homogeneous and heterogeneous optical and thermal electron transfer. *Electrochimica Acta*, 13(5):1005–1023, 1968. ISSN 00134686.

[109] Robert S. Mulliken. Molecular Compounds and their Spectra. II. *Journal of the American Chemical Society*, 74(3):811–824, 1952. ISSN 15205126.

[110] Veaceslav Coropceanu, Xian Kai Chen, Tonghui Wang, Zilong Zheng, and Jean Luc Brédas. Charge-transfer electronic states in organic solar cells. *Nature Reviews Materials*, 4(11):689–707, 2019. ISSN 20588437.

[111] Alexander S. Romanov and Manfred Bochmann. Gold(I) and Gold(III) Complexes of Cyclic (Alkyl)(amino)carbenes. *Organometallics*, 34(11):2439–2454, 2015.

[112] Alexander S Romanov, Saul T E Jones, Le Yang, Patrick J Conaghan, Dawei Di, Mikko Linnolahti, Dan Credgington, and Manfred Bochmann. Mononuclear Silver Complexes for Efficient Solution and Vacuum-Processed OLEDs. *Avdanced optical materials*, 1801347:1–5, 2018.

[113] Ying Diao, Leo Shaw, Zhenan Bao, and Stefan C. B. Mannsfeld. Morphology control strategies for solution-processed organic semiconductor thin films. *Energy Environ. Sci.*, 2014.

[114] D. F. Swineharf. The Beer-Lambert Law. *Journal of Chemical Education*, 39(7):1–8, 1962. ISSN 0021-9584.

[115] Adolf Smekal. Zur Quantentheorie der Streuung und Dispersion, 1928.

[116] C. V. Raman and K. S. Krishnan. A New Type of Secondary Radiation. *Nature*, 1928.

[117] Ewen Smith and Geoffrey Dent. *Modern Raman Spectroscopy-A Practical Approach*. Wiley-VCH, 2005.

[118] Peter Vandenabeele. *Practical Raman Spectroscopy - An Introduction*. Wiley-VCH, 2013.

[119] Mello John C. de, Wittmann H. Felix, and Richard H. Friend. An Improved Experimental Determination of External Photoluminescence Quantum Efficiency. *Advanced Materials*, 9:230–232, 1997.

[120] Rene Guinebretiere. *X-ray Diffraction by Polycrystalline Materials*. Wiley, 2007.

[121] Frank Neese. The ORCA program system. *Wiley Interdisciplinary Reviews: Computational Molecular Science*, 2(1):73–78, 2012.

[122] Axel D. Becke. Density-functional thermochemistry. III. The role of exact exchange. *The Journal of Chemical Physics*, 98(7):5648–5652, 1993.

[123] Chengteh Lee, Weitao Yang, and Robert G. Parr. Development of the Colle-Salvetti correlation-energy formula into a functional of the electron density. *Physical Review B*, 37(2):785–789, 1988.

[124] R. Ditchfield, W. J. Hehre, and J. A. Pople. Self-Consistent Molecular-Orbital Methods. IX. An Extended Gaussian-Type Basis for Molecular-Orbital Studies of Organic Molecules. *The Journal of Chemical Physics*, 54(2):724–728, 1971.

[125] Julian Tirado-Rives and William L. Jorgensen. Performance of B3LYP density functional methods for a large set of organic molecules. *Journal of Chemical Theory and Computation*, 4(2):297–306, 2008.

[126] Si Mohamed Bouzzine, Saïd Bouzakraoui, Mohammed Bouachrine, and Mohamed Hamidi. Density functional theory (B3LYP/6-31G*) study of oligothiophenes in their aromatic and polaronic states. *Journal of Molecular Structure: THEOCHEM*, 726 (1-3):271–276, 2005.

[127] M. A. Baldo, C. Adachi, and S. R. Forrest. Transient analysis of organic electrophosphorescence. II. Transient analysis of triplet-triplet annihilation. *Physical Review B - Condensed Matter and Materials Physics*, 62(16):10967–10977, 2000. ISSN 01631829.

[128] Sebastian Reineke, Karsten Walzer, and Karl Leo. Triplet-exciton quenching in organic phosphorescent light-emitting diodes with Ir-based emitters. *Physical Review B - Condensed Matter and Materials Physics*, 75(12):1–13, 2007. ISSN 10980121.

[129] Alexander S. Romanov, Le Yang, Saul T. E. Jones, Dawei Di, Olivia J. Morley, Bluebell H. Drummond, Antti P. M. Reponen, Mikko Linnolahti, Dan Credgington, and Manfred Bochmann. Dendritic Carbene Metal Carbazole Complexes as Photoemitters for Fully Solution-Processed OLEDs. *Chemistry of Materials*, 31:3613–3623, 2019. ISSN 0897-4756.

[130] Rasha Hamze, Shuyang Shi, Savannah C. Kapper, Daniel Sylvinson Muthiah Ravinson, Laura Estergreen, Moon Chul Jung, Abegail C. Tadle, Ralf Haiges, Peter I. Djurovich, Jesse L. Peltier, Rodolphe Jazzar, Guy Bertrand, Stephen E. Bradforth, and Mark E. Thompson. "Quick-Silver" from a Systematic Study of Highly Luminescent, Two-Coordinate, d10 Coinage Metal Complexes. *Journal of the American Chemical Society*, 141(21):8616–8626, 2019. ISSN 15205126.

[131] Rasha Hamze, Jesse L Peltier, Daniel Sylvinson, Moonchul Jung, Jose Cardenas, Ralf Haiges, Michele Soleilhavoup, Rodolphe Jazzar, Peter I Djurovich, Guy Bertrand, and Mark E Thompson. Eliminating nonradiative decay in Cu(I) emitters: >99% quantum efficiency and microsecond lifetime. *Science*, 606(February):601–606, 2019.

[132] Patrick J. Conaghan, S. Matthew Menke, Alexander S. Romanov, Saul T.E. Jones, Andrew J. Pearson, Emrys W. Evans, Manfred Bochmann, Neil C. Greenham, and Dan Credgington. Efficient Vacuum-Processed Light-Emitting Diodes Based on Carbene–Metal–Amides. *Advanced Materials*, 30(35):1–5, 2018. ISSN 15214095.

[133] Jiale Feng, Lupeng Yang, Alexander S. Romanov, Jirawit Ratanapreechachai, Antti-Pekka M. Reponen, Saul T. E. Jones, Mikko Linnolahti, Timothy J. H. Hele, Anna Köhler, Heinz Bässler, Manfred Bochmann, and Dan Credgington. Environmental Control of Triplet Emission in Donor–Bridge–Acceptor Organometallics. *Advanced Functional Materials*, page 1908715, Jan 2020. ISSN 1616-301X.

[134] S Thompson, J Eng, and T J Penfold. The intersystem crossing of a cyclic (alkyl)(amino) carbene gold (i) complex. *The Journal of Chemical Physics*, 149 (014304), 2018.

[135] Jelena Föller and Christel M. Marian. Rotationally Assisted Spin-State Inversion in Carbene-Mental-Amides Is an Artifact. *The Journal of physical chemistry letters*, 22 (8):5643–5647, 2017.

[136] Elliot J. Taffet, Yoann Olivier, Frankie Lam, David Beljonne, and Gregory D. Scholes. Carbene-Metal-Amide Bond Deformation, Rather Than Ligand Rotation, Drives Delayed Fluorescence. *The Journal of physical chemistry letters*, 7(9):1620–1626, 2018.

[137] Nadzeya A. Kukhta, Heather F. Higginbotham, Tomas Matulaitis, Andrew Danos, Aisha N. Bismillah, Nils Haase, Marc K. Etherington, Dmitry S. Yufit, Paul R. McGonigal, Juozas Vidas Gražulevičius, and Andrew P. Monkman. Revealing resonance effects and intramolecular dipole interactions in the positional isomers of benzonitrile-core thermally activated delayed fluorescence materials. *Journal of Materials Chemistry C*, 7(30):9184–9194, 2019. ISSN 2050-7526.

[138] T. Northey, J. Stacey, and T. J. Penfold. The role of solid state solvation on the charge transfer state of a thermally activated delayed fluorescence emitter. *Journal of Materials Chemistry C*, 5(42):11001–11009, 2017. ISSN 20507526.

[139] Benjamin L. Cotts, Dannielle G. McCarthy, Rodrigo Noriega, Samuel B. Penwell, Milan Delor, David D. Devore, Sukrit Mukhopadhyay, Timothy S. De Vries, and Naomi S. Ginsberg. Tuning Thermally Activated Delayed Fluorescence Emitter Photophysics through Solvation in the Solid State. *ACS Energy Letters*, 2(7):1526–1533, 2017. ISSN 23808195.

[140] Christopher R. Hall, Alexander S. Romanov, Manfred Bochmann, and Stephen R. Meech. Ultrafast Structure and Dynamics in the Thermally Activated Delayed Fluorescence of a Carbene-Metal-Amide. *The Journal of physical chemistry letters*, 9: 5873–5876, 2018.

[141] Kyoung Soo Yook and Jun Yeob Lee. Small molecule host materials for solution processed phosphorescent organic light-emitting diodes, 2014. ISSN 15214095.

[142] J. Lange, B. Ries, and H. Bässler. Diffusion and relaxation of triplet excitations in binary organic glasses. *Chemical Physics*, 128(1):47–58, 1988. ISSN 03010104.

[143] Paloma L. Dos Santos, Jonathan S. Ward, Andrei S. Batsanov, Martin R. Bryce, and Andrew P. Monkman. Optical and Polarity Control of Donor-Acceptor Conformation and Their Charge-Transfer States in Thermally Activated Delayed-Fluorescence Molecules. *Journal of Physical Chemistry C*, 121(30):16462–16469, 2017. ISSN 19327455.

[144] Timothy J. H. Hele and Dan Credgington. Theoretical description of Carbene-Metal-Amides. *arXiv*, feb 2018.

[145] Emrys W. Evans, Yoann Olivier, Yuttapoom Puttisong, William K. Myers, Timothy J.H. Hele, S. Matthew Menke, Tudor H. Thomas, Dan Credgington, David Beljonne, Richard H. Friend, and Neil C. Greenham. Vibrationally Assisted Intersystem Crossing in Benchmark Thermally Activated Delayed Fluorescence Molecules. *Journal of Physical Chemistry Letters*, 9(14):4053–4058, 2018. ISSN 19487185.

[146] Marc K. Etherington, Flavio Franchello, Jamie Gibson, Thomas Northey, Jose Santos, Jonathan S. Ward, Heather F. Higginbotham, Przemyslaw Data, Aleksandra Kurowska, Paloma Lays Dos Santos, David R. Graves, Andrei S. Batsanov, Fernando B. DIas, Martin R. Bryce, Thomas J. Penfold, and Andrew P. Monkman. Regio-A nd conformational isomerization critical to design of efficient thermally-activated delayed fluorescence emitters. *Nature Communications*, 8:1–11, 2017. ISSN 20411723.

[147] Alexander S. Romanov, Ciaran R. Becker, Charlotte E. James, Dawei Di, Dan Credgington, Mikko Linnolahti, and Manfred Bochmann. Copper and Gold Cyclic (Alkyl)(amino)carbene Complexes with Sub-Microsecond Photoemissions: Structure and Substituent Effects on Redox and Luminescent Properties. *Chemistry - A European Journal*, 23(19):4625–4637, 2017. ISSN 15213765.

[148] Alexander S. Romanov, Saul T. E. Jones, Qinying Gu, Patrick J. Conaghan, Bluebell H. Drummond, Jiale Feng, Florian Chotard, Leonardo Buizza, Morgan Foley, Mikko Linnolahti, Dan Credgington, and Manfred Bochmann. Carbene metal amide photoemitters: tailoring conformationally flexible amides for full color range emissions including white-emitting OLED. *Chemical Science*, pages 7–15, 2019. ISSN 2041-6520.

[149] Roberto S. Nobuyasu, Jonathan S. Ward, Jamie Gibson, Beth A. Laidlaw, Zhongjie Ren, Przemyslaw Data, Andrei S. Batsanov, Thomas J. Penfold, Martin R. Bryce, and Fernando B. Dias. The influence of molecular geometry on the efficiency of thermally activated delayed fluorescence. *Journal of Materials Chemistry C*, 7(22):6672–6684, 2019. ISSN 20507526.

[150] Fernando B Dias, Thomas J Penfold, and Andrew Monkman. Photophysics of thermally activated delayed fluorescence. *Methods Applied Fluorescence*, pages 425–463, 2018.

[151] Fernando B. Dias, Jose Santos, David R. Graves, Przemyslaw Data, Roberto S. Nobuyasu, Mark A. Fox, Andrei S. Batsanov, Tiago Palmeira, Mário N. Berberan-Santos, Martin R. Bryce, and Andrew P. Monkman. The role of local triplet excited states and D-A relative orientation in thermally activated delayed fluorescence: Photophysics and devices. *Advanced Science*, 3(12):1–10, 2016. ISSN 21983844.

[152] Soren K. Mellerup and Suning Wang. Boron-Doped Molecules for Optoelectronics. *Trends in Chemistry*, 1(1):77–89, 2019. ISSN 25895974.

[153] Noriko Yamaguchi and Sato Mari. Dipole Moment of Poly (ethylene oxide) in Solution and Its Dependence on Molecular Weight and Temperature. *Polymer Journal*, 41(8):588–594, 2009.

[154] J. A. Faucher, J. V. Koleske, E. R. Santee, J. J. Stratta, and C. W. Wilson. Glass transitions of ethylene oxide polymers. *Journal of Applied Physics*, 37(11):3962–3964, 1966. ISSN 00218979.

[155] Chongyun Wang, Feng Lili, Yang Huazhe, Xin Gongbiao, Wei Li, Jie Zheng, Wenhuai Tian, and Xingguo Li. Graphene oxide stabilized polyethylene glycol for heat storage. *Phys. Chem. Chem. Phys.*, 14:13233–13238, 2012.

[156] Melisa K Barron, Timothy J Young, Keith P Johnston, and Robert O Williams Iii. Investigation of Processing Parameters of Spray Freezing Into Liquid to Prepare Polyethylene Glycol Polymeric Particles for Drug Delivery. *AAPS PharSciTech*, 4(2): 1–13, 2003.

[157] Haopeng Wang, Jong K. Keum, Anne Hiltner, and Eric Baer. Impact of nanoscale confinement on crystal orientation of poly(ethylene oxide). *Macromolecular Rapid Communications*, 31(4):356–361, 2010. ISSN 10221336.

[158] Chuan Yar Lai, Anne Hiltner, Eric Baer, and Lashanda T.J. Korley. Deformation of confined poly(ethylene oxide) in multilayer films. *ACS Applied Materials and Interfaces*, 4(4):2218–2227, 2012. ISSN 19448244.

[159] Pachaiyappan Rajamalli, Natarajan Senthilkumar, Parthasarathy Gandeepan, Chen Zheng Ren-Wu, Hao Wu Lin, and Chien Hong Cheng. A thermally activated delayed blue fluorescent emitter with reversible externally tunable emission. *Journal of Materials Chemistry C*, 4(5):900–904, 2016. ISSN 20507526.

[160] Simon Gélinas, Olivier Paré-Labrosse, Colin Nadeau Brosseau, Sebastian Albert-Seifried, Christopher R. McNeill, Kiril R. Kirov, Ian A. Howard, Richard Leonelli, Richard H. Friend, and Carlos Silva. The binding energy of charge-transfer excitons localized at polymeric semiconductor heterojunctions. *Journal of Physical Chemistry C*, 115(14):7114–7119, 2011. ISSN 19327447.

[161] Akshay Rao, Philip C.Y. Chow, Simon Gélinas, Cody W. Schlenker, Chang Zhi Li, Hin Lap Yip, Alex K.Y. Jen, David S. Ginger, and Richard H. Friend. The role of spin in the kinetic control of recombination in organic photovoltaics. *Nature*, 500(7463): 435–439, 2013. ISSN 00280836.

[162] I. Tamm. Relativistic Interaction of Elementary Particles. *J. Phys.(USSR)*, 9:449, 1945.

[163] So Hirata and Martin Head-Gordon. Time-dependent density functional theory within the Tamm-Dancoff approximation. *Chemical Physics Letters*, 314(3-4):291–299, 1999. ISSN 00092614.

[164] S.M. Dancoff. Non-Adiabatic Meson Theory of Nuclear Forces. *Physical Review*, 78 (4):382–385, 1950.

[165] Christel M. Marian. Spin-orbit coupling and intersystem crossing in molecules. *Wiley Interdisciplinary Reviews: Computational Molecular Science*, 2(2):187–203, 2012. ISSN 17590876.

[166] V. G. Plotnikov. Regularities of the processes of radiationless conversion in polyatomic molecules. *International Journal of Quantum Chemistry*, 16(3):527–541, 1979. ISSN 1097461X.

[167] Patrick J Conaghan, Campbell S B Matthews, Florian Chotard, Saul T E Jones, Neil C Greenham, Manfred Bochmann, Dan Credgington, and Alexander S Romanov. Highly efficient blue organic light-emitting diodes based on carbene-metal-amides. *Nature Communications*, 11(1):1758, dec 2020. ISSN 2041-1723.

[168] Jamie Gibson, Andrew P. Monkman, and Thomas J. Penfold. The Importance of Vibronic Coupling for Efficient Reverse Intersystem Crossing in Thermally Activated Delayed Fluorescence Molecules. *ChemPhysChem*, 17(1):2956–2961, 2016. ISSN 14397641.

[169] Andrew Monkman. Photophysics of thermally activated delayed fluorescence. *Highly Efficient OLEDs: Materials Based on Thermally Activated Delayed Fluorescence*, pages 425–463, 2018.

[170] Julien Eng, Stuart Thompson, Heather Goodwin, Dan Credgington, and Thomas James Penfold. Competition between the heavy atom effect and vibronic coupling in donor–bridge–acceptor organometallics. *Physical Chemistry Chemical Physics*, pages 4659–4667, 2020. ISSN 1463-9076.

[171] Richard D. Burkhart, Norris J. Caldwell, and Gregory Haggquist. Polystyrene as an inert matrix for photophysical investigations. *Journal of Photochemistry and Photobiology, A: Chemistry*, 45(3):369–378, 1988. ISSN 10106030.

[172] G. Capano, U. Rothlisberger, I. Tavernelli, and T. J. Penfold. Theoretical Rationalization of the Emission Properties of Prototypical Cu(I)–Phenanthroline Complexes. *The Journal of Physical Chemistry A*, 119(27):7026–7037, 2015. ISSN 1089-5639.

[173] Xian Kai Chen, Dongwook Kim, and Jean Luc Brédas. Thermally Activated Delayed Fluorescence (TADF) Path toward Efficient Electroluminescence in Purely Organic Materials: Molecular Level Insight. *Accounts of Chemical Research*, 51(9):2215–2224, 2018. ISSN 15204898.

[174] Masaki Saigo, Kiyoshi Miyata, Sei'ichi Tanaka, Hajime Nakanotani, Chihaya Adachi, and Ken Onda. Suppression of Structural Change upon S 1 –T 1 Conversion Assists the Thermally Activated Delayed Fluorescence Process in Carbazole-Benzonitrile Derivatives. *The Journal of Physical Chemistry Letters*, 10(10):2475–2480, may 2019. ISSN 1948-7185.

[175] Till Biskup. Structure–Function Relationship of Organic Semiconductors: Detailed Insights From Time-Resolved EPR Spectroscopy. *Frontiers in Chemistry*, 7(Feb): 1–22, 2019. ISSN 2296-2646.

[176] Leah R. Weiss, Sam L. Bayliss, Felix Kraffert, Karl J. Thorley, John E. Anthony, Robert Bittl, Richard H. Friend, Akshay Rao, Neil C. Greenham, and Jan Behrends. Strongly exchange-coupled triplet pairs in an organic semiconductor. *Nature Physics*, 13(2):176–181, 2017. ISSN 17452481.